Summer 2024

Investigation of Cooperative Subradiance in Dense Ultracold Rubidium Ensembles

Brent Michael Jones
Old Dominion University, brent13jones@gmail.com

INVESTIGATION OF COOPERATIVE SUBRADIANCE IN DENSE ULTRACOLD RUBIDIUM ENSEMBLES

by

Brent Michael Jones
B.S. August 2016, Old Dominion University
M.S. May 2018, Old Dominion University

A Dissertation Submitted to the Faculty of
Old Dominion University in Partial Fulfillment of the
Requirements for the Degree of

DOCTOR OF PHILOSOPHY

PHYSICS

OLD DOMINION UNIVERSITY
August 2024

Approved by:

Charles Sukenik (Director)

Lawrence Weinstein (Member)

Anatoly Radyushkin (Member)

Ted Rogers (Member)

Richard Zimmerman (Member)

ABSTRACT

INVESTIGATION OF COOPERATIVE SUBRADIANCE IN
DENSE ULTRACOLD RUBIDIUM ENSEMBLES

Brent Michael Jones
Old Dominion University, 2024
Director: Dr. Charles Sukenik

This dissertation presents results of an experimental investigation of the time resolved fluorescence from a cold and dense ensemble of ^{87}Rb atoms after the sample is illuminated by a short probe pulse. The goal of the experiment was to investigate cooperative subradiant behavior, characterized by a much longer decay time compared to the natural lifetime, induced in an off resonant probe regime. Such long lived states, if controllable, would provide a means to store quantum information. The samples were initially created in a magneto-optical trap before atoms were loaded into a far off resonance trap to achieve atomic densities of $\approx 10^{14}$ atoms/cm^3. The off-resonant temporal response due to a 4 ns probe pulse was the main focus of the investigation, where the probe was blue-detuned $50 - 295$ MHz from the $5S_{1/2}\ F = 2 \rightarrow 5P_{3/2}\ F' = 3$ transition. Furthermore, by using a short probe pulse, we were able to probe the response outside of the typically explored steady state regime. Our results demonstrate subradiant behavior that is well described by the weak field coupled dipole model.

ACKNOWLEDGMENTS

The time I've spent at Old Dominion University has given me the most enriching experience in my life. That experience is defined not only by the knowledge and skills I've gained, but by the people who were a part of my journey. First, I'd like to sincerely thank Dr. Mark Havey for giving me the opportunity to achieve a goal I always thought would be out of reach. Without him, I would not be the person I am today. We miss you. Obviously, I must thank, from the bottom of my heart, Dr. Sukenik. He has done so much for me as an educator and as my advisor that it is hard to sum up in a few words. He is such a great person and I am honored to have been his student. I thank the physics department staff, Annette Guzman-Smith, Delicia Malin, and Lisa Okun (Physics Mom, you are greatly missed), who have continuously offered endless support and encouragement. I thank my lab partner and close friend, Joshua Carter. For the past 10 years we have worked together, through successes, hardship, and loss, and there is no one else I would have rather have had by my side. Thanks for dealing with my antics, making me laugh, and being a great person. Of course, I wholeheartedly thank Kitty Price, who has been by my side with endless encouragement, support, and love, through this academic endeavor. Undeniably, I am a better person because of Kitty, and I love you. I must also acknowledge various university faculty members who have supported me. Thank you Justin Mason, Charlotte Kimbro, and Tom Hartlove. Thanks to Charles Hyde and the nuclear group for allowing me to commandeer a particular oscilloscope for the entirety of my graduate career. Finally, with respect to my graduate experience, thanks to Dr. Dodge, my committee, and all of my professors throughout my time at ODU. Thanks to Dima Kupriyanov for insight on theoretical aspects of the

project. And a special thanks to my immediate predecessor in the lab, Stetson Roof.

Outside of the university I have had an abundance of support from my friends. Even though we do not get together often, their support has meant the world to me. Thank you Will, Whitney, Mike, Kerrie, and the entire Shively crew for accepting me as part of your family. Thank you Daniel Watson for the hockey nights, movies, and most importantly your friendship. Will and Danny, seriously, thank you so much, I love you guys. I must also mention Phil(UT), Ashley, Barbara, and Bob Dragan, who have acted as my second family since I've been 16 years old. I appreciate, more than you know, everything you've done for me over the years. The following is a list of people who have made an impact, at some point in my life, to whom I must give recognition. Thank you Clayton K., Adam A., Matthew Y.(Pio), Arty, Ben R., Marshall R., Josh C.(Runner), Tyler V., Greg B., Connor G., Kevin(Unx), Sterling G., Pat A., Levi W., Aimee C., Ashley A., Stephanie(Maz)., Jessica E., Jeremy P., Christina R., Mikhaila, Robert K.(robwizUp), Jason B., Grady W., Kate J., Caleb F., and Shae Brophy. I apologize to those not included, you are appreciated.

Next, I'd like to thank my family. Even though they live 1000 miles away, I literally and figuratively wouldn't be where I am today without them. Special thanks to my Grandma Alice who has always given me endless encouragement and support through every phase of my life. Of course, thanks to my Dad for the road trips, camping trips, and simply for being a great Dad. I appreciate all of the time and effort you gave to me as I grew up. Thanks to my Mom, April, Mitchel, Morgan, Sindy, Gayle, John, Jon, Lindsay, and Nick.

Finally, thank you to my companions, past and present, for their unconditional love. Mr. Beebs, Pippin, Edelweiss, Link, Charlie, Zelda, TeenyTiny, Beebles, and Squeebles.

TABLE OF CONTENTS

Page

LIST OF TABLES

LIST OF FIGURES

Figure Page

Figure Page

Figure Page

Figure Page

Figure Page

CHAPTER 1

INTRODUCTION

The study of the collective and cooperative behavior of many-body atomic systems has been a rich area of experimental and theoretical exploration over the past several decades. Many-body systems are interesting because the constituents not only interact with the external environment, but can also interact with each other. The result of these interactions can lead to a response of the system that diverges significantly from single atom behavior.

Investigation of light scattering is one of the main experimental avenues in the regime of light-matter interactions. Light scattering theory and experiments have tackled topics including, but not limited to, superradiance [1–10], subradiance [11–27], coherent back scattering [28–38], electromagnetically induced transparency (EIT) [39–46], and multiple scattering [47–52]. Investigating methods to control and read quantum systems is a common theme among a majority of these experiments. A controllable long-lived quantum system would be beneficial to the production of quantum memories and sensors.

An interesting set of topics in the realm of collective and cooperative effects of many-body systems is superradiance and subradiance, which were originally formulated by Dicke [1] in 1954. Dicke proposed that an ensemble of N two-level atoms separated by a distance much less than the excitation wavelength can interact cooperatively in such a way that modifies the decay rate of the system. In the most general sense these effects manifest themselves, due to the contribution of a set of atoms in a light field, in such a way that the excited state lifetime is enhanced or suppressed. Enhancement of the decay rate has been given the name superradiance while the suppression of the decay rate is known as subradiance. Superradiance has been studied to a much greater extent in comparison to subradiance, including in our laboratory by previous students [6, 7], due to the fragility of such long-lived subradiant states. Creating long-lived coherent states is a challenge because they are typically weakly coupled to excitation channels and highly susceptible to decoherence due to interaction with the surrounding environment. The experimental endeavour to directly observe subradiance in a extended, dense atomic sample is the main focus of this dissertation.

Subradiance has been reportedly observed using ions [11], molecular systems [13, 15], atomic lattices [16, 23], cold dilute atomic samples [17–22, 25, 27], and cold dense atomic

samples [26], where the authors have used direct and indirect evidence to justify their findings. Our experiment focused on the direct temporal decay behavior of both a cold dilute and dense atomic sample of ^{87}Rb under experimental conditions that have not yet been explored by other research groups.

Now a short history of several experiments involving the observation of subradiance in cold dilute and dense samples of ^{87}Rb will be given to provide context to the experimental landscape that has been explored in the past. There is one main group that has performed the bulk of the experimental observations of subradiance in dilute samples in recent years. The following experiments have all been performed on ^{87}Rb with a linearly polarized probe pulse where the given detuning is with respect to the $5S_{1/2}\ F = 2 \rightarrow 5P_{3/2}\ F = 3'$ transition. Subradiance has been reported to be observed in a cold ($T \approx 100\ \mu$K) spatially large (Gaussian radius $R \approx 1$ mm) but dilute ($\rho_0 \approx 10^{10}$-10^{11} cm^{-3}) ensemble after a weak probe pulse is introduced under several different experimental conditions [17, 20, 21, 25]. Probe pulse lengths were between 10-30 μs with detunings of -60 to 10 MHz. Guerin *et al.* [17] reported the first direct evidence of subradiance in a large dilute sample and determined the decay rate was dependent on optical depth. Weiss *et al.* [20] investigated subradiant decay and the significance of the probe beam size with respect to the sample size. Their findings suggest that radiation trapping, rather than subradiance, may dominate decay dynamics at large optical depths. Weiss *et al.* [21] analyzed subradiance over a large temperature range and discovered that the subradiant decay did not appreciably change until reaching temperatures upward of 500 μK. Cipris *et al.* [25] observed that the subradiant state population was enhanced by increasing the probe intensity. Within this dilute regime there were two main consensuses. The first was that the subradiant lifetime scaled with optical depth. Even at very low optical depth ($b_0 \leq 1$), the subradiant lifetime was shown to increase as optical depth was increased by Das *et al.* [22]. The second was, even though experimental and theoretical advances have been made, that the full analytical nature of subradiance is incomplete and further experimental and theoretical endeavors will be needed to paint a full picture. Analysis in this regime was typically accompanied with the comparison to the numerical results of the coupled dipole model. The coupled dipole model, which will be explained in more detail in a later chapter, requires an important rescaling of spatial parameters due to computational limitations on the number of atoms. In the dilute regime it was found that the coupled dipole model predicts the subradiant behavior when rescaling at constant optical depth. Although in the dense regime ($\rho_0 \approx 10^{13}$-10^{14} cm^{-3}), where less work has been done, Ferioli *et al.* [26] observed subradiance after a 150 ns probe pulse within a detuning

range between 0 and 18 MHz. They found the subradiant lifetime was found to scale with the number of atoms rather than the optical depth as for the dilute case, and was intensity independent for saturation parameters between 0.125 and 250. The coupled dipole model was also used during this analysis and the spatial rescaling was performed under constant density, which is in contrast to the dilute case. In summary, subradiance has been observed and analyzed in dilute and dense atomic samples due to a near resonant and long probe pulse. The long duration of the probe pulse, with respect to the natural lifetime, allows the system to largely achieve steady state and has been analyzed as such within the coupled dipole model.

Another interesting subradiance observation was attributed to two-body molecular experiments where typically dipole forbidden excited state molecular transitions were populated. The experiments were performed on Yb by Takasu *et al.* [13] and Sr by McGuyer *et al.* [15] which were able to take advantage of a simplified atomic energy level structure of these atoms. ^{87}Rb on the other hand has a much more complex molecular structure, described in more detail in the next chapter, which presents some challenges for populating long lived or 'forbidden' molecular transitions. While not the focus of this dissertation, our experiment explores a regime where many nearby repulsive ^{87}Rb molecular transitions are known to exist. Therefore, the two-body molecular mechanism was kept in mind. Creation of subradiant states in this case would likely manifest itself a strong detuning dependence in the subradiant state creation amplitude, thus showing deviations from expected many-body cooperative behavior. As will be shown, the many-body description models our results well, which leaves the molecular framework an open topic for future exploration.

The interpretation of subradiance has evolved over the years, which has led to some ambiguity. Subradiance can be attributed to several effects, which include cooperative many-body systems, forbidden two-body molecular transitions, and multiple scattering. Interesting challenges present themselves in attempting to separate these similar behaviors. For instance, our interpretation of multiple scattering is due to a photon traversing through the sample one atom at a time and exiting at a much later time than a single scatter. Although both multiple scattering and cooperative subradiance are attributed to delayed light exits, multiple scattering is not necessarily a cooperative excitation effect but simply due to the optical depth of the sample. Subradiance from the two-body molecular system has an entirely different foundational principle where a typically forbidden excited state that is weakly coupled to the ground state is populated. A possible avenue to decouple the different long lived effects is through the polarization dependence of the scattered light. Single scattering

events retain polarization information, which is in contrast to the random walk nature of multiple scattering where the scattered light is depolarized.

Our experiment probes dilute and dense ^{87}Rb ensembles at detunings of 50-295 MHz with respect to the $5S_{1/2}\ F = 2 \rightarrow 5P_{3/2}\ F = 3$ transition and for pulse widths of ≈ 4 ns. The short pulse does not allow for steady state approximations and the full temporal response was taken into account, which is in contrast to the aforementioned experiments where only the decay after probe shut off was analyzed. In summary, our experiment explored a new region of detuning space associated with many overlapping repulsive excited state molecular curves and analyzed temporal data with methods proven to be viable for many-body cooperative behavior. One motivation of our investigation was to determine if large deviations from the expected many-body behavior occur, and if so, can the behavior provide evidence of subradiance due to the mixing of molecular states. Another key facet of our experiment was the collection of subradiant decay with a pulse shorter than the natural lifetime, which, to our knowledge, has not been performed before.

The dissertation is organized as follows: The theory for the applicable atomic systems explored in this dissertation, from a simple two-level single atom, to multi-level two-body interactions, to many-body interactions will be discussed in Chapter 2. Most notably, the derivations and equations will provide insight into the physics involved with atom trapping, molecular excitations, and many-body cooperative behavior. Building off Chapter 2, atom trapping and characterization techniques used to create cold atomic ensembles will be presented in Chapter 3. Chapter 4 discusses the experimental arrangement and data acquisition techniques used to obtain the temporally resolved scattered light data that is presented and analyzed in Chapter 5. Finally, we conclude in Chapter 6 with a summary of our results and prospects for future investigations.

CHAPTER 2

THEORETICAL BACKGROUND

2.1 WIGNER-ECKART THEOREM

The Wigner-Eckart theorem (WET) is a powerful tool used in a significant number of atomic physics calculations due to its elegant ability to simplify matrix elements dealing with angular momentum eigenstates. Over the years the Wigner-Eckart theorem has evolved in such a way that, unfortunately, several different notation schemes which may or may not be equivalent to each other have been introduced. For clarity, the convention used in this section is equivalent to that of [53–55]. Similar conventions can also be found in Refs. [56–58]; these are extremely helpful resources.

The importance of the Wigner-Eckart theorem is that it allows the calculation of a matrix element of an irreducible tensor operator T^k_q where k is the tensor rank and q is the component. Many important interaction potentials, such as the dipole operator, take the form of irreducible tensors.

The generalized Wigner-Eckart theorem [54] is

$$\left\langle \alpha' j' m' | T^k_q | \alpha j m \right\rangle = (-1)^{j'-m'} \begin{pmatrix} j' & k & j \\ -m' & q & m \end{pmatrix} \left\langle \alpha' j' || T^k || \alpha j \right\rangle , \tag{1}$$

where α represents all other quantum numbers. The double bar matrix element is known as the reduced matrix element and it is independent of m, m', and q. The 2×3 matrix is known as the Wigner 3-j symbol. Since rubidium will be studied throughout this dissertation, namely the $5S_{1/2} \rightarrow 5P_{3/2}$ transition, only the relevant quantum numbers will be used from now on. The Wigner-Eckart theorem now reads

$$\left\langle J' I F' m'_F | T^k_q | J I F m_F \right\rangle = (-1)^{F'-m'_F} \begin{pmatrix} F' & k & F \\ -m'_F & q & m_F \end{pmatrix} \left\langle J' I F' || T^k || J I F \right\rangle , \tag{2}$$

where I is the nuclear spin, J is the electronic angular momentum, $F = I + J$ is the total atomic angular momentum, and m_F is the component of the total angular momentum in z.

The reduced matrix element can be further reduced to eliminate the F dependence by the following relation,

$$\begin{aligned}\left\langle J'IF'||T^k||JIF\right\rangle &= (-1)^{F+I+J'+k}\sqrt{(2F'+1)(2F+1)} \\ &\times \begin{Bmatrix} F' & k & F \\ J & I & J' \end{Bmatrix} \left\langle J'||T^k||J\right\rangle, \end{aligned} \tag{3}$$

where the 2×3 matrix in curly brackets is known as a 6-j symbol. The 3-j and 6-j symbols represent real numbers which can be calculated via tables or much more easily using Mathematica. The final matrix element is found by substitution of Eq. (3) into Eq. (2) which results in

$$\begin{aligned}\left\langle J'IF'm'_F|T^k_q|JIFm_F\right\rangle &= (-1)^{F'+F+I+J'+k-m'_F}\sqrt{(2F'+1)(2F+1)} \\ &\times \begin{pmatrix} F' & k & F \\ -m'_F & q & m_F \end{pmatrix} \begin{Bmatrix} F' & k & F \\ J & I & J' \end{Bmatrix} \left\langle J'||T^k||J\right\rangle, \end{aligned} \tag{4}$$

where the $\left\langle J'||T^k||J\right\rangle$ reduced matrix elements can be found experimentally.

The Hermitian adjoint of a spherical tensor operator, which acts as a spherical harmonic, is defined as [55]

$$T^{k\dagger}_q = (-1)^q T^k_{-q}. \tag{5}$$

Another useful property is

$$\left\langle Fm_F|T^k_q|F'm'_F\right\rangle^* = \langle Fm_F|T^{k\dagger}_q|F'm'_F\rangle. \tag{6}$$

Utilizing Eq. (5) and Eq. (6) together yields

$$\begin{aligned}\left\langle Fm_F|T^k_q|F'm'_F\right\rangle &= (-1)^q\langle Fm_F|T^{k\dagger}_{-q}|F'm'_F\rangle \\ &= (-1)^q\left\langle F'm'_F|T^k_{-q}|Fm_F\right\rangle^*, \end{aligned} \tag{7}$$

which is used to flip the prime and unprimed values and will be used in future sections.

2.2 SEMI-CLASSICAL ATOMIC THEORY

The discussion in this section will focus on a semi-classical theory where the atomic states are represented quantum-mechanically and interact with a classical electric field. Taking on the fully quantum picture also returns the same results, therefore either method is sufficiently appropriate. Certain results from this section will be referenced in various apparatus theory

sections. The basic concepts of this section are based primarily on discussions by Refs. [59, 60].

2.2.1 OPTICAL BLOCH EQUATIONS

The optical Bloch equations utilize the so-called density matrix which will be used to solve the Schrödinger equation for a two level atom in the interaction representation.

The density operator is defined as

$$\rho = \sum_i P_i |\psi_i\rangle\langle\psi_i|, \tag{8}$$

where $|\psi_i\rangle$ is an orthonormal state of the system. P_i is the probability of $|\psi_i\rangle$ existing in some arbitrary state. The probability follows the property of $\sum_i P_i = 1$ since the states $|\psi_i\rangle$ comprise a complete orthonormal set. Therefore the density operator acts on the state $|\psi_n\rangle$ as given by

$$\rho|\psi_n\rangle = \sum_i P_i |\psi_i\rangle\langle\psi_i|\psi_n\rangle = P_n|\psi_n\rangle. \tag{9}$$

The state vectors $|\psi_i\rangle$ can be expanded into a complete orthonormal basis set

$$|\psi_i\rangle = \sum_n a_{ni}|n\rangle = \sum_n |n\rangle\langle n|\psi_i\rangle, \tag{10}$$

where the completeness relation is

$$\sum_n |n\rangle\langle n| = 1. \tag{11}$$

The amplitude, or projection of the state $|\psi_i\rangle$ onto the basis state $|n\rangle$, is given by

$$\langle n|\psi_i\rangle = a_{ni}. \tag{12}$$

The density operator can be written in the matrix representation in the set of $|n\rangle$ basis states by substituting Eq. (10) into Eq. (8), which yields

$$\begin{aligned}\rho &= \sum_i P_i |\psi_i\rangle\langle\psi_i| = \sum_i \sum_{nm} P_i |n\rangle\langle n|\psi_i\rangle\langle\psi_i|m\rangle\langle m| \\ &= \sum_i \sum_{nm} a_{ni} a_{mi}^* P_i |n\rangle\langle m|,\end{aligned} \tag{13}$$

where the completeness relation Eq. (11) was inserted from the left and right sides. The specific matrix elements of the density operator are

$$\rho_{nm} = \langle n|\rho|m\rangle = \sum_i P_i a_{ni} a_{mi}^*, \tag{14}$$

where

$$\rho^*_{nm} = \langle n|\rho|m\rangle^* = \langle m|\rho|n\rangle = \rho_{mn}. \tag{15}$$

An important property of the density matrix is the trace, or the sum of the diagonal matrix elements, is exactly unity, and is given by

$$\begin{aligned}\mathrm{Tr}\left[\rho\right] &\equiv \sum_n \langle n|\rho|n\rangle = \sum_{ni} P_i \langle n|\psi_i\rangle\langle\psi_i|n\rangle = \sum_{ni} P_i \langle\psi_i|n\rangle\langle n|\psi_i\rangle \\ &= \sum_i P_i \langle\psi_i| \left(\sum_n |n\rangle\langle n|\right) |\psi_i\rangle = \sum_i P_i \langle\psi_i|\psi_i\rangle = 1.\end{aligned} \tag{16}$$

The Schrödinger equation in the density matrix representation is

$$\dot{\rho} = -\frac{i}{\hbar}\left[\hat{H}, \rho\right], \tag{17}$$

where the Hamiltonian is given by

$$\hat{H} = H_0 + V. \tag{18}$$

A particular matrix element is then given by

$$\dot{\rho}_{jk} = -\frac{i}{\hbar}\left[\langle j|\left(H_0 + V\right)\sum_{m,n}\rho_{mn}|m\rangle\langle n|k\rangle - \langle j|\sum_{m,n}\rho_{mn}|m\rangle\langle n|\left(H_0 + V\right)|k\rangle\right]. \tag{19}$$

The unperturbed energies follow

$$H_0|n\rangle = E_n|n\rangle = \hbar\omega_n|n\rangle, \tag{20}$$

which leads to a simplification of the matrix element

$$\dot{\rho}_{jk} = -i\rho_{jk}\left(\omega_j - \omega_k\right) - \frac{i}{\hbar}\left[\langle j|V\sum_{m,n}\rho_{mn}|m\rangle\langle n|k\rangle - \langle j|\sum_{m,n}\rho_{mn}|m\rangle\langle n|V|k\rangle\right]. \tag{21}$$

The matrix elements further simplify due to orthogonality of the states to

$$\dot{\rho}_{jk} = -i\rho_{jk}\left(\omega_j - \omega_k\right) - \frac{i}{\hbar}\sum_l \left(\rho_{lk}\langle j|V|l\rangle - \rho_{jl}\langle l|V|k\rangle\right). \tag{22}$$

In order to get the set of ODEs in a form viable for numerical calculations a rotation must be made by introducing a new matrix defined as

$$C_{jk} = \rho_{jk}e^{i(\omega_j - \omega_k)t}. \tag{23}$$

Taking the time derivative of Eq. (23) leads to a new set of differential equations given by

$$\begin{aligned}\dot{C}_{jk} &= \dot{\rho}_{jk}e^{i(\omega_j-\omega_k)t} + i\left(\omega_j-\omega_k\right)\rho_{jk}e^{i(\omega_j-\omega_k)t} \\ &= \dot{\rho}_{jk}e^{i(\omega_j-\omega_k)t} + i\left(\omega_j-\omega_k\right)C_{jk}. \end{aligned} \tag{24}$$

Substitution of Eq. (22) into Eq. (24) cancels out the oscillating terms and gives

$$\begin{aligned}\dot{C}_{jk} &= -\frac{i}{\hbar}\sum_l \left(\rho_{lk}\langle j|V|l\rangle - \rho_{jl}\langle l|V|k\rangle\right)e^{i(\omega_j-\omega_k)t} \\ &= -\frac{i}{\hbar}\sum_l \left(C_{lk}e^{-i(\omega_l-\omega_k)t}\langle j|V|l\rangle - C_{jl}e^{-i(\omega_j-\omega_l)t}\langle l|V|k\rangle\right)e^{i(\omega_j-\omega_k)t} \\ &= -\frac{i}{\hbar}\sum_l \left(C_{lk}e^{-i(\omega_l-\omega_j)t}\langle j|V|l\rangle - C_{jl}e^{-i(\omega_k-\omega_l)t}\langle l|V|k\rangle\right). \end{aligned} \tag{25}$$

The perturbation matrix elements due to the dipole operator are given by

$$\langle j|V|k\rangle = -eE_0\langle j|\hat{\boldsymbol{\epsilon}}\cdot\mathbf{r}|k\rangle\cos(\omega^\alpha t) = \frac{-eE_0}{2}\langle j|\hat{\boldsymbol{\epsilon}}\cdot\mathbf{r}|k\rangle\left[e^{i\omega^\alpha t}+e^{-i\omega^\alpha t}\right], \tag{26}$$

where ω^α is the frequency of the driving field and α is used to designate multiple lasers if necessary. The α superscript and sums can be dropped if there is only one laser. The perturbation is further simplified by the introduction of the Rabi frequency Ω^α_{jk} and the detuning Δ^α_{jk} of a particular laser ω^α from the resonance frequency between the j and k states

$$R^\alpha_{jk} = \frac{eE_0}{2\hbar}\langle j|\hat{\boldsymbol{\epsilon}}\cdot\mathbf{r}|k\rangle = \frac{\Omega^\alpha_{jk}}{2} \tag{27}$$

$$\omega^\alpha = (\omega_k-\omega_j) + \Delta^\alpha_{jk}. \tag{28}$$

It is important to note that a particular R^α_{jk} is half the Rabi frequency Ω^α_{jk} between states j and k. The Rabi frequency Ω^α_{jk} is a real value therefore $\Omega^\alpha_{kj} = \Omega^{*\alpha}_{jk} = \Omega^\alpha_{jk}$. If multiple lasers are used in the calculations many of the R^α_{jk} can be set to zero if the states are far away from each other. Substitution of Eq. (28) into Eq. (26) gives a result of

$$\begin{aligned}\langle j|V|k\rangle &= -\hbar\sum_\alpha R^\alpha_{jk}\left[e^{i\omega^\alpha t}+e^{-i\omega^\alpha t}\right] \\ &= -\hbar\sum_\alpha R^\alpha_{jk}\left[e^{i\left(\omega_k-\omega_j+\Delta^\alpha_{jk}\right)t}+e^{-i\left(\omega_k-\omega_j+\Delta^\alpha_{jk}\right)t}\right]. \end{aligned} \tag{29}$$

Substitution of Eq. (29) into Eq. (25) with the appropriate subscripts gives

$$\begin{aligned}\dot{C}_{jk} &= i\sum_l C_{lk}\sum_\alpha R^\alpha_{jl}\left[e^{i\Delta^\alpha_{jl}t}+e^{-i\left(2(\omega_l-\omega_j)+\Delta^\alpha_{jk}\right)t}\right] \\ &\quad - i\sum_l C_{jl}\sum_\alpha R^\alpha_{lk}\left[e^{i\Delta^\alpha_{lk}t}+e^{-i\left(2(\omega_k-\omega_l)+\Delta^\alpha_{lk}\right)t}\right], \end{aligned} \tag{30}$$

where the oscillating terms can be removed after invoking the rotating wave approximation which yields

$$\dot{C}_{jk} = i \sum_{l,\alpha} \left[C_{lk} R^{\alpha}_{jl} e^{i\Delta^{\alpha}_{jl} t} - C_{jl} R^{\alpha}_{lk} e^{i\Delta^{\alpha}_{lk} t} \right]. \tag{31}$$

The next appropriate step is to separate Eq. (31) into diagonal and off diagonal terms, which are given by

$$\dot{C}_{jk} = i \sum_{l,\alpha} \left[C_{lk} R^{\alpha}_{jl} e^{i\Delta^{\alpha}_{jl} t} - C_{jl} R^{\alpha}_{lk} e^{i\Delta^{\alpha}_{lk} t} \right] - \frac{\Gamma_j + \Gamma_k + \Gamma_L}{2} C_{jk} \tag{32}$$

$$\dot{C}_{jj} = \sum_{l,\alpha} \left[i C_{lj} R^{\alpha}_{jl} e^{i\Delta^{\alpha}_{jl} t} - i C_{jl} R^{\alpha}_{lj} e^{i\Delta^{\alpha}_{lj} t} + A_{lj} C_{ll} \right] - \Gamma_j C_{jj}, \tag{33}$$

where Γ_j is spontaneous emission/decay and Γ_L represents the linewidth of the laser. The reasoning behind the inclusion of the decay terms in this form can be seen by analyzing Eq. (32) and Eq. (33) in the absence of an electric field and assuming that the amplitudes decay exponentially. This can be seen by first defining the matrix elements C_{jk} in terms of the amplitudes of the j^{th} and k^{th} state, which is given by

$$C_{jk} = a_j(t) a^*_k(t). \tag{34}$$

In the absence of an electric field the amplitudes are assumed to decay as $a_i = a_i(0) e^{-\frac{\Gamma_i}{2} t}$ and therefore $C_{jk} = a_j(0) a^*_k(0) e^{-\frac{\Gamma_j + \Gamma_k}{2} t}$. This is based on the empirical nature of atomic systems that exponentially decay at their respective natural decay rate. With the aforementioned in mind Eq. (32) and Eq. (33) follow the same behavior. The spontaneous decay term is defined as

$$\Gamma_j = \sum_{l=1} A_{jl}, \tag{35}$$

where A_{jl} is the decay rate from state j to state l. Non-zero values of A_{jl} occur when $j > l$ for most applications since spontaneous decay happens from an upper state to a lower state, therefore $\Gamma_{21} \neq \Gamma_{12} = 0$ if state 2 is defined as the upper state and the transition from $2 \rightarrow 1$ is dipole allowed. Depending on the initial labeling of the states this may change and must be taken care of appropriately.

At this point the $\dot{C}_{jk}$ matrix elements can be determined by Eq. (32) and Eq. (33). The detuning values Δ^{α}_{jk} have an important property where

$$\Delta^{\alpha}_{kj} = -\Delta^{\alpha}_{jk}. \tag{36}$$

The trend of Δ^{α}_{jk} where $j < k$ is used. For example, if laser 1 is above the resonance energy between a lower state 1 and upper state 2, then Δ^{1}_{12} is taken as a positive value from state 2. Rabi frequencies follow the property where

$$R^{\alpha}_{kj} = R^{\alpha}_{jk}. \tag{37}$$

The matrix elements Eq. (32) and Eq. (33) still have oscillatory behavior due to the $e^{i\Delta^{\alpha}_{jk}t}$ terms, therefore another rotation must be made to further simplify the equations for numerical computation. Most texts typically stop at this point because the next rotation is dependent on the type of system, number of lasers, and number of states. The next substitutions are typically non-trivial but a method was found that depends on the excitation path an atom could take from state $j \to k$.

For the next rotation, lets define the following

$$\sigma^{\alpha}_{jk} = C_{jk}e^{-i\Delta_{jk,\text{path}}t}, \tag{38}$$

where $\Delta_{jk,\text{path}}$ is the sum of the detunings going from j to k if both j and k are directly accessed by lasers. There is a small modification for states which are not accessed by lasers, as in a state which an excited state can decay to and then decay back to a ground state. The modification is small and still follows the same logic. An example is needed to clarify. First, assume a system of eight states and two lasers. The first laser connects states $1 \to 2$ with detuning Δ^{1}_{12} and $1 \to 3$ with Δ^{1}_{13}. The ground state, state 1, is analogous to ^{85}Rb $5S_{1/2}$ $F = 3$, while states 2 and 3 are analogous to the $5P_{3/2}$ $F = 3$ and $F = 4$ respectively. The second laser connects states 2 and 3 to 4,5,6, and 7, which are analogous to the $5D_{5/2}$ $F = 5, 4, 3, 2$ respectively. Finally state 8 is analogous to the $6P_{3/2}$ state which the $5D_{5/2}$ can decay to. State 8 can then decay to state 1. Therefore the following laser transitions are allowed. $(1 \to 2, 3)$, $(2 \to 5, 6, 7)$, and $(3 \to 4, 5, 6)$.

After performing the $\dot{C}_{jk}$ sum in Eq. (31), substitutions to go from $C_{jk} \to \sigma_{jk}$ is approached in the following way. As mentioned in the description of Eq. (38) a *path* from state j to k must be obtained and then a direct substitution can be made. For example the path $\Delta_{jk,\text{path}}$ for σ_{12} is simply Δ^{1}_{12} because a laser is directly connected to those two states. A more complex example would be σ_{47}. There is no laser connecting those states directly, therefore the path must go through the states as $(4 \to 3 \to 1 \to 2 \to 7)$. The detuning path will then be $\Delta^{2}_{43} + \Delta^{1}_{31} + \Delta^{1}_{12} + \Delta^{2}_{27}$, where after using the property in Eq. (36) becomes $-\Delta^{2}_{34} - \Delta^{1}_{13} + \Delta^{1}_{12} + \Delta^{2}_{27}$. The substitution, or rotation, is then

$$\sigma_{47} = C_{47}e^{-i\left(-\Delta^{2}_{34}-\Delta^{1}_{13}+\Delta^{1}_{12}+\Delta^{2}_{27}\right)t}. \tag{39}$$

Continuing the process, the time derivative yields

$$\dot{\sigma}_{47} = \dot{C}_{47} e^{-i\left(-\Delta^2_{34}-\Delta^1_{13}+\Delta^1_{12}+\Delta^2_{27}\right)t} - i\left(-\Delta^2_{34} - \Delta^1_{13} + \Delta^1_{12} + \Delta^2_{27}\right)\sigma_{47}, \tag{40}$$

where $\dot{C}_{47}$ was obtained by Eq. (31). All other substitutions for states connected by lasers follow the same simple path method. Now to discuss the aforementioned modification for states not directly connected by lasers, as in state 8 in this example. Essentially the process is the same but there is no "path" to 8. For example, σ_{58} the path must go through the states $(5 \to 2 \to 1 \to 8)$ which yields $\Delta^2_{52} + \Delta^1_{21} + \Delta^?_{18}$ but $\Delta^?_{18} = 0$ because no laser connects the states. The rotation for this element is given by

$$\sigma_{58} = C_{58} e^{-i\left(-\Delta^2_{25}-\Delta^1_{12}\right)t}. \tag{41}$$

There is also another path $(5 \to 3 \to 1 \to 8)$ which is equally correct and is exactly the same as the previous path. This can be seen because states 2 and 3 are split by a value S_{23}. The first laser connecting states $(1 \to 2, 3)$ is detuned a value of Δ^1_{13} from state 3, therefore it is detuned from state 2 by $\Delta^1_{12} = \Delta^1_{13} + S_{23}$. Similarly for the states $(2, 3 \to 5, 6)$, $\Delta^2_{25} = \Delta^2_{35} - S_{23}$. Substitutions can be made then which show $\Delta^2_{25} + \Delta^1_{12} = \Delta^2_{35} + \Delta^1_{13}$. In order to add a bit more completeness, it was determined there is no $(1 \to 8)$ path, therefore $\sigma_{18} = C_{18}$.

The possible paths were computationally determined by envisioning the paths from some $j \to k$ with a matrix. The matrix shown in Eq. (42) represents a simple 1/0 (allowed/not allowed) for a transition between $j \to k$. Selecting a particular j row of the matrix provides the states in which the j state can transition to.

$$\begin{pmatrix} 0 & 1 & 1 & 0 & 0 & 0 & 0 & 0 \\ 1 & 0 & 0 & 0 & 1 & 1 & 1 & 0 \\ 1 & 0 & 0 & 1 & 1 & 1 & 0 & 0 \\ 0 & 0 & 1 & 0 & 0 & 0 & 0 & 0 \\ 0 & 1 & 1 & 0 & 0 & 0 & 0 & 0 \\ 0 & 1 & 1 & 0 & 0 & 0 & 0 & 0 \\ 0 & 1 & 0 & 0 & 0 & 0 & 0 & 0 \\ 0 & 0 & 0 & 0 & 0 & 0 & 0 & 0 \end{pmatrix} \tag{42}$$

For an example $j = 5$ is chosen, $\begin{pmatrix} 0 & 1 & 1 & 0 & 0 & 0 & 0 & 0 \end{pmatrix}$, which opens up two new paths starting from 2 and 3. The path starting at 2, $\begin{pmatrix} 1 & 0 & 0 & 0 & \mathrm{X} & 1 & 1 & 0 \end{pmatrix}$, opens up

three new paths. The X is put in to eliminate simply going back to state 5 and signifies a stop to a particular path. As the process continues a list of paths is created. Some paths may end at the same value of k while others may end at different values of k. Therefore specifically searching for a path starting with $j = 5$ and ending at some k may return several paths, but the shortest path is always chosen for the substitutions. For states not connected by a laser the computational process is slightly different due to no path leading to state 8. The path which is chosen for some σ_{j8} is always the path that goes from $j \to 1$. Again there is no path from $1 \to 8$, therefore the path from $j \to 8$ is simply $j \to 1$. The last statement must be reiterated to avoid confusion. If state 8 is *not* connected by a laser, then the path to state 8 is instead defined as the path to state 1. It was found that, if these rules are followed, the results always agree with know results. With that in mind, the output of this method will be given for two and three level systems.

A few simple results will be presented since the two level atom approximation will be utilized in following sections. Solving the $\dot{\sigma}_{jk}$ terms for a two level system gives the following expected results.

$$\dot{\sigma}_{11} = -i\frac{\Omega_{12}}{2}\left(\sigma_{12} - \sigma_{21}\right) + \Gamma_{21}\sigma_{22} \tag{43}$$

$$\dot{\sigma}_{12} = -i\frac{\Omega_{12}}{2}\left(\sigma_{11} - \sigma_{22}\right) - \left(\frac{\Gamma_{21}}{2} + i\Delta_{12}\right)\sigma_{12} \tag{44}$$

$$\dot{\sigma}_{21} = i\frac{\Omega_{12}}{2}\left(\sigma_{11} - \sigma_{22}\right) - \left(\frac{\Gamma_{21}}{2} - i\Delta_{12}\right)\sigma_{21} \tag{45}$$

$$\dot{\sigma}_{22} = i\frac{\Omega_{12}}{2}\left(\sigma_{12} - \sigma_{21}\right) - \Gamma_{21}\sigma_{22}. \tag{46}$$

The steady state solutions can be found by setting the l.h.s. of each of the above equations to zero. After appropriate substitutions the steady state solutions are

$$\sigma_{12} = -\left(\frac{\Omega_{12}}{2}\right)\frac{\left(\Delta_{12} + i\frac{\Gamma_{21}}{2}\right)}{\Delta_{12}^2 + \left(\frac{\Gamma_{21}}{2}\right)^2 + \frac{1}{2}\Omega_{12}^2} \tag{47}$$

$$\sigma_{22} = \left(\frac{\Omega_{12}}{2}\right)^2\frac{1}{\Delta_{12}^2 + \left(\frac{\Gamma_{21}}{2}\right)^2 + \frac{1}{2}\Omega_{12}^2}, \tag{48}$$

where $\sigma_{21} = \sigma_{12}^*$ and $\sigma_{11} = \sigma_{22} - 1$. Solving for the original density matrix elements C_{jk} one must include the term substituted in Eq. (38), therefore yielding

$$C_{12} = \sigma_{12}e^{i\Delta_{12}t} = \sigma_{12}e^{i(\omega-\omega_0)t} \tag{49}$$

$$C_{22} = \sigma_{22}. \tag{50}$$

Although most of the upcoming derivations in the following sections rely on the two level atom approximation, I was also involved with a separate, electromagnetically induced transparency (EIT) project in our lab that required the optical Bloch equations to handle multiple lasers interacting with an atom of several levels. For example, the solutions to a three level atom system in the ladder configuration interacting with two lasers are given in Eq. (51). Ω_{12}^1 corresponds to the Rabi frequency due to the first laser on the $1 \rightarrow 2$ transition while Ω_{23}^2 corresponds to the second laser on the $2 \rightarrow 3$ transition. The results given in Eq. (51) are also consistent with previous works on EIT systems utilizing the three level approach in a ladder configuration [42, 45, 46].

$$\begin{aligned}
\dot{\sigma}_{11} &= -i\frac{\Omega_{12}^1}{2}\left(\sigma_{12}-\sigma_{21}\right)+\Gamma_{21}\sigma_{22} \\
\dot{\sigma}_{12} &= -i\frac{\Omega_{12}^1}{2}\left(\sigma_{11}-\sigma_{22}\right)-\left(\frac{\Gamma_{21}}{2}+i\Delta_{12}^1\right)\sigma_{12}-i\frac{\Omega_{23}^2}{2}\sigma_{13} \\
\dot{\sigma}_{13} &= -i\frac{\Omega_{23}^2}{2}\sigma_{12}+i\frac{\Omega_{12}^1}{2}\sigma_{23}-\left(\frac{\Gamma_{32}}{2}+i\left(\Delta_{12}^1+\Delta_{23}^2\right)\right)\sigma_{13} \\
\dot{\sigma}_{22} &= i\frac{\Omega_{12}^1}{2}\left(\sigma_{12}-\sigma_{21}\right)-\Gamma_{21}\sigma_{22}+\Gamma_{32}\sigma_{33}-i\frac{\Omega_{23}^2}{2}\left(\sigma_{23}-\sigma_{32}\right) \\
\dot{\sigma}_{23} &= i\frac{\Omega_{12}^1}{2}\sigma_{13}-i\frac{\Omega_{23}^2}{2}\left(\sigma_{22}-\sigma_{33}\right)-\left(\frac{\Gamma_{21}+\Gamma_{32}}{2}+i\Delta_{23}^2\right)\sigma_{23} \\
\dot{\sigma}_{33} &= i\frac{\Omega_{23}^2}{2}\left(\sigma_{23}-\sigma_{32}\right)-\Gamma_{32}\sigma_{33}.
\end{aligned} \tag{51}$$

The EIT project involved a system of nine levels and three lasers. Although it is not completely relevant for this dissertation, the research expanded the scope of EIT and its effect on coherent processes [61], which was built off previous works by [39–46]. The solutions to the 81 matrix elements are extremely long and cumbersome to present in this dissertation. Therefore, a Mathematica notebook which utilizes the path algorithm for the nine level system is available upon request.

2.2.2 TWO LEVEL ATOM

The aforementioned optical Bloch equations are simplified in the two level atom regime. This section will first discuss the two level atom with no broadening mechanisms and then include dampening factors to obtain useful experimental parameters and physical behaviors. In order to be complete, this section will begin with basic quantum mechanical relations and wave function definitions before applying the optical Bloch equations that were previously discussed.

The basic starting point is the time dependent Schrödinger equation

$$i\hbar\frac{d\Psi(\mathbf{r},t)}{dt} = \hat{H}\Psi(\mathbf{r},t), \tag{52}$$

where $\hat{H} = \hat{H}_0 + \hat{V}$ is the full quantum Hamiltonian. $\Psi(\mathbf{r},t)$ is the time dependent wave function defined as

$$\Psi(\mathbf{r},t) = \sum_n a_n(t)\psi_n(\mathbf{r},t) = \sum_n a_n(t)e^{-iE_nt/\hbar}\varphi_n(\mathbf{r}), \tag{53}$$

where $\varphi(\mathbf{r})$ is the purely radial portion of the wave function

$$\psi_n(\mathbf{r},t) = e^{-iE_nt/\hbar}\varphi_n(\mathbf{r}), \tag{54}$$

and the unperturbed Hamiltonian $\hat{H}_0$ acts as

$$\hat{H}_0\varphi_n(\mathbf{r}) = E_n\varphi_n(\mathbf{r}). \tag{55}$$

In the two atom case that is presented, Eq. (53) simplifies to

$$\begin{aligned}\Psi(\mathbf{r},t) &= a_1(t)\psi_1(\mathbf{r},t) + a_2(t)\psi_2(\mathbf{r},t)\\ &= a_1(t)|1(t)\rangle + a_2(t)|2(t)\rangle,\end{aligned} \tag{56}$$

where the time dependent amplitudes $a_n(t)$ are the same as the a coefficients first introduced in Eq. (10). The wavefunctions for the ground and excited state are

$$\begin{aligned}\psi_1(\mathbf{r},t) &= e^{-iE_1t/\hbar}\varphi_1(\mathbf{r}) = e^{-iE_1t/\hbar}|1\rangle\\ \psi_2(\mathbf{r},t) &= e^{-iE_2t/\hbar}\varphi_2(\mathbf{r}) = e^{-iE_2t/\hbar}|2\rangle.\end{aligned} \tag{57}$$

After this point, the functional dependencies of the particular wavefunctions will be omitted when not explicitly needed. In the two level regime there is an on resonance energy with resonant frequency ω_0 between the ground state and excited state that is defined as

$$\hbar\omega_0 = E_2 - E_1. \tag{58}$$

As a first step to solve for the a_1 and a_2 coefficients, the wavefunction Eq. (56) is substituted into Eq. (52). The left hand side is given by

$$\begin{aligned}i\hbar\left(\dot{a}_1\psi_1 + a_1\dot{\psi}_1 + \dot{a}_2\psi_2 + a_2\dot{\psi}_2\right) &= i\hbar\left(\dot{a}_1\psi_1 + a_1(-iE_1/\hbar)\psi_1 + \dot{a}_2\psi_2 + a_2(-iE_2/\hbar)\psi_2\right)\\ &= E_1a_1\psi_1 + E_2a_2\psi_2 + i\hbar\left(\dot{a}_1\psi_1 + \dot{a}_2\psi_2\right),\end{aligned} \tag{59}$$

and the right hand side is given by

$$\left(\hat{H}_0 + \hat{V}\right)(a_1\psi_1 + a_2\psi_2) = E_1 a_1\psi_1 + E_2 a_2\psi_2 + \hat{V}(a_1\psi_1 + a_2\psi_2). \tag{60}$$

Equating Eq. (59) and Eq. (60) yields

$$i\hbar(\dot{a}_1\psi_1 + \dot{a}_2\psi_2) = \hat{V}(a_1\psi_1 + a_2\psi_2). \tag{61}$$

Solving for $\dot{a}_1$ requires multiplication by ψ_1^* from the left side of Eq. (61) and then integrated over all space. The bra-ket notation will absorb the spatial integral.

$$\begin{aligned} i\hbar\psi_1^*(\dot{a}_1\psi_1 + \dot{a}_2\psi_2) &= \psi_1^*\hat{V}(a_1\psi_1 + a_2\psi_2) \\ i\hbar\left(\dot{a}_1\langle 1|1\rangle + \dot{a}_2\cancel{\langle 1|2\rangle}e^{-i\omega_0 t}\right) &= a_1\langle 1|\hat{V}|1\rangle + a_2\langle 1|\hat{V}|2\rangle e^{-i\omega_0 t} \\ i\hbar\dot{a}_1 &= a_1\langle 1|\hat{V}|1\rangle + a_2\langle 1|\hat{V}|2\rangle e^{-i\omega_0 t} \end{aligned} \tag{62}$$

Then solving for $\dot{a}_2$ in the same way but with multiplication of ψ_2^* yields

$$\begin{aligned} i\hbar\psi_2^*(\dot{a}_1\psi_1 + \dot{a}_2\psi_2) &= \psi_2^*\hat{V}(a_1\psi_1 + a_2\psi_2) \\ i\hbar\left(\dot{a}_1\cancel{\langle 2|1\rangle}e^{i\omega_0 t} + \dot{a}_2\langle 2|2\rangle\right) &= a_1\langle 2|\hat{V}|1\rangle e^{i\omega_0 t} + a_2\langle 2|\hat{V}|2\rangle \\ i\hbar\dot{a}_2 &= a_1\langle 2|\hat{V}|1\rangle e^{i\omega_0 t} + a_2\langle 2|\hat{V}|2\rangle. \end{aligned} \tag{63}$$

The interaction potential $\hat{V}$ is that of an atom acting as an electric dipole with dipole moment $\mathbf{d}$ in an electric field with amplitude E_0, frequency ω, and polarization $\hat{\boldsymbol{\epsilon}}$ is defined as

$$\hat{V} = e\mathbf{d}\cdot\mathbf{E} = eE_0\cos(\omega t)\mathbf{d}\cdot\hat{\boldsymbol{\epsilon}} = \hat{H}_{\mathrm{I}}. \tag{64}$$

The potential is defined to be in the dipole approximation regime where the electric field is near resonant with the atomic transition. The dipole approximation meets the conditions of

$$\Delta \ll \omega + \omega_0, \tag{65}$$

where Δ is the detuning from resonance which is given by

$$\Delta = \omega - \omega_0. \tag{66}$$

Taking the electric field as polarized in the $\hat{\mathbf{x}}$ direction Eq. (64) can be substituted into Eq. (62) and Eq. (63) gives

$$\begin{aligned}
i\hbar\dot{a}_1 &= eE_0\left(a_1\cancel{\langle 1|x|1\rangle}\cos(\omega t) + a_2\langle 1|x|2\rangle e^{-i\omega_0 t}\cos(\omega t)\right) \\
&= eE_0\langle 1|x|2\rangle e^{-i\omega_0 t}\cos(\omega t)a_2 \\
\dot{a}_1 &= -i\frac{eE_0X_{12}}{\hbar}e^{-i\omega_0 t}\cos(\omega t)a_2 \\
&= -i\Omega_{12}e^{-i\omega_0 t}\cos(\omega t)a_2 \qquad (67) \\
i\hbar\dot{a}_2 &= eE_0\left(a_1\langle 2|x|1\rangle e^{i\omega_0 t}\cos(\omega t) + a_2\cancel{\langle 2|x|2\rangle}\cos(\omega t)\right) \\
&= eE_0\langle 2|x|1\rangle e^{i\omega_0 t}\cos(\omega t)a_1 \\
\dot{a}_2 &= -i\frac{eE_0X_{12}^*}{\hbar}e^{i\omega_0 t}\cos(\omega t)a_1 \\
&= -i\Omega_{12}^*e^{i\omega_0 t}\cos(\omega t)a_1, \qquad (68)
\end{aligned}$$

where only off diagonal elements are non-zero because the dipole operator only couples states with an allowed transition. This simply means the electric field does not induce a ground state atom to undergo a transition and remain in the same state. $X_{21} = X_{12}^*$ and $\Omega_{12}^* = \Omega_{21}$. The dipole matrix element X_{12} and the so-called Rabi frequency Ω_{12} are defined as

$$X_{12} = \langle 1|\hat{\boldsymbol{\epsilon}}\cdot\mathbf{r}|2\rangle = \langle 1|x|2\rangle = \int \varphi_1^* x\varphi_2 dV, \qquad (69)$$

and

$$\Omega_{12} = \frac{eE_0X_{12}}{\hbar}, \qquad (70)$$

where they follow the condition of

$$X_{21} = X_{12}^* \quad \therefore \quad \Omega_{21} = \Omega_{12}^*. \qquad (71)$$

A weak field approximation is used to solve for the $a_1(t)$ and $a_2(t)$. The atom population starts in the ground state and a weak field is applied such that the excited state does not get appreciably populated. The conditions of this approximation are

$$a_1(0) = 1 \ \text{ and } \ a_2(0) = 0 \qquad (72)$$

$$a_1(t) \approx 1 \ \text{ and } \ a_2(t) \approx 0. \qquad (73)$$

Substituting $a_1(t)$ in Eq. (73) into Eq. (68) simplifies $\dot{a}_2$ to

$$\begin{aligned}
\dot{a}_2(t) &= -i\Omega_{12}^* e^{i\omega_0 t}\cos(\omega t)a_1 \\
&\approx -i\Omega_{12}^* e^{i\omega_0 t}\cos(\omega t) \\
&= \frac{-i\Omega_{12}^*}{2}e^{i\omega_0 t}\left(e^{i\omega t}+e^{-i\omega t}\right) \\
&= \frac{-i\Omega_{12}^*}{2}\left(e^{i(\omega_0+\omega)t}+e^{i(\omega_0-\omega)t}\right), \qquad (74)
\end{aligned}$$

which now can be integrated from 0 to t to give

$$\begin{aligned}
\int_0^t \dot{a}_2(t)dt = a_2(t) - \cancel{a_2(0)} &= \int_0^t \frac{-i\Omega_{12}^*}{2}\left(e^{i(\omega_0+\omega)t}+e^{i(\omega_0-\omega)t}\right)dt \\
a_2(t) &= \frac{\Omega_{12}^*}{2}\left(\frac{1-e^{i(\omega_0+\omega)t}}{(\omega_0+\omega)}+\frac{1-e^{i(\omega_0-\omega)t}}{(\omega_0-\omega)}\right). \qquad (75)
\end{aligned}$$

The on resonant behavior, when the electric field frequency ω is exactly the resonant frequency ω_0, Eq. (75) can be re-written as

$$\begin{aligned}
a_2(t) &= \lim_{\omega\to\omega_0}\frac{\Omega_{12}^*}{2}\left(\frac{1-e^{i(\omega_0+\omega)t}}{(\omega_0+\omega)}+\frac{1-e^{i(\omega_0-\omega)t}}{(\omega_0-\omega)}\right) \\
&= \frac{\Omega_{12}^*}{2}\left(\frac{-ie^{i\omega_0 t}\sin(\omega_0 t)}{\omega_0}+\lim_{\omega\to\omega_0}\frac{1-e^{i(\omega_0-\omega)t}}{(\omega_0-\omega)}\right) \\
&= \frac{\Omega_{12}^*}{2}\left(\frac{-ie^{i\omega_0 t}\sin(\omega_0 t)}{\omega_0}-it\right) \\
&= -\frac{i\Omega_{12}^*}{2\omega_0}\left(e^{i\omega_0 t}\sin(\omega_0 t)+\omega_0 t\right), \qquad (76)
\end{aligned}$$

where L'Hôspital's rule was used on the second term of the second line.

Further simplification can be achieved by invoking the rotating wave approximation (r.w.a.) where the highly oscillatory terms $(\omega_0+\omega)$ can be ignored. Along with the dipole approximation Eq. (65), the use of the r.w.a. is justified because typical atomic transition times are in the 10^{-7}s range and the resonant frequencies ω_0 are in the 10^{15} s^{-1} range. Therefore the condition

$$\omega_0 t \gg 1 \qquad (77)$$

is satisfied, which means a significant amount of oscillations of the electric field occur before the probability of excitation is appreciable. These oscillations average to zero. When applying this condition to Eq. (76), only the second term would be taken.

For the arbitrary ω case the r.w.a. sets the first term on the right hand side of Eq. (75) to zero and the amplitude of $a_2(t)$ is simplified to yield

$$\begin{aligned} a_2(t) &= \frac{\Omega^*}{2}\left(\frac{1-e^{i(\omega_0-\omega)t}}{(\omega_0-\omega)}\right) \\ &= -\frac{\Omega^*}{2}e^{i(\omega_0-\omega)t/2}\left(\frac{e^{i(\omega_0-\omega)t/2}-e^{-i(\omega_0-\omega)t/2}}{(\omega_0-\omega)}\right) \\ &= -i\Omega^* e^{i(\omega_0-\omega)t/2}\frac{\sin\left((\omega_0-\omega)\,t/2\right)}{(\omega_0-\omega)}. \end{aligned} \tag{78}$$

At this point all of the factors are needed to utilize the optical Bloch equations. A two level system simplifies the formulation and symbolism. The density operator Eq. (8) in the two level notation loses the i subscript and simply becomes

$$\rho = |\Psi\rangle\langle\Psi|, \tag{79}$$

where $|\Psi\rangle$ is shown in Eq. (53). The individual matrix elements are now represented as

$$\rho_{nm} = \langle n|\rho|m\rangle = a_n a_m^*, \tag{80}$$

and the full density matrix for a two level atom can be written as

$$\rho = \begin{pmatrix} \rho_{11} & \rho_{12} \\ \rho_{21} & \rho_{22} \end{pmatrix} = \begin{pmatrix} a_1 a_1^* & a_1 a_2^* \\ a_2 a_1^* & a_2 a_2^* \end{pmatrix}. \tag{81}$$

The trace of the density matrix now provides a relation given by

$$\mathrm{Tr}\left[\rho\right] = a_1(t)a_1^*(t) + a_2(t)a_2^*(t) = \rho_{11} + \rho_{22} = 1, \tag{82}$$

and the probability to be in state n at time t is

$$\mathcal{P}_n(t) = \rho_{nn} = |a_n(t)|^2. \tag{83}$$

Therefore, the transition probability of an atom which started in the ground state to be in the excited state at time t is given by

$$\mathcal{P}_2(t) = |a_2(t)|^2 = |\Omega|^2\frac{\sin^2\left((\omega_0-\omega)\,t/2\right)}{(\omega_0-\omega)^2}, \tag{84}$$

and the on-resonance case ($\omega = \omega_0$) probability is

$$\mathcal{P}_2(t) = |a_2(t)|^2 = \frac{|\Omega|^2}{4}t^2. \tag{85}$$

The results presented in this portion did not include spontaneous emission or power broadening. These effects enter the equations as dampening factors which will be included next.

2.2.2.1 Spontaneous Emission

This section will include the spontaneous emission process, which is also known as radiative broadening, with the addition of a dampening factor. At this point the approximation still resides in the weak field limit where power broadening effects are neglected, which will be addressed in a following section.

The spontaneous emission process includes an electric field acting onto an atom with the same interaction potential shown in Eq. (64). The electric field is given as

$$\mathbf{E}(t) = \mathbf{E}_0 \cos(\omega t) = \frac{1}{2}\mathbf{E}_0 \left(e^{-i\omega t} + e^{i\omega t}\right). \tag{86}$$

The polarization is defined as

$$\mathbf{P}(t) = \frac{1}{2}\epsilon_0 \mathbf{E}_0 \left(\chi(\omega)e^{-i\omega t} + \chi(-\omega)e^{i\omega t}\right), \tag{87}$$

where $\chi(\omega)$ is the frequency dependent susceptibility of the atom which is related to the electric dipole moment by

$$\mathbf{P}(t) = \frac{N}{V}\mathbf{d}_{12}(t). \tag{88}$$

The electric field can be assumed to be polarized in the $\hat{\mathbf{x}}$ direction therefore the electric dipole moment is given as

$$d_{12}(t) = -e \int \Psi^*(t) X \Psi(t)\ dV. \tag{89}$$

Substitution of the wavefunction Eq. (56) into the electric dipole moment Eq. (89) yields

$$\begin{aligned}
d_{12}(t) &= -e \int \left(a_1^*\psi_1^* + a_2^*\psi_2^*\right) X \left(a_1\psi_1 + a_2\psi_2\right)\ dV \\
&= -e \left(a_1^* a_2 \int \psi_1^* X \psi_2\ dV + a_2^* a_1 \int \psi_2^* X \psi_1\ dV\right) \\
&= -e \left(a_1^* a_2 e^{-i\omega_0 t} \int \varphi_1^* X \varphi_2\ dV + a_2^* a_1 e^{i\omega_0 t} \int \varphi_2^* X \varphi_1\ dV\right) \\
&= -e \left(a_1^* a_2 X_{12} e^{-i\omega_0 t} + a_2^* a_1 X_{21} e^{i\omega_0 t}\right) \\
&= -e \left(\rho_{21} X_{12} e^{-i\omega_0 t} + \rho_{12} X_{21} e^{i\omega_0 t}\right),
\end{aligned} \tag{90}$$

where X_{12} is defined in Eq. (69).

In order to include the spontaneous emission process a modification to Eq. (68) must be made by the addition of a dampening factor of $\Gamma/2$. The equation shown in Eq. (68) then becomes

$$\dot{a}_2(t) = -i\Omega_{12}^* e^{i\omega_0 t} \cos(\omega t) a_1 - \frac{\Gamma}{2} a_2. \tag{91}$$

The choice of $\Gamma/2$ is justified by looking at the behavior of the excited state if there was no applied field $\Omega = 0$. The expectation is that an atom in the excited state decays as $e^{-\Gamma t}$. Assuming an atom is in the excited state $a_2(0) \propto 1$, with no applied field, the solution for the amplitude would simply be

$$a_2(t) = a_2(0)e^{-\Gamma t/2}, \tag{92}$$

therefore the probability that the atom resides in the excited state decays as expected

$$|a_2(t)|^2 = |a_2(0)|^2 e^{-\Gamma t}. \tag{93}$$

To solve for the amplitude $a_2(t)$ in Eq. (91) the $\tilde{a}_2$ parameter will be introduced as

$$\tilde{a}_2(t) = a_2(t)e^{\Gamma t/2} \tag{94}$$

$$\dot{\tilde{a}}_2(t) = \dot{a}_2(t)e^{\Gamma t/2} + \frac{\Gamma}{2}a_2(t)e^{\Gamma t/2}$$

$$\dot{a}_2(t) = \dot{\tilde{a}}_2(t)e^{-\Gamma t/2} - \frac{\Gamma}{2}a_1(t). \tag{95}$$

Substitution of Eq. (95) in the weak field limit where $a_1 \approx 1$ into Eq. (91) yields

$$\begin{aligned}
\dot{a}_2(t) &= \frac{1}{i}\Omega_{12}^* e^{i\omega_0 t}\cos(\omega t) - \frac{\Gamma}{2}a_2(t) = \dot{\tilde{a}}_2(t)e^{-\Gamma t/2} - \frac{\Gamma}{2}a_2(t) \\
\dot{a}_2(t) &= \frac{1}{i}\Omega_{12}^* e^{i\omega_0 t}\cos(\omega t) = \dot{\tilde{a}}_2(t)e^{-\Gamma t/2} \\
\dot{\tilde{a}}_2(t) &= \frac{1}{i}\Omega_{12}^* e^{i\omega_0 t}\cos(\omega t)e^{\Gamma t/2} = \frac{\Omega_{12}^*}{2i}\left(e^{i(\omega_0+\omega-i\Gamma/2)t} + e^{i(\omega_0-\omega-i\Gamma/2)t}\right),
\end{aligned} \tag{96}$$

where $\tilde{a}_2(t)$ can be solved for by indefinite integration of Eq. (96) and is given by

$$\tilde{a}_2(t) = \frac{\Omega_{12}^*}{2i}\left(\frac{e^{i(\omega_0+\omega)t}}{i(\omega_0+\omega-i\Gamma/2)} + \frac{e^{i(\omega_0-\omega)t}}{i(\omega_0-\omega-i\Gamma/2)}\right)e^{\Gamma t/2} = a_2(t)e^{\Gamma t/2}, \tag{97}$$

where the definition of $\tilde{a}_2$ is on the right hand side. Therefore the probability amplitudes in the weak field limit with the addition of spontaneous emission are the given as

$$a_1(t) \approx 1 \tag{98}$$

$$a_2(t) = -\frac{\Omega_{12}^*}{2}\left(\frac{e^{i(\omega_0+\omega)t}}{(\omega_0+\omega-i\Gamma/2)} + \frac{e^{i(\omega_0-\omega)t}}{(\omega_0-\omega-i\Gamma/2)}\right). \tag{99}$$

Substituting the amplitudes Eq. (98) and Eq. (99) into Eq. (90) provides the solution for the electric dipole moment given by

$$d(t) \approx -e\left(a_2 X_{12}e^{-i\omega_0 t} + a_2^* X_{21}e^{i\omega_0 t}\right) \tag{100}$$

$$= \frac{e^2|X_{12}|^2}{\hbar}\frac{E_0}{2}\left(\frac{e^{-i\omega t}}{\omega_0-\omega-i\Gamma/2} + \frac{e^{-i\omega t}}{\omega_0+\omega+i\Gamma/2} + \frac{e^{i\omega t}}{\omega_0+\omega-i\Gamma/2} + \frac{e^{i\omega t}}{\omega_0-\omega+i\Gamma/2}\right), \tag{101}$$

where the relation for Ω_{12} in Eq. (70) was substituted. For a sample of atomic gas with random orientations to the electric field an extra factor of 1/3 comes in due to averaging $|X_{12}|^2$ over all orientations. The relation is the following $|X_{12}|^2 \rightarrow \overline{|X_{12}|^2} = \frac{1}{3}|D_{12}|^2$. Making this substitution into Eq. (101) yields the macroscopic dipole moment of the atomic gas or the average dipole moment per atom. For now it is assumed the dipole, or atom, is aligned with the electric field.

The susceptibility $\chi(\omega)$ can now be found by comparing Eq. (101) to the form of the polarization shown in Eq. (87) which yields

$$\chi(\omega) = \frac{N}{V}\frac{e^2|X_{12}|^2}{\hbar\epsilon_0}\left(\frac{1}{\omega_0 - \omega - i\Gamma/2} + \frac{1}{\omega_0 + \omega + i\Gamma/2}\right). \tag{102}$$

A value of particular interest, as will be seen in later sections, is the complex polarizability and is related to the susceptibility by

$$\alpha(\omega) = \frac{V}{N}\chi(\omega)\epsilon_0. \tag{103}$$

After substitution the atomic polarizability is

$$\begin{aligned}\alpha(\omega) &= \frac{e^2|X_{12}|^2}{\hbar}\left(\frac{1}{\omega_0 - \omega - i\Gamma/2} + \frac{1}{\omega_0 + \omega + i\Gamma/2}\right) \\ &= 3\pi\epsilon_0 c^3\frac{\Gamma}{\omega_0^3}\left(\frac{1}{\omega_0 - \omega - i\Gamma/2} + \frac{1}{\omega_0 + \omega + i\Gamma/2}\right),\end{aligned} \tag{104}$$

where the natural decay rate is $\Gamma = \dfrac{e^2\omega_0^3}{3\pi\epsilon_0\hbar c^3}|X_{12}|^2$ [62]. The polarizability takes on the more common form after invoking the r.w.a. in Eq. (104) given by

$$\begin{aligned}\alpha(\omega) &= \frac{e^2|X_{12}|^2}{\hbar}\left(\frac{1}{\omega_0 - \omega - i\Gamma/2}\right) = \frac{e^2|X_{12}|^2}{\hbar}\left(\frac{(\omega_0 - \omega) + i\Gamma/2}{(\omega_0 - \omega)^2 + (\Gamma/2)^2}\right) = \\ &= \frac{3\pi\epsilon_0 c^3\Gamma}{\omega_0^3}\left(\frac{(\omega_0 - \omega) + i\Gamma/2}{(\omega_0 - \omega)^2 + (\Gamma/2)^2}\right).\end{aligned} \tag{105}$$

The polarizability can be solved for without taking the r.w.a. and is performed in order to compare results in a later section covering a far-off resonance condition. Starting with Eq.

(104) the polarizability takes on the form of

$$\begin{aligned}\alpha(\omega) &= 3\pi\epsilon_0 c^3 \frac{\Gamma}{\omega_0^3}\left(\frac{1}{\omega_0-\omega-i\Gamma/2}+\frac{1}{\omega_0+\omega+i\Gamma/2}\right)= \\ &= 3\pi\epsilon_0 c^3 \frac{\Gamma}{\omega_0^3}\left(\frac{2\omega_0}{(\omega_0^2-\omega^2)+\left(\frac{\Gamma}{2}\right)^2-i\Gamma\omega}\right)= \\ &= 3\pi\epsilon_0 c^3 \frac{\Gamma}{\omega_0^3}(2\omega_0)\left(\frac{(\omega_0^2-\omega^2)+\left(\frac{\Gamma}{2}\right)^2+i\Gamma\omega}{\left[(\omega_0^2-\omega^2)+\left(\frac{\Gamma}{2}\right)^2\right]^2+(\Gamma\omega)^2}\right). \end{aligned} \tag{106}$$

For light detuned far from resonance the following approximations are made due to the fact ω is of the order of 10^{14} and Γ is of the order 10^6.

$$\begin{aligned} &|\omega_0-\omega| \gg \Gamma \\ &|\omega_0^2-\omega^2| \approx \omega|\omega_0-\omega| \ \gg \Gamma\omega \gg \Gamma^2 \end{aligned} \tag{107}$$

The expression for the complex polarizability takes on a more simple form given by

$$\alpha(\omega) = 3\pi\epsilon_0 c^3 \frac{\Gamma}{\omega_0^3}(2\omega_0)\left(\frac{1}{(\omega_0^2-\omega^2)}+\frac{i\Gamma\omega}{(\omega_0^2-\omega^2)^2}\right). \tag{108}$$

The real and imaginary parts after partial fraction decomposition (pfd) are given by

$$\begin{aligned}\mathrm{Re}\left[\alpha(\omega)\right] &= 3\pi\epsilon_0 c^3 \frac{\Gamma}{\omega_0^3}(2\omega_0)\left(\frac{1}{\omega_0^2-\omega^2}\right)= \\ &= 3\pi\epsilon_0 c^3 \frac{1}{\omega_0^3}\left(\frac{\Gamma}{\omega_0-\omega}+\frac{\Gamma}{\omega_0+\omega}\right) \end{aligned} \tag{109}$$

$$\begin{aligned}\mathrm{Im}\left[\alpha(\omega)\right] &= 3\pi\epsilon_0 c^3 \frac{\Gamma}{\omega_0^3}(2\omega_0)\left(\frac{\Gamma\omega}{(\omega_0^2-\omega^2)^2}\right)= \\ &= 3\pi\epsilon_0 c^3 \frac{1}{2\omega_0^3}\left(\frac{\omega}{\omega_0}\right)\left(\frac{\Gamma}{\omega_0-\omega}+\frac{\Gamma}{\omega_0+\omega}\right)^2, \end{aligned} \tag{110}$$

where the pfd of

$$\frac{1}{\omega_0^2-\omega^2} = \frac{1}{2\omega_0}\left(\frac{1}{\omega_0-\omega}+\frac{1}{\omega_0+\omega}\right), \tag{111}$$

and the pfd of $\frac{1}{\left(\omega_0^2-\omega^2\right)^2}$ for the imaginary part is obviously just the square of the result in Eq. (111). The results given by Eq. (109) and Eq. (110) are used in the later discussion of far-off resonance traps.

Solving for the absorption cross section, starting with the polarizability $\alpha(\omega)$ taken with the r.w.a. form shown in Eq. (105) yields

$$\sigma = \frac{\omega_0}{\epsilon_0 c}\mathrm{Im}\left[\alpha(\omega)\right] = \frac{\omega_0 e^2 |X_{12}|^2}{\hbar\epsilon_0 c}\left(\frac{\Gamma/2}{\left(\omega_0-\omega\right)^2+(\Gamma/2)^2}\right). \tag{112}$$

The optical Bloch equations have not been fully utilized because of the weak field approximation which simplified the equations. In the following section no such approximation is made and power broadening is discussed.

2.2.2.2 Power Broadening

Up until this point a weak field approximation has been where $a_1(t) = 1$ in the rate equations. This corresponds to a linear response of the susceptibility Eq. (102) with respect to the electric field because the solution is of second order in the dipole matrix element X_{12}. Increasing the electric field amplitude above the weak field limit allows full use of the optical Bloch equations. Utilizing this method automatically includes spontaneous emission.

The rate equations that will be used for $\dot{a}_1(t)$ and $\dot{a}_2(t)$ are Eq. (67) and Eq. (91) respectively. The coefficients are simplified after invoking the r.w.a and are given by

$$\dot{a}_1 = -i\frac{\Omega}{2}a_2(t)e^{-i(\omega_0-\omega)t} \tag{113}$$

$$\dot{a}_2 = -i\frac{\Omega^*}{2}a_1(t)e^{i(\omega_0-\omega)t} - \frac{\Gamma}{2}a_2(t). \tag{114}$$

The equations of motion for the density matrix elements can be written using the property

$$\dot{\rho_{ij}} = \dot{a}_i a_j^* + a_i \dot{a}_j^*. \tag{115}$$

Substitution of the amplitudes Eq. (113) and Eq. (114) into Eq. (115) give

$$\begin{aligned}\dot{\rho}_{22} &= \left(-i\frac{\Omega^*}{2}a_1(t)e^{i(\omega_0-\omega)t} - \frac{\Gamma}{2}a_2(t)\right)a_2^* + a_2\left(i\frac{\Omega}{2}a_1^*(t)e^{-i(\omega_0-\omega)t} - \frac{\Gamma}{2}a_2^*(t)\right)\\ &= -i\frac{\Omega^*}{2}e^{i(\omega_0-\omega)t}\rho_{12} + i\frac{\Omega}{2}e^{-i(\omega_0-\omega)t}\rho_{21} - \Gamma\rho_{22} \qquad (116)\\ \dot{\rho}_{12} &= \left(-i\frac{\Omega}{2}a_2(t)e^{-i(\omega_0-\omega)t}\right)a_2^*(t) + a_1(t)\left(i\frac{\Omega}{2}a_1^*(t)e^{-i(\omega_0-\omega)t} - \frac{\Gamma}{2}a_2^*(t)\right)\\ &= i\frac{\Omega}{2}e^{-i(\omega_0-\omega)t}\left(\rho_{11}-\rho_{22}\right) - \frac{\Gamma}{2}\rho_{12}, \qquad (117)\end{aligned}$$

where $\dot{\rho}_{21} = \dot{\rho}_{12}^*$. In order to remove the oscillatory exponentials, the following substitutions are made into the previous equations

$$\tilde{\rho_{12}} = \rho_{12}e^{i(\omega_0-\omega)t}, \qquad \tilde{\rho_{21}} = \rho_{21}e^{-i(\omega_0-\omega)t}, \tag{118}$$

which leads to simplified equations given by

$$\dot{\rho}_{22} = -i\frac{\Omega^*}{2}\tilde{\rho}_{12} + i\frac{\Omega}{2}\tilde{\rho}_{21} - \Gamma\rho_{22} \tag{119}$$

$$\dot{\tilde{\rho}}_{12} = i\frac{\Omega}{2}\left(\rho_{11} - \rho_{22}\right) - \frac{\Gamma}{2}\tilde{\rho}_{12} + i\left(\omega_0 - \omega\right)\tilde{\rho}_{12} \tag{120}$$

$$\dot{\tilde{\rho}}_{21} = \dot{\tilde{\rho}}^*_{12}. \tag{121}$$

To solve for the steady state solutions these three rate equations set are to zero along with the property of the density matrix $\rho_{11} + \rho_{22} = 1$. First solving Eq. (119) for ρ_{22} as a function of $\tilde{\rho}_{12}$ and $\tilde{\rho}_{21}$, then substituting in $\tilde{\rho}_{12}$ from Eq. (120) and $\tilde{\rho}_{21}$ from Eq. (121) will yield the result. The equations needed to solve for ρ_{22} are given by

$$\begin{aligned}
\dot{\rho}_{22} = 0 &= -i\frac{\Omega^*}{2}\tilde{\rho}_{12} + i\frac{\Omega}{2}\tilde{\rho}_{21} - \Gamma\rho_{22} \\
\rho_{22} &= \frac{i}{2\Gamma}\left(\Omega\tilde{\rho}_{21} - \Omega^*\tilde{\rho}_{12}\right) \qquad (122) \\
\dot{\tilde{\rho}}_{21} = 0 &= i\frac{\Omega}{2}\left(1 - 2\rho_{22}\right) - \frac{\Gamma}{2}\tilde{\rho}_{12} + i\left(\omega_0 - \omega\right)\tilde{\rho}_{12} \\
\tilde{\rho}_{12} &= \frac{i\Omega}{2}\frac{\left(1 - 2\rho_{22}\right)}{\frac{\Gamma}{2} - i\left(\omega_0 - \omega\right)} \qquad (123) \\
\tilde{\rho}_{21} = \tilde{\rho}^*_{12} &= \frac{-i\Omega^*}{2}\frac{\left(1 - 2\rho_{22}\right)}{\frac{\Gamma}{2} + i\left(\omega_0 - \omega\right)}, \qquad (124)
\end{aligned}$$

where Eq. (123) and Eq. (124) are substituted into Eq. (122). To solve for ρ_{12} similar substitutions are made with Eq. (122) and Eq. (124) into Eq. (123) along with the relation in Eq. (118). The results after substitution and a bit of algebra are given by

$$\begin{aligned}
\rho_{22} &= \frac{|\Omega|^2}{4}\frac{1}{\left(\omega_0 - \omega\right)^2 + \left(\frac{\Gamma}{2}\right)^2 + \frac{1}{2}|\Omega|^2} \\
&= \frac{\left(\frac{\Omega}{\Gamma}\right)^2}{1 + \left(\frac{2\Delta}{\Gamma}\right)^2 + 2\left(\frac{\Omega}{\Gamma}\right)^2} \qquad (125) \\
\rho_{12} &= e^{-i(\omega_0 - \omega)t}\frac{\frac{\Omega}{2}\left(\omega_0 - \omega - i\frac{\Gamma}{2}\right)}{\left(\omega_0 - \omega\right)^2 + \left(\frac{\Gamma}{2}\right)^2 + \frac{1}{2}|\Omega|^2}, \qquad (126)
\end{aligned}$$

where $\Delta \equiv \omega - \omega_0$ and the Rabi frequency can be related to the saturation intensity [62] as

$$2\frac{|\Omega|^2}{\Gamma^2} = \frac{I}{I_{\text{sat}}} \quad \text{and} \quad I_{\text{sat}} = \frac{c\epsilon_0\Gamma^2\hbar^2}{4e^2|\hat{\boldsymbol{\epsilon}}\cdot\mathbf{r}|^2}. \tag{127}$$

This is the same result that was given in Eq. (47).

As a reminder $\rho_{22} = a_2(t)a_2^*(t) = |a_2(t)|^2$ is the probability of finding an atom in the excited state at time t. The choice of setting the time derivatives equal to zero assumes

steady state over a long period of time which essentially removes the time dependence by taking $t \to \infty$. This choice is justified by including the spontaneous emission damping terms into the density matrix rate equations which dampens the oscillatory behavior, which can be seen in Eq. (84), after a sufficient amount of time.

The dipole moment in Eq. (90) can be rewritten in terms of the off diagonal density matrix elements as

$$d(t) = -e\left(\rho_{21}X_{12}e^{-i\omega_0 t} + \rho_{12}X_{21}e^{i\omega_0 t}\right), \tag{128}$$

and the susceptibility $\chi(\omega)$ can be solved for in the same way as before by substituting Eq. (126) and its complex conjugate into Eq. (128). The susceptibility is then given by

$$\chi(\omega) = \frac{N}{V}\frac{e^2|X_{12}|^2}{\hbar\epsilon_0}\left(\frac{\omega_0 - \omega + i\Gamma/2}{(\omega_0-\omega)^2 + \left(\frac{\Gamma}{2}\right)^2 + \frac{1}{2}|\Omega|^2}\right), \tag{129}$$

and the polarizability is

$$\begin{aligned}\alpha(\omega) &= \frac{e^2|X_{12}|^2}{\hbar}\left(\frac{\omega_0 - \omega + i\Gamma/2}{(\omega_0-\omega)^2 + \left(\frac{\Gamma}{2}\right)^2 + \frac{1}{2}|\Omega|^2}\right) \\ &= 3\pi\epsilon_0 c^3\frac{\Gamma}{\omega_0^3}\left(\frac{\omega_0 - \omega + i\Gamma/2}{(\omega_0-\omega)^2 + \left(\frac{\Gamma}{2}\right)^2\left(1 + \frac{I}{I_{\text{sat}}}\right)}\right).\end{aligned} \tag{130}$$

The $\frac{1}{2}|\Omega|^2$ term in the denominator is associated with the saturation intensity I_{sat} and introduces the radiative, or power broadening behavior. The susceptibility and polarizability, for significant values of I, are no longer linear with respect to the electric field since $I = \frac{1}{2}\epsilon_0 c|E_0|^2$. Making the approximations of a weak field where $I \ll I_{\text{sat}}$ and $\Delta \gg \Gamma$, Eq. (130) simplifies to same form as Eq. (111) without power broadening.

The absorption cross section, defined in Eq. (112), is given by

$$\begin{aligned}\sigma &= \frac{\omega_0}{\epsilon_0 c}\text{Im}\left[\alpha(\omega)\right] = \frac{\omega_0 e^2|X_{12}|^2}{\hbar\epsilon_0 c}\left(\frac{\Gamma/2}{(\omega_0-\omega)^2 + (\Gamma/2)^2 + \frac{1}{2}|\Omega|^2}\right) \\ &= \frac{\omega_0 e^2|X_{12}|^2}{\hbar\epsilon_0 c}\frac{2}{\Gamma}\left(\frac{1}{1 + \left(\frac{2\Delta}{\Gamma}\right)^2 + 2\frac{|\Omega|^2}{\Gamma^2}}\right) = \frac{\omega_0 e^2|X_{12}|^2}{\hbar\epsilon_0 c}\frac{2}{\Gamma}\left(\frac{1}{1 + \left(\frac{2\Delta}{\Gamma}\right)^2 + \frac{I}{I_{\text{sat}}}}\right) \\ &= \frac{\sigma_0}{1 + \left(\frac{2\Delta}{\Gamma}\right)^2 + \frac{I}{I_{\text{sat}}}},\end{aligned} \tag{131}$$

where the so-called on resonant cross section, after substitutions shown in Eq. (127), is defined as

$$\sigma_0 = \frac{\omega_0 e^2|X_{12}|^2}{\hbar\epsilon_0 c}\frac{2}{\Gamma} = \frac{\hbar\omega_0}{I_{\text{sat}}}\frac{\Gamma}{2}, \tag{132}$$

which is the same value obtained without power broadening shown in Eq. (112) with $\omega = \omega_0$.

2.3 RUBIDIUM ENERGY LEVELS

Rubidium is the 37^{th} element of the periodic table and is classified as an alkali metal. Natural Rubidium is comprised of two main isotopes which are the nuclear stable ^{85}Rb and the *slightly* radioactive ^{87}Rb with a half life of 5 $\times 10^{10}$ years [63]. Natural abundances of ^{85}Rb and ^{87}Rb are 72% and 28% respectively. Rubidium is a convenient element for experimental purposes because its absorption spectrum corresponds to wavelengths accessible with inexpensive, common, and commercially available lasers and the high vapor pressure of solid rubidium provides a source of atomic gas, even at room temperature. Rubidium is also theoretically convenient due to only having one electron in its outer shell, which makes it a hydrogen-like atom.

The atomic states of Rb are denoted by $n^{2S+1}L_J$ where S, L, and J are the spin, orbital, and total angular momentum quantum numbers respectively. Although the value of L is replaced by the common spectroscopy notation of s, p, d, f, etc for $L = 0$, 1, 2, 3, etc. In the following discussion only the ground state $L = 0$ and the first excited P states $L = 0$,1 are relevant. n is the principle quantum number and only states of $n = 5$ are relevant to further discussions. The fine structure energy level of a particular nL_J state is determined by values given by NIST [64]. For an atom with one valence electron the spin angular momentum is $S = 1/2$.

The total angular momentum is given by

$$\mathbf{J} = \mathbf{L} + \mathbf{S}, \tag{133}$$

and is allowed to exist in the range of

$$|L - S| \leq J \leq |L + S|. \tag{134}$$

Therefore, $J = 1/2$ for the ground state $L = 0$ and $J = (1/2, 3/2)$ for the first excited state $L = 1$. The $L = 0 \rightarrow L = 1$ transition has two components known as the D lines. The $^2\mathrm{S}_{1/2} \rightarrow {}^2\mathrm{P}_{1/2}$ transition is called the D_1 line and the $^2\mathrm{S}_{1/2} \rightarrow {}^2\mathrm{P}_{3/2}$ is the D_2 line.

Due to the coupling of $\mathbf{J}$ with the total nuclear angular momentum $\mathbf{I}$, the hyperfine structure appears as the total atomic angular momentum $\mathbf{F}$ which is given by

$$\mathbf{F} = \mathbf{J} + \mathbf{I}, \tag{135}$$

where it takes on values of

$$|J - I| \leq F \leq |J + I|. \tag{136}$$

The hyperfine structure Hamiltonian is

$$H_{\rm hfs} = A_{\rm hfs}\mathbf{I}\cdot\mathbf{J} + B_{\rm hfs}\frac{3\left(\mathbf{I}\cdot\mathbf{J}\right)^2 + \frac{3}{2}\left(\mathbf{I}\cdot\mathbf{J}\right) - I\left(I+1\right)J\left(J+1\right)}{2I(2I-1)J(2J-1)}, \tag{137}$$

The energy level shifts due to the hyperfine splitting is given by [62]

$$\Delta E_{\rm hfs} = \frac{1}{2}A_{\rm hfs}K + B_{\rm hfs}\frac{\frac{3}{2}K(K+1) - 2I(I+1)J(J+1)}{2I(2I-1)2J(2J-1)}, \tag{138}$$

where

$$K = F(F+1) - I(I+1) - J(J+1). \tag{139}$$

The value obtained from the hyperfine matrix element represents the energy shift relative to the fine structure level. For states with $J = 1/2$ the $B_{\rm hfs}$ constants are zero. The energy level diagram shown in Fig. 1 utilizes the hyperfine constants listed in Tables 11-12 and calculated using Eq. (138). The ^{87}Rb ground state is shifted down with respect to the ^{85}Rb level by the so-called isotope shift.

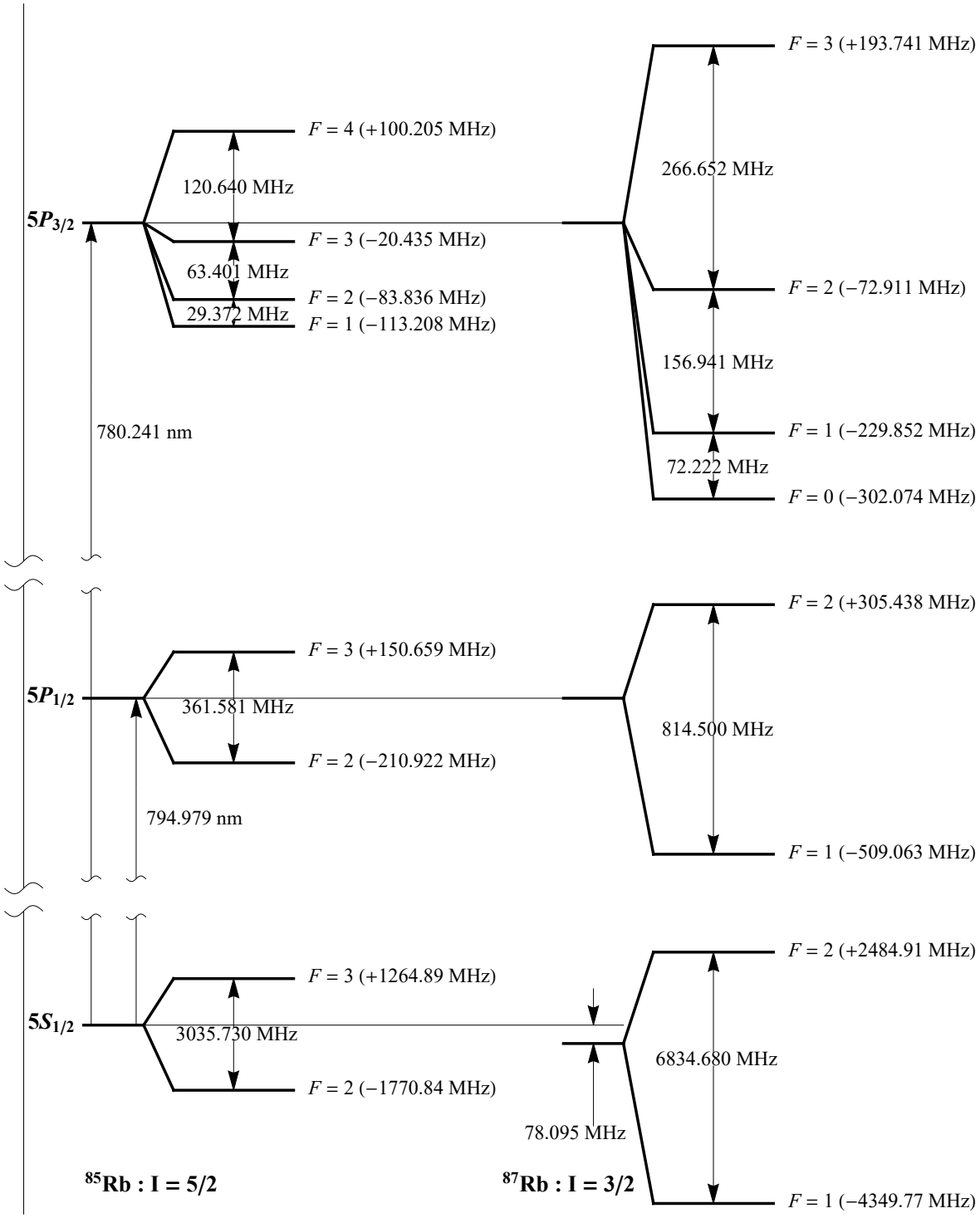

FIG. 1: ^{85}Rb and ^{87}Rb hyperfine energy levels for the $5^2S_{1/2}$, $5^2P_{1/2}$, and $5^2P_{3/2}$ states.

2.3.1 INTERACTION WITH STATIC ELECTRIC FIELD

Although the interaction of atoms with static fields is not directly relevant for the experiment it utilizes a similar formulation to the relevant dynamic case, which gives confidence to the procedure. The purpose of this section is to introduce and define the scalar α_0 and tensor α_2 polarizabilities.

The shift of atomic energy levels due to a static electric field is given by the potential

$$V_{\text{dip}} = -\frac{1}{2}\mathbf{p}\cdot\mathbf{E} = -\frac{1}{2}\alpha|E_0|^2, \tag{140}$$

where α in this case is the static polarizability. Similar to, but different from the frequency dependent polarizability discussed earlier where the electric field $\mathbf{E}$ was oscillating and time averaging needed to be included. The case of an oscillating electric field will be discussed in section 3.2.

To obtain the energy shift, known as the quadratic Stark shift, the dipole operator must be used in second order perturbation theory. The energy shift is given by

$$\delta\mathrm{E}(a) = \sum_i \frac{\langle a|V_{\text{dip}}|i\rangle\langle i|V_{\text{dip}}|a\rangle}{\mathrm{E}_a - \mathrm{E}_i}, \tag{141}$$

where a represents all relevant quantum numbers $nlsJIFm_F$ to the state in question and i represents quantum numbers of intermediate states. Discussions in Ref. [65] provide the rigor of expanding the dipole operator in such a way that the potential V_{dip} remains in the same form Eq. (140) but the polarizability α is given by

$$\alpha = \alpha_0\mathbb{I} + \alpha_2\hat{Q}, \tag{142}$$

where $\mathbb{I}$ is the identity matrix and $\hat{Q}$ is a second rank tensor operator. α_0 and α_2 are real constants and are known as the scalar and tensor polarizabilities respectively. The $\hat{Q}$ operator allows for coupling between different F hyperfine levels. In a linearly polarized electric field in the $\hat{z}$ direction the $\hat{Q}$ operator elements take the form of

$$\begin{aligned}\hat{Q}_{FF';m_Fm'_F} &= (-1)^{I+J+F-F'-m_F}\left[(2F+1)(2F'+1)\right]^{1/2} \\ &\times \left[\frac{(J+1)(2J+1)(J+3)}{J(2J-1)}\right]^{1/2} \\ &\times \begin{pmatrix} F & 2 & F' \\ m_F & 0 & -m'_F \end{pmatrix}\begin{Bmatrix} F & 2 & F' \\ J & I & J \end{Bmatrix},\end{aligned} \tag{143}$$

where the last two terms are Wigner (3-j) and {6-j} symbols. The Wigner notation is derived from angular momentum algebra where the 3-j symbol is essentially a Clebsch-Gordon coefficient and the 6-j symbol represents the sum of four 3-j's multiplied together. Wigner 6-j symbols are related to Racah W coefficients. An important property of the $\hat{Q}$ matrix elements is that the (3-j) symbol points to the fact that $m_F = m'_F$ therefore the operator is block diagonal in m_F. In the case of ^{87}Rb where $I = 3/2$ and the excited state $J = 3/2$ the $\hat{Q}_{m_F}$ block matrices are given by

$$\hat{Q}_{m_F=\pm 3} = \begin{pmatrix} 1 \end{pmatrix} \tag{144}$$

$$\hat{Q}_{m_F=\pm 2} = \begin{pmatrix} 0 & \mp 1 \\ \mp 1 & 0 \end{pmatrix} \tag{145}$$

$$\hat{Q}_{m_F=\pm 1} = \begin{pmatrix} -\frac{3}{5} & \mp\sqrt{\frac{2}{5}} & \frac{\sqrt{6}}{5} \\ \mp\sqrt{\frac{2}{5}} & 0 & \mp\sqrt{\frac{3}{5}} \\ \frac{\sqrt{6}}{5} & \mp\sqrt{\frac{3}{5}} & -\frac{2}{5} \end{pmatrix} \tag{146}$$

$$\hat{Q}_{m_F=0} = \begin{pmatrix} -\frac{4}{5} & 0 & \frac{3}{5} & 0 \\ 0 & 0 & 0 & 1 \\ \frac{3}{5} & 0 & \frac{4}{5} & 0 \\ 0 & 1 & 0 & 0 \end{pmatrix}, \tag{147}$$

where each sub-matrix is in the $|F, m_F\rangle$ basis. With the new polarizability defined, the full Hamiltonian is now given by

$$H = V_{\text{hfs}} - \frac{1}{2}\alpha_0 E^2 \mathbb{I} - \frac{1}{2}\alpha_2 E^2 \hat{Q}, \tag{148}$$

where V_{hfs} is given by Eq. (138).

Since $\hat{Q}$ is block diagonal in m_F, a particular m_F can be chosen and then the ensuing matrix diagonalized to find the eigenvalues which determine the energy level shift as a function of E^2. For example, the matrix to be diagonalized for the case of $m_F = \pm 1$ is given by

$$\begin{pmatrix} \mathrm{hfs}_{F=3} - \frac{E^2}{2}\left(\alpha_0 - \frac{3}{5}\alpha_2\right) & -\frac{E^2}{2}\left(\mp\sqrt{\frac{2}{5}}\alpha_2\right) & -\frac{E^2}{2}\left(\frac{\sqrt{6}}{5}\alpha_2\right) \\ -\frac{E^2}{2}\left(\mp\sqrt{\frac{2}{5}}\alpha_2\right) & \mathrm{hfs}_{F=2} - \frac{E^2}{2}\alpha_0 & -\frac{E^2}{2}\left(\mp\sqrt{\frac{3}{5}}\alpha_2\right) \\ -\frac{E^2}{2}\left(\frac{\sqrt{6}}{5}\alpha_2\right) & -\frac{E^2}{2}\left(\mp\sqrt{\frac{3}{5}}\alpha_2\right) & \mathrm{hfs}_{F=1} - \frac{E^2}{2}\left(\alpha_0 - \frac{2}{5}\alpha_2\right) \end{pmatrix}, \qquad (149)$$

where Mathematica can be used to easily determine the eigenvalues after substituting in values of hfs, α_0, and α_2 but leaving E a variable. Using the static polarizabilities for the $5P_{3/2}$ state listed in Table 10 and the hyperfine energies determined previously, the energy level shifts as a function of the electric field are shown in Fig. 2.

The reason for approaching the energy shifts in this manner is because values of α_0 and α_2 have been experimentally determined for the static case and also for relevant dynamic cases which will be explored in later sections describing optical traps.

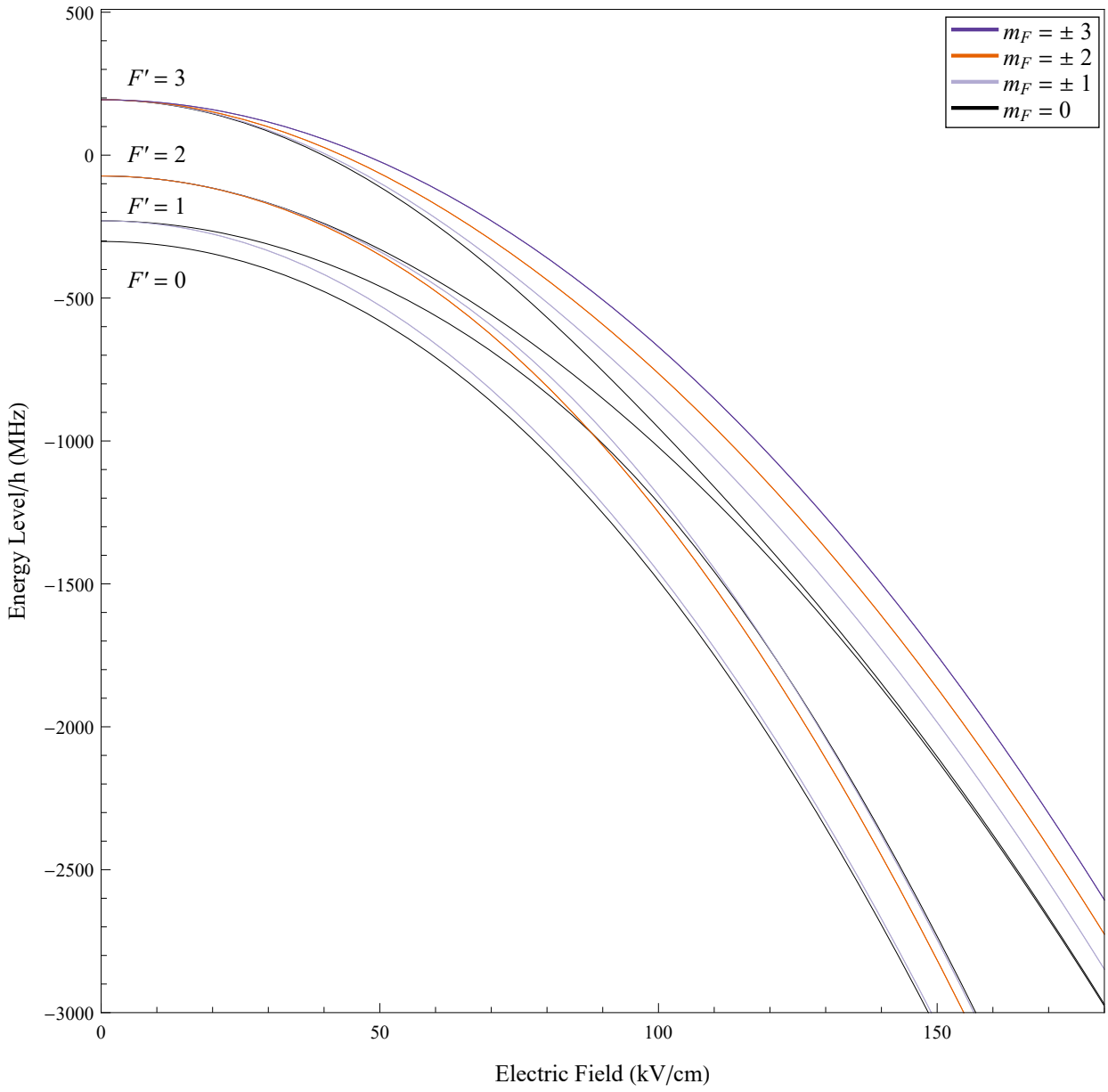

FIG. 2: ^{87}Rb $5P_{3/2}$ static quadratic Stark energy shifts.

2.4 RUBIDIUM TWO-BODY INTERACTION

The Hamiltonian to be used to describe the interaction between two atoms is

$$H = H_0 + H_I, \tag{150}$$

where H_0 is the unperturbed term which represents the energy of the atoms at large internuclear distances. In other words the unperturbed Hamiltonian describes the energy of individual non-interacting atoms and can be written as

$$H_0 = \sum_i E_i |a_i\rangle_i \, {}_i\langle a_i| \tag{151}$$

for $i = 1, 2$. The state $|a_i\rangle_i$ is an eigenvector of H_0 and represents the atomic state a_i of the ith atom. The individual atomic states $|a_i\rangle$ are defined by values of n, l, F, J, m_F, etc. Specifically, the values of H_0 are taken as the hyperfine splitting energies relative to the $F = 2$ for the ground state and the $F' = 3$ for the excited states.

The two body electric dipole-dipole interaction Hamiltonian H_I is defined as [66]

$$\begin{aligned} H_I \equiv V_{dd} &= \frac{1}{R^3}\left(\mathbf{d}_1 \cdot \mathbf{d}_2 - \frac{3\left(\mathbf{d}_1 \cdot \mathbf{r}\right)\left(\mathbf{d}_2 \cdot \mathbf{r}\right)}{R^2}\right) \\ &= -\frac{e^2}{R^3}\left(2z_1 z_2 - x_1 x_2 - y_1 y_2\right), \end{aligned} \tag{152}$$

where the subscripts correspond to the specific atom, R is the internuclear separation, and the z axis is defined along the internuclear axis. The Cartesian coordinate operators are rotated into the spherical basis with the following relations

$$\begin{aligned} r_0 &= z \\ r_1 &= -\frac{1}{\sqrt{2}}\left(x + iy\right) \\ r_{-1} &= \frac{1}{\sqrt{2}}\left(x - iy\right), \end{aligned} \tag{153}$$

which create the components of an irreducible tensor defined generally as T^k_q. The k value represents the rank of the tensor and q is the component. In this case the tensor is of rank 1 and $q = 0, \pm 1$ which correspond to the operators in Eq. (153). The Hamiltonian in the spherical basis is

$$V_{dd} = -\frac{e^2}{R^3}\left(2r_{1,0}r_{2,0} + r_{1,1}r_{2,-1} + r_{1,-1}r_{2,1}\right), \tag{154}$$

where $r_{i,q}$ represents the operator which will act on the ith atom with the qth component.

The molecular quantum states will be defined as a product state of individual atoms. The two indistinguishable atoms are coupled by $\phi = |m_g + m_F|$ which represents the component of the total angular momentum of both atoms along the internuclear axis. ϕ is a good quantum number therefore the molecular states are orthogonal in ϕ. The quantum state must allow for the interchange of the two atoms since they are indistinguishable. This interchange introduces the $g(u)$ labels which correspond to the states being even(odd) or $+(-)$ and are known as gerade(ungerade). The two atom molecular states will use the following notation

$$\begin{aligned}
|\phi_u^g J_g G J F m_F\rangle &= \frac{1}{\sqrt{2}} \left(|J_g G m_G; J F m_F\rangle \pm |J F m_F; J_g G m_G\rangle\right) \\
&= \frac{1}{\sqrt{2}} \left(|J_g G m_G\rangle_1 |J F m_F\rangle_2 \pm |J F m_F\rangle_1 |J_g G m_G\rangle_2\right) \\
&= \frac{1}{\sqrt{2}} \left(|G\rangle_1 |F\rangle_2 \pm |F\rangle_1 |G\rangle_2\right). \qquad (155)
\end{aligned}$$

The left hand side represents the so-called molecule while the right hand side represents the single atom product states along with their interchange. The ket subscripts correspond to the specific atom. The bottom line represents convenient shorthand notation since one atom is always in a ground state G and one in an excited state F.

Taking the matrix elements of V_{dd} Eq. (154) using the molecular states Eq. (155) yields

$$\begin{aligned}
&\langle \phi_u^g J_g' G' J' F' m_F' | V_{dd} | \phi_u^g J_g G J F m_F\rangle = \\
&= \frac{1}{2} \left({}_1\langle G'|_2\langle F'| \pm {}_1\langle F'|_2\langle G'|\right) V_{dd} \left(|G\rangle_1 |F\rangle_2 \pm |F\rangle_1 |G\rangle_2\right) \\
&= \pm \frac{1}{2} \Big[{}_1\langle G'|_2\langle F'|V_{dd}|F\rangle_1 |G\rangle_2 + {}_1\langle F'|_2\langle G'|V_{dd}|G\rangle_1 |F\rangle_2 \Big] \\
&= \pm \left(-\frac{e^2}{R^3}\right) \frac{1}{2} \Big[2 \left({}_1\langle G'|r_{1,0}|F\rangle_1 \, {}_2\langle F'|r_{2,0}|G\rangle_2 + {}_1\langle F'|r_{1,0}|G\rangle_1 \, {}_2\langle G'|r_{2,0}|F\rangle_2\right) \\
&+ \left({}_1\langle G'|r_{1,1}|F\rangle_1 \, {}_2\langle F'|r_{2,-1}|G\rangle_2 + {}_1\langle F'|r_{1,1}|G\rangle_1 \, {}_2\langle G'|r_{2,-1}|F\rangle_2\right) \\
&+ \left({}_1\langle G'|r_{1,-1}|F\rangle_1 \, {}_2\langle F'|r_{2,1}|G\rangle_2 + {}_1\langle F'|r_{1,-1}|G\rangle_1 \, {}_2\langle G'|r_{2,1}|F\rangle_2\right) \Big]. \qquad (156)
\end{aligned}$$

All elements of $\langle G'|r_q|G\rangle = 0$ and $\langle F'|r_q|F\rangle = 0$ because the selection rules of dipole operator require $\Delta L \neq 0$. Therefore only ground state ($5S_{1/2}$) to excited state ($5P_{1/2}$ or $5P_{3/2}$) transitions are non-zero. The omitted quadrupole term of the Hamiltonian would have to be evaluated in order to calculate the ground state shifts. The subscripts will now be dropped for the individual atoms $i = 1, 2$ since they are identical particles. The matrix element is

now represented as

$$\begin{aligned}
&\langle \phi_u^g J_g' G' J' F' m_F' | V_{dd} | \phi_u^g J_g G J F m_F \rangle = \\
&= \pm \left(-\frac{e^2}{R^3} \right) \Big[2 \langle G' | r_0 | F \rangle \langle F' | r_0 | G \rangle \\
&+ \langle G' | r_1 | F \rangle \langle F' | r_{-1} | G \rangle \\
&+ \langle G' | r_{-1} | F \rangle \langle F' | r_1 | G \rangle \Big],
\end{aligned} \tag{157}$$

and can be evaluated with the Wigner-Eckart theorem. In order to avoid confusion in the following calculations, the primed quantum numbers in Eq. (4) correspond to the excited states while the un-primed correspond to the ground states. This is in contrast to the matrix element formula Eq. (157) where the excited states are labeled as F, the ground states labeled as G, and the primed are intermediary.

To simplify the process only one of the three sets of $\langle\ |r|\ \rangle \langle\ |r|\ \rangle$ inside the square brackets of Eq. (157) need to be calculated because they all take a general form of

$$\begin{aligned}
&\langle G' | r_q | F \rangle \langle F' | r_{-q} | G \rangle \\
&= (-1)^q \langle F | r_{-q} | G' \rangle^* \langle F' | r_{-q} | G \rangle,
\end{aligned} \tag{158}$$

where second line was transformed with the two identities in Eq. (5) and Eq. (6) in order to obtain all matrix elements in terms of $\langle J || r || J_g \rangle$. The left-most matrix element in Eq. (158) is

$$\begin{aligned}
\langle G' | r_q | F \rangle &= (-1)^q \langle F | r_{-q} | G' \rangle \\
&= (-1)^q (-1)^{G'+F+J+I+1-m_F} \sqrt{(2G'+1)(2F+1)} \\
&\times \begin{pmatrix} F & 1 & G' \\ -m_F & -q & m_g' \end{pmatrix} \begin{Bmatrix} F & 1 & G' \\ J_g' & I & J \end{Bmatrix} \langle J || r || J_g' \rangle^*,
\end{aligned} \tag{159}$$

and the right-most is

$$\begin{aligned}
\langle F' | r_{-q} | G \rangle &= (-1)^{G+F'+J'+I+1-m_F'} \sqrt{(2G+1)(2F'+1)} \\
&\times \begin{pmatrix} F' & 1 & G \\ -m_F' & -q & m_g \end{pmatrix} \begin{Bmatrix} F' & 1 & G \\ J_g & I & J' \end{Bmatrix} \langle J' || r || J_g \rangle .
\end{aligned} \tag{160}$$

The general term is found by multiplying Eq. (159) and Eq. (160) together which results in

$$\begin{aligned}\langle G'|r_q|F\rangle\langle F'|r_{-q}|G\rangle &= (-1)^q\langle F|r_{-q}|G'\rangle\langle F'|r_{-q}|G\rangle \\ &= (-1)^q(-1)^{G'+G+F'+F+2I+J'+J+2-m'_F-m_F} \\ &\times \sqrt{(2G'+1)\,(2G+1)\,(2F'+1)\,(2F+1)} \\ &\times \begin{pmatrix} F & 1 & G' \\ -m_F & -q & m'_g \end{pmatrix}\begin{pmatrix} F' & 1 & G \\ -m'_F & -q & m_g \end{pmatrix} \\ &\times \begin{Bmatrix} F & 1 & G' \\ J'_g & I & J \end{Bmatrix}\begin{Bmatrix} F' & 1 & G \\ J_g & I & J' \end{Bmatrix} \\ &\times \langle J||r||J'_g\rangle^*\langle J'||r||J_g\rangle. \end{aligned} \tag{161}$$

By applying the 3-j identity

$$\begin{pmatrix} a & b & c \\ \alpha & \beta & \gamma \end{pmatrix} = (-1)^{a+b+c}\begin{pmatrix} a & c & b \\ \alpha & \gamma & \beta \end{pmatrix}, \tag{162}$$

Eq. (161) becomes

$$\begin{aligned}\langle G'|r_q|F\rangle\langle F'|r_{-q}|G\rangle &= (-1)^q\langle F|r_{-q}|G'\rangle\langle F'|r_{-q}|G\rangle \\ &= (-1)^q(-1)^{2I+J'+J-m'_F-m_F} \\ &\times \sqrt{(2G'+1)\,(2G+1)\,(2F'+1)\,(2F+1)} \\ &\times \begin{pmatrix} F & G' & 1 \\ -m_F & m'_g & -q \end{pmatrix}\begin{pmatrix} F' & G & 1 \\ -m'_F & m_g & -q \end{pmatrix} \\ &\times \begin{Bmatrix} F & 1 & G' \\ J'_g & I & J \end{Bmatrix}\begin{Bmatrix} F' & 1 & G \\ J_g & I & J' \end{Bmatrix} \\ &\times \langle J||r||J'_g\rangle^*\langle J'||r||J_g\rangle. \end{aligned} \tag{163}$$

The matrix element of V_{dd} can be determined by applying to Eq. (163) to each set of terms in Eq. (157) and yields

$$
\begin{aligned}
&\langle \phi_u^g J'_G G' J' F' m'_F | V_{dd} | \phi_u^g J_G G J F m_F \rangle = \\
&= \pm \left(-\frac{e^2}{R^3} \right) \langle J || r || J'_g \rangle^* \langle J' || r || J_g \rangle (-1)^{J+J'+2I-m_F-m'_F} \\
&\times \sqrt{(2G'+1)(2G+1)(2F'+1)(2F+1)} \\
&\times \begin{Bmatrix} F & 1 & G' \\ J'_g & I & J \end{Bmatrix} \begin{Bmatrix} F' & 1 & G \\ J_g & I & J' \end{Bmatrix} \\
&\times \left[2 \begin{pmatrix} F & G' & 1 \\ -m_F & \phi - m'_F & 0 \end{pmatrix} \begin{pmatrix} F' & G & 1 \\ -m'_F & \phi - m_F & 0 \end{pmatrix} \right. \\
&\quad - \begin{pmatrix} F & G' & 1 \\ -m_F & \phi - m'_F & -1 \end{pmatrix} \begin{pmatrix} F' & G & 1 \\ -m'_F & \phi - m_F & -1 \end{pmatrix} \\
&\quad \left. - \begin{pmatrix} F & G' & 1 \\ -m_F & \phi - m'_F & 1 \end{pmatrix} \begin{pmatrix} F' & G & 1 \\ -m'_F & \phi - m_F & 1 \end{pmatrix} \right].
\end{aligned} \tag{164}
$$

Since the $5S_{1/2} \rightarrow 5P_{3/2}$ transitions are being evaluated $J_g = J'_g = 1/2$ and $J = J' = 3/2$, the matrix element simplifies to

$$
\begin{aligned}
&\langle \phi_u^g J'_g G' J' F' m'_F | V_{dd} | \phi_u^g J_g G J F m_F \rangle = \\
&= \pm \left(-\frac{C_3}{R^3} \right) 2 (-1)^{2J+2I-m_F-m'_F} \\
&\times \sqrt{(2G'+1)(2G+1)(2F'+1)(2F+1)} \\
&\times \begin{Bmatrix} F & 1 & G' \\ J'_g & I & J \end{Bmatrix} \begin{Bmatrix} F' & 1 & G \\ J_g & I & J' \end{Bmatrix} \\
&\times \left[2 \begin{pmatrix} F & G' & 1 \\ -m_F & \phi - m'_F & 0 \end{pmatrix} \begin{pmatrix} F' & G & 1 \\ -m'_F & \phi - m_F & 0 \end{pmatrix} \right. \\
&\quad - \begin{pmatrix} F & G' & 1 \\ -m_F & \phi - m'_F & -1 \end{pmatrix} \begin{pmatrix} F' & G & 1 \\ -m'_F & \phi - m_F & -1 \end{pmatrix} \\
&\quad \left. - \begin{pmatrix} F & G' & 1 \\ -m_F & \phi - m'_F & 1 \end{pmatrix} \begin{pmatrix} F' & G & 1 \\ -m'_F & \phi - m_F & 1 \end{pmatrix} \right],
\end{aligned} \tag{165}
$$

where the new parameter C_3 is defined as [67]

$$
C_3 = \frac{1}{2} \langle J || er || J_g \rangle^2, \tag{166}
$$

and has usually been given in units of either (eV Å^3) or (MHz nm^3). C_3 must be divided by $4\pi\epsilon_0$ to obtain value in standard units. The reduced dipole matrix element can be calculated by the definition for the lifetime [53]

$$\begin{aligned}\frac{1}{\tau} &= \frac{e^2\omega_0^3}{3\pi\epsilon_0\hbar c^3}\frac{|\langle J||r||J_g\rangle|^2}{2J+1} \\ &= \left(\frac{2\pi}{\lambda}\right)^3 \frac{1}{3\pi\epsilon_0\hbar}\frac{|\langle J||er||J_g\rangle|^2}{2J+1},\end{aligned} \tag{167}$$

where $\langle J||er||J_g\rangle$ is in units of ea_0, λ is the wavelength of the transition, and τ is the natural lifetime. Solving for the reduced dipole matrix element and substituting in the latest values [62] yields

$$\begin{aligned}\langle J||er||J_g\rangle &= \sqrt{\left(\frac{\lambda}{2\pi}\right)^3 \frac{3\pi\epsilon_0\hbar}{\tau}(2J+1)} \\ &= 5.9785\ ea_0.\end{aligned} \tag{168}$$

The value of C_3 is determined by substituting Eq. (168) into Eq. (166) along with dividing by $4\pi\epsilon_0$. The calculated value is $C_3 = 72.064$ eVÅ^3 but the value used in the upcoming matrix diagonalization is 1.7425×10^7 MHz nm^3 because the values of H_0 are also taken in MHz.

The matrix describing the interaction for each value of ϕ can now be determined. For example, the matrix for $5g$ molecular state for ^{87}Rb is only a 1×1 matrix because the only molecular state consisting of $|5g2\frac{3}{2}33\rangle$ contribute since $\phi = |m_g + m_F|$. For a non-trivial example, the matrix for the $4g$ molecular states corresponds to the following 4×4 matrix

$$\begin{pmatrix} 0 & \frac{C_3}{\sqrt{6}R^3} & \frac{C_3}{2\sqrt{6}R^3} & 0 \\ \frac{C_3}{\sqrt{6}R^3} & -\frac{C_3}{3R^3} & \frac{C_3}{3R^3} & 0 \\ \frac{C_3}{2\sqrt{6}R^3} & \frac{C_3}{3R^3} & -\frac{C_3}{3R^3} & \frac{C_3}{2\sqrt{2}R^3} \\ 0 & 0 & \frac{C_3}{2\sqrt{2}R^3} & 0 \end{pmatrix}. \tag{169}$$

This matrix along with H_0 can be diagonalized to obtain eigenvalues associated with the energy shift due to the dipole-dipole potential at a particular value of R. The $4g$ molecular states are linear combinations of $|4g2\frac{3}{2}33\rangle$, $|4g2\frac{3}{2}32\rangle$, $|4g2\frac{3}{2}22\rangle$, and $|4g1\frac{3}{2}33\rangle$. Diagonalizing is performed numerically by Mathematica while iterating R over a specified range. The

matrix for the $3g$ molecular states is

$$\begin{pmatrix}
0 & 0 & \frac{C_3}{\sqrt{10}R^3} & 0 & \frac{C_3}{4R^3} & \frac{C_3}{4\sqrt{15}R^3} & 0 & 0 & 0 \\
0 & \frac{C_3}{3R^3} & -\frac{2\sqrt{\frac{2}{5}}C_3}{3R^3} & \frac{C_3}{6R^3} & \frac{C_3}{6R^3} & \frac{C_3}{2\sqrt{15}R^3} & 0 & 0 & 0 \\
\frac{C_3}{\sqrt{10}R^3} & -\frac{2\sqrt{\frac{2}{5}}C_3}{3R^3} & \frac{C_3}{30R^3} & \frac{2\sqrt{\frac{2}{5}}C_3}{3R^3} & -\frac{C_3}{6\sqrt{10}R^3} & \frac{C_3}{10\sqrt{6}R^3} & 0 & 0 & 0 \\
0 & \frac{C_3}{6R^3} & \frac{2\sqrt{\frac{2}{5}}C_3}{3R^3} & \frac{C_3}{12R^3} & -\frac{C_3}{6R^3} & -\frac{C_3}{2\sqrt{15}R^3} & 0 & \frac{C_3}{2\sqrt{3}R^3} & \frac{C_3}{4\sqrt{3}R^3} \\
\frac{C_3}{4R^3} & \frac{C_3}{6R^3} & -\frac{C_3}{6\sqrt{10}R^3} & -\frac{C_3}{6R^3} & \frac{C_3}{12R^3} & -\frac{C_3}{4\sqrt{15}R^3} & \frac{C_3}{4R^3} & -\frac{C_3}{2\sqrt{3}R^3} & \frac{C_3}{2\sqrt{3}R^3} \\
\frac{C_3}{4\sqrt{15}R^3} & \frac{C_3}{2\sqrt{15}R^3} & \frac{C_3}{10\sqrt{6}R^3} & -\frac{C_3}{2\sqrt{15}R^3} & -\frac{C_3}{4\sqrt{15}R^3} & \frac{C_3}{20R^3} & \frac{\sqrt{\frac{5}{3}}C_3}{4R^3} & \frac{\sqrt{5}C_3}{6R^3} & -\frac{\sqrt{5}C_3}{6R^3} \\
0 & 0 & 0 & 0 & \frac{C_3}{4R^3} & \frac{\sqrt{\frac{5}{3}}C_3}{4R^3} & 0 & 0 & 0 \\
0 & 0 & 0 & \frac{C_3}{2\sqrt{3}R^3} & -\frac{C_3}{2\sqrt{3}R^3} & \frac{\sqrt{5}C_3}{6R^3} & 0 & 0 & 0 \\
0 & 0 & 0 & \frac{C_3}{4\sqrt{3}R^3} & \frac{C_3}{2\sqrt{3}R^3} & -\frac{\sqrt{5}C_3}{6R^3} & 0 & 0 & \frac{C_3}{4R^3}
\end{pmatrix}, \tag{170}$$

which correspond to the molecular states of $|3g2\frac{3}{2}33\rangle$, $|3g2\frac{3}{2}32\rangle$, $|3g2\frac{3}{2}31\rangle$, $|3g2\frac{3}{2}22\rangle$, $|3g2\frac{3}{2}21\rangle$, $|3g2\frac{3}{2}11\rangle$, $|3g1\frac{3}{2}33\rangle$, $|3g1\frac{3}{2}32\rangle$, and $|3g1\frac{3}{2}22\rangle$. The matrices for the $2g$ (16×16), $1g$ (22×22), and $0g$ (24×24) molecular states will be omitted due to their size. The only difference between the g and u molecular states is an extra a factor of (-1).

The diagonalization was performed in Mathematica utilizing the Old Dominion University High Performance Computing hardware where 200,000 values of R were evaluated for each ϕ. The resulting energy shifts of the ^{87}Rb $5P_{3/2}$ $F = 3$ state are shown in Fig. 3.

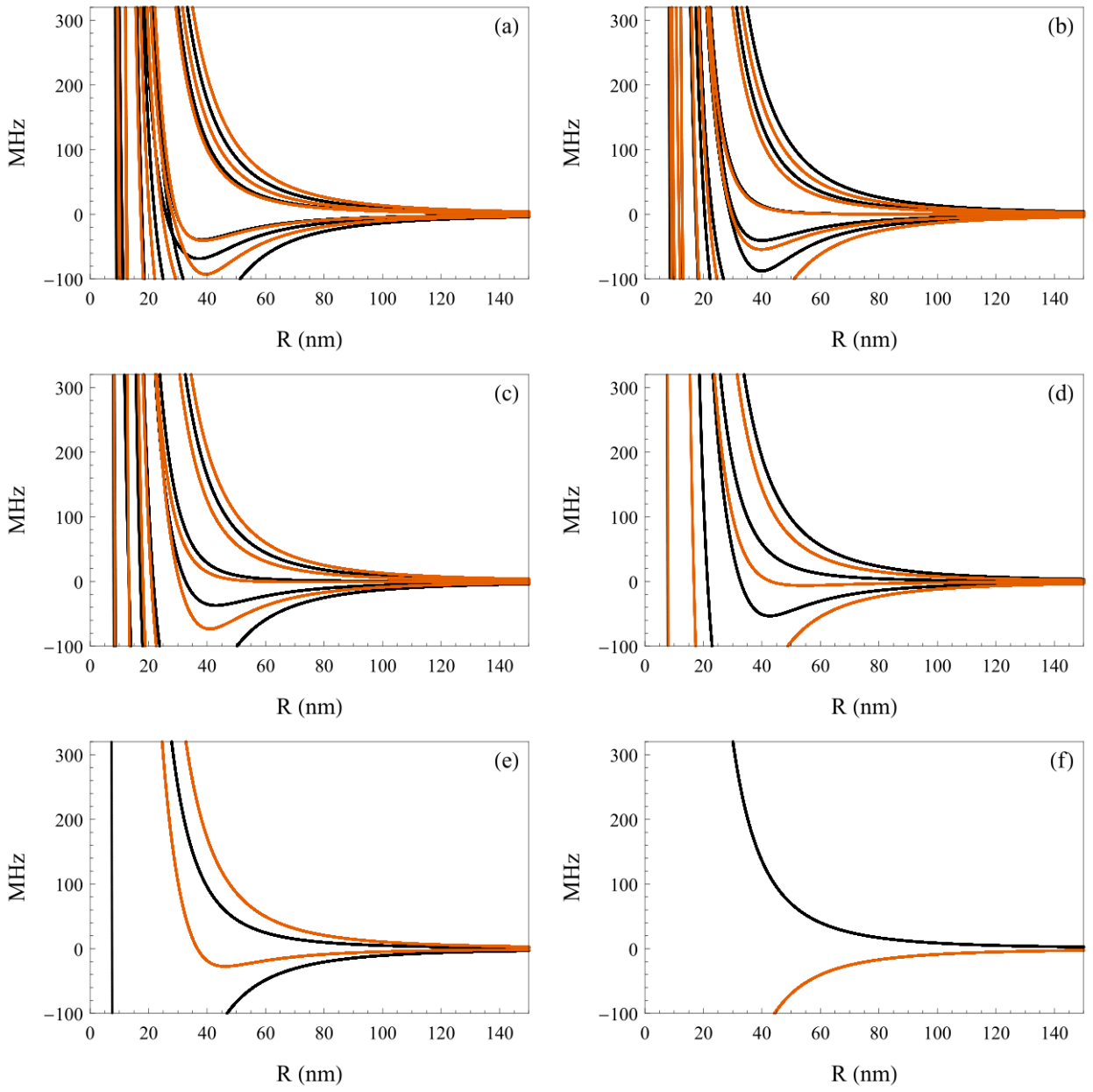

FIG. 3: ^{87}Rb two-body $5P_{3/2}$ $F = 3$ dipole-dipole energy shifts. (a-f) correspond to $\phi = (0 - 5)$ respectively. The black(red) lines represent the gerade(ungerade) states.

An initial inspiration for our experiment was based on previous works involving the creation of subradiant molecular states in an optical lattice [13, 15]. The main idea was to excite a molecule, where a pair of atoms separated by a distance d interact with each

other and the light field, in such a way to populate a typically forbidden molecular dipole transition. The molecule would then be in an excited state that would live much longer due to being weakly coupled to the ground state. In the typical molecular nomenclature, violation of the symmetry rules regarding gerade and ungerade states must occur to populate the subradiant states where only gerade $\rightarrow$ ungerade optical dipole transitions are allowed. Therefore, subradiant states were to be created by populating an excited state with gerade $\rightarrow$ gerade symmetry. Systems of Yb and Sr were used in these lattice experiments which offer a simple system with a nondegenerate ground state and well defined excited states where the energy level shifts are smaller than the excited state fine structure splitting. However, our ^{87}Rb system does not have such a simplified structure. Alkali dimers have a complicated structure due to ground state gerade-ungerade mixing [68] and excited state hyperfine mixing. For example, Fig. 4 shows a comparison between the energy level structure in the Yb system [13] and our Rb system. Due to the visual complexity, it must also be noted that curves that originate at -6.8 GHz, which are associated with the ground state hyperfine splitting, are also involved with the structure shown in Fig. 4(b). Characterizing the mixing of molecular states induced by the long-range interaction between two ^{87}Rb atoms in a dense cloud, rather than a lattice, is a much more complex endeavour. A lattice provides the ability to individually control pairs of atoms separated by a known distance, while pairs in an atomic ensemble carry a distribution of separation distances. Therefore, randomly separated atomic pairs throughout the sample would essentially remove the ability to single out a particular molecular state. With that in mind, a pivot was made to directly analyze the temporal atomic decay of an ensemble due to a short probe pulse, where results would be compared to previous experiments in a similar regime. A decision was made to explore in a detuning range of 150-295 MHz with respect to the $5S_{1/2}\ F = 2 \rightarrow 5P_{3/2}\ F = 3$ transition where many repulsive molecular states reside. Therefore, the idea was to analyze our results with methods known to be valid for large atomic samples near resonance, and compare those results against the expected cooperative subradiant behavior.

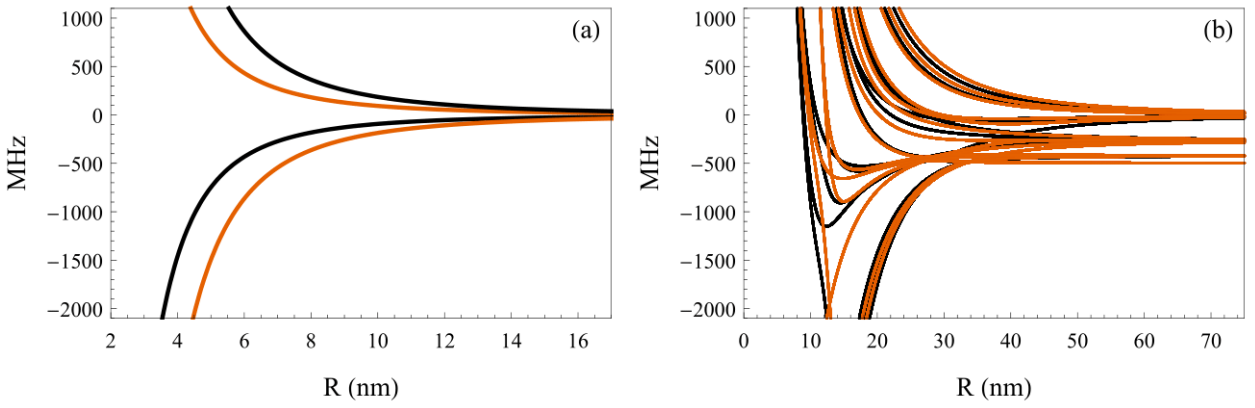

FIG. 4: Molecular excited state energy levels of ^{174}Yb and ^{87}Rb. Black(red) represent gerade(ungerade) states. (a) corresponds to $0_{g/u}$ and $1_{g/u}$ excited states in a ^{174}Yb molecule. The attractive curves are 0_u and 1_g while the repulsive are 0_g and 1_u. (b) corresponds to the only the $0_{g/u}$ set of molecular states and the asymptotic values are associated with the single atom $5P_{3/2}$ $F = 0,\ 1,\ 2,\ 3$ energy levels. Increased complexity is associated with the F and m_F quantum numbers.

2.5 COUPLED DIPOLE MODEL

The coupled dipole model will be an important tool during the analysis of experimental data. This model utilizes a quantized scalar photon field that interacts with atomic systems. Although this formulation does not include polarization effects or the multi-level energy structure, the results agree well with experimental data. The presented formulas will be limited to key points which are applicable to the experiments here while the full mathematical rigor has been preformed by [6, 69–72] and is known as the Wigner-Weisskopf theory for many atoms [73].

The system that will be described is an ensemble of N two-level atoms with positions $\mathbf{r}_j$ that are driven by a plane wave with wave vector $\mathbf{k}$. Calculations are performed with the scalar form of the interaction Hamiltonian, which assumes linear polarized light and the atomic dipoles are aligned with the electric field. Within this framework, and considering a weak probe, the change in the excited state amplitude is written as [70, 74]

$$\dot{\beta}_j = -i\frac{\Omega_0}{2}e^{i\mathbf{k}_0\cdot\mathbf{r}_j} + \left(i\Delta - \frac{\Gamma}{2}\right)\beta_j - \frac{\Gamma}{2}\sum_{m\neq j}\beta_m\frac{e^{ik_0 r_{jm}}}{ik_0 r_{jm}}, \tag{171}$$

where Ω_0 is the Rabi frequency, Δ is the detuning from resonance, and $r_{jm} = |\mathbf{r}_j - \mathbf{r}_m|$ is the separation between atom j and m. The first term in Eq. (171) corresponds to the external field driving the system and imparts a unique phase on each atom based on the atom location $\mathbf{r}_j$ and field direction $\mathbf{k}_0$. The second term describes the single atom decay behavior of atom j. The final term represents scattered light, real and virtual photons, from all other atoms in the ensemble onto atom j. The third term is what couples the individual atoms together and allows for cooperative effects to emerge. It can also be seen that the cooperative term will be highly dependent on the spatial configuration of the ensemble.

When the interaction term is neglected one should expect agreement with the single atom result given by the optical Bloch equations under the same approximations. Starting with Eq. (120) and taking the complex conjugate yields

$$\begin{aligned}\dot{\tilde{\rho}}_{21} = \dot{\tilde{\rho}}^*_{12} &= -i\frac{\Omega}{2}\left(\rho_{11} - \rho_{22}\right) - \frac{\Gamma}{2}\tilde{\rho}_{21} - i\left(\omega_0 - \omega\right)\tilde{\rho}_{21} \\ &= -i\frac{\Omega}{2}\left(\rho_{11} - \rho_{22}\right) + \left(i\Delta - \frac{\Gamma}{2}\right)\tilde{\rho}_{21},\end{aligned} \tag{172}$$

and then applying the property of Eq. (115) results in

$$\dot{\tilde{\rho}}_{21} = a_2\dot{a}^*_1 + a^*_1\dot{a}_2 = -i\frac{\Omega}{2}\left(a_1a^*_1 - a_2a^*_2\right) + \left(i\Delta - \frac{\Gamma}{2}\right)a_2a^*_1. \tag{173}$$

Now making the weak field approximation of $a_1 \approx 1$ yields

$$\dot{a}_2 = -i\frac{\Omega}{2} + \left(i\Delta - \frac{\Gamma}{2}\right)a_2, \tag{174}$$

which is equivalent to Eq. (171) when the multi-body coupling is neglected.

In consideration with the experiment, the scattered light from the sample will be collected, therefore the time dependent excited state amplitude must be calculated to obtain the radiated intensity. The time dependent radiated intensity is given by [6, 69]

$$\langle I(\mathbf{r}_s, t)\rangle = \frac{\hbar\omega_0\Gamma}{8\pi r_s^2}\left|\sum_j \beta_j(t)e^{-i\mathbf{k}_s\cdot\mathbf{r}_j}\right|^2, \tag{175}$$

where $\mathbf{k}_s$ corresponds to the scattered photon wave vector, which points towards the detector, and r_s is the distance to the detector. Emergent cooperative behavior will be dependent on the relative phases of each atom as well as the detection angle with respect to the initial probe direction. It must be noted that the result given in Eq. (175) is only valid under the weak excitation regime and the ensemble must have small enough spatial parameters for which retardation effects are neglected.

2.5.1 NUMERICAL SOLUTION

In order to obtain solutions of the radiated intensity given in Eq. (175), the solution to the time dependent amplitudes $\beta_j(t)$ for each atom must be obtained. The amplitudes are determined by numerically solving Eq. (171). First, Eq. (171) will be put into dimensionless form by converting the time scale to units of $1/\Gamma$ and the length scale to units of $1/k_0$ yielding,

$$\dot{\beta}_j = -i\frac{\Omega_0}{2}e^{i\hat{\mathbf{k}}_0\cdot\tilde{\mathbf{r}}_j} + \left(i\Delta - \frac{1}{2}\right)\beta_j + \frac{i}{2}\sum_{m\neq j}\beta_m\frac{e^{i\tilde{r}_{jm}}}{\tilde{r}_{jm}}, \tag{176}$$

where $\Delta \equiv \Delta/\Gamma$, $\Omega_0 \equiv \Omega_0/\Gamma$, $\tilde{r}_{jm} \equiv k_0 r_{jm}$, $\tilde{r}_j \equiv k_0 r_j$, and the unit vector $\hat{\mathbf{k}}_0$ points in the direction of beam propagation. Equation (176) can be put into matrix form defined as,

$$\dot{\boldsymbol{\beta}} = \boldsymbol{\Omega} + \hat{M}\boldsymbol{\beta}, \tag{177}$$

where $\boldsymbol{\Omega}_j = -i\frac{\Omega_0}{2}e^{i\hat{\mathbf{k}}_0\cdot\tilde{\mathbf{r}}_j}$ and $\hat{M}_{jm} = \left(i\Delta - \frac{1}{2}\right)\delta_{jm} + \frac{i}{2}\frac{e^{i\tilde{r}_{jm}}}{\tilde{r}_{jm}}(1-\delta_{jm})$. The driving pulse characterized by Ω_0 is technically time dependent based the pulse shape and pulse length, but a short square pulse will be used in later simulations.

The 4th-order Runge-Kutta method will be used numerically solve for the amplitudes $\beta_j(t)$ from Eq. (177) in discrete time-steps h. Typical equations using the Runge-Kutta method are in the form of $y' = Ay + b(t)$ and the solution is given by

$$y_{i+1} = y_i + \frac{1}{6}\left(k_1 + 2k_2 + 2k_3 + k_4\right), \tag{178}$$

where

$$k_1 = h\left[Ay_i + b(t_i)\right] \tag{179}$$

$$k_2 = h\left[A\left(y_i + \frac{k_1}{2}\right) + b\left(t_i + \frac{h}{2}\right)\right] \tag{180}$$

$$k_3 = h\left[A\left(y_i + \frac{k_2}{2}\right) + b\left(t_i + \frac{h}{2}\right)\right] \tag{181}$$

$$k_4 = h\left[A\left(y_i + k_3\right) + b(t_i + h)\right]. \tag{182}$$

After substituting $y \to \boldsymbol{\beta}$, $A \to \hat{M}$, and $b \to \boldsymbol{\Omega}$ one may obtain the value of all the β_j at all times. Once the time dependence of the β_j are known, the sum given in Eq. (175) can be performed for a specific scattering angle to obtain the time dependent scattered intensity. The simulation was written in Mathematica and it was found to be relatively fast for atom

numbers $N \leq 100$ with a time-step $h = 0.001$. Unfortunately for $N > 1000$, memory issues would arise and the duration of the simulation would take several days. Simulations were performed with the initial condition that all $\beta_j(0) = 0$ and averaged over a number of random atom distributions.

Experimental conditions were modelled by choosing Gaussian spatial distributions for the atomic ensembles. The spatial parameters for the experimental ensembles will be presented in the next chapter but there are two geometries, spherically and cylindrically symmetric, that will be utilized in the coupled dipole model are

$$\rho(r) = \rho_0 e^{-r^2/2r_0^2}, \tag{183}$$

and

$$\rho(r, z) = \rho_0 e^{-r^2/2r_0^2 - z^2/2z_0^2}, \tag{184}$$

where an example of the distributions are shown in Fig. 5.

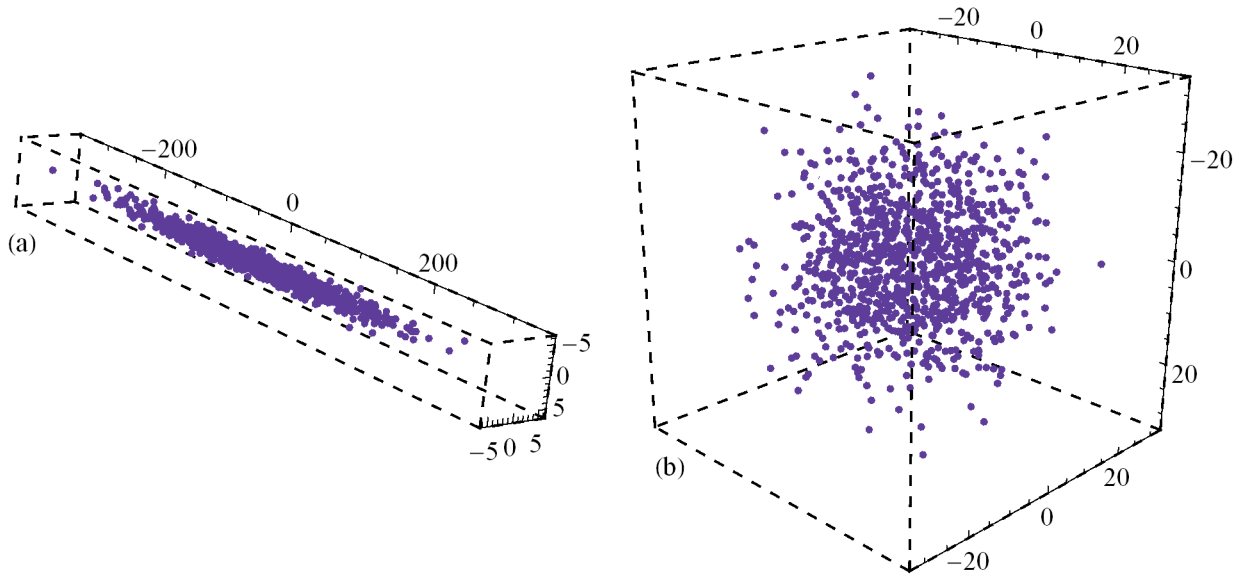

FIG. 5: Randomized ensemble distributions for the coupled dipole simulation at $N = 1000$. Axes are in units of $\lambda/2\pi$. (a) corresponds to the distribution given in Eq. (184) with $r_0 = 1.3$ and $z_0 = 127.3$. (b) corresponds to the distribution given in Eq. (183) with $r_0 = 14.7$.

The angle of the probe with respect to the ensemble as well as the detection angle are important to calculating the scattered light. Previous experiments in our lab, performed by Stetson Roof [6], examined the forward scattered light due to a probe aligned with the long axis of the distribution shown in Fig. 5(a). The angular intensity distribution can be determined from Eq. (175) by iterating the direction of detection $\hat{\mathbf{k}}_s$. The angular intensity distribution for the on axis probe geometry is shown in Figs. 6(a) and (b) for $N = 10$ and 100. For our experiment however, as shown in Figs. 6(c) and (d), the probe is off axis and the detection is perpendicular to the long axis of the sample geometry. An interesting result of our geometry under experimental rescaling conditions is the prediction of a reflected scattered lobe which can be attributed to Bragg scattering [71, 72]. Unfortunately, our apparatus does not allow for further study of this or characterization of the angular distribution, therefore it may be an interesting topic for future research.

To add a bit of clarity, the angular distribution that is depicted in Fig. 6 can be attributed to superradiance due to the inherently low amplitude of subradiance. As will be shown later, the subradiant amplitude is typically more than 5 orders of magnitude smaller than the peak of the signal. The angular dependence of the subradiant fluorescence, shown as the red line in Figs. 6(c) and (d), was calculated by only considering the fluorescence after 10 τ and depicted with arbitrary normalization. This computational result suggests, as expected, that subradiant behavior is more isotropic than the superradiant dominated total signal due to the dephasing of longer lived modes of the system.

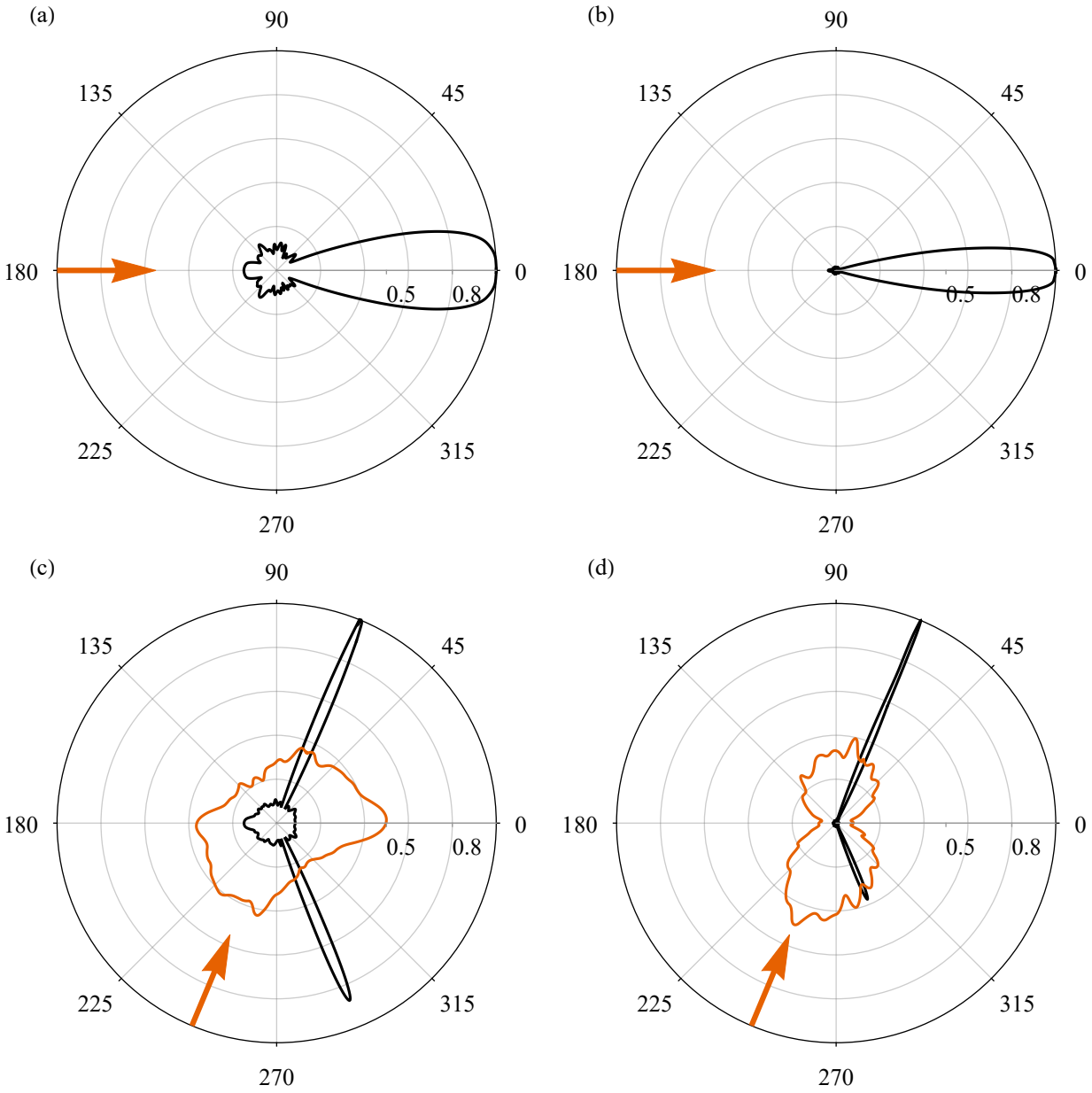

FIG. 6: Intensity of the scattered light from an extended sample as a function of detection angle from the coupled dipole model simulation. The long axis of the ensemble lays along the horizontal plane. The arrow represents the propagation direction of the probe laser. (a-b) correspond to the previous experimental alignment where the forward scattered light was collected at 0° for $N = 10$ and $N = 100$ respectively [6]. (c-d) correspond to the experimental orientation of this dissertation where the scattered light was collected at 270° for $N = 10$ and $N = 100$ respectively. Red lines represent fluorescence collected after 10 τ. The ensembles spatial parameters were rescaled to maintain constant density at each N.

CHAPTER 3

ATOM TRAPPING

This chapter introduces the concepts of laser cooling and trapping of atomic ensembles in magneto-optical traps (MOT) and far-off resonance traps (FORT). A MOT utilizes laser cooling techniques within a magnetic field gradient to exploit the atomic Zeeman splittings to create relatively large dilute atomic ensembles. A FORT on the other hand utilizes optical dipole forces created by a high intensity beam which spatially confines atoms at the focus for red-detuned light. The main advantage of a FORT is that it can have a density several orders of magnitude larger than a MOT, but is much smaller in both size and number of atoms. Further discussions in this chapter will go over the theoretical basis, experimental setup, and characterization of the MOT and FORT. Although the basis of understanding how the traps work is relatively straightforward, it can not be understated how complex the application of such knowledge in the laboratory can be. Dozens of mechanical, optical, and electrical systems must work together flawlessly to provide a reliable, controllable, and stable environment for the experimental apparatus.

3.1 MAGNETO-OPTICAL TRAP

A magneto-optical trap is an incredibly important tool in the field of ultracold atomic physics [75]. The introduction of the MOT has directly led to an abundant amount of research topics including but not limited to laser cooling, laser trapping, trap loss mechanics, and cross sections [76–84]. Recently, even complex polyatomic molecular MOTs have been created [85]. Today, MOTs are a very common and simple tool to cool and spatially confine atomic samples due to the exhaustive research devoted to laser cooling. This section will discuss the foundational mechanisms for creating a MOT, the experimental arrangement, and characterization techniques.

3.1.1 MAGNETO-OPTICAL TRAP THEORY

In order to cool atoms a force must be applied in the opposite direction to which the atom is travelling. Lasers are used to apply such a force by means of absorption. The absorbed photon is then spontaneously emitted in a random direction which equates to zero force due

to emission over many cycles. Therefore, for a two level system, the average force due to absorption and spontaneous emission of a photon is [86]

$$F_{\text{abs}} = \hbar k \Gamma \rho_{22} = \frac{\hbar k s_0 \Gamma/2}{1 + 4\left(\frac{\Delta}{\Gamma}\right)^2 + s_0}, \tag{185}$$

where $s_0 = I/I_{\text{sat}}$ is known as the saturation parameter. The value of ρ_{22} is given by Eq. (125) and derived in a previous section. An atom in motion with velocity $\mathbf{v}$ will observe the detuning of the incident photons to be Doppler shifted by $\omega_D = \mathbf{k} \cdot \mathbf{v}$. Taking a look at the one dimensional case where an atom is moving within counter-propagating beams at velocity v, the force felt by the atom is $F_{\text{Total}} = F_+ + F_-$ where

$$F_\pm = \frac{\pm\hbar k s_0 \Gamma/2}{1 + 4\left(\frac{\Delta \mp \omega_D}{\Gamma}\right)^2 + s_0}. \tag{186}$$

In the regime of $kv \ll \Gamma$ the total force on the atom is

$$\mathbf{F}_{\text{Total}} = \frac{8\hbar k^2 s_0 \Delta \mathbf{v}}{\Gamma\left[1 + 4\left(\frac{\Delta}{\Gamma}\right)^2 + s_0\right]}. \tag{187}$$

It is clear to see that for detunings to the red of resonance $\Delta < 0$ the force dampens the atomic motion. What is known as an optical molasses is created when three orthogonal sets of counter-propagating beams cool a sample of atoms. Although this describes a method to rapidly cool atoms within a six beam geometry, it does not take into account the behavior of an optical molasses in steady state where the atoms obtain diffusive properties which heat the sample [86, 87]. The cooling limit is

$$T_D = \frac{\hbar\Gamma}{2k_B}, \tag{188}$$

and is known as the Doppler temperature. Sub-Doppler cooling can be achieved via a method called polarization gradient cooling where the counter-propagating beams have opposite circular polarization. Polarization gradient cooling along with extensive derivations for several optical molasses properties are presented in Ref. [88] and references within.

At this point atoms can be cooled within the overlapping beams but are not spatially confined due to the aforementioned diffusive behavior and the fact that the force, as shown in Eq. (187), only depends on velocity. The Zeeman structure of the atom can be taken advantage of to spatially confine the ensemble due to the presence of a magnetic field. The

magnetic field for a MOT is provided by two N turn coils of radius R, each with current flowing the opposite direction and separated by R, which is known as an anti-Helmholtz configuration. The magnetic field along the axis (z) of the anti-Helmholtz coils is given by

$$B(z) = \frac{\mu_0 N I}{2R}\left[\frac{1}{\left(1+(z/R-1/2)\right)^{3/2}-\left(1+(z/R+1/2)\right)^{3/2}}\right]. \tag{189}$$

The magnetic field strength around the center of the trap becomes approximately linear, which can be seen by expanding Eq. (189) around $z = 0$. The atomic hyperfine levels split linearly in the presence of a weak magnetic field. If the magnetic field is taken in the z direction the energy levels split as [62]

$$\Delta E = \mu_B g_F m_F B_z, \tag{190}$$

where μ_B is the Bohr magneton. g_F is the hyperfine Landé g-factor given by

$$g_F \simeq \left(1+\frac{J\left(J+1\right)+S\left(S+1\right)-L\left(L+1\right)}{2J\left(J+1\right)}\right)\left(\frac{F\left(F+1\right)+J\left(J+1\right)-I\left(I+1\right)}{2F\left(F+1\right)}\right). \tag{191}$$

Utilizing the Zeeman splitting is visualized in Fig. 7 where the m_F levels are shifted with respect to the center of the trap in the presence of a magnetic field $B(z) = B_0 z$. The $m_F = 1$ energy level of an atom on the left ($-z$) will be shifted downward closer to the laser frequency ω_L with circular polarization σ_+ but further from resonance on the right ($+z$) side. Likewise, the $m_F = -1$ energy level of an atom on the right ($+z$) will be shifted downward closer to the laser frequency ω_L with circular polarization σ_- but further from resonance on the left ($-z$) side. Therefore, by counter-propagating circular polarized beams of opposite circular polarization in the presence of a magnetic field, the atoms are spatially selected to preferentially interact with only one beam. That concept is what defines the basic spatial confinement property of a MOT.

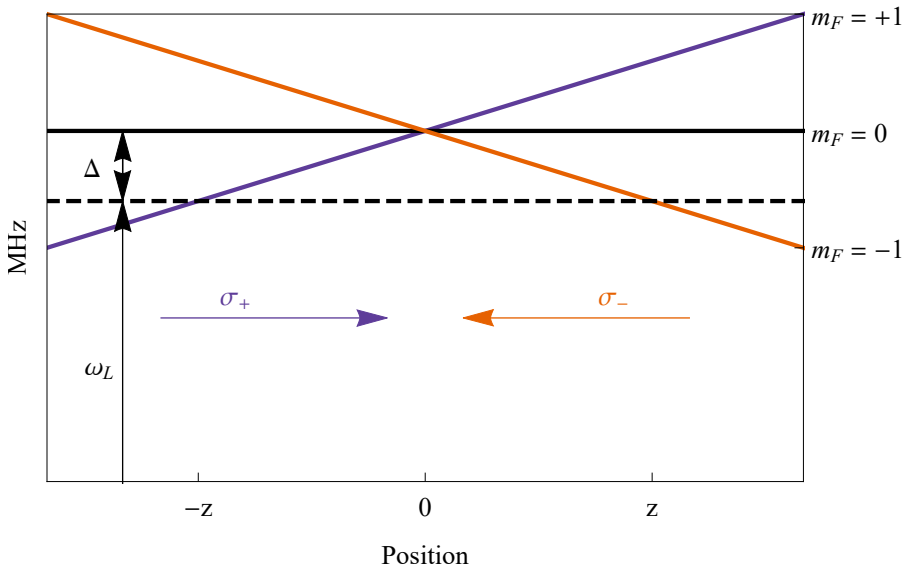

FIG. 7: Zeeman splitting diagram of an atom in the presence of a magnetic field $B(z) = B_0 z$. An atom on the left $(-z)$ of the trap has a higher transition probability to scatter a σ_+ photon and be forced towards the center. Likewise and opposite for an atom on the right $(+z)$ side of the trap. For purposes of clarity, this figure represents a $F = 0 \rightarrow F = 1$ transition but is perfectly applicable for atoms with a more complex structure.

A MOT can be realized by combining the concept of an optical molasses with the addition of a magnetic field gradient. The optical molasses properties introduce a dampening or cooling force on the atoms while an applied magnetic field gradient results in a spatial dependence to the atom's interaction with counter-propagating, oppositely circular polarized light. Putting these concepts to practice will now be discussed.

3.1.2 MOT EXPERIMENTAL SETUP

The optical, mechanical, and electrical components utilized to create a MOT in the laboratory will now be addressed. Important components will be briefly described as they are introduced into the apparatus explanation.

The creation of a ^{87}Rb MOT in the lab is straightforward but comes with a nuance which introduces the need for a second laser. The preceding section described the laser cooling process under the assumption of a simple closed two-level cycling system, but rubidium is a slightly more complex system with multiple ground and excited states. Under the right

circumstances atoms will be pumped out of the cycling transition and lost from the trap. A second laser is required to re-introduce these atoms into the cooling cycle before it can leave the confines of the trap. To address a technicality and for clarity, a second physical laser is not necessarily required. Sidebands at the correct frequency may be added to the MOT laser and achieve the same effect. Although adding sidebands may reduce the complexity of the apparatus in some respects, the ability to directly control the frequency, power, and timing of the second laser is lost. With that said, further discussions utilize two different lasers.

The MOT trapping laser utilizes the ^{87}Rb $5S_{1/2}$ $F = 2 \rightarrow 5P_{3/2}$ $F' = 3$ nearly closed transition to cool and trap the atomic ensemble, but due to off resonant scattering there is a small probability for the $F' = 2$ state to become populated and then decay to the $F = 1$ ground state. A second laser is needed on the $5S_{1/2}$ $F = 1 \rightarrow 5P_{3/2}$ $F' = 2$ transition in order to *repump* the atoms back into the cooling cycle and is called the repumper laser. The aforementioned hyperfine energy levels and splittings were shown in Fig. 1.

The MOT trapping beam is derived from a laser diode (Thorlabs DL7140-201S) arranged in the so-called Littrow configuration, which is a type of external cavity diode laser (ECDL). The laser diode is housed in a home-built mount designed and created by Salim Balik [89]. The linewidth of the laser was measured to be roughly 500 kHz by Stetson Roof [6]. The laser is driven and temperature stabilized by a SRS LDC501 laser controller. The temperature stabilization utilizes a 50 kΩ thermistor (Digi-Key RL0503-27.53K-120-MS) and a thermo-electric cooler (Marlow Industries DT12-6-01L) installed in the ECDL housing. The frequency of the laser is tuned by adjusting the current, temperature, and diffraction grating angle of the ECDL. The grating angle is adjustable by applying a voltage to a piezo-electric transducer (PZT) located on the grating mount. Locating the correct parameter space can be laborious due to the home-built nature of the ECDLs. Daily adjustments were typically needed due to fluctuating building temperatures. It cannot be understated how much the lasers are coupled to the building environment. Temperature, humidity, and even the circuitry the building had to be taken into account to minimize adverse effects to the laboratory. Throughout this dissertation it will be clear that steps were taken at every opportunity to improve consistency of the apparatus.

The frequency of the laser is stabilized by utilizing Doppler-free saturated absorption (SA) spectroscopy [90], laser current modulation, and an electronic feedback loop. SA is a very common technique which outputs the absorption spectrum as the laser scans over an atomic transition. The laser is frequency modulated (FM) by modulating the current delivered to the diode via a function generator (BK Precision 4003A) connected to the SRS

LDC501. The FM then causes amplitude modulation of the SA output. The modulation frequency and SA signal are sent to a lock-in amplifier (SCITEC 410) which outputs a so-called derivative-like signal. The derivative-like signal is used to lock the laser at a zero crossing via a home-built lock box that corrects for frequency drifts by applying appropriate voltage to the PZT. The SA and derivative signal for the MOT laser is shown in Fig. 8,

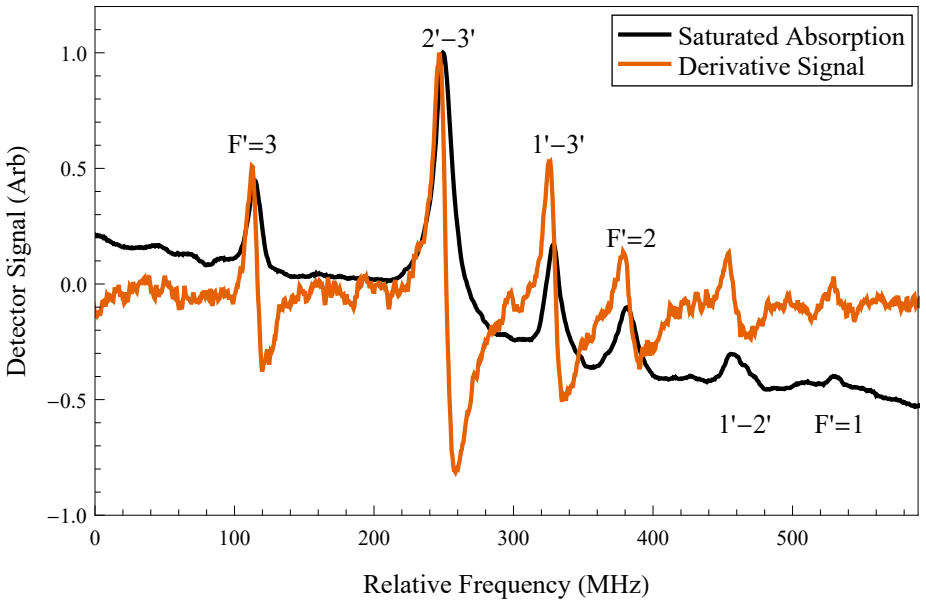

FIG. 8: Saturated absorption and derivative signal for the MOT laser. The saturated absorption signal represents the $5S_{1/2}$ $F = 2 \rightarrow 5P_{3/2}$ transitions. The laser is locked on the $F' = 3$ transition.

where the MOT trapping laser is usually locked on the $F' = 3$ peak. The trapping laser may also be referenced simply as the MOT laser throughout this text. Additional frequency tuning is required due to the limitation of the SA locking scheme which requires a zero crossing of the derivative signal. A device known as an acousto-optic modulator (AOM) is used for further frequency tuning.

An AOM is an important tool used not only for frequency tuning but also for switching a beam on/off. An AOM is a device that propagates sound waves through a crystal launched

by a piezoelectric transducer. Light passing through the crystal will then diffract into spatially separated orders that are frequency shifted in multiples of the frequency applied to the transducer. Essentially the photon energy is shifted either by gaining or losing multiples of the crystal phonon energy. Also, the photon direction is changed due to the momentum imparted by the orthogonally travelling crystal phonons. The most commonly used diffraction orders are $\pm 1^{\text{st}}$ and the unchanged 0^{th} is also still available to be utilized. The 1^{st} order beam is always deflected in the direction of sound wave propagation which is away from the transducer, while the -1^{st} is deflected the opposite direction. Turning an AOM on/off can be used as a switch by coupling a diffracted order of the laser into an optical fiber. The basic electronics to drive the AOMs will be described later.

The optical setup for the MOT beam is shown in Fig. 9 and the description can be broken up into two main parts, namely the left and right side. The left side is responsible for locking and frequency tuning while the right side provides laser power for several purposes. All of the optical element graphics that are used throughout this dissertation are defined in Fig. 103 in Appendix C.

Staring with the left side of Fig. 9, the MOT ECDL beam measures roughly 26 mW after the first optical isolator (ISO1). Optical isolators are important to eliminate reflections back into the laser which cause unwanted instabilities and sidebands. At the first polarizing beam splitter cube (PBS) 2 mW is sent towards AOM1 (Brimrose TEM-200-50-780) in a double-pass (DP) configuration while the rest continues through. The yellow optics represent half-wave plates control how much power is split at the PBS. The DP setup reflects the diffracted -1^{st} order beam directly back along its trajectory where it returns through AOM1. On the return pass through AOM1 the -1^{st} order beam is diffracted again where its propagation direction is opposite to the initial beam and is frequency shifted twice. The red optic represent a quarter-wave plate which when double passed through rotate the polarization $90°$. The doubly frequency shifted beam is sent to the SA cell for locking the laser. The balanced photodiode (PD) is a home-built device which outputs the difference between the two SA beams. The portion of the beam which initially passed through the first PBS goes to the AOM2 (Brimrose TEM-200-50-780) DP configuration and towards the right side of the optics setup through ISO2 where it is used to injection lock the distributed feedback laser (DFB Eagleyard EYP-DFB-0780-00080-1500-TOC03-0000). The DFB is driven by a Vescent D2-105 laser controller and D2-005 power supply. Injection locking causes the DFB to follow the frequency of the MOT ECDL. The DFB then passes through AOM3 (Gooch & Housego R23080-1) where the 1^{st} order beam is sent to the vacuum chamber as the MOT

beam via a polarizing preserving fiber (OZ Optics PMJ-3A3A-850-5/3-2.5-1). A portion 0^{th} order of the beam is sent to a spectrum analyzer (Thorlabs SA200-5B 1.5 GHz FSR) and to probe beam optics which will be discussed later. AOM3 is also used as a switch to turn on/off the MOT beam. The spectrum analyzer is used to ensure proper injection locking and single mode operation due to the extreme sensitivity of the DFB to reflections. A special note must be made that reflections from every optical element in the path of the DFB have to be taken into consideration. For instance, optics directly in front of the DFB must be rotated slightly to ensure surface reflections do not make it back into the laser.

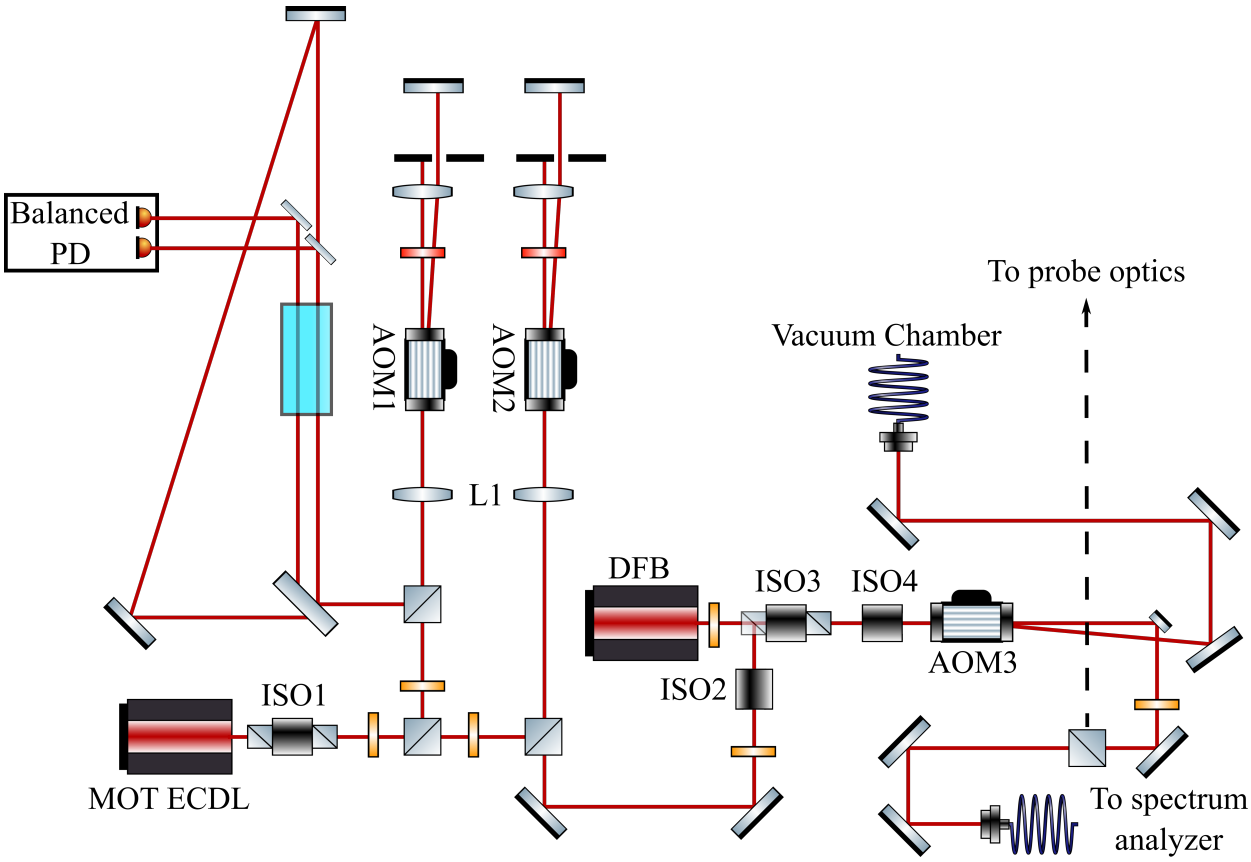

FIG. 9: MOT laser optics diagram. The MOT ECDL (Thorlabs DL7140-201S) is used to lock the laser and to provide a frequency shift from the lock point before injection locking into the DFB (EYP-DFB-0780-00080-1500-TOC03-0000). The DFB provides power for the MOT beam, a spectrum analyzer, and a future probe beam. Optical components are L1 (LA1509-B), ISO1 (OFR IO-3-780-LP), ISO2 (Thorlabs IO-3D-780-VLP), ISO3 (Thorlabs IO-8-780-PBS), ISO4 (OFR IO-3-780-VLP), AOM1 (Brimrose TEM200-50-780), AOM2 (Brimrose TEM200-50-780), and AOM3 (Gooch & Housego R23080-1).

The frequency of the MOT laser with respect to the $F' = 3$ locking point can now be determined with the MOT optics setup in mind and typical AOM settings. The AOM1 is set at 175 MHz, therefore the beam entering the SA is -350 MHz from the ECDL output. Locking on the $F' = 3$ now means that the frequency of the beam entering AOM2 is +350 MHz of the transition. AOM2 is set at 219 MHz, therefore the DFB will be injection locked -84 MHz from the $F' = 3$. Finally, AOM3 is set at 66 MHz which puts the MOT beam at -18 MHz (-3Γ) from the $F' = 3$. This detuning value is a common set point for the ^{87}Rb MOT beam. The frequency of AOM2 can be adjusted electronically between 160-240 MHz in order to change the detuning of the MOT and probe beams. The frequency tuning range is limited due to the efficiency of the AOM changing as a function of applied frequency.

The repumper laser is derived from the same model diode, mounting components, and laser controller that was listed for the MOT laser and utilizes the same locking technique. The SA and derivative signal for the repumper is shown in Fig. 10,

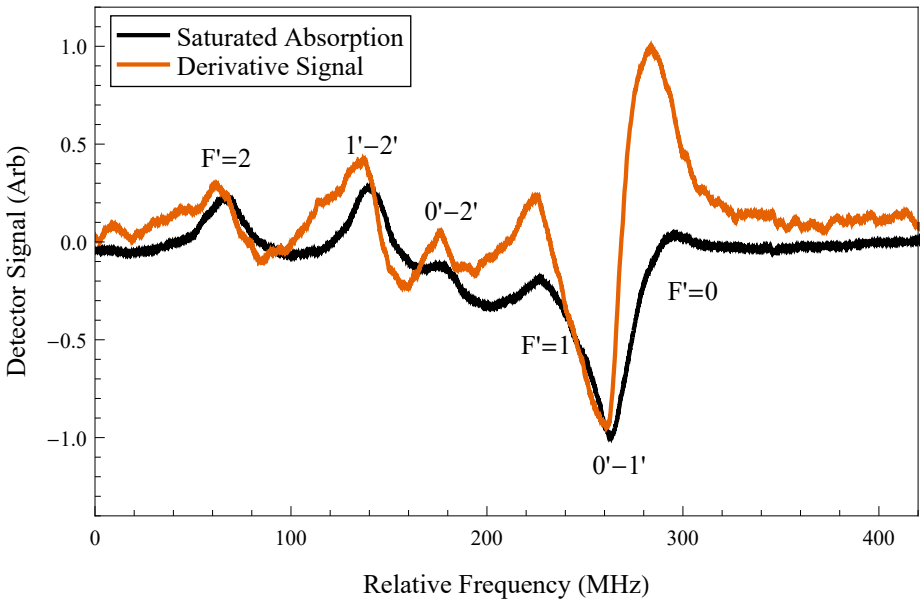

FIG. 10: Saturated absorption and derivative signal for the repumper laser. The saturated absorption signal represents the $5S_{1/2}$ $F = 1 \rightarrow 5P_{3/2}$ transitions. The laser is locked on the $1' - 2'$ crossover.

where the laser is locked on the $1' - 2'$ crossover peak. The optical setup for the repumper beam is shown in Fig. 11. The AOM (Gooch & Housego R23080-1) is set at 78.47 MHz which puts the repumper frequency on resonance with the $F = 1 \rightarrow F = 2'$ transition.

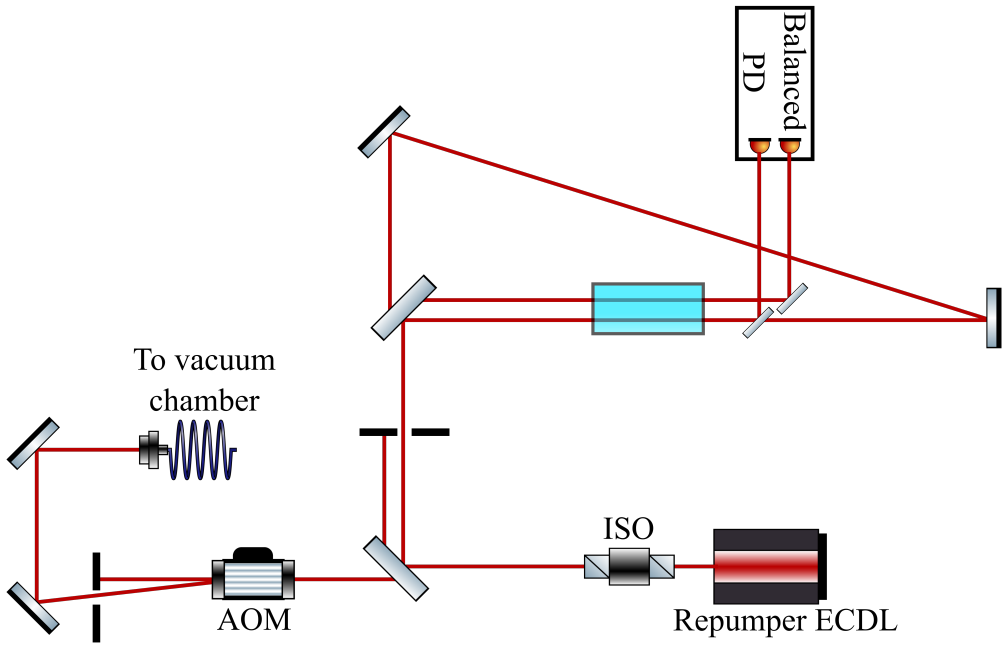

FIG. 11: Repumper laser optics diagram. The optical isolator ISO (OFR IO-3-780-LP) is used to prevent feedback into the laser. The AOM (Gooch & Housego R23080-1) is used to put the beam on resonance and acts as a switch to turn the beam on and off. ECDL (Thorlabs DL7140-201S).

The MOT and repumper beams are sent to a nearby optics table where the vacuum chamber is located. The optics setup for the MOT is shown in Fig. 12 where the MOT and repumper beams are combined before being directed into the chamber. The MOT beam has a power of approximately 24 mW while the repumper has about 1 mW. The first cube directs a portion of the beam upward but the vertical MOT beam is omitted to reduce visual clutter of the diagram. The beams are expanded and collimated to ≈ 1 cm^2 by lenses that are also omitted from the figure. The half-wave plates (yellow) allow for power control of each arm of the apparatus. The quarter-wave plates (red) transform the linearly polarized

light into circular and cause the counter-propagating beam to be of the opposite polarization. Although they will be discussed later, the PIXIS CCD is used for fluorescence imaging and the Thorlabs PD is used for recording the behavior of a probe beam. A photo of an atomic ensemble of ^{87}Rb cooled and spatially confined in the MOT is shown in Fig. 13.

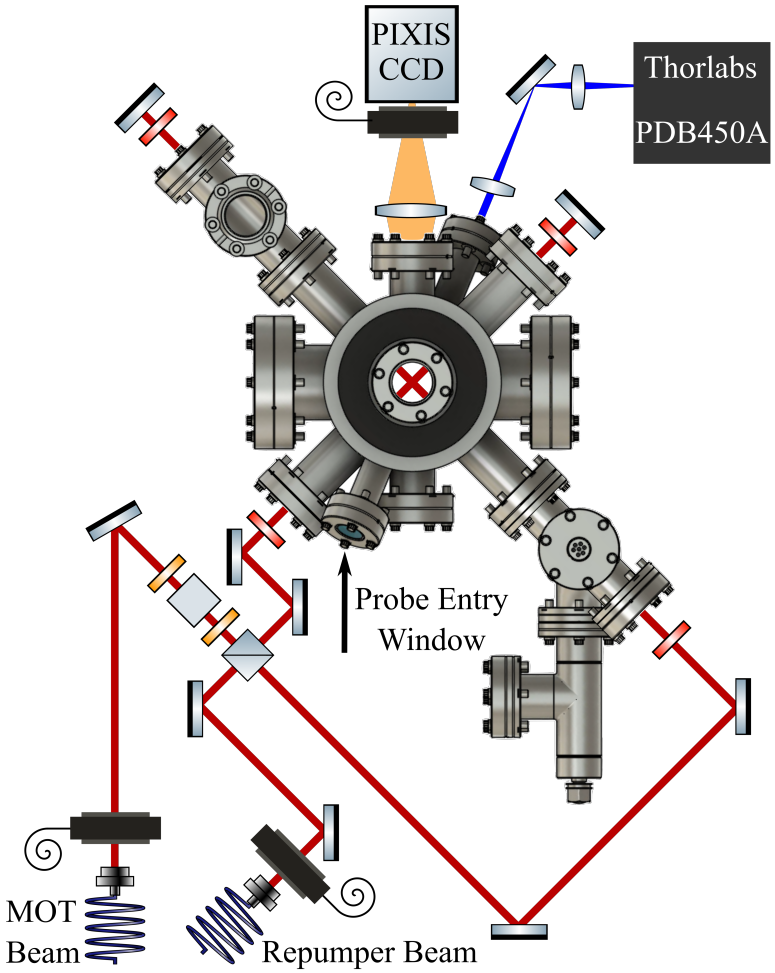

FIG. 12: MOT chamber optics diagram. The shutters (Uniblitz LS6Z2) in front of the MOT and repumper beams are used to fully extinguish any residual light leak through the fiber. The vertical MOT beams are omitted form the diagram for visual clarity. Yellow optics are half-wave plates. Red optics are quarter-wave plates.

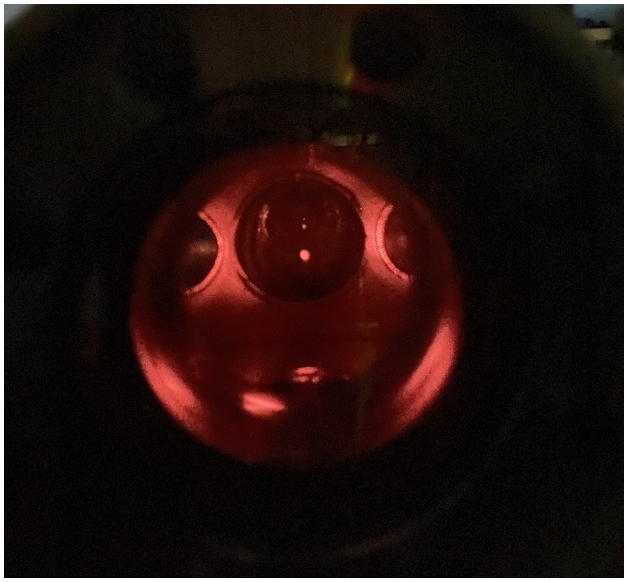

FIG. 13: Photo of an ensemble of confined atoms in a MOT.

The ultrahigh vacuum chamber is shown in Fig. 14 and was re-created in Fusion 360 with dimensions provided by Salim Balik [89]. Having a 3D model of the chamber was extremely useful for testing optical arrangements before purchasing and implementing real life changes. The vacuum chamber consists of 12 viewports, an electrical feedthrough, and an ion pump (VacIon 20 l/s 911-5036). Of the 12 viewports, 8 are 2-3/4" Del-Seal conflat (CF) flanges with 780 nm antireflection (AR) coated windows, 2 are 4-1/2" CF with 1064 nm AR coated windows, and the 2 off axis are 2-1/8" CF with no AR coating. The electrical feedthrough is connected to rubidium alkali dispensers, known as 'getters' (SAES Rb/NF/3.4/12FT10+10). Running current through the getters supplies the chamber with rubidium atoms. The ion pump is driven by a Varian 921-0062 controller and maintains the chamber at a pressure of $\approx 10^{-9}$ Torr.

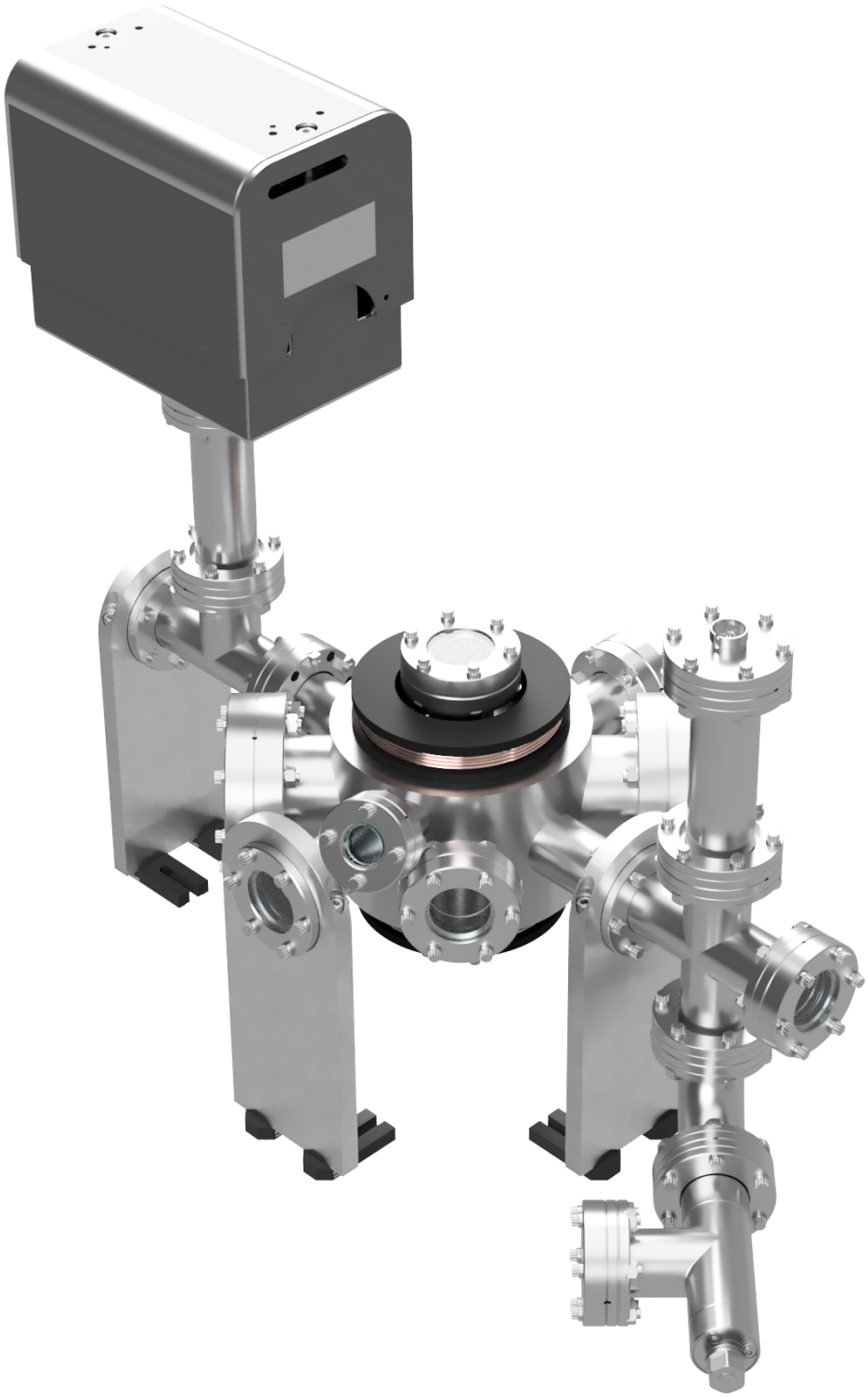

FIG. 14: Vacuum chamber assembly 3D model created in Fusion 360.

The magnetic field is provided by the anti-Helmholtz coils placed above and below the chamber which are supplied with 10 A. The coils can be seen in Fig. 14 and are clearly pointed out in Fig. 15. The coils create a field gradient of ≈ 10 Gauss/cm with respect to the center of the chamber.

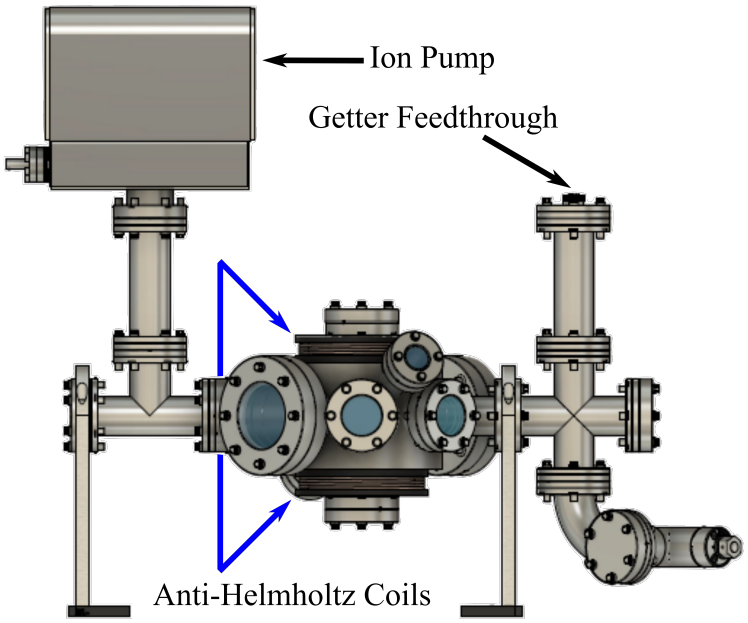

FIG. 15: MOT chamber sideview highlighting the anti-Helmholtz coil positions.

Additional shim coils are also needed to cancel out external magnetic fields. Initially the chamber had three shim coils mounted on the input ports for the MOT beams. A small upgrade project was undertaken to replace the old shim coil arrangement with six that are individually adjustable. The new coils are made from ribbon cables (3M 3365/16) and are shown in Fig. 16. Inside the shim coil control box are 2 PCBs, shown in Fig. 17, which connect the power supplies to the six ribbon cables. The PCB was designed to make each ribbon cable act as one long wire instead of 16 individual wires. The X and Y coils consist of 7 wraps (112 turns) and the Z coils are 5 wraps (80 turns). Optimal current values delivered to each of the six shim coils were painstakingly determined by observing the quality of the optical molasses as the anti-Helmholtz coils were turned off.

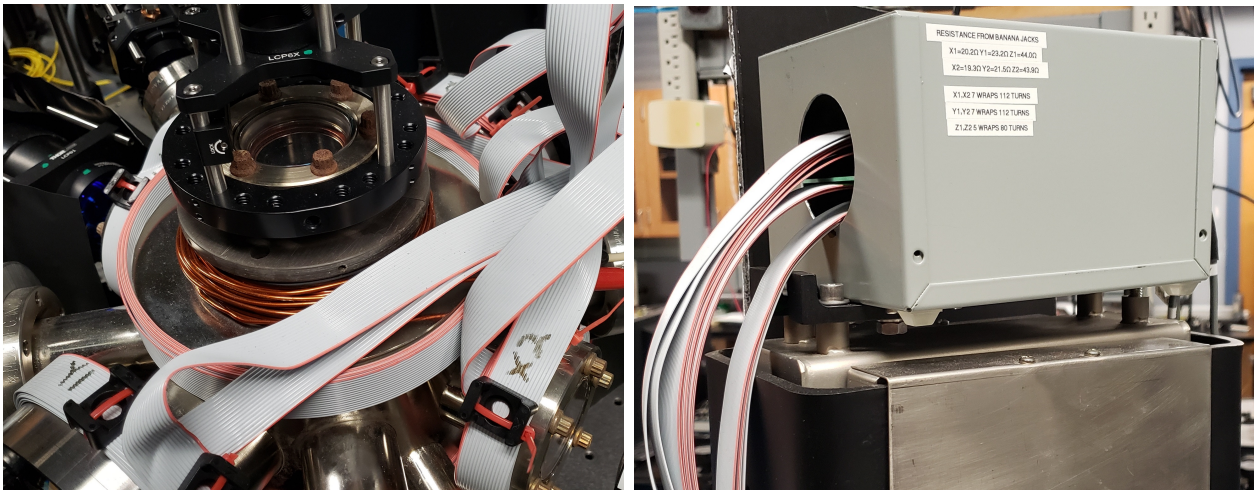

FIG. 16: New magnetic shim coil arrangement and control box housing.

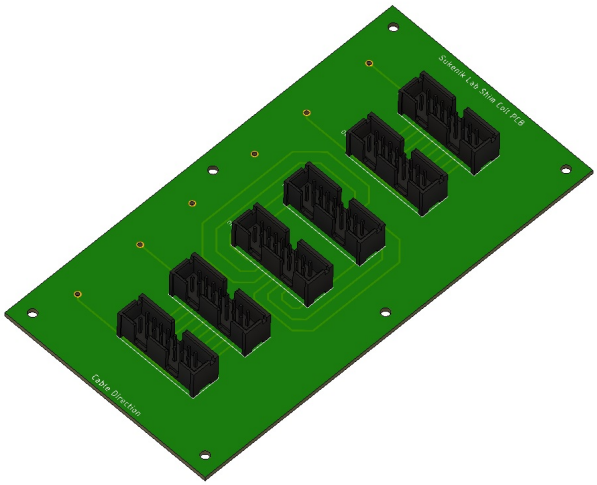

FIG. 17: Magnetic shim coil PCB created by Josh Frechem. Three shim coils can be connected on each PCB.

3.1.3 MOT CHARACTERIZATION

The following will describe techniques and results to obtain the number of atoms, spatial

parameters, and temperature of the MOT.

3.1.3.1 Atom Number

Absorption imaging and optical pumping are two techniques that can be used to determine the number of atoms in a MOT. Even though the optical pumping method was used in the final calculation of the atom number, both techniques will be discussed. Absorption imaging along with fluorescence detection is a common method to determine the number of atoms in an atomic ensemble. Once the number of atoms in the MOT are determined from absorption imaging, fluorescence detection can be used to calibrate the number of atoms per count on a CCD. This calibration factor can then be used to determine the number of atoms in a FORT where absorption imaging cannot be applied. The number of atoms can also be determined with an optical pumping technique which also can be paired up with fluorescence detection to determine a calibration. The optical pumping method was investigated over a large parameter space and therefore is described in a separate chapter.

Absorption imaging is a method that analyzes the intensity of a probe beam through the MOT over a range of detunings. Using Beer's Law, the amount of light transmitted through a medium is

$$I_T(r,\Delta) = I_0 e^{-b(r,\Delta)}, \tag{192}$$

where I_0 is the initial intensity before the medium and b is known as the optical depth. The MOT has a Gaussian spatial distribution defined by

$$\rho(r) = \rho_0 e^{-\frac{r^2}{2r_0^2}}, \tag{193}$$

where ρ_0 is the peak density and r_0 is the Gaussian radius. The optical depth b is a unitless parameter given by

$$\begin{aligned} b(r,\Delta) &= -\ln\left(I_T/I_0\right) = \sqrt{2\pi} r_0 \rho(r) \sigma(\Delta) \\ &= \sqrt{2\pi} r_0 \rho(r) \frac{\sigma_0}{1+\left(\frac{2\Delta}{\Gamma}\right)^2} = \frac{b_0}{1+\left(\frac{2\Delta}{\Gamma}\right)^2} e^{-\frac{r^2}{2r_0^2}}, \end{aligned} \tag{194}$$

where $b_0 = \sqrt{2\pi} r_0 \rho_0 \sigma_0$ is the peak optical depth, σ_0 is the on resonant cross section, Δ is the detuning from resonance, and Γ is the natural decay rate. The total number of atoms is

found by integrating Eq. (193) over all space which yields

$$N = (2\pi)^{3/2}\,\rho_0 r_0^3 = 2\pi\frac{r_0^2}{\sigma_0}b_0. \tag{195}$$

Therefore, the number of atoms can be determined from extracting the peak optical depth in the center of the MOT along with the Gaussian radius. Experimentally this is performed by recording CCD (Princeton Instruments PIXIS 1024 7520-00 13) images of the probe transmission with ($I_T(r,\Delta)$) and without (I_0) the MOT present over a range of detunings around the $F = 2 \rightarrow F' = 3$ transition. Figure 18 shows an example of an absorption imaging data set with the probe on resonance without (left) and with (right) the MOT present. The probe pulse was roughly 10 μW for a duration of $50 - 100$ μs and attenuated before the CCD to prevent saturation if needed. The $1/e^2$ radius r_0 can be determined by fitting a cross section of either the absorption image or a fluorescence image of the MOT to a Gaussian line shape. A fluorescence image is obtained by flashing the MOT and repumper beams for 100μs and recorded by the same CCD used for absorption imaging. A fluorescence image will provide a more accurate representation of the size of the MOT if $b > 1$.

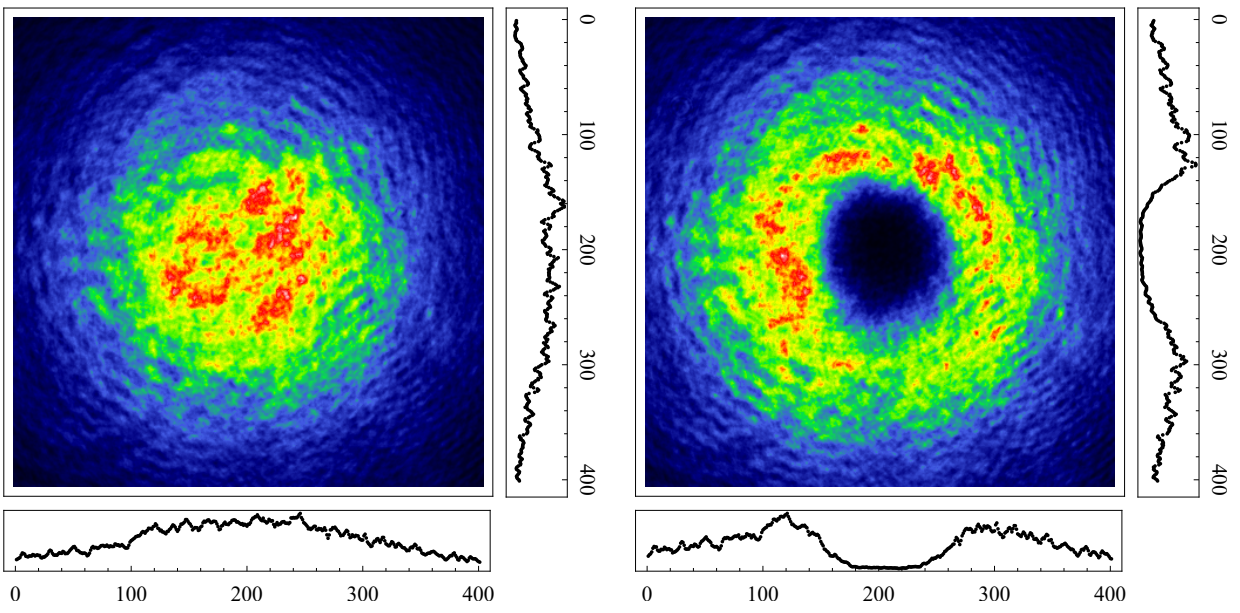

FIG. 18: Absorption imaging of a MOT. The left is the probe profile (I_0) while the right is with the MOT present with the probe on resonance (I_T). The cross-section profiles displayed on the bottom and right of the figures are with respect to the center pixel. The axis labels represent the number of pixels. (13x13 μm per pixel)

The peak optical depth is determined by dividing the two images and taking the natural logarithm as given by Eq. (194) over a range of detunings. A central 5×5 pixel area (b around $r = 0$) is typically averaged over for each detuning and then fit to a Lorentzian. There is an unfortunate downside to this method due to the spectral line shape deviating from a true Lorentzian when $b > 1$. Allowing the MOT to expand before probing may help this issue as long as the probe beam is large enough. The number of atoms can then be obtained once b_0 and r_0 are determined. A calibration factor can then be determined by associating the number of atoms to the number of counts from the fluorescence image.

In summary, under the proper conditions, the number of atoms can be determined with the absorption imaging method but requires a multitude of CCD images to be taken. The aforementioned two absorption profiles and one fluorescence image must be obtained along with their corresponding background images for every detuning, which is rather time consuming. If the optical depth is > 1 the MOT must be allowed to expand. Therefore, the temperature of the MOT must be determined in order to extrapolate backwards to the unexpanded MOT size. Temperature measurements, described later, would add several more steps to this process.

This method was determined to be nonviable due to the limited viewports of the vacuum chamber in the final experimental arrangement. A solid foundation of laboratory knowledge was formed during this introductory experience where important skills in optimizing optical arrangements, timing procedures, RF electronics, data acquisition, and creating data analyzing tools were obtained. A more direct method involving optical pumping was used to determine the atom number and will be described next.

The following text describes an optical pumping atom counting technique that benefits from being experimentally simple to apply and has a rather straightforward theoretical background. The technique also claims to be independent of detuning and intensity of the probe beam, which was found to not always be the case and will be discussed more thoroughly towards the end of this section. This atom counting project was initially intended to be simply a characterization technique but after obtaining interesting results much more time was spent investigating a larger parameter space as well as creating a simulation to compare with experimental results. With that said, the following text will first discuss the straightforward implementation of the optical pumping method and then present interesting data that diverges from the detuning independent behavior that is claimed.

An optical pumping technique [91] was used to determine the atoms in the MOT by analyzing absorption from a probe beam. The idea is to prepare the ^{87}Rb MOT in the

$F = 2$ ground state and apply a probe beam on the $5S_{1/2}$ $F = 2 \rightarrow 5P_{3/2}$ $F' = 2$ transition where the atom can decay back to either the $F = 2$ or the $F = 1$ ground state. Once an atom falls into the $F = 1$ it will not interact with the probe. The relative probability that an atom will decay from a particular excited state to any specific allowed ground state transition is known as the branching ratio. The branching ratio can be determined by the normalized line strength factor of a $F' \rightarrow F$ decay, which is given by [62]

$$S_{FF'} = (2J' + 1)(2F + 1) \begin{Bmatrix} J & F & I \\ F' & J' & 1 \end{Bmatrix}^2 . \tag{196}$$

Conveniently, the values for the $F' = 2 \rightarrow F = 2$ and $F' = 2 \rightarrow F = 1$ decay channels are both 1/2. The expected value for the number of photons an atom absorbs in order to decay to the $F = 1$ ground state is

$$\langle N_p \rangle = \sum_{n=1}^{\infty} n(1-p)^{n-1}p = \frac{1}{p}, \tag{197}$$

where p is the probability decay to the $F = 1$. Therefore, it will take an average of two photons to optically pump an atom from the $F = 2$ to $F = 1$ ground state. The result obtained by Eq. (197) converges for small atom numbers ($\gtrapprox 20$) therefore it is perfectly valid assumption for typical MOT values of $10^7 - 10^8$ atoms. The number of atoms in a MOT can then be determined by recording the amount of photons absorbed from a probe and dividing by two.

The optical pumping experiment is preformed by introducing a probe laser on resonance with the $F = 2 \rightarrow F' = 2$ transition. The probe enters the chamber through the viewport labeled in Fig. 12 and is recorded by a photodetector (Thorlabs PDB450A). Probe transmission data is recorded with and without the MOT present in order to determine the amount of light absorbed by the atoms. The timing diagram is shown in Fig. 19. The repumper was kept on for 100 μs after extinguishing the MOT beam to ensure a maximum amount of atoms in the $F = 2$ ground state before probing. The typical duration of the probe was 600 μs but can be changed depending on the intensity and detuning. Figure 20 presents probe transmission data with and without the MOT (a) while the subtracted signal (b) represents the amount of light absorbed by the MOT. Data were taken and averaged over 128 cycles on an oscilloscope (Tektronix MDO4054C). The number of atoms can be determined by integrating the subtracted signal and therefore is given by

$$N_A = \frac{\lambda}{2hc}\chi \int_{t_0}^{t_f} V(t)dt, \tag{198}$$

where χ is the conversion factor of the Thorlabs PDB450A in W/V and the factor of $1/2$ corresponds to the process taking an average of two photons for each atom. The error for the number of atoms due to the oscilloscope and detector is determined by taking the standard deviation per data point of a segment of the subtracted signal at a much later time when the absorption process has finished. The error was then applied to the number of points used to calculate the atom number, therefore signals which take longer will have a larger error. The error value is typically on the order of 10^5 atoms and is also in line with the approximate output noise amplitude provided in the photodetector documentation. Error analysis was performed on the averaged oscilloscope signal and not on a shot by shot basis. An error on the order of 10^5 was also found by performing the same measurement several times and taking the standard deviation of the calculated number of atoms. The optical pumping method can improve the accuracy of the number of atoms counted in a MOT by at least an order of magnitude in comparison to absorption imaging while also being less complex to implement.

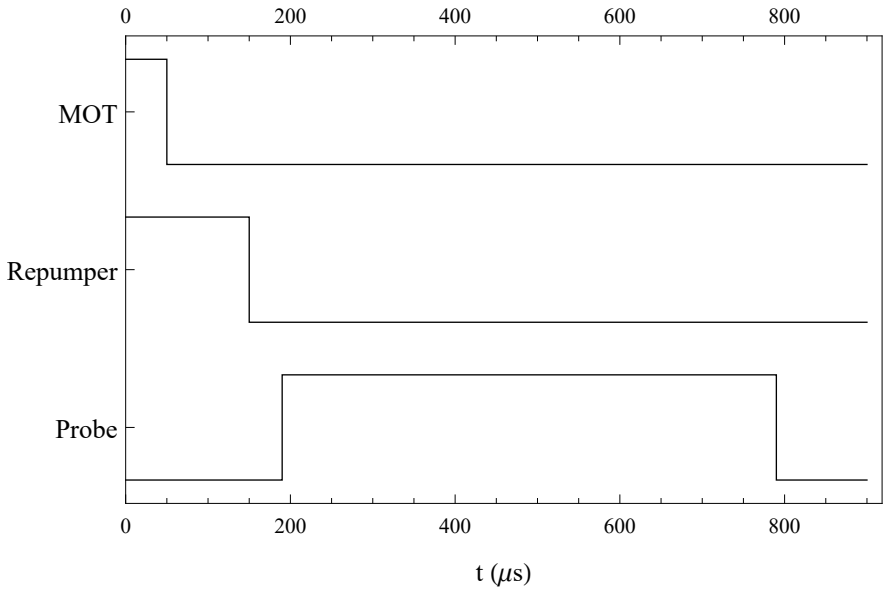

FIG. 19: Optical pumping timing diagram.

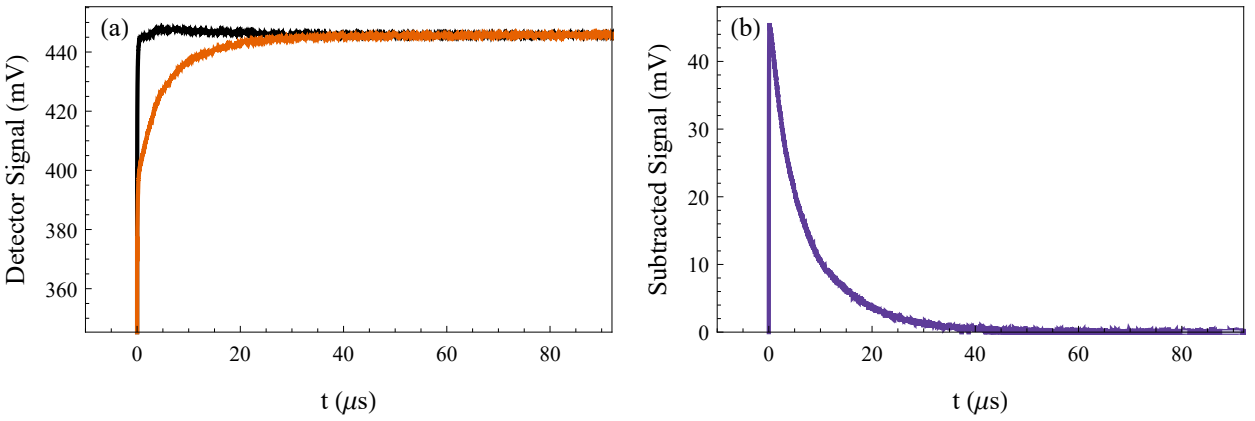

FIG. 20: Optical pumping signal from a 0.25 mW probe on resonance to the $F = 2 \rightarrow F' = 2$ transition. (a) represents the absorption signal with (red) and without (black) the MOT present. (b) represents the amount of light absorbed by the MOT. The number of atoms determined from this signal is $2.484 \pm 0.002 \times 10^8$.

As mentioned in the introduction to the optical pumping method, the technique claims to be detuning and intensity independent. At first glance this claim appears to be obvious because the optical pumping process will simply take longer if the detuning is off resonance due to the detuning dependent scattering cross-section. Similarly, the process will take more time if the intensity of the probe is reduced. In both cases the atom number, or amount of light absorbed by the sample, should remain the same. Since this was found to not always be the case, a large parameter space was explored in order to understand and possibly introduce a model to explain the results. Data were analyzed from probe absorption, fluorescence, and simulation results.

Several techniques were used in order to explore different experimental regimes by changing the optical depth, density, and atom number. Probing at different expansion times allowed for the number of atoms to remain the same while changing the optical depth and density, while reducing the current to the getters decreased the amount of atoms available to be trapped in the MOT.

Typical detuning-dependent results obtained from the optical pumping experiment at different optical depths are shown in Fig. 21. The approximate magnitude of the detuning dependent behavior can be found by dividing each set of data by the number of atoms found at $\pm$ 12 MHz and will be called overcounting. The magnitude of overcounting was found to

be an optical depth b_0 effect rather than dependent on purely density or atom number. The optical depth dependence can be seen in Figs. 22-23 where the overcounting is the same at different atom number and density regimes as long as the optical depth is the same. The data in Fig. 22 was taken where the larger atom number corresponds to the smaller density while the opposite is the case for Fig. 23. The overcounting error bars were omitted to reduce visual clutter but have a typical value of approximately $\pm$ 0.025.

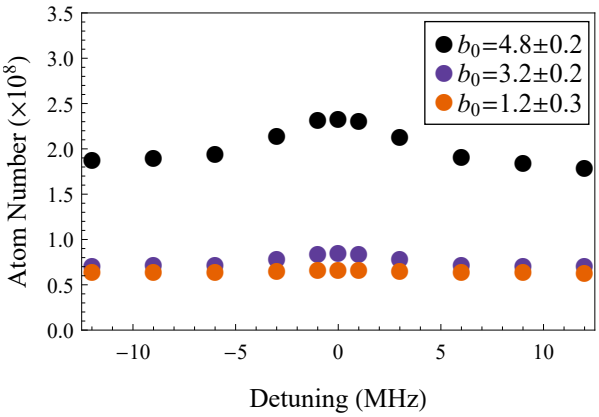

FIG. 21: Number of atoms calculated using the optical pumping technique at several detunings and under different conditions. The probe power was 0.25 mW and detuned around the $F = 2 \rightarrow F' = 2$ transition. The optical depth b_0 values were determined by using the number of atoms calculated at $\pm$ 12 MHz along with r_0 obtained from fluorescence imaging.

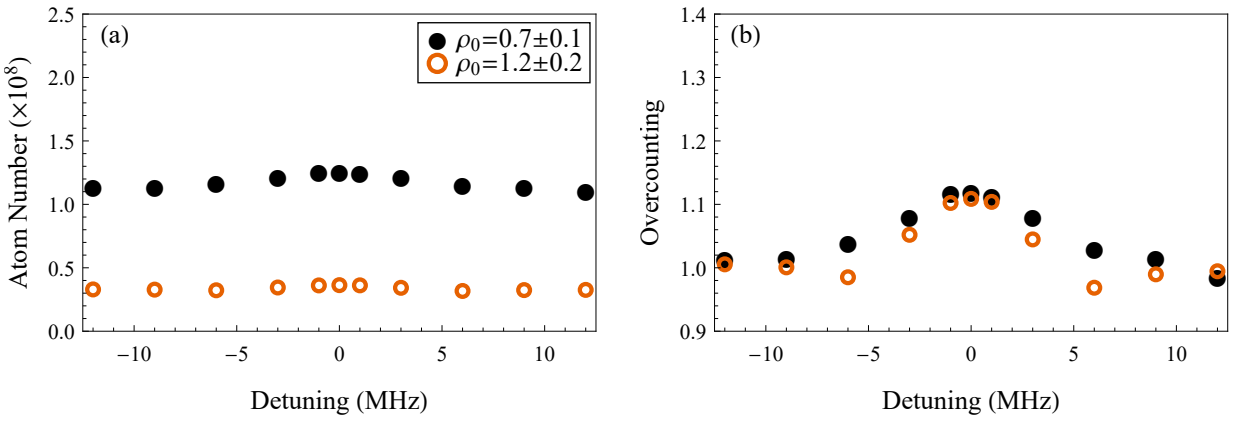

FIG. 22: Atom number and overcounting results for $b_0 = 1.7 \pm 0.3$. The density of the samples are 0.7 ± 0.1 (circles) and 1.2 ± 0.2 (open circles) in units of 10^{10} atoms/cm^3. (a) represents the atom number while (b) corresponds to overcounting.

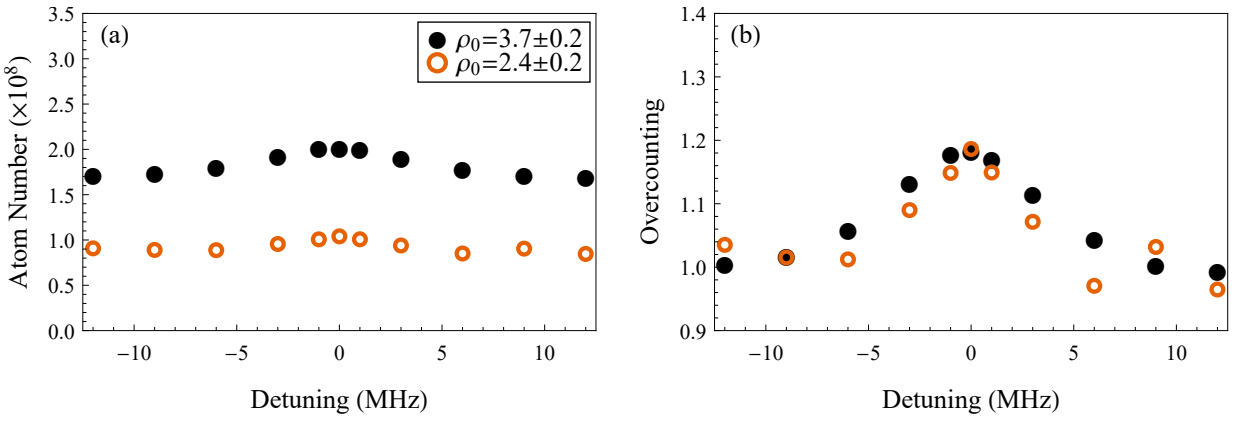

FIG. 23: Atom number and overcounting results for $b_0 = 4.5 \pm 0.3$. The density of the samples are 3.7 ± 0.2 (circles) and 2.4 ± 0.2 (open circles) in units of 10^{10} atoms/cm^3. (a) represents the atom number while (b) corresponds to overcounting.

The attributed reason for the occurrence of the overcounting effect is due to the depumping of atoms which have already been counted, therefore re-introducing them to be counted again. The atoms are excited from the $5S_{1/2}$ $F = 2 \rightarrow 5P_{3/2}$ $F' = 2$ and decay to either

the $F = 2$ (Rayleigh scattering) or $F = 1$ (Raman scattering) ground state. An atom is considered counted once it decays to the $F = 1$ ground state, but the photon that is released can cause an already counted atom to optically pump back to the $F = 2$ where it will interact with the probe again. While the explanation is simple, the process is very dynamic and non-trivial. It is dependent on the optical depth and the populations of the atoms in their respective ground states at a particular time.

An optical pumping simulation was created that allowed for pumped atoms to be depumped via the Raman scattered photons within the sample. The simulation tracked the amount of photons that were absorbed and the number of photons that exited the sample each time step. Each photon that exited the sample retained information on its trajectory and whether it was Rayleigh or Raman scattered. Figure 24 shows an example of the trajectories of several photons which exited the sample at the end of a particular time step. The simulated atomic ensembles were randomly generated with N atoms in a Gaussian spatial distribution. Each atom acted as a hard target with an approximated cross sectional area based on the atomic cross section. The optical depth of the simulated sample cannot be calculated simply with the number of atoms and the Gaussian radius due to this approximation. Therefore, a phenomenological approach was taken to extract an effective optical depth and will be explained further in the text.

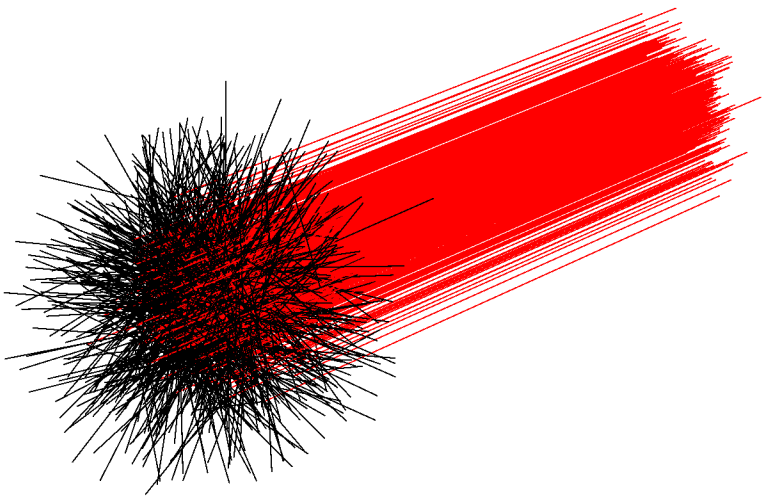

FIG. 24: Photon trajectories from the optical pumping simulation. The red lines denote the incoming photons while the black represent the scattered trajectories. All photons that do not interact are ignored.

A few simple checks and comparisons were made between the simulation results and experimental data to analyze the behavior. First and foremost, the simulation reproduced the expected result of taking an average of two photons to pump a single atom from the $F = 2$ to $F = 1$ ground state. This result was independent of all parameters when the Raman scattered photons were not allowed to interact. The comparison between the simulation and experimental time resolved fluorescence at similar optical depth and probe intensity is shown in Fig. 25. The pump rates were then determined by fitting the time dependent fluorescence data to a decaying single exponential. It must be noted that the behavior of the fluorescence begins to depart from a true single exponential as the optical depth increases. The on resonant pump rates as a function of probe intensity is shown in Fig. 26 where it was found that the pump rates increase linearly as the probe intensity increases. The linear behavior of the pump rates as a function of probe intensity hold for all detuning values.

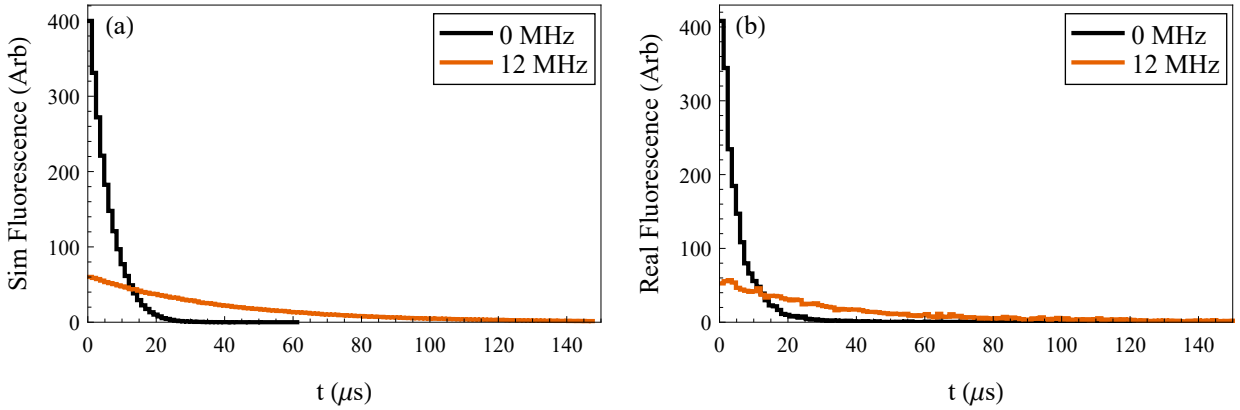

FIG. 25: Time resolved fluorescence from the (a) optical pumping simulation and (b) experimental data. The optical depth for both data sets was approximately 2.3. The data were taken at two detunings and the probe intensity was 0.125 mW/cm^2.

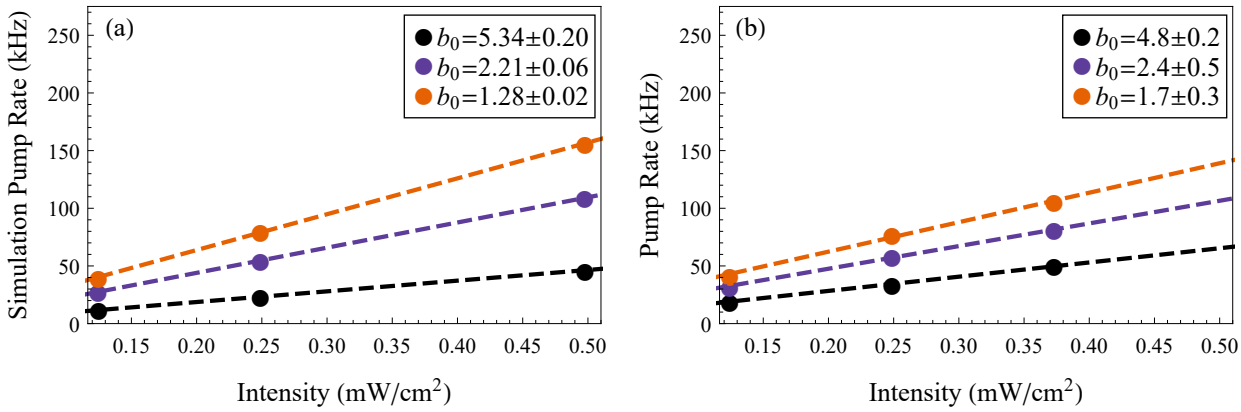

FIG. 26: On resonant pump rate from the (a) optical pumping simulation and (b) experimental data. The simulation reproduces the expected linear behavior within the same optical depth and probe intensity regime as the experimental data. The simulation shows a slower(faster) rate at a larger(smaller) optical depth compared to the experimental data, which is an expected result.

The overcounting effect as a function of detuning is shown in Fig. 27. The simulation

overcounting value was directly determined since the simulation tracks the amount of photons absorbed and the number of atoms is a user input. The experimental overcounting values were determined by dividing the atom number data shown in Fig. 21 by the values at ±12 MHz. An interesting result is that the simulation data noticeably overcounts even at ±12 MHz as b_0 increases. The simulation also provides results that show the magnitude of overcounting was only dependent on b_0 and independent of probe intensity, number of atoms, and sample density.

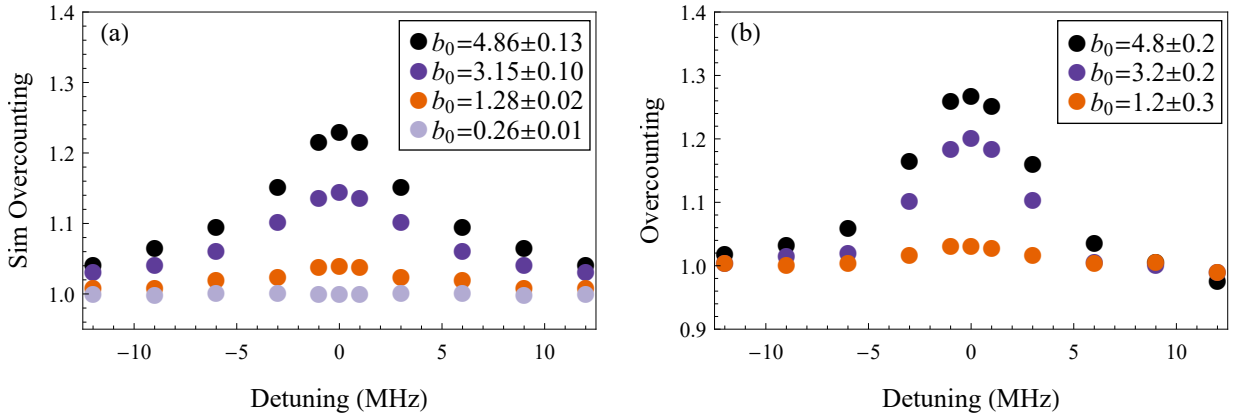

FIG. 27: Optical pumping overcounting vs detuning from the (a) optical pumping simulation and (b) experimental data. The experimental overcounting values were determined by dividing the atom number data shown in Fig. 21 by the values at ±12 MHz. A value of 1 corresponds to two photons absorbed per atom in the sample.

Previous discussions on the topic of scattering from a Gaussian sample on the $5S_{1/2}$ $F = 2 \rightarrow 5P_{3/2}$ $F' = 3$ cycling transition have found that the total scattering cross section, and therefore the amount of scattered photons, scale as $\mathrm{Ein}(b)/b$ [49–52]. The $\mathrm{Ein}(b)/b$ scaling was found to break down when analyzing the optical pumping process due to the dynamic behavior of the open transition, therefore a different direction was taken. A phenomenological approach was derived to obtain the optical depth b_0 from the detuning dependent optical pumping rate of the fluorescence. Using a simple model with the use of the Beer-Lambert

law, the transmitted light through a sample of optical depth b and probe intensity I_0 is

$$I_T(\Delta) = I_0 e^{-b(\Delta)}, \tag{199}$$

where $b(\Delta) = b_0/(1+(2\Delta/\Gamma)^2)$. This is a steady state solution and is used as an initial value. The measurements are taken with a PMT which record the incoming intensity, or rate, at which the photons exit the sample. The measurements record the fluorescence, which is the light that is not transmitted, namely

$$I_F(\Delta, 0) = I_0(1 - e^{-b(\Delta)}). \tag{200}$$

The PMT records a signal that decays at some constant rate $R_F(\Delta)$ over time. This single exponential decay is an approximation that is used. The approximate time dependent fluorescence is then given by

$$I_F(\Delta, t) = I_0(1 - e^{-b(\Delta)})e^{-R_F(\Delta)t}. \tag{201}$$

The total fluorescence, or number of photons per area, given off by the sample will then be given by

$$\mathrm{N}_F(\Delta) = \int_0^\infty I_0(1 - e^{-b(\Delta)})e^{-R_F(\Delta)t} = \frac{I_0}{\mathrm{R}_F(\Delta)}(1 - e^{-b(\Delta)}). \tag{202}$$

At this point both sides of the equation are simply constant values and the total amount of fluorescence depends on the sample itself and should not depend on I_0. Therefore, in this approximation $R_F(\Delta) \propto I_0$ since $I_0/R_F(\Delta) =$ constant. The linear proportionality behavior of the rate as a function of probe intensity was shown in Fig. 26 for the simulated and experimental data. Applying this proportionality to Eq. (200) yields

$$R_F(\Delta) \propto I_0(1 - e^{-b(\Delta)}). \tag{203}$$

Finally, taking the ratio of Eq. (203) at some detuning Δ and on resonance gives

$$\mathrm{R}_F(\Delta) = \mathrm{R}_F(0)\frac{(1 - e^{-b_0/(1+(\frac{2\Delta}{\Gamma})^2)})}{(1 - e^{-b_0})}. \tag{204}$$

The line shape flattens out around resonance as b_0 increases, while the expected single atom Lorentzian behavior returns as b_0 goes to zero. Equation 204 was used to fit the fluorescence rate vs detuning data of the simulation to obtain the b_0 values listed in previous figures. Applying this fitting procedure to experimental data also provided predictions to b_0 comparable to the values obtained by using the optical pumping atom number and spatial parameter r_0. Simulation and experimental data fit to Eq. (204) is shown in Fig. 28.

The behavior of the simulation is consistent to that of the experimental data under similar conditions. The predicted optical depth of the experimental data obtained from the fit to Eq. (204) is displayed in the legend as the second value in Fig. 28b.

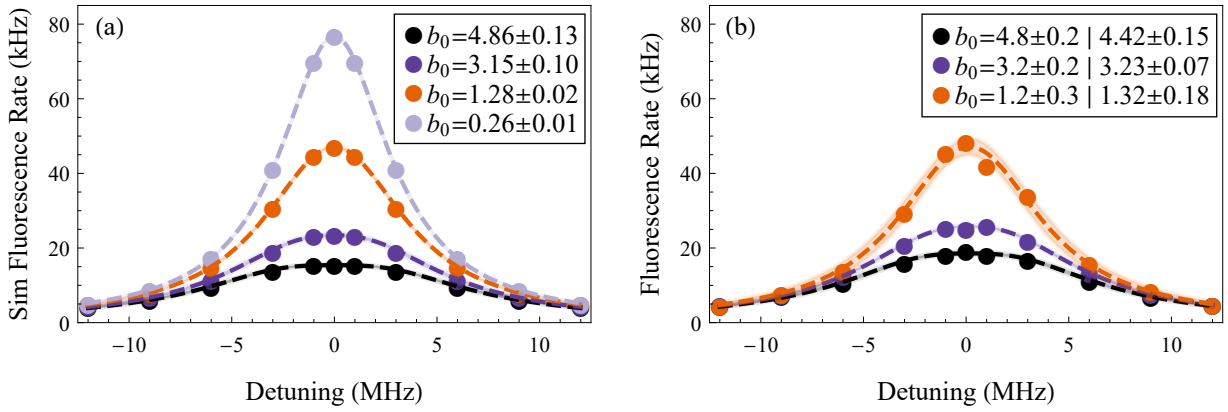

FIG. 28: Fluorescence rate vs detuning from the (a) optical pumping simulation and (b) experimental data. The first b_0 value in the legend for the the experimental data (b) corresponds to the original method while the second value was obtained from the fit to Eq. (204). The dashed lines correspond to the fit with a 95% confidence band.

In an effort to maintain clarity and consistency with presenting the comparison of the experimental data to simulation results, the same three experimental data sets were used in Figs. 21, 27, and 28. The predictive analysis was performed on several data sets that were acquired under a multitude of different conditions and is presented in Fig. 29, where the calculated value is compared to the predicted value of b_0. Even though the predicted b_0 values are in line with the calculated values, it must be noted that data could only be taken over a limited optical depth regime, therefore the validity of the phenomenological approach at greater optical depths is unknown a this time.

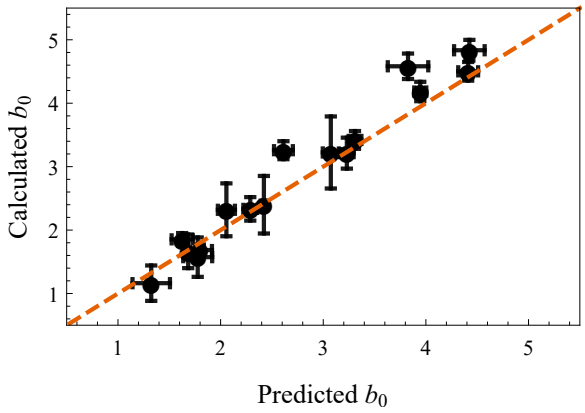

FIG. 29: Calculated vs predicted optical depth. The predicted optical depth b_0 was obtained by fitting the fluorescence rates as a function of detuning to Eq. (204). The dashed line represents where calculated is equal to predicted. Experimental data were acquired under several different conditions at a probe intensity of 0.125 mW/cm^2.

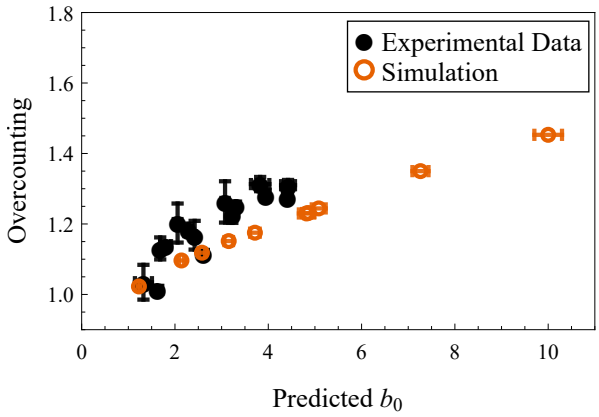

FIG. 30: Overcounting vs predicted optical depth comparison between simulation (open circles) and experimental (circles) data. The predicted optical depth b_0 was obtained by fitting the fluorescence rates as a function of detuning to Eq. (204). Experimental data were acquired under several different conditions at a probe intensity of 0.125 mW/cm^2.

The final interesting pieces of simulation information that will be presented are related

to the separated time resolved fluorescence of the Rayleigh and Raman scattered photons. This type of data cannot be experimentally obtained in the current apparatus because the difference between the two photons is only around 6.8 GHz or 0.0139 nm. Separating the two frequencies and detecting them independently is non-viable because typical filters used in the lab have a FWHM of 1 nm around the central wavelength. Figure 31 presents the on resonance simulation fluorescence associated with the $b_0 = 4.86$ data set shown in Fig. 28 for the Raman (black) and Rayleigh (red) photons. The two signals overlap for samples with $b_0 < 1$ and diverge from each other as b_0 increases. The detuning dependent pump rates for the Raman and Rayleigh fluorescence, shown in Fig. 32, also have their own behavior that differs as b_0 increases. Namely, the Rayleigh fluorescence line shape broadens and ends up flattening out as b_0 increases. The FWHM of the detuning dependent pump rates as a function of b_0 is shown in Fig. 33. The FWHM of the Raman and Rayleigh fluorescence differ from another as b_0 increases and converges to the natural decay rate at $b_0 \ll 1$. The FWHM was determined computationally from the fit to detuning dependent pump rates using Eq. (204).

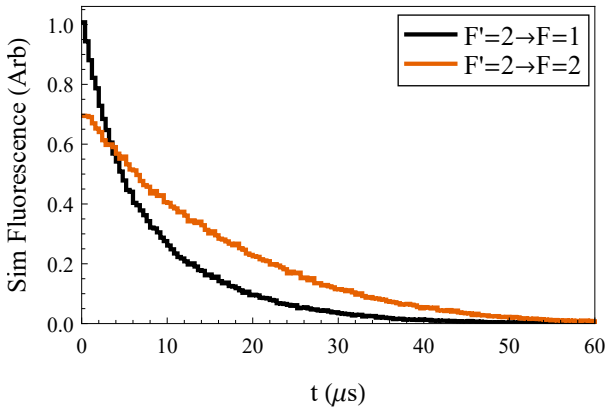

FIG. 31: Time resolved fluorescence of the Rayleigh and Raman scattered photons from the optical pumping simulation. The Raman (black) scattered photons correspond to atoms decaying from the $F' = 2 \rightarrow F = 1$ while the Rayleigh (blue) represent $F' = 2 \rightarrow F = 2$ decay. This data is associated with the on resonance simulation data point for $b_0 = 4.86$ in Fig. 28.

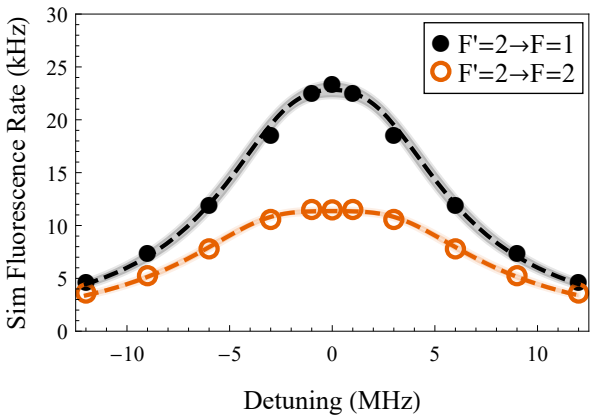

FIG. 32: Detuning dependent pump rates of the Raman and Rayleigh fluorescence from the optical pumping simulation. The Raman (circles) scattered photons correspond to atoms decaying from the $F' = 2 \rightarrow F = 1$ while the Rayleigh (open circles) represent $F' = 2 \rightarrow F = 2$ decay. This data is associated with the simulation data points for $b_0 = 4.86$ in Fig. 28.

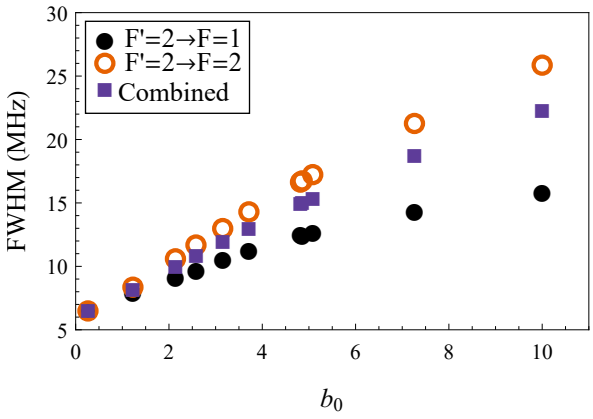

FIG. 33: Full width at half max vs b_0 of the Raman, Rayleigh, and total fluorescence from the optical pumping simulation. The Raman (circles) scattered photons correspond to atoms decaying from the $F' = 2 \rightarrow F = 1$, the Rayleigh (open circles) represent $F' = 2 \rightarrow F = 2$ decay, and the combined (squares) is the total fluorescence.

In summary, this phenomenological approach utilized the Beer-Lambert law with a single exponential temporal decay behavior to obtain the optical depth of the sample. It is important to note that the Beer-Lambert law does not take into account multiple scattering and the real decay behavior is not a simple single exponential, especially at larger optical depths. Multiple scattering, optical pumping, and saturation effects were not directly included in this derivation. The resulting fits to fluorescence rates of experimental data predicted, within reason, the previously calculated values of b_0. Depending on the validity of this approach, b_0 can be determined directly from the detuning dependence of the fluorescence rates. That is in contrast to the typical method of requiring atom number and the sample Gaussian radius r_0. A simulation was then created to analyze the optical pumping process and provided results consistent with multiple scattering induced de-pumping of the atomic sample. The simulation also provided predictions of the fluorescence that is outside the capabilities of the current apparatus to confirm. At larger optical depths the simulation time resolved fluorescence data diverges further from single exponential behavior. Therefore, this may be an interesting area of continued exploration where modifications to the phenomenological approach will be required for a more complete description of the multiple scattering process.

3.1.3.2 Temperature

The temperature of the MOT was obtained by recording the density distribution of the atoms after being released from the trap as a function of time. The spatial profile of the MOT was approximated by

$$\rho\left(x,y,z\right)=\rho_0 e^{-\frac{x^2}{2r_x^2(t)}}e^{-\frac{y^2}{2r_y^2(t)}}e^{-\frac{z^2}{2r_z^2(t)}}. \tag{205}$$

where the squared Gaussian radii expand as

$$r_i^2(t)=r_i^2(0)+v_i^2t^2. \tag{206}$$

The atomic cloud is assumed to have a Maxwell-Boltzmann velocity distribution, therefore the velocity is related to the temperature by $v_i^2=\dfrac{k_BT}{m}$.

The observation of the expansion of the MOT was performed by turning off the MOT and repumper beams, allowing the MOT to expand for some given time, and then flashing the MOT and repumper beams. The fluorescence of the atoms during the flash was recorded on a cooled CCD (PIXIS 1024BR) with 13×13 μm pixel size. The beams were flashed for 50 μs for 10 accumulations over several expansion times. Figure. 34 shows the MOT images

at different expansion times. A cross section of each image was then fit to a Gaussian to obtain the horizontal r_x and vertical r_y at several expansion times.

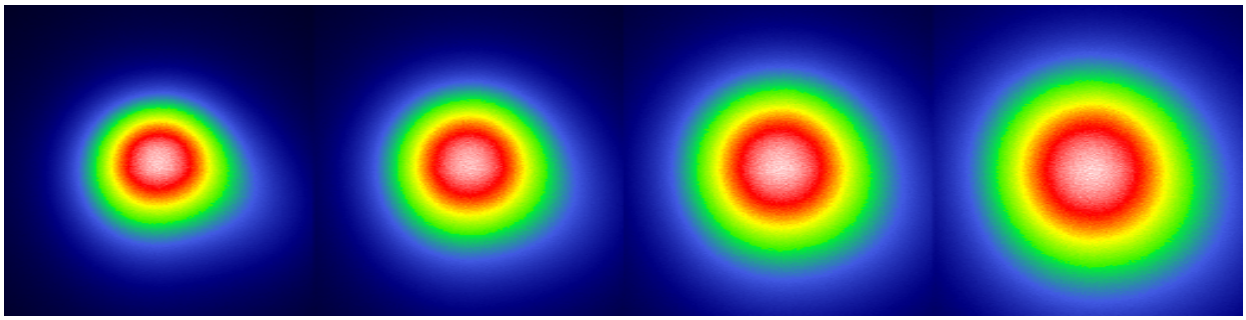

FIG. 34: Spatial profile of MOT at various expansion times. Expansion times from left to right are 3, 4, 5, and 6 ms. Each square is 3393×3393 μm.

The temperature of the MOT can now be determined by fitting the evolution of the squared Gaussian radii as a function of t^2 as shown in Fig. 35. A compressed MOT will be described during the FORT loading procedure but the temperature was determined in the same way as for the regular MOT. Typical MOT temperatures are around 150 μK while the compressed MOT is around 50 μK. The temperature uncertainties shown in Fig. 35 are the standard errors given the Mathematica.

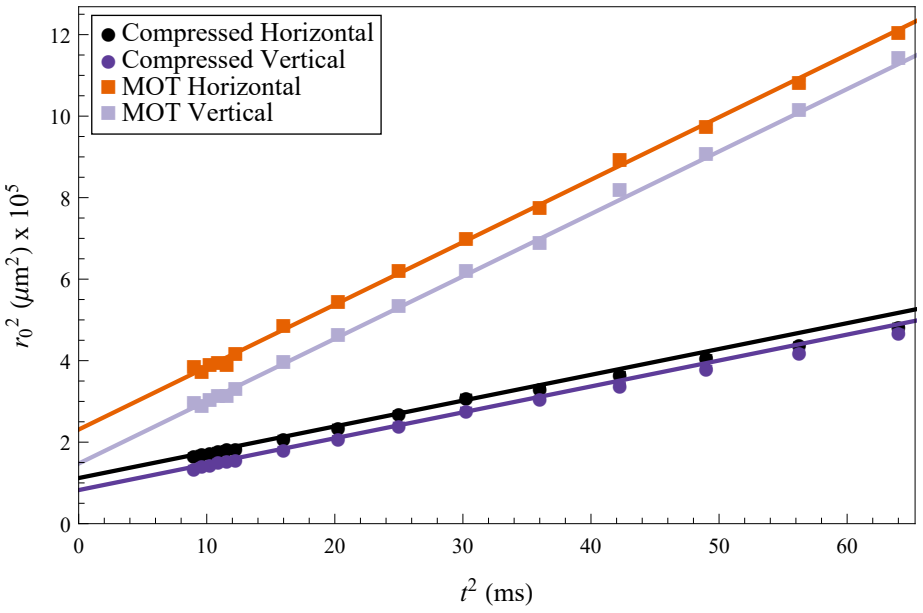

FIG. 35: Temperature measurements of the MOT (squares) and compressed MOT (circles) were determined from fit parameters using Mathematica 10.4. The horizontal(vertical) MOT temperature was found to be 160 ± 4(160 ± 3) μK while the compressed MOT was found to be 66.2 ± 1.4(66.5 ± 0.9) μK.

The initial density of the MOT can also be determined from the temperature fit by evaluating the Gaussian radii at $t = 0$. The number of atoms can be determined by integrating Eq. (193) over all space

$$N = \int \rho_0 e^{-\frac{x^2}{2r_x^2(t)}} e^{-\frac{y^2}{2r_y^2(t)}} e^{-\frac{z^2}{2r_z^2(t)}} dxdydz = \rho_0 \left(\sqrt{2\pi}\right)^3 r_x(t) r_y(t) r_z(t). \tag{207}$$

Solving for initial peak density simply yields

$$\rho_0 = \frac{N}{\left(\sqrt{2\pi}\right)^3 r_x(0) r_y(0) r_z(0)}, \tag{208}$$

where r_x and r_y will be defined as the horizontal and vertical Gaussian radii. The value of $r_z = r_x$ since the MOT shape is slightly pancaked in the horizontal direction. Typical MOT parameters under experimental conditions are shown in Table 1 where the given uncertainties were extracted from 95% mean prediction bands calculated in Mathematica. Increasing the amount of Rubidium in the chamber allows for larger MOTs with upwards of 4×10^8

atoms with r_0 around 600 μm but doing so increases the amount background gas without significantly improving the loading of the dipole trap.

TABLE 1: Typical MOT characteristics during experimental runs.

Parameter	MOT	Compressed MOT
$N(\times 10^6)$	74.9 ± 1.5	37.3 ± 0.8
T (μK)	160 ± 4	66.2 ± 1.4
$r_x(0)$ (μm)	480 ± 16	335 ± 9
$r_y(0)$ (μm)	384 ± 14	287 ± 7
ρ_0 (10^{10} cm^{-3})	5.4 ± 0.4	7.4 ± 0.5

3.2 DIPOLE TRAPS

In contrast to the magneto-optical trap which utilizes forces from scattered photons to produce a cold dilute sample, an optical dipole trap spatially confines atoms in a potential well with the dipole force with minimal scattering. Dipole trap depths are usually in the mK range therefore atoms must be pre-cooled by a MOT.

This section will describe the theory from a classical and semi-classical point of view. Specifically with approximations for far-off resonance traps (FORT). The derivations presented in this section are primarily based on discussions in Refs. [59, 60, 92]. A multi level atom approach will also be taken to calculate the polarizabilities to compare to accepted and experimental results. The experimental arrangement and characterization of the FORT will also be discussed in similar fashion as the MOT.

3.2.1 THEORY OF DIPOLE TRAPS

3.2.1.1 Classical Approach

An external electric field $\mathbf{E}$ acting on a polarizable atom induces an atomic dipole moment $\mathbf{p}$ which is given by [66, 92, 93]

$$\mathbf{p}(t) = q\mathbf{x}(t) = \alpha \mathbf{E}(t), \tag{209}$$

where $q = -e$ is the charge of an electron and α is the complex polarizability. The electric field can be put in the following form $\mathbf{E}(t) = |E_0|\cos(\omega t)\hat{\boldsymbol{\epsilon}} = \mathrm{Re}\left[E_0 e^{-i\omega t}\right]\hat{\boldsymbol{\epsilon}} = \frac{1}{2}\left[E_0 e^{-i\omega t} + E_0^* e^{i\omega t}\right]\hat{\boldsymbol{\epsilon}}$, where E_0 is generally a complex amplitude with a phase factor.

The potential of the induced dipole moment $\mathbf{p}$ in the external driving field $\mathbf{E}$ is given by

$$U_{\mathrm{dip}} = -\frac{1}{2}\langle \mathbf{p}\cdot\mathbf{E}\rangle_T = -\frac{1}{2\epsilon_0 c}\mathrm{Re}(\alpha)I(\mathbf{r}), \tag{210}$$

where $\langle..\rangle_T$ denotes the time average which picks a factor of $1/2$ and $I = \frac{1}{2}\epsilon_0 c|E|^2$. The factor of $1/2$ in front of the equation is due to the dipole being induced.

The power absorbed by the oscillating dipole from the driving field is

$$P_{\mathrm{abs}} = \langle \dot{\mathbf{p}}\cdot\mathbf{E}\rangle_T = \frac{\omega}{\epsilon_0 c}\mathrm{Im}(\alpha)I(\mathbf{r}). \tag{211}$$

The power absorbed must then be emitted by the dipole by photons with energy $\hbar\omega$, therefore the scattering rate is given by

$$\Gamma_{sc} = \frac{P_{\mathrm{abs}}}{\hbar\omega} = \frac{1}{\hbar\epsilon_0 c}\mathrm{Im}(\alpha)I(\mathbf{r}). \tag{212}$$

The interaction potential Eq. (210) and the scattering rate Eq. (212) as a function of the polarizability $\alpha(\omega)$ and intensity $I(\mathbf{r})$ are the two important quantities which govern the physics for dipole traps. At this point, the previous equations are valid for polarizable neutral particles in an oscillating electric field.

The classical approach of the Drude-Lorentz oscillator model will be used to determine the polarizability [92]. In this model an electron is bound to an atomic core with a resonant frequency ω_0. The electron is driven by an external field at frequency ω and radiates at the rate Γ_ω. $\mathbf{x}(t)$ and α can be derived by solving the following equation of motion knowing that $\mathbf{p}(t)$ is in the same form as $\mathbf{E}(t)$.

$$\ddot{\mathbf{x}}(t) + \Gamma_\omega\dot{\mathbf{x}}(t) + \omega_0^2\mathbf{x}(t) = -\frac{e}{m_e}\mathbf{E}(t) \tag{213}$$

The resulting polarizability is

$$\alpha = \frac{e^2}{m_e}\frac{1}{\omega_0^2 - \omega^2 - i\omega\Gamma_\omega}, \tag{214}$$

where

$$\Gamma_\omega = \frac{e^2\omega^2}{6\pi\epsilon_0 m_e c^3} \rightarrow \frac{e^2}{m_e} = \frac{6\pi\epsilon_0 c^3\Gamma_\omega}{\omega^2}. \tag{215}$$

The polarizability can be put into a different form by substituting the r.h.s. of Eq. (215) and introducing the on resonance damping rate, or the excited state spontaneous decay

rate, $\Gamma \equiv \left(\frac{\omega_0}{\omega}\right)^2 \Gamma_\omega$ into Eq. (214). The justification for using Eq. (215) substitution is the spontaneous decay rate Γ for the D lines of alkali atoms only differs from Γ_ω by only a few percent. Specifically 4.3% for Rb. The result after substitutions is given by,

$$\begin{aligned}\alpha &= 6\pi\epsilon_0 c^3 \frac{\Gamma/\omega_0^2}{\omega_0^2 - \omega^2 - i\left(\omega^3/\omega_0^2\right)\Gamma} \\ &= 6\pi\epsilon_0 c^3 \frac{\Gamma}{\omega_0^2}\left(\frac{(\omega_0^2-\omega^2)}{(\omega_0^2-\omega^2)^2 + \left(\frac{\omega^3}{\omega_0^2}\Gamma\right)^2} + i\frac{\left(\frac{\omega^3}{\omega_0^2}\Gamma\right)}{(\omega_0^2-\omega^2)^2 + \left(\frac{\omega^3}{\omega_0^2}\Gamma\right)^2}\right)\end{aligned} \tag{216}$$

The denominator of the polarizability can be further simplified the factor $(\omega_0^2-\omega^2)^2$ is on the order of 10^{57} while the $\left(\frac{\omega^3}{\omega_0^2}\Gamma\right)^2$ factor is on the order of 10^{41}, therefore $(\omega_0^2-\omega^2)^2 \gg \left(\frac{\omega^3}{\omega_0^2}\Gamma\right)^2$ and it can be neglected.

$$\alpha = 6\pi\epsilon_0 c^3 \frac{\Gamma}{\omega_0^2}\left(\frac{1}{(\omega_0^2-\omega^2)} + i\frac{\left(\frac{\omega^3}{\omega_0^2}\Gamma\right)}{(\omega_0^2-\omega^2)^2}\right) \tag{217}$$

The real and imaginary components of the polarizability, after partial fraction decomposition, are given by

$$\mathrm{Re}(\alpha) = 6\pi\epsilon_0 c^3 \frac{1}{2\omega_0^3}\left(\frac{\Gamma}{\omega_0-\omega} + \frac{\Gamma}{\omega_0+\omega}\right) \tag{218}$$

$$\mathrm{Im}(\alpha) = 6\pi\epsilon_0 c^3 \left(\frac{\omega^3}{\omega_0^3}\right)\frac{1}{4\omega_0^3}\left(\frac{\Gamma}{\omega_0-\omega} + \frac{\Gamma}{\omega_0+\omega}\right)^2. \tag{219}$$

Therefore in the classical representation the potential Eq. (210) and the scattering rate Eq. (212) are given by,

$$U_{\mathrm{dip}} = -\frac{3\pi c^2}{2\omega_0^3}\left(\frac{\Gamma}{\omega_0-\omega} + \frac{\Gamma}{\omega_0+\omega}\right) I(\mathbf{r}) \tag{220}$$

$$\Gamma_{\mathrm{sc}} = \frac{3\pi c^2}{2\hbar\omega_0^3}\left(\frac{\omega}{\omega_0}\right)^3\left(\frac{\Gamma}{\omega_0-\omega} + \frac{\Gamma}{\omega_0+\omega}\right)^2 I(\mathbf{r}) \tag{221}$$

The rotating wave approximation can be used in this particular case because the detuning $\Delta \equiv \omega - \omega_0 \ll \omega_0$ and $\omega/\omega_0 \approx 1$. This simplifies the above expressions to the following,

$$U_{\mathrm{dip}} \approx \frac{3\pi c^2}{2\omega_0^3}\frac{\Gamma}{\Delta} I(\mathbf{r}) \tag{222}$$

$$\Gamma_{\mathrm{sc}} \approx \frac{3\pi c^2}{2\hbar\omega_0^3}\left(\frac{\Gamma}{\Delta}\right)^2 I(\mathbf{r}) \tag{223}$$

Equations Eq. (222) and Eq. (223) show the two important features and the basic physics that are taken advantage for far-off resonance trapping. The first is that the potential scales as $\frac{I}{\Delta}$ while the scattering rate goes as $\frac{I}{\Delta^2}$. Therefore dipole traps with very large detunings and large intensity create a strong spatially confined trapping potential with minimal radiation trapping due to scattering. The second is sign of the potential which is determined by the detuning of the driving field. The potential is negative for a red-detuned trap $\Delta < 0$ and attracts atoms into positions of maximum intensity. In cases where Δ is on the order of ω_0, such as in an quasi-electrostatic trap (QUEST), the forms shown in Eq. (220) and Eq. (221) must be used.

It must be noted that the validity of the polarizability shown in Eq. (217) does not hold where saturation effects are significant. There should technically be a saturation term in the denominator which is omitted due to the far-off resonance condition.

3.2.1.2 Semiclassical Approach

In the semiclassical approach the polarizability is calculated by considering a quantum two-level atom interacting with a classical radiation field. The basis of this approach was performed rigorously in Section 2.2.2 where saturation effects are neglected.

The potential and scattering rate are given by the same relations in Eq. (210) and Eq. (212) but can be derived using the semi-classical results for the polarizability. Starting with the polarization presented in Eq. (87)

$$\mathbf{P}(t) = \frac{1}{2}\epsilon_0 \mathbf{E}_0 \left(\chi(\omega)e^{-i\omega t} + \chi(-\omega)e^{i\omega t}\right),$$

where the susceptibility $\chi(\omega)$ can be written as a sum of its real an imaginary parts given by

$$\chi(\omega) = \chi_r(\omega) + i\chi_i(\omega). \tag{224}$$

Considering the form of the susceptibility shown in Eq. (102) it is easily seen that

$$\chi_r(-\omega) = \chi_r(\omega) \tag{225}$$

$$\chi_i(-\omega) = -\chi_i(\omega), \tag{226}$$

therefore the polarization can be rewritten as

$$\mathbf{P}(t) = \epsilon_0 \mathbf{E}_0 \left(\chi_r(\omega)\cos(\omega t) + \chi_i \sin(\omega t)\right), \tag{227}$$

and the dipole moment is then given by

$$\mathbf{p}(t) = \mathbf{E}_0 \left(\alpha_r(\omega)\cos(\omega t) + \alpha_i \sin(\omega t)\right). \tag{228}$$

The potential of an induced dipole due to an electric field in the form of $\mathbf{E} = \mathbf{E}_0\cos(\omega t)$ is given by

$$\begin{aligned} U_{\text{dip}} &= -\frac{1}{2}\mathbf{p}\cdot\mathbf{E} \\ &= -\frac{|E_0|^2}{2}\left(\alpha_r(\omega)\cos^2(\omega t) + \alpha_i(\omega)\sin(\omega t)\cos(\omega t)\right). \end{aligned} \tag{229}$$

After time averaging the first term picks up a factor of 1/2 while second term vanishes to give

$$U_{\text{dip}} = -\frac{1}{4}\alpha_r(\omega)|E_0|^2 = -\frac{1}{2\epsilon_0 c}\alpha_r(\omega)I(\mathbf{r}) \tag{230}$$

To solve for the potential the polarizability value given in Eq. (109) is substituted into Eq. (230) to give

$$U_{\text{dip}} = -\frac{3\pi c^2}{2\omega_0^3}\left(\frac{\Gamma}{\omega_0-\omega} + \frac{\Gamma}{\omega_0+\omega}\right) I(\mathbf{r}) \tag{231}$$

which is the exact result as the classical approach.

The power absorbed by the dipole, which will be re-emitted, is given by

$$P_{\text{abs}} = \dot{\mathbf{p}}\cdot\mathbf{E} = |E_0|^2\left(-\omega\alpha_r(\omega)\sin(\omega t)\cos(\omega t) + \omega\alpha_i(\omega)\cos^2(\omega t)\right), \tag{232}$$

where the first term vanishes while the second term picks up a factor of 1/2 after time averaging and yields

$$P_{\text{abs}} = \frac{1}{2}\omega\alpha_i(\omega)|E_0|^2 = \frac{\omega}{\epsilon_0 c}\alpha_i(\omega)I(\mathbf{r}). \tag{233}$$

The scattering rate is simply the amount of power absorbed, which equals the power emitted, divided by the energy of a photon with frequency ω. Therefore the scattering rate is

$$\Gamma_{\text{sc}} = \frac{P_{\text{abs}}}{\hbar\omega} = \frac{1}{\hbar\epsilon_0 c}\alpha_i(\omega)I(\mathbf{r}). \tag{234}$$

To solve for the scattering rate the imaginary part of the polarizability obtained in Eq. (110) is substituted into Eq. (234) to give

$$\Gamma_{\text{sc}} = \frac{3\pi c^2}{2\hbar\omega_0^3}\left(\frac{\omega}{\omega_0}\right)\left(\frac{\Gamma}{\omega_0-\omega} + \frac{\Gamma}{\omega_0+\omega}\right)^2 I(\mathbf{r}) \tag{235}$$

which is similar to the classical method.

The significant result of either approach reveals that the strength of the potential scales as I/Δ and the scattering rate as I/Δ^2. Therefore, with the appropriate intensity, the potential is strong in the far off resonance regime while the scattering rate is diminished allowing for tight spatial confinement when $\Delta < 0$.

3.2.1.3 Multilevel Atoms - Quantum Mechanical

The previous two level approximation provided an expected behavior of an optical dipole trap but a multilevel atom approach must be taken in order to calculate realistic energy level shifts. The approach will be the same as discussed in section 2.3.1 but with an oscillating electric field and is based on discussions in [65, 92].

The dipole potential for the multilevel case in an oscillating electric field is the same as given in Eq. (140) but now the time average must be taken to become what was shown in Eq. (210) namely

$$U_{dip} = -\frac{1}{2}\langle \mathbf{p} \cdot \mathbf{E} \rangle_T = -\frac{1}{2\epsilon_0 c}\mathrm{Re}(\alpha) I(\mathbf{r}),$$

where now

$$\mathrm{Re}(\alpha) = \alpha_0 \mathbb{I} + \alpha_2 \hat{Q}. \tag{236}$$

The polarizability for a particular state ν can be approximated as the sum of the ionic core and valence electron polarizabilities given by [94],

$$\alpha^{\nu} \approx \alpha_{\mathrm{core}} + \alpha^{\nu}_{\mathrm{val}} \tag{237}$$

where the state is represented by $\nu = nL$. The atomic core polarizability is taken as $\alpha_{\mathrm{core}} = 9.1$ for Rubidium [95]. The scalar portion of the valence polarizability is given by

$$\alpha_0^{\nu}(\omega) = \frac{2}{3\left(2J_\nu + 1\right)} \sum_k \frac{|\langle k||d||\nu\rangle|^2 \left(E_k - E_\nu\right)}{\left(E_k - E_\nu\right)^2 - \omega^2}, \tag{238}$$

where k is an intermediate state, $\langle k||d||\nu\rangle$ is the reduced dipole matrix element, and ω is the laser frequency. The tensor portion of the valance polarizability is given by

$$\alpha_2^{\nu}(\omega) = -4C \sum_k (-1)^{J_\nu + J_k + 1} \begin{Bmatrix} J_\nu & 1 & J_k \\ 1 & J_\nu & 2 \end{Bmatrix} \frac{|\langle k||d||\nu\rangle|^2 \left(E_k - E_\nu\right)}{\left(E_k - E_\nu\right)^2 - \omega^2}, \tag{239}$$

where

$$C = \left(\frac{5J_\nu \left(2J_\nu - 1\right)}{6\left(J_\nu + 1\right)\left(2J_\nu + 1\right)\left(2J_\nu + 3\right)} \right)^{1/2}. \tag{240}$$

The polarizabilities given in Eq. (238) and Eq. (239) are in atomic units. Multiply α by $4\pi\epsilon_0 a_0^3$ to convert to standard units. The reduced dipole matrix element is in units of ea_0 and the energies E_i and laser frequency ω in terms of the Hartree energy E_h. Values for the Hartree energy are given in Table 9.

The energy levels are obtained from NIST [64] which are essentially the value of $1/\lambda$ relative to the lowest ground state ($5S_{1/2}$) and are in units of cm^{-1}. The energies are converted to atomic units with the Hartree energy. To be clear, an energy $E_i = \dfrac{\hbar\omega_i}{E_h}$, where the substitution goes as

$$E_i = \frac{\hbar\omega_i}{E_h} = \frac{\hbar\omega_i}{\hbar\omega_h} = \frac{\omega_i}{\omega_h} = \frac{2\pi c}{\omega_h \lambda_i}, \tag{241}$$

therefore

$$E_k - E_\nu = \frac{2\pi c}{\omega_h}\left(\frac{1}{\lambda_k} - \frac{1}{\lambda_\nu}\right), \tag{242}$$

where $1/\lambda_i$ is the value given by NIST.

The standard procedure to calculate the polarizabilities is to sum over the first several n states which connect to the state of interest. Therefore to calculate the $5S_{1/2}$ ground state polarizability, both the $nP_{1/2}$ and $nP_{3/2}$ states must be taken into account over several values of n. The contributions to the static ($\alpha_{0,S}$) and dynamic polarizabilities at 1064 nm ($\alpha_{0,D}$) of the $5S_{1/2}$ state from each $nP_{1/2,3/2}$ state are shown in Table 2. Static polarizabilities are found by setting the laser frequency ω to zero in Eq. (238) and Eq. (239). λ_{res} is determined by the difference in energy values given by NIST between the k and ν states. All reduced dipole matrix elements used in calculations have been obtained from Safronova et al. [94–98] and are given in the symmetric convention in the J basis. Steck [62] uses the asymmetric convention which differs by a factor of $\sqrt{2J+1}$.

TABLE 2: $5S_{1/2}$ ground state static and 1064 nm dynamic polarizability contributions.

Contribution	λ_{res}	RDME	$\alpha_{0,S}$	$\alpha_{0,D}$
$5S_{1/2} \rightarrow 5P_{1/2}$	794.979	4.227	103.618	235.230
$5S_{1/2} \rightarrow 6P_{1/2}$	421.673	0.342	0.361	0.4280
$5S_{1/2} \rightarrow 7P_{1/2}$	359.260	0.118	0.0366	0.0413
$5S_{1/2} \rightarrow 8P_{1/2}$	335.177	0.059	0.0085	0.0095
$5S_{1/2} \rightarrow 9P_{1/2}$	323.009	0.046	0.0050	0.0055
$5S_{1/2} \rightarrow 5P_{3/2}$	780.241	5.977	203.913	441.126
$5S_{1/2} \rightarrow 6P_{3/2}$	420.299	0.533	0.9403	1.114
$5S_{1/2} \rightarrow 7P_{3/2}$	358.807	0.207	0.1125	0.1269
$5S_{1/2} \rightarrow 8P_{3/2}$	334.966	0.114	0.0318	0.0353
$5S_{1/2} \rightarrow 9P_{3/2}$	322.891	0.074	0.0129	0.0142
α_{core}			9.1	9.1
Total			318.435	687.231

In order to calculate the $5P_{3/2}$ polarizabilities the $nS_{1/2}$, $nD_{3/2}$, and $nD_{5/2}$ state contributions are taken. The contributions to the polarizabilities of the $5P_{3/2}$ excited state are shown in Table 3. The calculations were performed in Mathematica and the basic functions are presented in Appendix B. The calculated values for the $5S_{1/2}$ ground state and $5P_{3/2}$ excited state agree well within 0.1% of the accepted and experimental values listed in Table 13. The dynamic polarizabilities at 1064 nm were also calculated using the ARC python package [99] and a small compendium of values are listed in Table 14 of Appendix A.

TABLE 3: $5P_{3/2}$ excited state static and 1064 nm dynamic polarizability contributions.

Contribution	λ_{res}	RDME	$\alpha_{0,S}$	$\alpha_{2,S}$	$\alpha_{0,D}$	$\alpha_{2,D}$
$5P_{3/2} \rightarrow 5S_{1/2}$	-780.241	5.977	-101.957	101.957	-220.563	220.563
$5P_{3/2} \rightarrow 6S_{1/2}$	1366.87	6.047	182.822	-182.822	-281.117	281.117
$5P_{3/2} \rightarrow 7S_{1/2}$	741.021	1.350	4.9399	-4.9399	9.5928	-9.5928
$5P_{3/2} \rightarrow 8S_{1/2}$	616.133	0.708	1.1297	-1.1297	1.6996	-1.6996
$5P_{3/2} \rightarrow 9S_{1/2}$	565.531	0.466	0.4492	-0.4492	0.6261	-0.6261
$5P_{3/2} \rightarrow 10S_{1/2}$	539.206	0.341	0.2293	-0.2293	0.3086	-0.3086
$5P_{3/2} \rightarrow 4D_{3/2}$	1529.26	3.633	73.830	59.064	-69.2744	-55.4195
$5P_{3/2} \rightarrow 5D_{3/2}$	776.157	0.665	1.255	1.004	2.6834	2.1467
$5P_{3/2} \rightarrow 6D_{3/2}$	630.097	0.506	0.590	0.472	0.9088	0.7271
$5P_{3/2} \rightarrow 7D_{3/2}$	572.621	0.370	0.2867	0.2294	0.4036	0.3229
$5P_{3/2} \rightarrow 8D_{3/2}$	543.334	0.283	0.1592	0.1273	0.2153	0.1723
$5P_{3/2} \rightarrow 9D_{3/2}$	526.169	0.225	0.0974	0.0779	0.1290	0.1032
$5P_{3/2} \rightarrow 4D_{5/2}$	1529.37	10.899	664.515	-132.903	-623.347	124.669
$5P_{3/2} \rightarrow 5D_{5/2}$	775.979	1.983	11.161	-2.232	23.843	-4.769
$5P_{3/2} \rightarrow 6D_{5/2}$	630.007	1.512	5.268	-1.054	8.112	-1.6225
$5P_{3/2} \rightarrow 7D_{5/2}$	572.571	1.104	2.553	-0.5105	3.593	-0.7186
$5P_{3/2} \rightarrow 8D_{5/2}$	543.304	0.845	1.419	-0.2838	1.919	-0.3839
$5P_{3/2} \rightarrow 9D_{5/2}$	526.149	0.672	0.8691	-0.1738	1.150	-0.2301
α_{core}			9.1		9.1	
Total			858.718	-163.795	-1130.02	554.452

The same approach which was taken in Section 2.3.1 will be used determine the atomic energy level shifts due to the interaction of a linearly polarized 1064 nm FORT beam. The main difference is the time averaged term shown in Eq. (210), therefore the matrix element for a particular state is given by

$$\begin{aligned}
&\langle F'm'_F|U_{\text{dip}}|Fm_F\rangle \\
&= \langle F'm'_F|V_{\text{hfs}} - \frac{I(\mathbf{r})}{2\epsilon_0 c}\left(\alpha_0 + \alpha_2\hat{Q}\right)|Fm_F\rangle \\
&= \langle F'm'_F|V_{\text{hfs}}|Fm_F\rangle - \langle F'm'_F|\frac{I(\mathbf{r})}{2\epsilon_0 c}\left(\alpha_0 + \alpha_2\hat{Q}\right)|Fm_F\rangle,
\end{aligned} \tag{243}$$

where $\langle F'm'_F|V_{\rm hfs}|Fm_F\rangle$ is defined by Eq. (138) and $\langle F'm'_F|\hat{Q}|Fm_F\rangle$ by Eq. (143) and is block diagonal in m_F.

The FORT beam is Gaussian in nature with an intensity profile given by

$$I\left(\mathbf{r}\right) = I\left(\rho, z\right) = I_0 \left(\frac{w_0}{w_z}\right)^2 e^{-2\rho^2/w_z^2}, \tag{244}$$

where w_0 is the $1/e^2$ radial beam radius at $z = 0$, $w_z = w_0\sqrt{1 + \left(z/z_R\right)^2}$, $z_R = \frac{\pi w_0^2}{\lambda}$ is the Rayleigh length, λ is the FORT beam wavelength, and the peak intensity is defined as $I_0 = \frac{2P}{\pi w_0^2}$. The power P is in units of watts. Determining values of w_0, w_z, and z_R will be discussed in Section 3.2.3.

At this point it is useful to define the units of the dynamic α_0 and α_2 values in a.u. listed in Table 13. Therefore to correctly coincide with the units of $V_{\rm hfs}$, the second term in Eq. (243) becomes

$$\begin{aligned}
&\frac{I\left(\mathbf{r}\right)}{2\epsilon_0 c}\langle F'm'_F|\frac{4\pi\epsilon_0 a_0^3}{h}\left(\alpha_0 + \alpha_2\hat{Q}\right)|Fm_F\rangle \\
&= \frac{1}{2}\left(\frac{4\pi a_0^3}{hc}\right) I\left(\mathbf{r}\right)\langle F'm'_F|\left(\alpha_0 + \alpha_2\hat{Q}\right)|Fm_F\rangle \\
&= \frac{1}{2}\left(\frac{8a_0^3 P}{hcw_0^2}\right)\frac{1}{1 + \left(z/z_R\right)^2}\langle F'm'_F|\left(\alpha_0 + \alpha_2\hat{Q}\right)|Fm_F\rangle,
\end{aligned} \tag{245}$$

where the final line represents the energy level shift as a function of z at $\rho = 0$ at some power P and $1/e^2$ beam radius w_0. Mathematica was used to diagonalize the matrix and obtain eigenvalues which represent the energy level shift of a particular $|F, m_F\rangle$ state as a function of z. The resulting shifts for the $5P_{3/2}$ hyperfine manifold under typical experimental conditions are shown in Fig. 36.

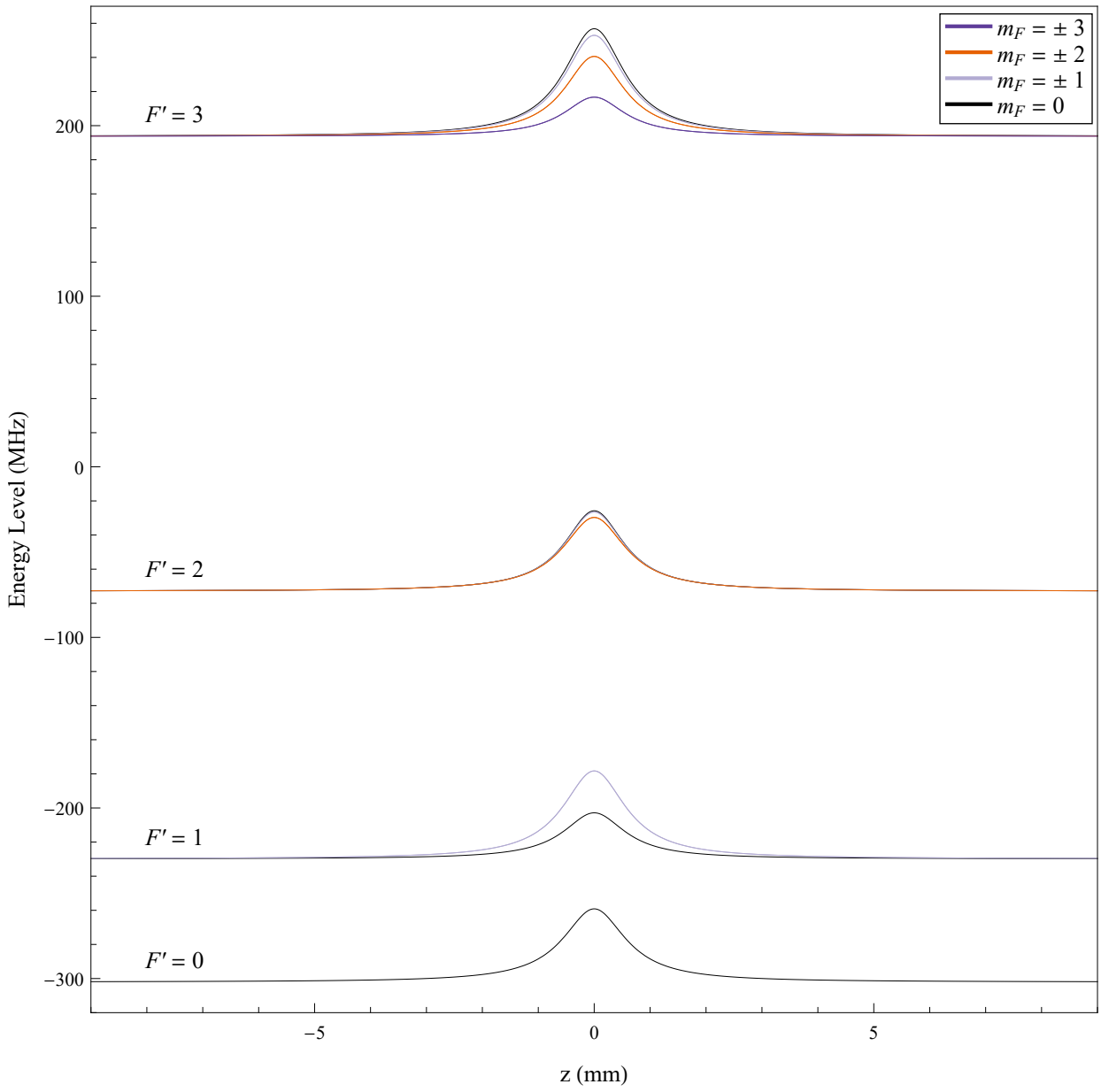

FIG. 36: ^{87}Rb $5P_{3/2}$ hyperfine manifold energy level shifts due to a 1064 nm FORT beam with $P = 2.8$ W and $w_0 = 14.6$ μm.

The spatially dependent shifts for the $5S_{1/2}$ ground state and $5P_{3/2}$ excited state are shown Fig. 37. All m_F values are degenerate for the ground state because $\alpha_2(5S_{1/2}) = 0$ and therefore unable to couple to other states. The shifts are only degenerate in $|\pm m_F|$ for the $5P_{3/2}$. The peak depth of the ground state is also known as the well or trap depth U_0.

The trap depth is a parameter usually given in units of MHz or mK and will be determined via parametric resonance in the FORT characterization section.

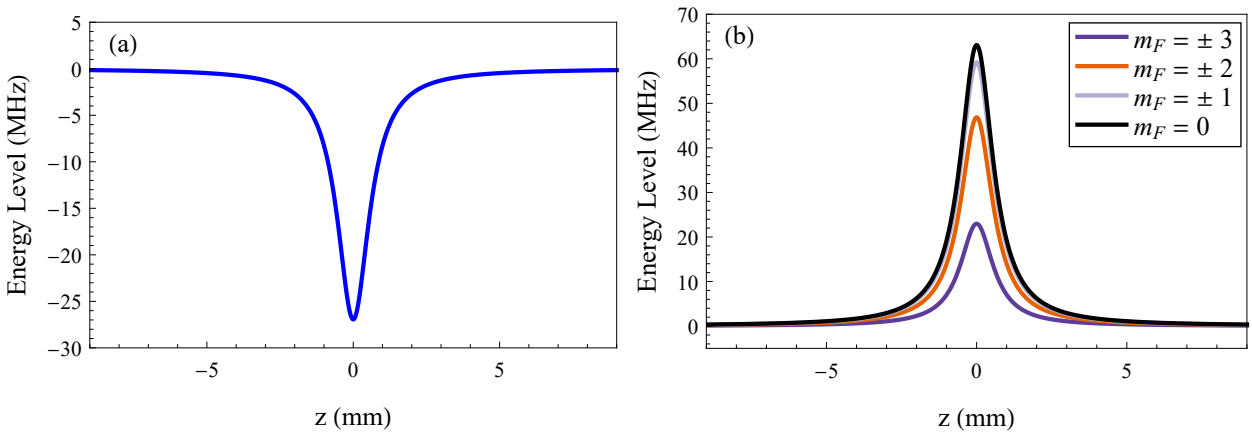

FIG. 37: Energy level shifts of the (a) ^{87}Rb $5S_{1/2}$ and (b) $5P_{3/2}$ states due to a 1064 nm FORT beam with $P = 2.8$ W and $w_0 = 14.6$ μm.

Although the physics behind creating a FORT have been well studied, out of curiosity, a simple experiment was devised to directly show the atomic resonance shift while in the presence of the FORT beam. An experimental example of this effect can be easily shown by first creating a FORT and then analyzing the response when probing the sample over a range of detunings around the ^{87}Rb $5S_{1/2}$ $F = 2 \rightarrow 5P_{3/2}$ $F' = 3$ transition. The result is shown in Fig. 38 where the peak is shifted to higher frequency. This was consistent with the calculated behavior of the ground state and excited states shifting in opposite directions of one another. CCD images were recorded when flashing the detunable MOT beam for 50 μs with and without the FORT beam present. Ten accumulations were recorded for each detuning and the total counts from a 81×13 pixel area around the center of the FORT was calculated after background subtraction. While this may possibly be used as a tool to analyze FORT parameters or atomic responses, the experiment was only performed to show a shift and was not scrutinized any further.

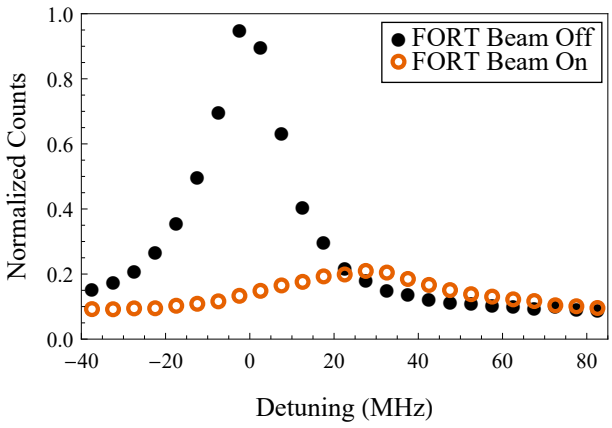

FIG. 38: Response of a ^{87}Rb FORT with (open circles) and without (circles) the FORT beam on while probing. The broadness of the data points when the FORT beam was off might be explained due to the fact that the FORT was only allowed to expand for ≈ 10 μs before being probed, therefore the sample maintained a large optical depth. The on resonant light then may not have fully penetrated the sample and therefore scattered less light. The FORT beam power was 2.8 W.

3.2.2 FORT EXPERIMENTAL SETUP

The beam used to create the FORT is from a fiber laser (IPG, YLR-30-1064-LP PL1211875) running at 1064 nm. The FORT beam is focused approximately at the center of the MOT as shown in Fig. 39. The L1 lenses are $f = 300$ mm (Thorlabs, LE1929-C), L2 are $f = 40$ mm (Thorlabs, LBF254-040-C), L3 is $f =$ -100 mm (Thorlabs, LF1822-C), L4 is $f = 100$ mm (Unknown model), L5 is $f = 150$ mm (Thorlabs, AC508-150-B), BS1 is a 1064 nm polarizing beam splitter cube (Newport, 05BC16PC.9), and BS2 is essentially a dichroic mirror (CVI, SWP RS1064/TU780) which reflects 1064 nm and allows 780 nm through to the CCD (Sanyo VCB-3524). The AOM (Gooch & Housego, I-M080-1.5C10G-4-AM3) is used to switch the FORT beam on and off. The RF driver (Gooch & Housego, QC080-15DC-m05-24V) allows for on/off control via a TTL, max RF power delivered to the AOM via a DC power supply, and a RF power modulation input.

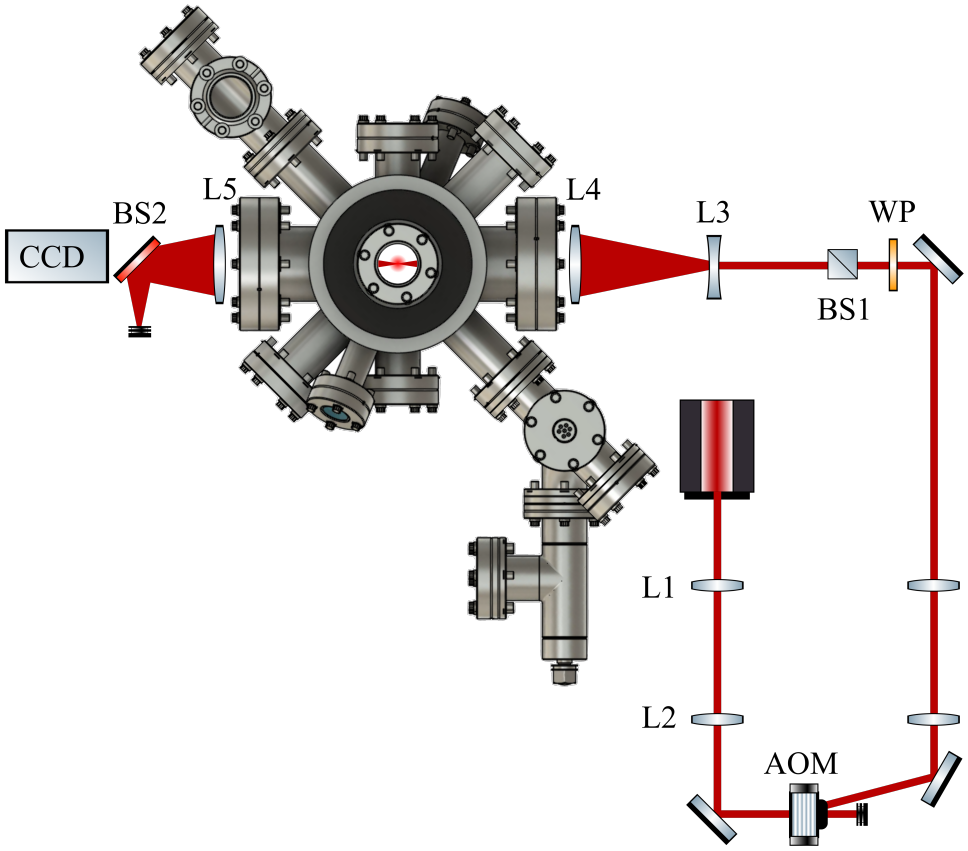

FIG. 39: FORT beam optics diagram. L1 and L2 reduce the size and recollimate the beam for the AOM. The lenses after the AOM are the same as L1 and L2. The half wave plate WP is aligned to optimize transmission through the beam splitter BS1. L3 and L4 resize and focus the beam onto the MOT. L5 is positioned at $2f$ from the MOT. BS2 is a dichroic beam splitter which reflects 1064 nm and allows 780 nm to pass. The CCD is placed $2f$ from L5 and is used to monitor the MOT on a TV as well as a FORT beam alignment tool.

Initially the FORT AOM RF driver was affixed to the optics table via a metal slab. This allowed for ample heat dissipation but had a side effect of causing electrical noise throughout the lab. Simply turning on the RF amplifier would change VCO frequencies several meters away. The RF amplifier was removed from the table and housed in a box in order to alleviate this issue. A large heat sink and fan had to be installed to manage heat while in operation.

The new RF amplifier housing and improved control box are shown in Fig. 40. A FLIR camera was used to ensure the amplifier maintained an operating temperature below 50°C and is shown in Fig. 41.

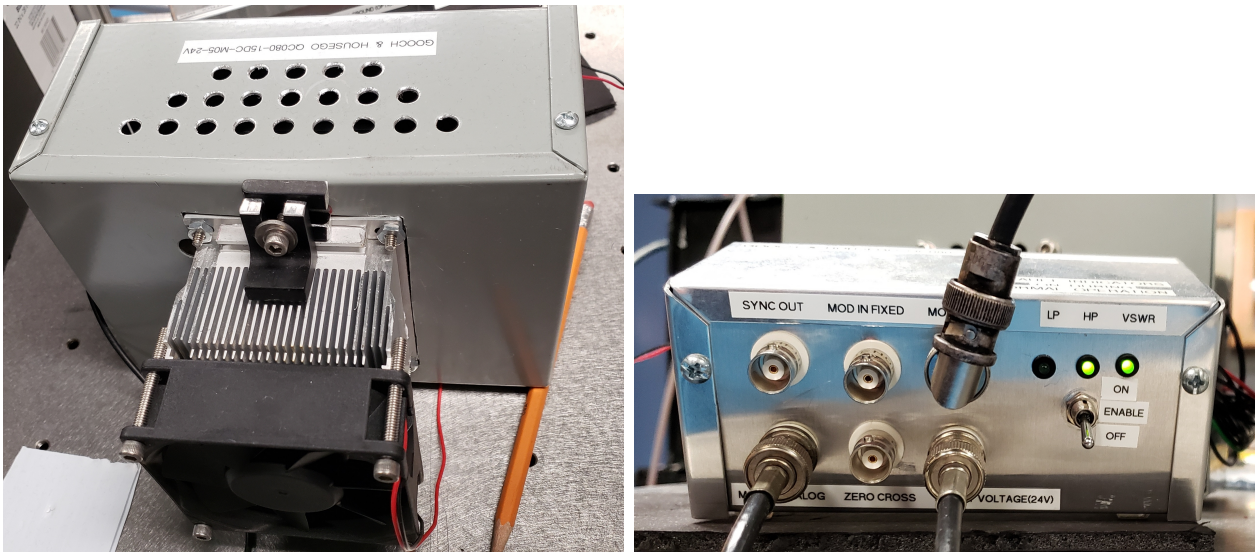

FIG. 40: New FORT AOM RF amplifier and electronics housings. Gooch & Housego QC080-15DC-m05-24V RF amplifier housing and control electronics.

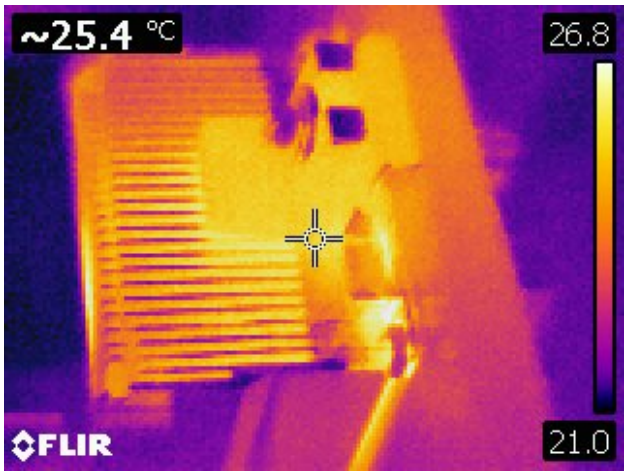

FIG. 41: Gooch & Housego QC080-15DC-m05-24V RF amplifier heat sink FLIR image.

Now that the optical arrangement and basic electronics have been discussed, the next step is to align the 1064 nm beam with the MOT. An earlier method of aligning the FORT involved overlapping the 1064 nm beam with a 780 nm tuned to an atomic resonance and observing the distortion of the MOT due to the 780 nm. This method is straightforward but is extremely time consuming due to the second laser requirement which had to be perfectly overlapped. A new alignment procedure was implemented which utilized the MOT monitor CCD behind BS2 that was shown in Fig 39. A very small amount of 1064 nm ($\ll 1\%$) is transmitted through the dichroic mirror which is more than enough to be detectable on the CCD. There is also a ND filter wheel, short pass filter (Thorlabs, FGL850SP), and a bandpass filter (Thorlabs, FB780-10) in front of the CCD for further attenuation of the FORT beam. The FORT beam is aligned when the beam appears to be a small point on the TV while also appearing to be centered on the MOT due to the $2f$-$2f$ configuration of L5. The beam itself was aligned with the MOT by translating L4. A home built x-y-z translation stage was created, shown in Fig 42, in order to align and optimize the FORT precisely. This new method was extremely easy, fast, and reproducible without the need of a second laser.

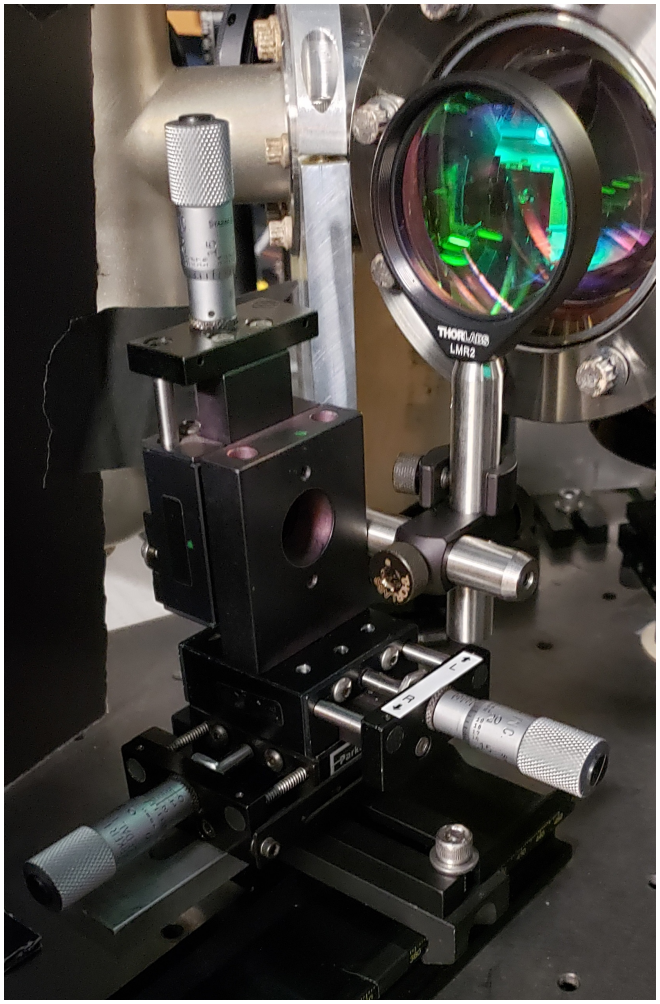

FIG. 42: FORT beam alignment x-y-z translation mount. The three translators provide very precise adjustment for alignment of the 1064 nm fiber laser with the MOT. Two of the translators are Edmund Optics model 3161 and the third is a Parker 4046 series.

The beam waist, or $1/e^2$ radius, at the focus of the FORT was determined by first obtaining the size of the beam before the L3 lens with a beam profiler (Thorlabs, BC106N-VIS). Appropriate attenuation was required to avoid damaging the device. The beam waist was found to be ≈ 1.3 mm before the diverging L3 lens. The L3 and L4 lenses are separated by 183 mm which corresponds to a calculated focused beam waist of 14.24 μm located 155 mm from L4.

The process of creating a FORT starts with a MOT. When the FORT beam turns on the MOT enters the compression phase which is done to increase the density and to further cool

the atoms. The compression phase is performed by detuning the MOT beam from $-3\ \Gamma$ to about $-6\ \Gamma$ while the repumper beam power is reduced from 1 mW to about 3 μW at the same time. The duration of the compression phase is usually between 50-100 ms but can be a variable for FORT optimization. At the end of the compression phase the repumper beam is shut off 5 ms before the MOT beam to optically pump the atoms into the $F = 1$ ground state. Even though the well depths created by the FORT beam for the $F = 2$ and $F = 1$ ground states are the same, two-body collisions are much more likely in the upper $F = 2$ ground state which can lead to trap loss [92]. Once the MOT and repumper beams are extinguished, via switching off their respective AOMs, the atoms are held in the FORT usually between 100-200 ms which allows the atomic ensemble to thermalize. The general timing diagram is shown in Fig. 43 where both the compression time and FORT hold time can be varied.

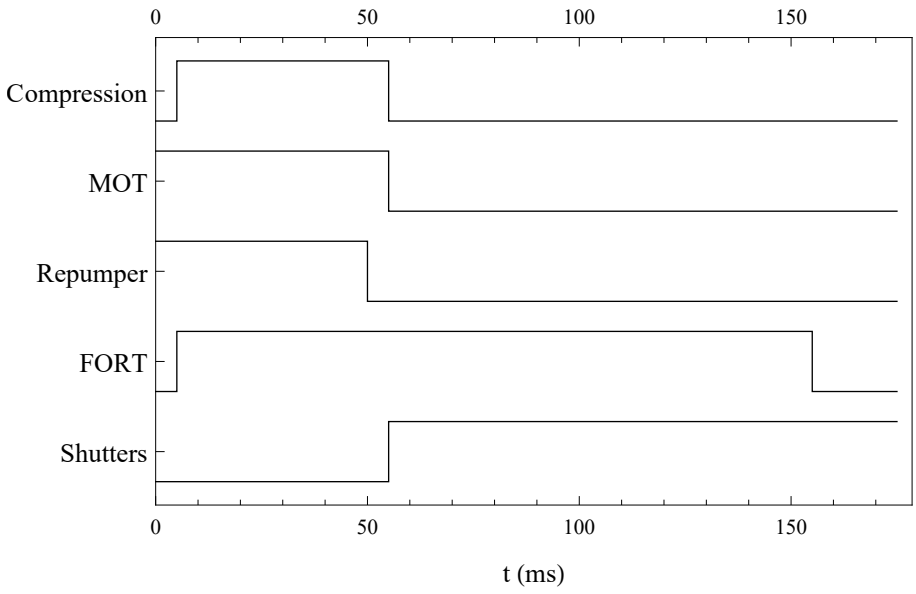

FIG. 43: FORT loading timing diagram. The compression phase represents when the MOT detuning and repumper power change. The shutters fully extinguish any light leak of the MOT and repumper beams.

3.2.3 FORT CHARACTERIZATION

3.2.3.1 Temperature

The temperature of the FORT was obtained with the same method that was used for the MOT. The FORT was allowed to expand for some amount of time and then flashed the MOT and repumper lasers while recording a CCD image. Figure 44 presents such images at different expansion times.

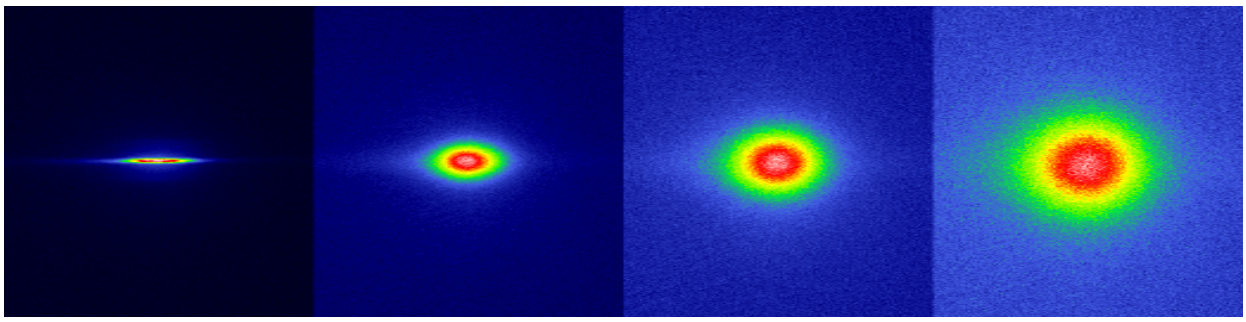

FIG. 44: Spatial profile of the FORT at various expansion times. Expansion times from left to right are 0.1, 1, 2, and 3 ms. Each image is 3393 × 3393 μm.

The spatial profile of the FORT is represented by the following bi-Gaussian

$$\rho(r,z) = \rho_0 e^{\left(-\frac{r^2}{2r_0^2} - \frac{z^2}{2z_0^2}\right)}, \tag{246}$$

and similarly to the MOT, the sample radii expand as

$$\begin{aligned} r^2 &= r_0^2 + \frac{k_B T}{m} t^2 \\ z^2 &= z_0^2 + \frac{k_B T}{m} t^2. \end{aligned} \tag{247}$$

The fits to r^2 and z^2 vs t^2 are shown in Fig. 45 where the temperature was obtained from the resulting slopes. Typical FORT temperatures were around 100-150 μK at a FORT beam power of 2.8 W. The temperature of the FORT will always be some percentage of the well depth, which is dependent on the trap geometry and beam power. Unlike the MOT, the

Gaussian radii cannot be determined by extrapolating to $t = 0$ due to the small size of the FORT. A different method will be used to determine the spatial parameters in the following section.

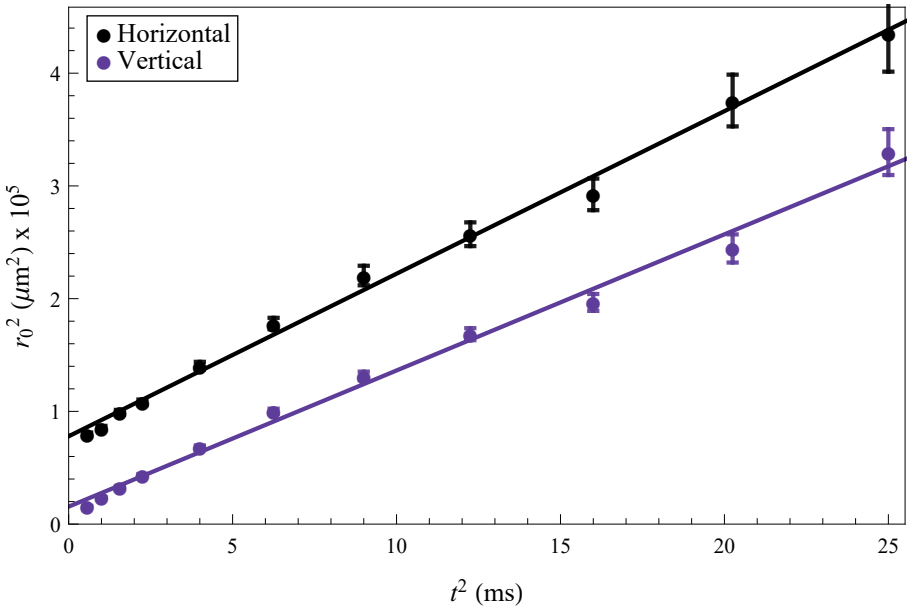

FIG. 45: Temperatures of the FORT in the horizontal and vertical directions. The horizontal is 150 $\pm$ 4 μK and vertical is 126 $\pm$ 4 μK. The FORT beam power was 2.8 W which corresponds to a trap depth of $\approx$ 1.3 mK.

3.2.3.2 Spatial Parameters

The spatial parameters of the MOT were obtained by extrapolating the time dependent Gaussian radii to $t = 0$ from the temperature fits. The extrapolation method fails when applying it to the FORT due to the high density and small size. A technique called parametric resonance will be used to obtain the important spatial parameters. Parametric resonance involves modulating the well depth at a particular frequency, which is related to the sample size, to thermally induce loss in the trap.

The dynamics of an atom moving within a modulated harmonic trap follow

$$\ddot{x} + \omega_0^2(1 + h\cos(\omega t))x = 0, \tag{248}$$

where h is the modulation amplitude. This is known as Mathieu's equation and has resonances at $\omega = \frac{2\omega_0}{n}$ where n is any integer and the amplitude of the resonance decreases as n increases [100]. Solving Eq. (248) begins by analyzing the region around $\omega = 2\omega_0 + \epsilon$, where $\epsilon < 1$. After substitution the equation becomes

$$\ddot{x} + \omega_0^2(1 + h\cos[(2\omega_0 + \epsilon)t])x = 0, \tag{249}$$

where the general solution takes the form of

$$x(t) = a(t)\cos[(\omega_0 + \frac{\epsilon}{2})t] + b(t)\sin[(\omega_0 + \frac{\epsilon}{2})t]. \tag{250}$$

Substituting Eq. (250) into Eq. (249) yields

$$\omega_0\cos[(\omega_0 + \frac{\epsilon}{2})t]\left(\frac{1}{2}ah\omega_0 - \epsilon a + 2\dot{b}\right) - \omega_0\sin[(\omega_0 + \frac{\epsilon}{2})t]\left(\frac{1}{2}bh\omega_0 + \epsilon b + 2\dot{a}\right) = 0, \tag{251}$$

where only first order terms in ϵ were taken. $\ddot{a}$, $\ddot{b}$, and $\frac{\epsilon}{\omega_0}$ terms were also omitted. The terms in parenthesis must be zero in order to satisfy the equation, therefore

$$\begin{aligned}\left(\frac{1}{2}ah\omega_0 - \epsilon a + 2\dot{b}\right) &= 0\\ \left(\frac{1}{2}bh\omega_0 + \epsilon b + 2\dot{a}\right) &= 0.\end{aligned} \tag{252}$$

Solutions of the amplitudes are taken to be increasing exponentials $a(t) = ae^{st}$ and $b(t) = be^{st}$. Substituting these amplitudes into Eq. (252) yields

$$\begin{aligned}as + \frac{1}{2}\left(\frac{h\omega_0}{2} + \epsilon\right)b &= 0\\ \frac{1}{2}\left(\frac{h\omega_0}{2} - \epsilon\right)a + bs &= 0,\end{aligned} \tag{253}$$

where the parameter s can be solved for giving

$$s^2 = \frac{1}{4}\left[\left(\frac{h\omega_0}{2}\right)^2 - \epsilon^2\right]. \tag{254}$$

The sign of s determines the stability of the system. The parametric resonance condition occurs when the system is unstable, namely when s is real and positive, or when $s^2 > 0$. For this condition to hold

$$-\frac{1}{2}h\omega_0 < \epsilon < \frac{1}{2}h\omega_0. \tag{255}$$

Under the first order assumptions made, the concept of parametric resonance can be used to obtain the oscillation frequencies of the dipole trap by modulating the intensity of the beam with an amplitude of h at $2\omega_0$ of the trap. As the amplitude h of modulation increases, the width ϵ of the resonance will become larger.

The shape of the beam defines the potential of the FORT and defined as

$$U(r,z) = -\frac{U_0}{1+\left(\frac{z}{z_R}\right)^2} e^{-\frac{2r^2}{w_0^2}}, \tag{256}$$

where U_0 is the well depth, $z_R = \frac{\pi w_0^2}{\lambda}$ is the Rayleigh range, and w_0 is the $1/e^2$ beam radius. For a Gaussian beam $U_0 = \frac{2P}{\pi w_0^2}$ where P is the power of the laser. The atoms do not completely fill the trap since the temperature of the atoms (≈ 150) μK is smaller than the typical well depth (≈ 1) mK. Therefore, the radial and axial extensions of the atomic sample will be smaller than the beam waist and Rayleigh range respectively. The potential can then be approximated as a cylindrically symmetric harmonic oscillator [92]. Taylor expanding Eq. (256) around $r = 0$ and $z = 0$ yields

$$U(r,z) \approx -U_0 \left(1 - \left(\frac{z}{z_R}\right)^2 - 2\left(\frac{r}{w_0}\right)^2\right). \tag{257}$$

The harmonic potential can also be written in terms of the oscillation frequencies

$$U(r,z) \approx -U_0 + \frac{1}{2}m\omega_r^2 r^2 + \frac{1}{2}m\omega_z^2 z^2. \tag{258}$$

The resonant oscillation frequencies as a function of beam parameters can be determined by comparing Eq. (257) and Eq. (258) which yield

$$\begin{aligned} \omega_r &= \sqrt{\frac{4U_0}{mw_0^2}} \\ \omega_z &= \sqrt{\frac{2U_0}{mz_R^2}}. \end{aligned} \tag{259}$$

The sample is approximated as a Maxwell-Boltzmann distribution in thermal equilibrium and can be approximated by

$$\rho(r,z) = \rho_0 e^{-\frac{U(r,z)}{k_B T}}. \tag{260}$$

The unexpanded spatial parameters of the FORT as a function of trap frequency can be determined by substituting Eq. (258) into Eq. (260) and comparing to the spatial profile given in Eq. (246). The resulting radii are

$$r_0 = \sqrt{\frac{k_B T}{m\omega_r^2}}$$
$$z_0 = \sqrt{\frac{k_B T}{m\omega_z^2}}. \tag{261}$$

With this formulation in mind, the resonant trap frequencies can be determined by modulating the FORT beam with power P with amplitude h. The sample radii can then be determined once the temperature is obtained from ballistic expansion.

In order to realize the parametric resonance method in the lab, a function generator (BK Precision, 4084) adds a sinusoidal signal to a DC voltage via a bias tee which is connected to the MOD In Analog of the FORT AOM RF amplifier control box. This in turn modulates the power of the FORT beam while the function generator is triggered. After the FORT loading procedure takes place, the modulation was triggered for 100 ms at a set amplitude and frequency. The duration of modulation was chosen to match later experimental timings but extending the modulation time will produce better results. The FORT beam was turned off after the modulation duration and the sample was allowed to expand for 2 ms before flashing the MOT and repumper beams for 50 μs. A fluorescence image was taken during the flash and the process was repeated over a range of frequencies. The atoms in the FORT will be at a minimum when the frequency of the modulation is twice the resonant trap frequency. The parametric resonance response of the FORT under typical experimental conditions is shown in Fig. 46. The FORT spatial parameters are given in Table 4 and the trap parameters are in Table 5. It is important to note that the beam waist w_0 obtained from parametric resonance agrees with the previously calculated value presented in the description of the optical arrangement of the FORT. Going forward however, the value that will be used in later calculations for axial radius will be obtained by ballistic expansion ($z_0 = 250$ μm) rather than from parametric resonance. The harmonic oscillator was a very good approximation for the radial extension but does not fully represent the axial extension. The recalculated density $\rho_0 = 1.9 \times 10^{14}$ cm^{-3} is different by less than a factor of two of the value obtained by parametric resonance.

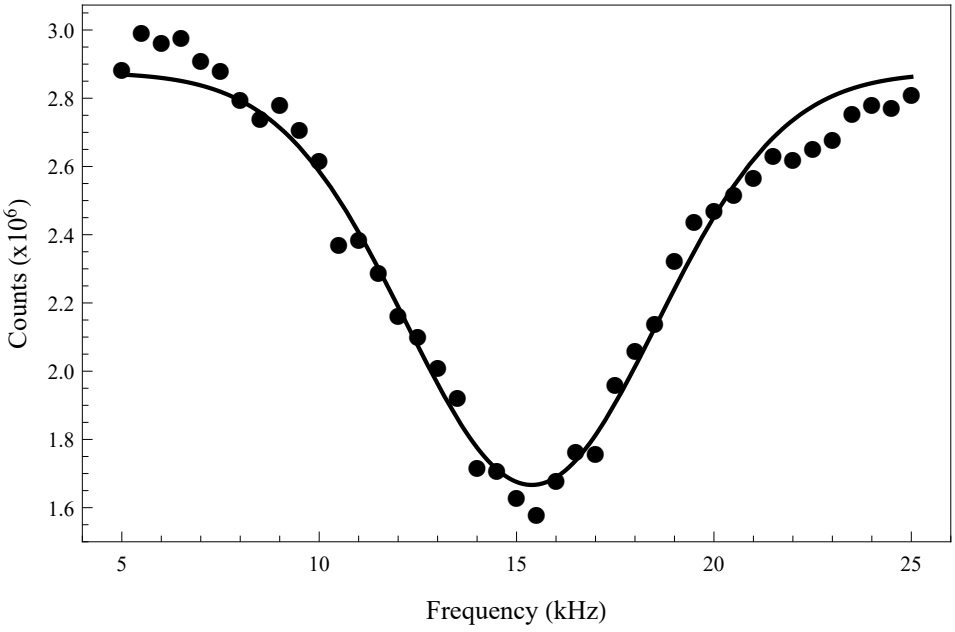

FIG. 46: Parametric resonance of the FORT. The dip corresponds to a function generator frequency of $f = 2f_0$, where f_0 is the radial resonance frequency of the FORT. Fitting the data to a Gaussian yields $\omega_r = 2\pi \times 7.69 \pm 0.04$ kHz. With the FORT beam at 2.8 W, this translates to $r_0 = 2.3 \pm 0.1$ μm and $z_0 = 151 \pm 2$ μm.

TABLE 4: Typical FORT sample characteristics during experimental runs with 2.8 W beam power. Uncertainties derived from fitting parameter errors given by Mathematica.

N	4.0 ± 0.1 $(\times 10^6)$
T	138 ± 4 μK
r_0	2.3 ± 0.1 μm
z_0	151 ± 2 μm
ρ_0	3.3 ± 0.3 $(\times 10^{14}$ cm$^{-3})$

TABLE 5: Typical FORT trap characteristics during experimental runs with 2.8 W beam power. Uncertainties derived from fitting parameter errors given by Mathematica.

ω_r	$2\pi \times (7.69 \pm 0.04)$ kHz
ω_z	$2\pi \times (126 \pm 1)$ Hz
w_0	14.57 ± 0.04 μm
z_R	627 ± 4 μm
U_0/k_B	1300 ± 7 μK

Parametric resonance was also performed on a sample with a lower FORT beam power, shown in Fig. 47, in an effort to ensure consistency with the process. As expected, the trap frequency decreases as the FORT power decreases.

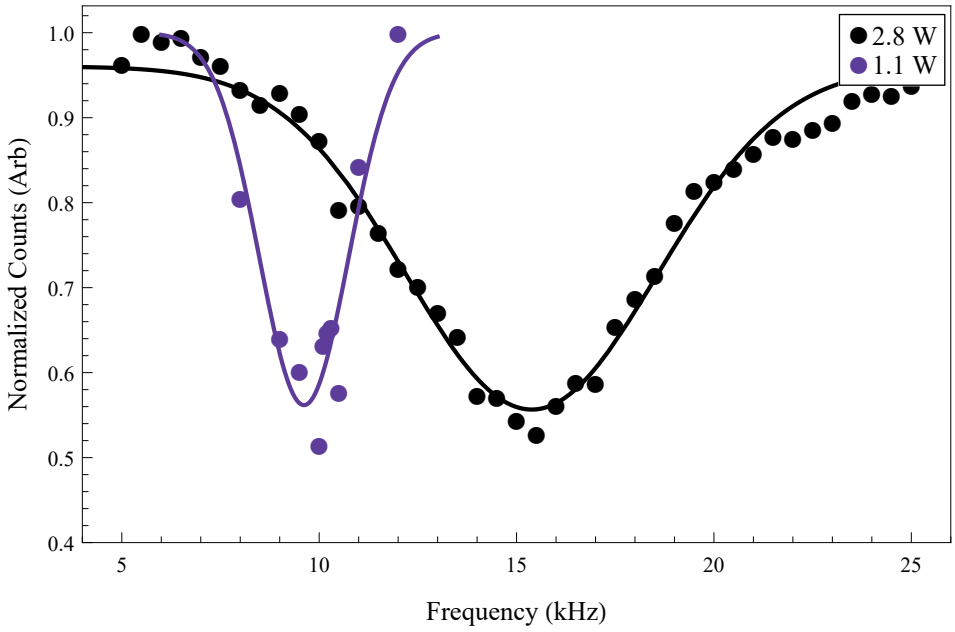

FIG. 47: Parametric resonance of the FORT at 1.1 (blue) and 2.8 W (black) beam power. The resonant frequency of the trap decreases as the power of the FORT beam decreases.

A possible topic for further investigation of parametric resonance is the rate of expansion of the FORT as a function of modulation frequency. Although no deep analysis was performed, after 2 ms of expansion, the Gaussian radii of the sample increase around $2f_0$ as the counts decrease due to parametric heating. The data in Fig. 48 shows an example of the heating effect.

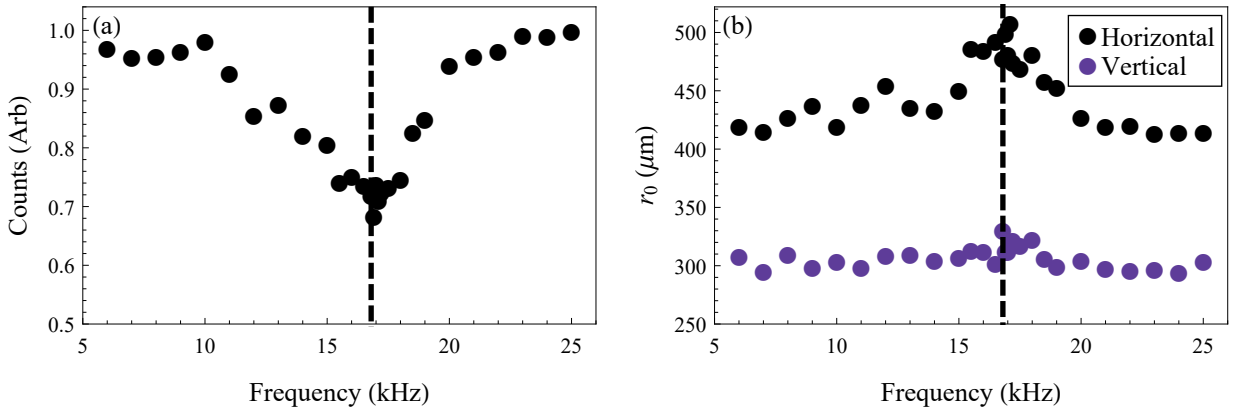

FIG. 48: Parametric resonance effect on FORT expansion at 3.1 W beam power. (a) corresponds to the total counts while (b) corresponds to the Gaussian radii. The Gaussian radii z_0 (horizontal) and r_0 (vertical) increase around the parametric resonance window. The dashed line provides reference to the same frequency on both graphs.

CHAPTER 4

EXPERIMENTAL ARRANGEMENT

This chapter will present both the optical and electronic experimental arrangements as well as the acquisition methods used for the collection of temporally-resolved fluorescence data. A photo of the experimental vacuum chamber can be seen in Fig. 49.

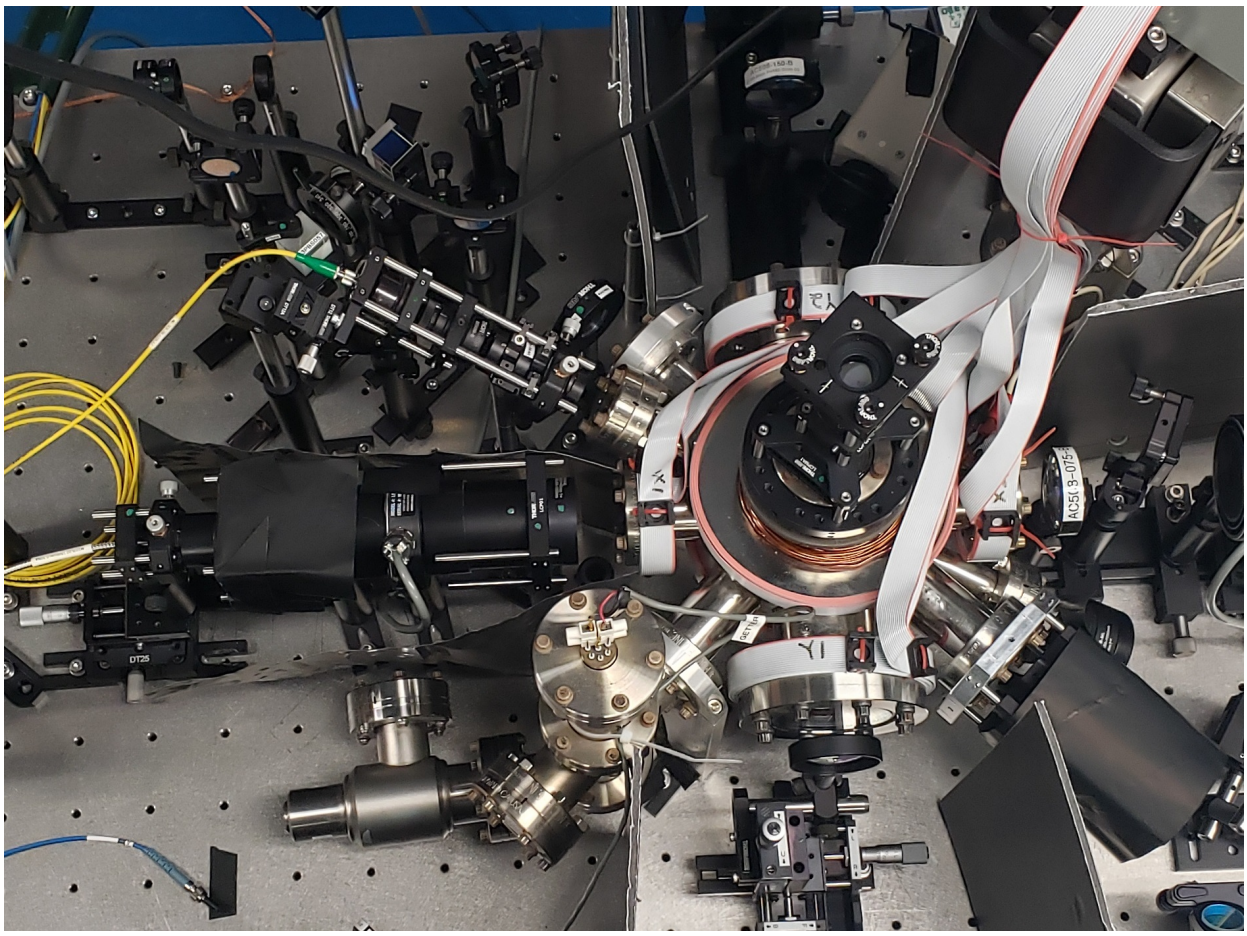

FIG. 49: Overhead image of the vacuum chamber and fluorescence collection optics.

4.1 EXPERIMENTAL SETUP

A straightforward but complex optical arrangement was created in order to optimize the available laser power provided by the DFB instead of introducing another laser into the apparatus. This approach was taken to ensure consistency and stability of the probe.

The beam for the probe pulse originates from the 0^{th} order MOT beam that was shown in Fig. 9 where the detuning of the beam is controlled by the DP AOM setup described in the MOT experimental setup section. Since the probe pulse occurs when the MOT is off, it is advantageous to utilize the 0^{th} order MOT beam which would otherwise be wasted. The optics diagram for creating the probe pulse is shown in Fig. 50. The optical isolator (ISO) was required to remove optical sidebands on the DFB caused by various reflections. Due to power and detuning limitations of the apparatus, two optical paths were used to cover the desired frequency range. The solid path corresponds to a detuning range of approximately 50-195 MHz while the dotted path corresponds to 150-295 MHz with respect to the $5S_{1/2}\ F = 2 \rightarrow 5P_{3/2}\ F' = 3$ transition. The frequency of both AOMs in the arrangement were determined by optimizing the power of the 1^{st} order beams. The AOM frequencies were static in order to maintain consistency of the experiment. Flip mirrors were used in order to switch from one path to the other. The polarizers are required to ensure proper coupling and transmission stability of the polarization preserving fiber input to the electro-optic modulator (EOM). The EOM acts as a fast optical switch and the photodiode (PD) was used as a monitoring tool. Specifics dealing with EOM operation and optimization will be described later.

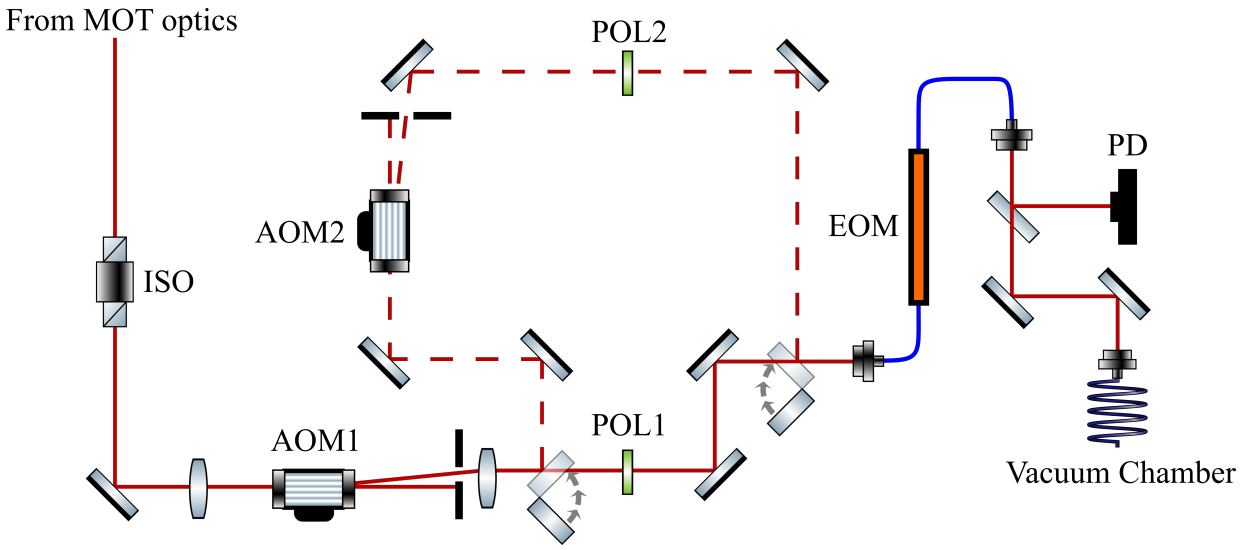

FIG. 50: Probe pulse optics diagram. The beam originates from the 0^{th} order MOT beam as shown in Fig. 9 and can be directed along two different paths. The solid line describes the beam trajectory when the flip mirrors are out of the beam path. The dashed line describes the trajectory with the flip mirrors redirecting the beam through both AOMs. Optical components are ISO (Thorlabs IO-3-780-HP), AOM1 (Brimrose TEM200-50-780), AOM2 (Gooch & Housego R23080-1), POL1 (3" Unknown Model), POL2 (Thorlabs LPNIRE 100-B), EOM (EOSpace AZ-0S5-10-PFU-PFU-780), and PD (Thorlabs DET36A).

In the experiment, the fluorescence due to the short probe pulse will be collected, focused into a fiber, and sent to a photomultiplier tube (PMT). The collection optics, while simple, were designed to minimize light leakage and maximize the amount of collected fluorescence into an optical fiber. A diagram of the collection optics is shown in Fig. 51. Creating a 3D rendering of the chamber and collection optics was vital in optimizing the lens arrangement in the limited space. Not only does the shutter block light when needed, it acts as an iris while open. The position of the shutter blocks essentially all of light that may scatter off the walls of the chamber while allowing all light from the probing region to pass. The resulting focus of the scattered light at the location of the fiber, after optimizing the lens system and shutter position, is shown in Fig. 52 where the large yellow circle represents the 1500 μm diameter fiber tip. The image was recorded with the beam profiler at the future location of the optical fiber. A photo of the collection optics in the lab is shown in Fig. 53. During data acquisition the collection optics are also surrounded by blackout foil to further decrease the

probability of unwanted light entering into the system.

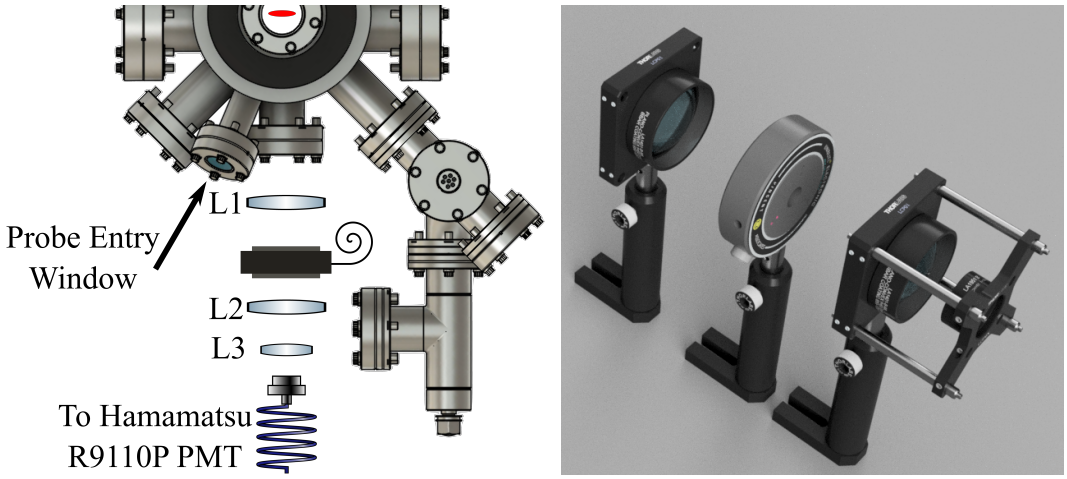

FIG. 51: Experimental fluorescence detection optics. The lenses L1 and L2 are $f = 59.8$ mm (Thorlabs LA1401-B-ML) and L3 is $f = 25.3$ mm (Thorlabs LA1951-B-ML). The fiber has a 1500 μm core diameter (Thorlabs M107L02). Omitted is a 780 nm line filter which was located between L3 and the fiber. 3D render made in Fusion360.

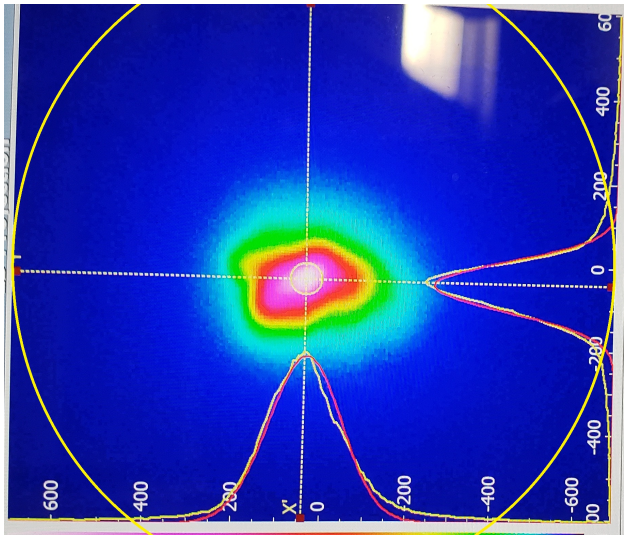

FIG. 52: Size of MOT fluorescence in comparison to optical fiber tip (yellow circle).

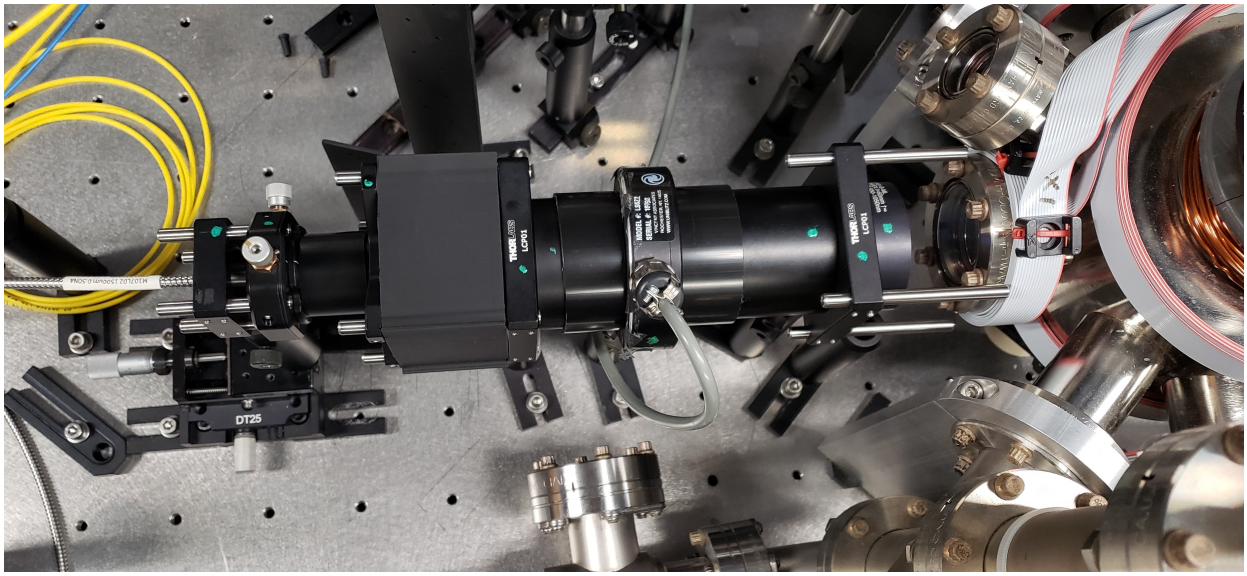

FIG. 53: Experimental fluorescence detection optics associated with Fig. 51. During operation blackout foil also surrounds the train of optics in this photo.

Preliminary experimental attempts were performed simply by using an AOM (Brimrose TEM200-50-780) as an optical switch to create the probe pulse. The determination to instead use an EOM for a switch was due to several factors. The rise and fall time of an AOM is about 15 ns which is longer than the desired pulse length. Switching the AOM on and off also depends on the TTL controlled electronic switch and the response of the RF amplifier. Most importantly, pulse widths of less than 50 ns were not viable due to the various response limitations. Example pulses from the EOM and AOM are shown in Fig. 54 where it is clear the EOM out performs the AOM in terms of pulse shape and width.

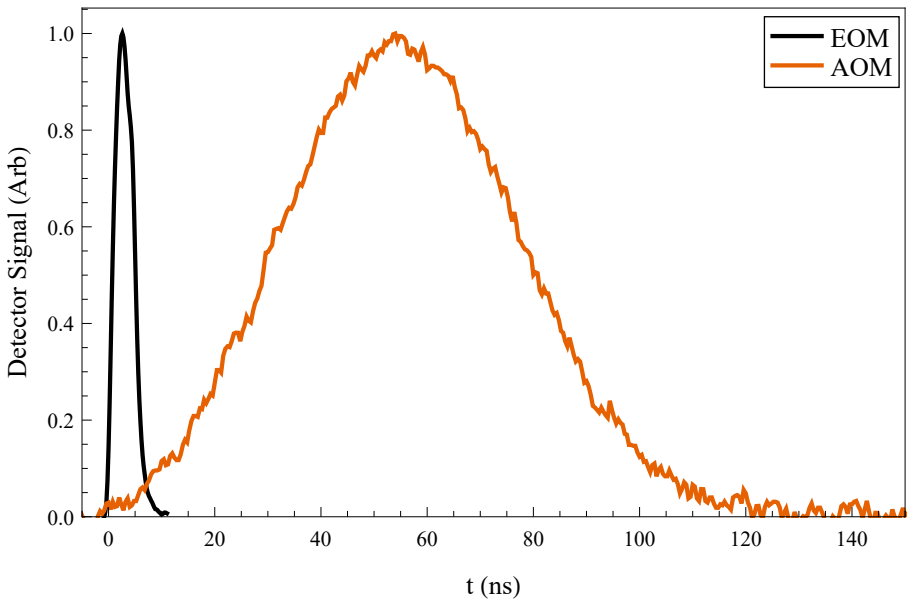

FIG. 54: Example pulses produced by the EOM (black) and AOM (red).

The type of EOM (EOSpace $LiNbO_3$ AZ-0S5-10-PFU-PFU-780) that was used is essentially a Mach-Zehnder interferometer where the index of refraction along one path is controlled by an applied voltage. Changing the index of refraction controls the relative phase between the two paths inside the device. The EOM is controlled by a DC bias and a RF input. The DC bias provides the means to balance the interferometer and the RF input accepts pulses which allow light to pass through depending on the amplitude of the pulse. Balancing the device is important to ensure maximum extinction when no pulses are present. Figure 55 presents the optimal voltage settings for optical extinction and transmission of the EOM. The basic idea is to extinguish the transmission with the DC bias and introduce a fast pulse to the RF input at an appropriate voltage for maximum transmission. It is important to note that the behavior shown in Fig. 55 is specific to when the polarization of the light was perpendicular to the input fiber key of the EOM. If the polarization is in line with the fiber key, the EOM will go through roughly nine cycles over the same voltage range, which is consistent with the data sheet provided by EOSpace. The perpendicular arrangement was chosen because it is less susceptible to voltage and temperature drifts.

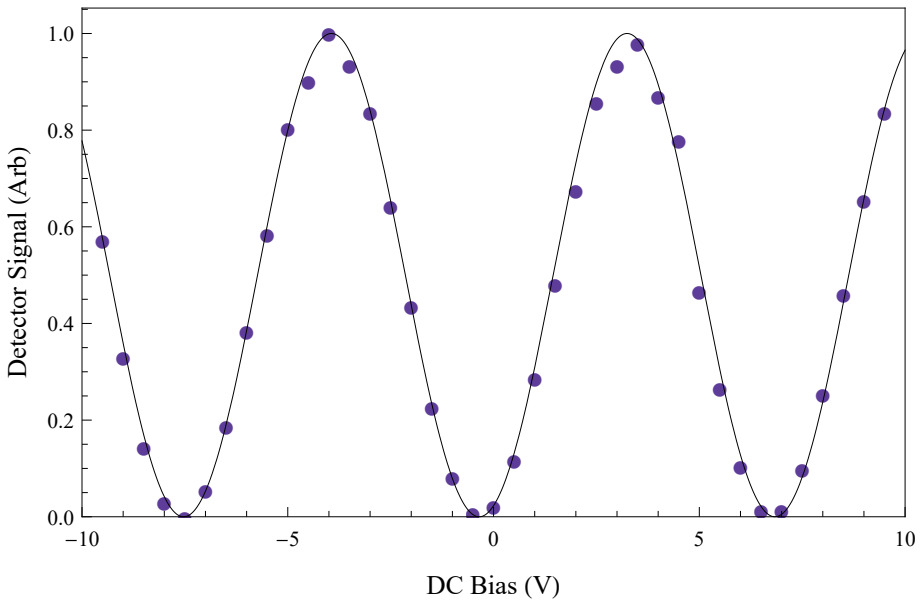

FIG. 55: Optical transmission through the EOM as a function of DC Bias.

The EOM is quite sensitive to the typical laboratory temperature fluctuations which cause significant shifts in the optimal DC bias voltage. Simply opening and closing the lab doors would change the temperature enough to cause the unwanted drifts. In the quest for experimental consistency, this was a problem which was addressed in a couple ways. The original method involved creating a LabVIEW feedback loop program that adjusted the DC bias in order to minimize the output of the EOM. While this was still an improvement over the AOM pulse method, the amount of light leak and pulse height would fluctuate over the course of several minutes leading to inconsistent experimental conditions. A heating module was then designed and created in order to improve the performance of the EOM. The module consisted of a thermoelectric cooler (TEC Marlow DT12-6L) sandwiched between two plates of aluminum and a thermistor installed into a hole drilled into the top plate. The EOM was lightly secured to the top plate and the entire module was covered by an aluminum laser housing to further increase temperature stability. The temperature controller of a SRS LDC501 was used to set and maintain the temperature of the unit at 49.000 °C. Care was taken to slowly warm the EOM at a rate of about 3 °C per minute until reaching the target temperature. The module required a roughly 24 hour period to completely stabilize which was determined by logging the light leakage through the EOM. Heating and temperature

controlling the EOM increased the stability so substantially that DC bias adjustments only had to be made every few days. It can not be understated how significant this improvement was for obtaining consistent pulses for the experiment.

The DC bias and the RF input are controlled by two separate systems to create a fast pulse with maximal amplitude. Firstly, the previously mentioned LabView program which controls the DC bias is ran on a PXI crate with a NI PXI-8108 controller unit and multi-function I/O module (NI PXI-6229). The I/O module output is connected to a terminal block (NI BNC-2120) which has several available analog I/O BNC connections. An analog out port of the terminal block is connected to the EOM DC bias input. The photodiode (Thorlabs DET36A) shown in Fig. 50 is connected to an analog input port on the terminal block in order to monitor the output of the EOM. The LabView program provides direct control of the analog out voltage while reading the photodiode signal. Although the equipment used may be over-kill for the task of maintaining a voltage, this system increases confidence in the experimental apparatus due to its stability and ability to immediately provide an alert to non-optimal behavior with its real time monitoring.

The RF input requires several other electronic devices in order to create a fast pulse with proper shape and amplitude. The pulse originates from a function generator (Quantum Composers 9520) with 50 ps jitter and sent to a fast voltage comparator (Analog Devices, ADCMP606 Evaluation Board) that has a rise/fall time of $\approx$ 200 ps and an output of 2 V. Although the function generator is capable of driving the EOM alone, it suffers from ringing and proper amplitude control. The comparator circuit shown in Fig. 56, originally created by Stetson Roof [6] and slightly modified, alleviates those issues and outputs a fast pulse with minimal noise and ringing. Eliminating the ringing entirely however was a tedious task of trial and error. Simply touching the resistors and capacitors would substantially change the magnitude of the ringing. The output of the comparator is connected to a variable attenuator (Kay Elemetrics, 1/839) before being amplified by a 1 ns response time pulse amplifier (Mini-Circuits, ZPUL-30P). The attenuator allows for control of the pulse height and the pulse width is determined by the original function generator pulse.

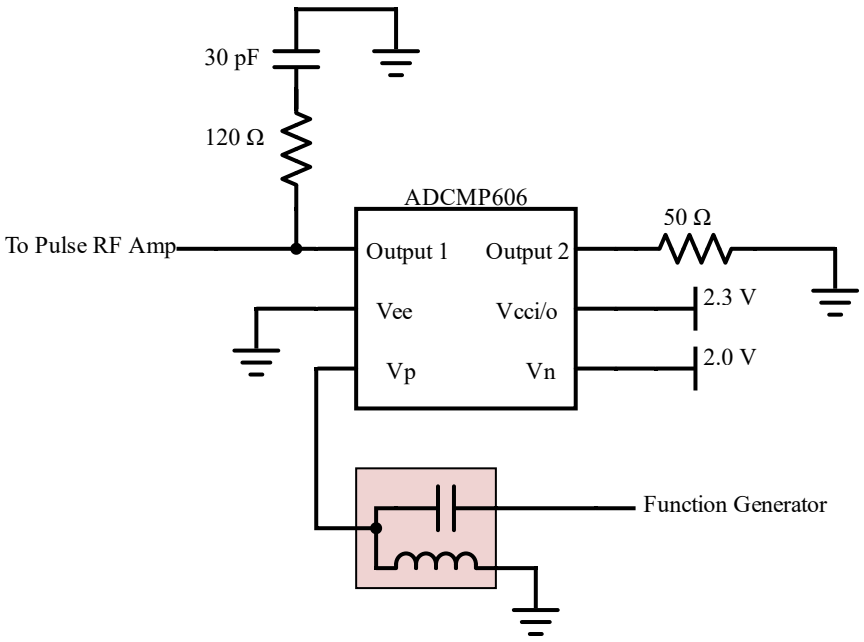

FIG. 56: Comparator circuit diagram for short pulses. A pulse from the function generator is sent to a bias-tee which has the DC input grounded to remove any offset the function generator may have as well as reducing noise. The comparator sends a high signal to Output 1 when the voltage at Vp is greater Vn.

Time resolved fluorescence detection via a photomultiplier tube (PMT) was used for data acquisition. A cooled Hamamatsu R9110P PMT rated for single photon counting was used along with a multi-channel scalar (SR430 MCS) to record fluorescence. Due to the semi-archaic nature of the SR430, a GPIB to USB converter (NI GPIB-USB-HS) was required to transfer acquired data efficiently and was controlled with a custom LabVIEW program. The timing resolution of the experiment is limited to 5 ns, which is the smallest bin size of the MCS and larger than the aforementioned jitter from the PMT, function generator, and pulse electronics.

Control of the experimental apparatus was mainly performed by utilizing LabVIEW programs on two PCs. The first PC controlled the overall apparatus timing while the second PC acquired data and controlled a voltage for a specific VCO. The experimental apparatus timing and control diagram is shown in Fig. 57. Each system will now be described in detail.

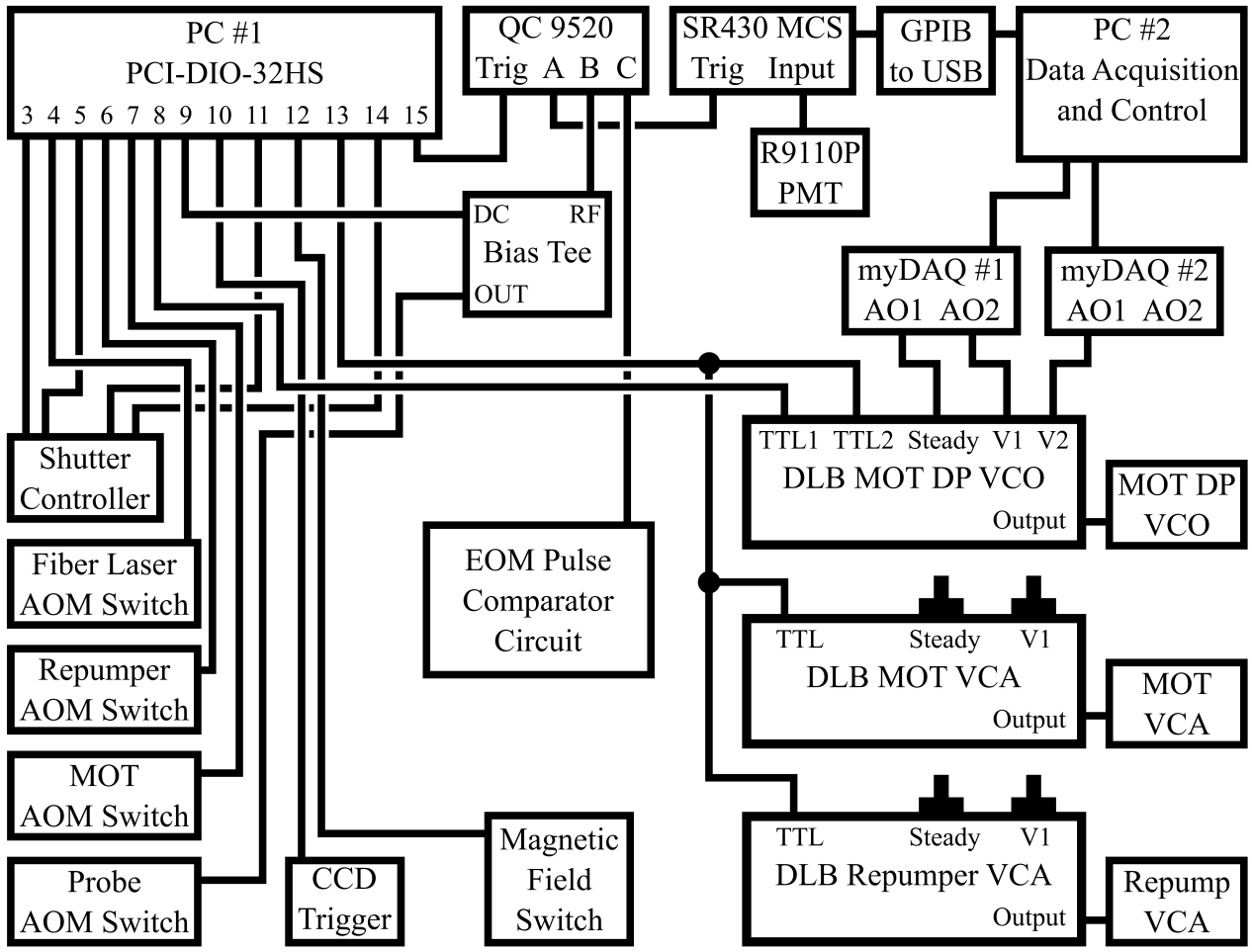

FIG. 57: Experimental timing and electronic control diagram. A LabVIEW program on PC #1 controls the main timing for the experiment. The pulse generator (QC 9520) was used for more precise timing. A LabVIEW program on PC #2 communicates with the SR430 for data acquisition and the NI myDAQs for electronic control of the MOT DP AOM frequency. The digital level boxes (DLB) are used to allow different input voltages to pass depending on the logic level of the TTL. The EOM pulse comparator circuit was shown in Fig. 56.

PC #1, running on Windows XP, performs the main timing loop for the apparatus via a LabVIEW program communicating with a data acquisition card (NI PCI-DIO-32HS) with 16 digital output channels. Unfortunately, National Instruments does not support

this particular device any further and therefore transferring the card to a newer PC was not viable. Hence, the need for two PC stations. The list of PCI-DIO-32HS channels and each of their usual functions are shown in Table 6. Depending on the specific experiment or characterization procedure, some channels were used for different purposes. The front panel of the LabVIEW timing control program is shown in Fig. 58 and corresponding block diagram in Fig. 59. The logic level of a specific channel is controlled by entering either a 0 (low) or 1 (high) at a specific time step entered into the left most column. Memory issues limit the minimum time step depending on the number of entries and the total required time of a loop. The minimum usable time step of the DAQ card is 1 μs but was set at 10 μs for the main experiment due to the aforementioned issue. The reason that channel 9 goes to the bias tee (DG535 OPT-04C) was to keep the probe AOM on as much as possible while also allowing precise timing by the QC 9520. The efficiency of the AOM increases as it was warmed up, which increases the available power during the probing phase. Allowing the probe AOM to remain on outside of the probing phase also aided in the EOM monitoring process.

TABLE 6: NI PCI-DIO-32HS channels and channel functions.

Channel	Function
3	MOT Shutter
4	Fiber Laser AOM (MOD IN VAR)
5	CCD Camera Shutter
6	Repumper AOM
7	MOT AOM
8	Probe Frequency (DLB MOT VCO TTL1)
9	Probe AOM (Via DG535 OPT-04C bias-tee)
10	CCD Camera Trigger
11	R9110P PMT Shutter
12	Magnetic Field
13	Compression Phase (DLB MOT VCO TTL2, MOT/Repumper VCA TTL)
14	Repumper Shutter
15	Trigger for Quantum Composers 9520

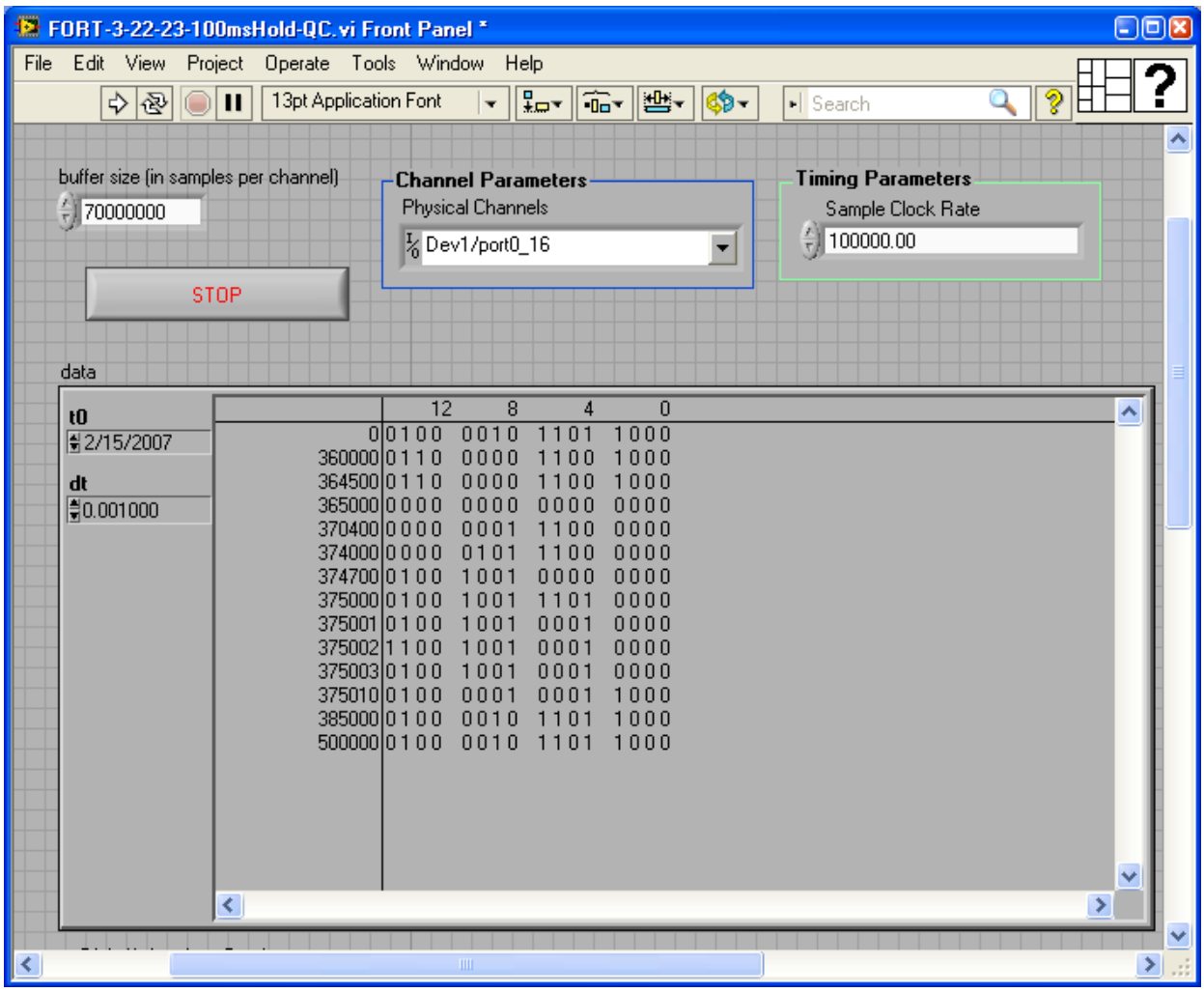

FIG. 58: LabVIEW timing program front panel for the NI PCI-DIO-32HS DAQ card. The displayed values represent a sequence that is 5 s long and each integer number corresponds to 10 μs. The sequence repeats until the user hits the stop button. Increasing the sample clock rate by an order of magnitude will cause each integer number to correspond to 1 μs but suffers from memory issues. The t0 an dt values can be ignored.

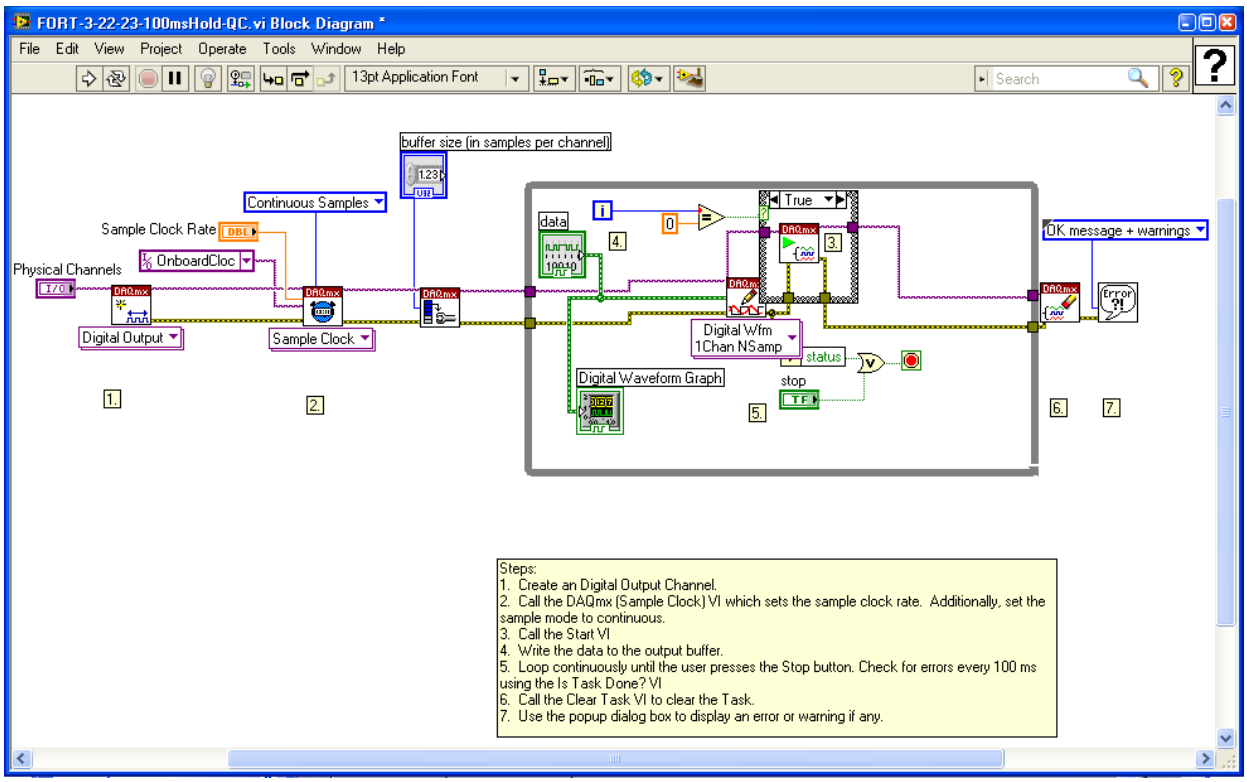

FIG. 59: LabVIEW timing program block diagram for the NI PCI-DIO-32HS DAQ card. The false case simply allows the paths of both input wires to pass through.

The digital level boxes (DLB) consist of one or more analog switches (Maxim DG419) and two or more voltage sources. The DG419 switches between two input voltages depending on the logic level. This creates a TTL controlled voltage selector to change the voltage to either a VCO or a VCA. The original design [89] uses a combination of voltage reference chips (Maxim REF01) and appropriate potentiometers to supply the DG419 with adjustable voltage sources. The downside to this design is that it is extremely inefficient because a potentiometer must be adjusted by hand to change an input voltage. A new circuit was built on the same concept but utilizes external analog sources instead of using internal voltage reference chips and potentiometers. The basic wiring diagram for the new DLB is shown in Fig. 60. The external analog voltage sources are provided from the analog outputs of NI myDAQs which are computer controlled by PC #2. As shown in Fig. 57, the DLB for the MOT DP VCO requires three voltage sources, therefore two NI myDAQs were required due to only having two analog outputs each. The MOT and repumper VCA DLBs use the

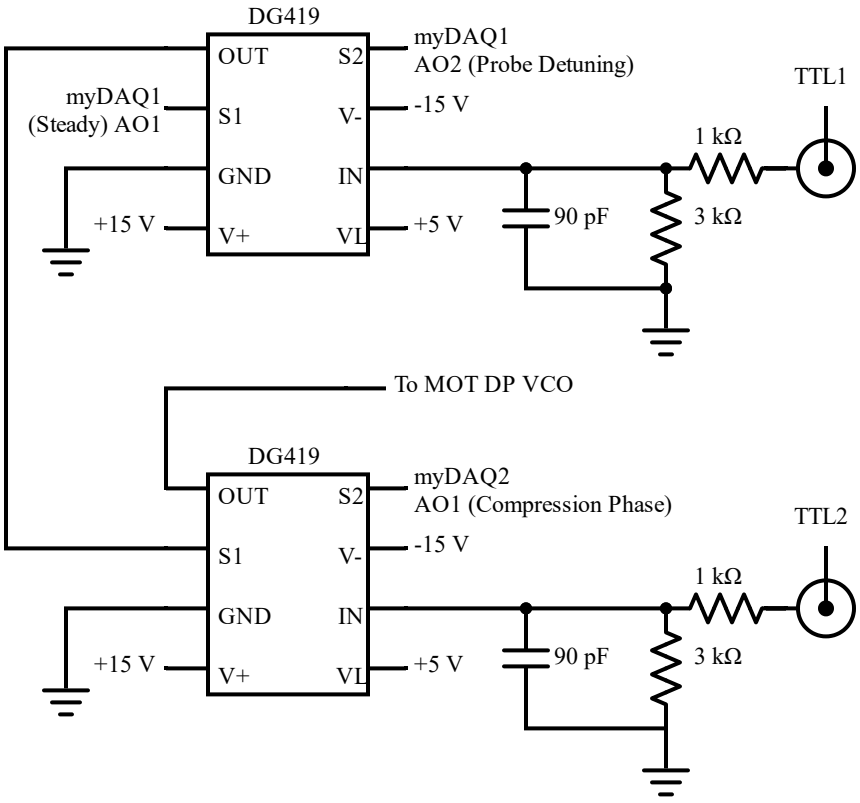

FIG. 60: Digital level box diagram for external voltage sources. Two NI myDAQs are used to control the three input voltages. If TTL1 and TTL2 are low the DLB outputs the voltage set by myDAQ1 AO1. If TTL1 is high and TTL2 is low the DLB outputs the voltage set by myDAQ1 AO2. If TTL2 is high the DLB outputs the voltage set by myDAQ2 AO1.

original design because adjustments to their voltages are uncommon.

In order to utilize the new DLB and myDAQs combination efficiently, a calibration was performed by a LabVIEW routine that iterated through the myDAQ voltage range and recorded the output frequency of the MOT DP VCO via a serial RS232 connection to frequency counter (BK Precision 1856D). The calibration routine was performed on the three analog outputs used on the DLB. Control of the VCO is now performed by entering the desired frequency into the LabVIEW front panel and a voltage is interpolated from the calibration data. The frequency is typically accurate to the kHz level. To put that in perspective, temperature fluctuations in the lab affect the VCO frequency much more than any

voltage instability in the myDAQ units.

The AOMs in the apparatus are all controlled and driven in a similar fashion. The basic setup is shown in Fig. 61. The VCOs that were used are the Mini-Circuits ZOS-100 for the Gooch & Housego R23080-1 AOMs and the ZOS-300 for the Brimrose TEM200-50-780 AOMs. The RF switches are Mini-Circuits ZYSWA-2-50DR. The VCAs are Mini-Circuits ZX73-2500 and only used on the MOT and repumper electronics. The RF amplifiers are either home built using CA2832C (32 dBm max output, 35.5 dB gain) or MHW1345 (31 dBm max output, 34.5 dB gain) chips, or Mini-Circuits ZHL-3A (29.5 dBm max output, 34 dB gain).

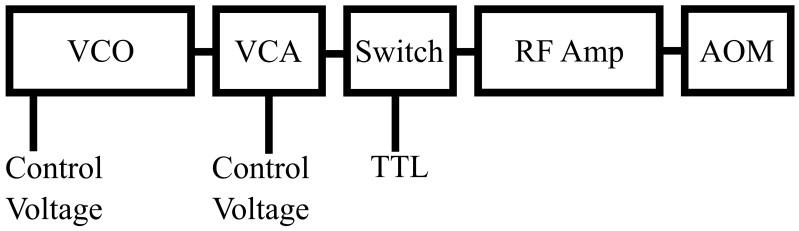

FIG. 61: AOM driving and control electronics diagram.

The RF electronics originally suffered from a strange grounding issue which needed to be addressed. When adjusting the control voltage to a particular VCO, the frequency of other VCOs would slightly change as well. An RF electronics housing was designed in Fusion360, shown in Figs. 62-63, and fabricated to hold six VCOs. The ± 12 and $+5$ V power supplies for the various electronics are connected via the banana jacks towards the top. The 5 kΩ potentiometers (Digikey, 3540S-1-502L) are used to control the first five VCO frequencies while the sixth is controlled by the aforementioned myDAQ setup via a DLB. The frequencies of each of the first five VCOs can be monitored via the SMA bulkheads (Amphenol, 132170) under the respective potentiometer. The monitor outputs are shown on the left side of Fig. 63 while the switch TTL BNC connections and RF output SMA bulkheads are shown on the right hand side. The RF amplifiers were then placed on top of the housing.

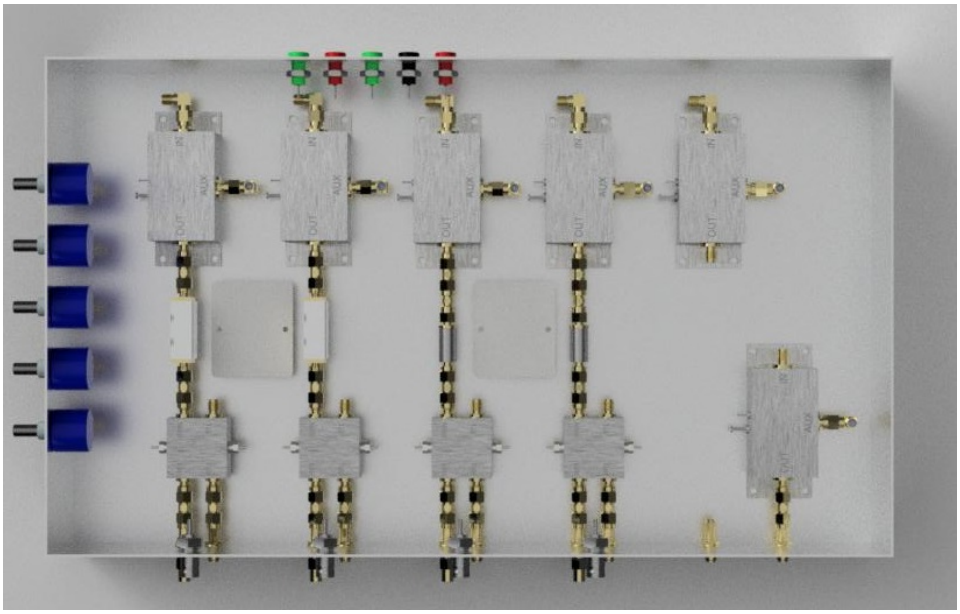

FIG. 62: New RF electronics housing top view with AOM control electronics. All VCO, VCA, attenuators, and switch models were personally created. Many connections are omitted to reduce visual clutter. The two unmarked rectangles represent Schottky diodes (Digikey, CMPSH-3SE TR) which eliminate TTL ringing and protect the PCI-DIO-32HS card from unwanted reflections. Designed in Fusion360.

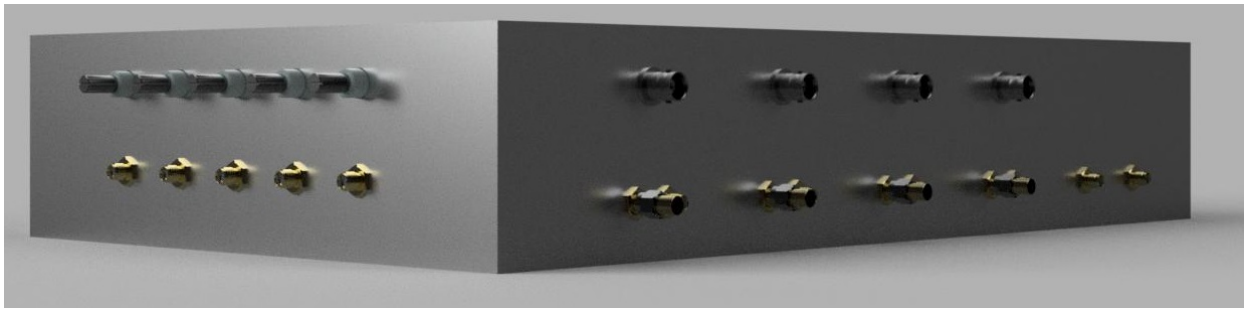

FIG. 63: New RF electronics housing. The potentiometers allow for frequency tuning of the individual VCOs. The frequency of each VCO can be monitored via the SMA output below each potentiometer. The BNC connectors are for the TTLs that drive the RF switches. The SMA connectors on the right output the desired frequency that is send to the appropriate RF amplifier. Designed in Fusion360.

The data acquisition LabVIEW program utilized the so-called producer/consumer architecture [101] which was found to be extremely robust. A typical use for this architecture is dealing with the situation when acquiring data is much faster than processing the data. The producer loop can continue to take data by queuing up previous data for the consumer to process. Of course this process is limited to how much data can be buffered but allows two processes to happen without limiting the program to the slowest. The main point is that the producer buffers information via a queue that the consumer will process.

The producer/consumer architecture was utilized in a slightly different manner for the data acquisition and instrument control required in the lab. The basic block diagram is shown in Fig. 64. The producer loop houses an event structure where each event is tied to a button press on the front panel. In this case, pressing a button enters a word into a queue. The consumer loop houses a case structure in which each case is given a unique name. Each case will be a set of instructions for the consumer loop to perform. In order to activate a particular case, the same word must be entered into the queue. A major benefit of utilizing case structures is that new cases may be added at any time without fear of interfering with the operation of the rest of the program.

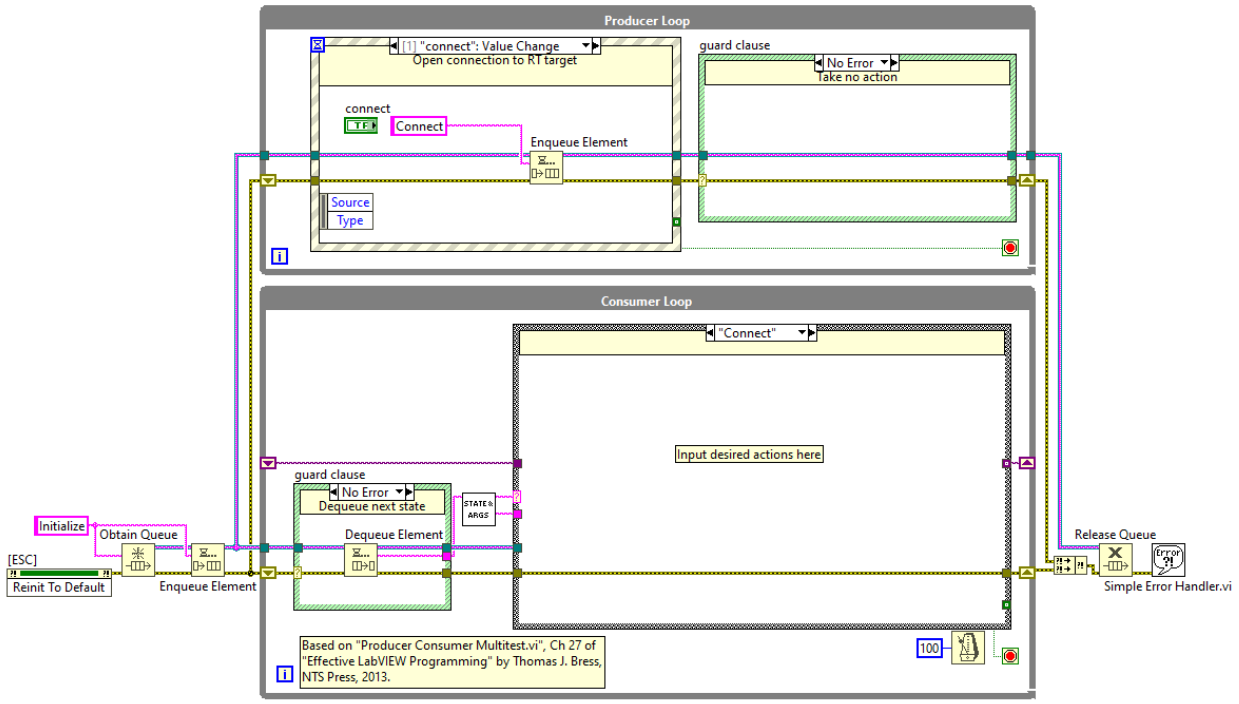

FIG. 64: LabVIEW basic producer/consumer loop block diagram [101]. Pressing the connect button on the front panel will cause the producer loop to queue the command Connect. The consumer loop has a case also named Connect, therefore the consumer loop removes the Connect command from the queue and then activates the Connect structure case.

The queue system can now be taken advantage of in order to create loops in this architecture. The case shown in Fig. 65 represents a simple example of a loop that is formed by a consumer case queuing itself after performing a desired action. Although this continues to enter the LoopMe case into the queue, commands originating from button presses also will be entered into the queue at the time of the press. Therefore, once a button press command enters the queue, it will perform the associated action and then continue the LoopMe case. Although this stripped down example is extremely basic, complex routines that communicate with several experimental instruments can be created with this basic idea in mind.

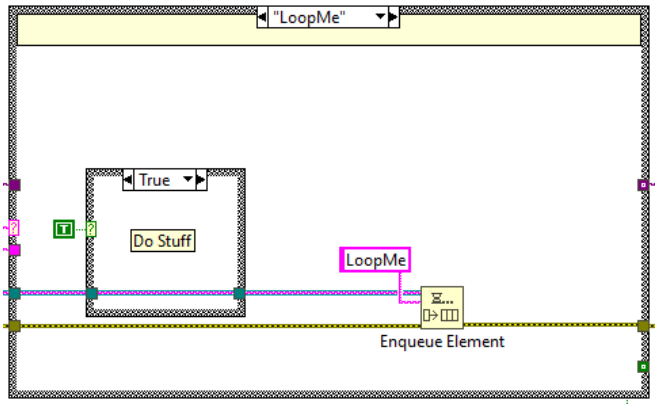

FIG. 65: LabVIEW basic producer/consumer architecture block diagram loop example. This particular case would queue simply re-queue itself.

The final program allows for voltage control of the two myDAQs, data acquisition and control of the MCS, data acquisition and control of an oscilloscope, and the ability to configure an experimental run that acquires data over a set of different parameters at the touch of a button. The latter significantly increases efficiency of an experiment because once a run is initiated, only periodic check-ins are required with little or no human interaction and the acquired data is saved in a systematic fashion allowing for straightforward data analysis. User defined runs are completely customizable within the program.

To simply summarize the laboratory control scheme, PC #1 controls the timing of the experiment while PC #2 acquires data and changes the MOT DP VCO frequency. At this point the two systems are independent but need to work together to obtain data correctly. During a typical experimental run PC #1 goes through its timing loop until the user presses the stop button. PC #1 triggers the QC 9520 pulse generator which in turn triggers the SR430 MCS to start taking data for a specified amount of time. The MCS defines this as acquiring a record. PC #2 communicates with the MCS and retrieves the number of accumulated records several times a second. Once the number of records reaches a user defined value the accumulated data is saved, the MCS is cleared, and another set of records begins. Voltages to the MOT DP VCO can be changed automatically while data is being acquired. This allows for a user defined experimental run over several detunings at the press of a button. Data acquisition from an oscilloscope was performed in the same way and was used in the optical pumping atom counting experiment.

4.2 DATA ACQUISITION

Daily experimental conditions were exponentially more consistent after all of the laboratory troubleshooting, upgrades, and the implementation of a much more automated experimental apparatus. Although making these changes consumed a lot of time, the improvements to the apparatus increased data acquisition capabilities by orders of magnitude. The only uncontrollable variable was the building HVAC system. The typical laboratory temperature fluctuations of 1°C were offset by the improvements to the apparatus. Data acquisition would not be performed when larger fluctuations would occur. Monitoring the frequency of a VCO was found to be the best indicator of temperature fluctuations. Data acquisition sessions were typically 8-12 hours during stable environmental conditions.

The time resolved fluorescence emitted by the FORT due to a short pulse was the desired information to collect. The data were acquired by coupling the collected fluorescence into a fiber, sent to a PMT, and the output of the PMT recorded by a MCS. The MCS records when a PMT pulse arrives after a trigger. The data is placed into a bin with a width of 5 ns, which is the smallest setting. The MCS can only record one event, or photon, per bin per trigger at this setting. Although this limitation restricts the data acquisition to the single photon regime, the typical amount fluorescence emitted per pulse under experimental conditions was significantly below any threshold which would require either attenuation or corrections due to pulse pile-up. The specific arrangement and devices used were described in the previous section.

The typical timing for the experimental apparatus during data acquisition is shown in Fig. 66. The MCS is triggered 420 ns before the first pulse and records data for 81.92 μs. Each of the 50 pulses are separated by 1.6 μs. The cycle of MOT formation, compression, and FORT creation then must happen again, which takes about 5 seconds. Thousands of records had to be collected over the course of several hours for each data point, therefore the previously mentioned improvements to the stability of the apparatus were key to obtaining consistent data.

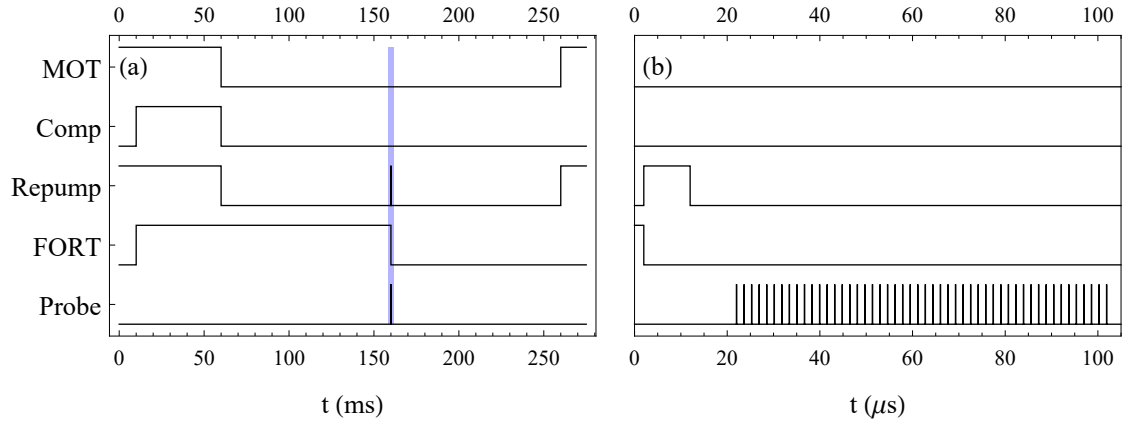

FIG. 66: Experimental timing diagram. (a) corresponds to the typical timing for FORT loading and probing. Data were acquired in the shaded region which corresponds to (b). Each of the 50 pulses are separated by 1.6 μs.

The LabView program automatically acquires and saves the MCS data once a set number of records have been accumulated. The MCS is then reset and the process repeats several times. All the acquired sets would then be combined in post processing. The purpose of acquiring many smaller data sets was to ensure consistency over the course of several hours. The theme of ensuring consistency, which has been mentioned numerous times throughout this text, was applied in every reasonable situation. Although obvious, this theme was an important ideal that gives confidence in the acquired data.

A program was created in Mathematica for post processing of the acquired data. The data sets were split into 50 equal segments. Each segment contained the data for each of the individual pulses. The segments were then summed together to create one time resolved signal. The time resolved data were typically the accumulation of the fluorescence from 1.3×10^5 pulses.

Before delving into the results, the choice of performing 50 pulses for each FORT realization will be briefly discussed. As previously mentioned, data from 50 pulses were combined in an effort to efficiently record data with the available electronics. Each of the 50 pulses were separated by 1.6 μs, which technically means that each pulse corresponds to a slightly different optical depth. The optical depth of the FORT along the axis of the probe evolves in time, as shown in Fig. 67, for the on resonant case and the off resonant regime of the experiment. The angle of the probe with respect to the orientation of the FORT along with

typical FORT spatial parameters were taken into account in the calculation. The optical depth of the MOT on the other hand does not appreciably change over the same time period. The temporal data from each of the individual 50 pulses were evaluated and no recognizable change was found between the first and last pulses. Therefore, the choice to sum the pulses together was deemed appropriate. To provide contrast, a completely different data acquisition method involving a time to amplitude converter (TAC) could have been used. The acquired data would correspond to the length of time between a trigger and the first photon signal. The upside to this method would have increased the number of pulses per FORT realization from 50 to upwards of 3000 by recapturing the FORT after each pulse. Unfortunately, the TAC setup only records the first photon event after a trigger. Photons that come much later will have a high chance to be ignored because the TAC already triggered. Furthermore, the MCS can not be used at such a high repetition rate because it requires about 1 ms to acquire and process data before accepting the next trigger.

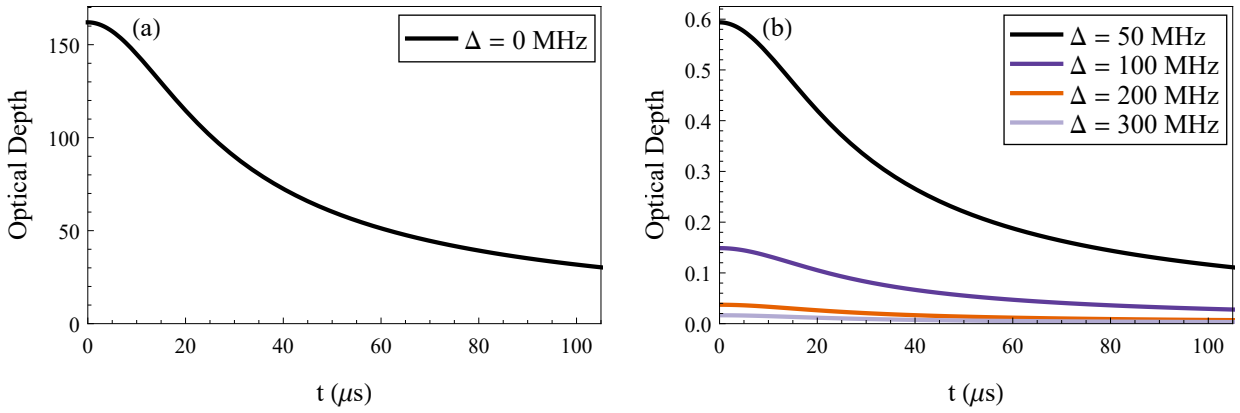

FIG. 67: FORT optical depth as a function of free expansion time along the axis of probe propagation. (a) corresponds to the on resonance case and (b) represents the typical experimental detuning regime. Probing typically begins 20 μs after the FORT beam is extinguished. The expansion corresponds to a FORT temperature of 138 μK.

CHAPTER 5

RESULTS AND COMPARISON

This chapter will present the results of the investigation into the fluorescence collected due to the introduction of a short pulse onto the FORT as well as onto a a MOT. Preliminary data will be presented first to show typical experimental behaviors under different input polarizations. Next, the complete set of temporal data at each probe detuning will be presented. Decay lifetimes from different temporal regions will be extracted from the temporal data and presented as a function of probe detuning. After the experimental data is provided, a comparison between the experimental data and numerical results obtained from the coupled dipole model will be discussed. This discussion will cover comparisons to the temporal and lifetime behavior under different spatial re-scaling.

5.1 EXPERIMENTAL RESULTS

Data were typically taken with the probe laser detuned 50-295 MHz from the $5S_{1/2}$ $F = 2 \rightarrow 5P_{3/2}$ $F' = 3$ transition in 25 MHz intervals. The probe pulses are approximately Gaussian shaped in the time domain with a FWHM of 4.04 ± 0.08 ns. The FWHM was determined by fitting a trace of the pulse shape to a Gaussian and the error corresponds to the standard error given by Mathematica. The temporal width of the probe pulse was also corroborated with the fluorescence detection system by placing a mirror at the output viewport which redirected the probe back into the chamber. The mirror was aligned in such a way that some of the light was directed into the fluorescence collection optics. The MCS recorded data under typical experimental conditions but with no MOT present and the MOT and repumper beams blocked. A singular bin of the MCS accumulated data corresponding to a pulse width of 5 ns or less. The size of the probe in the interaction region has a Gaussian radius of ≈ 300 μm, which is larger than the size of the FORT and comparable to the size of the MOT. The power of the probe was 1 mW.

An example of the temporal data recorded by the MCS, along with the associated natural log plot, is shown in Fig. 68. The bulk of the data that will be presented in this section will be parameters obtained from fits to the temporal signals in the three regions shown in Fig. 68b. Region 1 will always consist of the first 6 MCS bins after the peak, region 2 begins

at MCS bin 7 and varies in length depending on the detuning, and region 3 will only be analyzed on datasets with substantial signal at later times. Only region 1 and 2 will be fit for a majority of the datasets due to low signal amplitudes at later times. The temporal datasets that will be presented will be displayed with the y-axis on a log scale to show possible multi-exponential behavior more clearly. The error bars of the fitting parameters will be associated with the standard error to the fit.

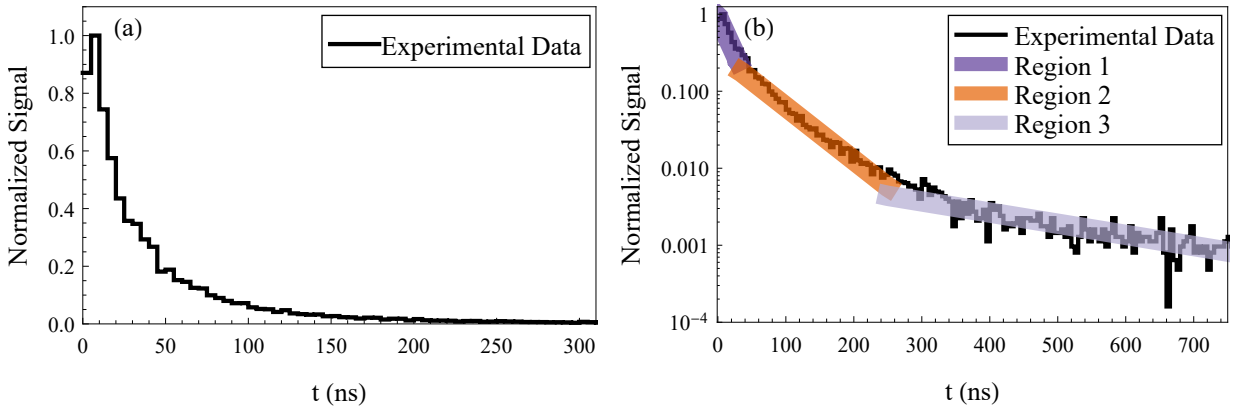

FIG. 68: Fluorescence recorded by the MCS (a) and the same data represented on a log scale (b) with the three fitting regions highlighted. Presented data were obtained from the accumulation of fluorescence from 52000 pulses onto the FORT at a detuning of 50 MHz. The data were normalized to the peak value.

5.1.1 PRELIMINARY DATA

Before several laboratory optimizations, preliminary data were taken at two orthogonal probe polarizations and fluorescence was collected with an analyzing polarizer over several angles. During the preliminary stage a probe rate of only 5 pulses per FORT realization was performed. Data were collected to investigate the polarization dependence of the total scattered light and compare the behavior to the a theoretical model of the angular dependence of fluorescence intensity [102]. This simple model describes single scattering and does not take into effect cooperative behavior. Preliminary data were also taken with different input

polarizations and over a range of detunings where lifetimes were extracted.

The general experimental geometry that is utilized to obtain the the total scattered light is shown in Fig. 69. The unprimed coordinate frame corresponds to the excitation, or collision frame, while the primed coordinates represent the detector frame. The z axis is chosen to be the axis of symmetry. Assuming the system has cylindrical symmetry the z axis corresponds to the polarization vector for linearly polarized light while representing the propagation direction for circularly polarized light. The Euler angles θ, ϕ, χ represent rotations in the order of z-y-z. The z' axis is chosen to point towards the detector. Therefore, in the detector frame, the polarization vector of a detected photon resides in the $x'y'$ plane and is given as

$$\hat{\varepsilon} = (\cos\beta, i\sin\beta, 0). \tag{262}$$

Detection of linearly polarized light along x' corresponds to $\beta = 0$, while circularly polarized light corresponds to $\beta = \pi/4$. The angle χ then represents the rotation of an analyzing polarizer initially aligned with x'.

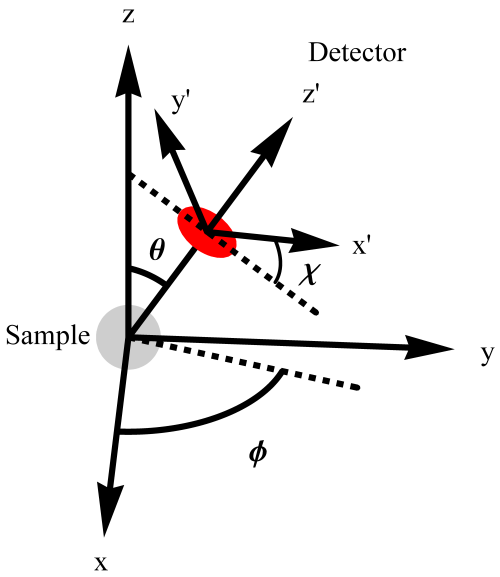

FIG. 69: Excitation frame x, y, z and detector frame x', y', z'. The Euler angles θ, ϕ, χ represent rotations around z-y-z. The z axis represents the polarization direction for linear polarized light while representing the propagation direction for circular. The z' axis points towards the detector.

Within this framework, the total scattered intensity can be written as [102]

$$I = \frac{I_0}{3}\left(1 - \frac{1}{2}h^{(2)}(F_i, F_f)\left[\mathcal{A}_0^{\text{det}} - 3\mathcal{A}_{2+}^{\text{det}}\cos 2\beta\right] + \frac{3}{2}h^{(1)}(F_i, F_f)\mathcal{O}_0^{\text{det}}\sin 2\beta\right), \tag{263}$$

where $\mathcal{A}_0^{\text{det}}$, $\mathcal{A}_{2+}^{\text{det}}$, and $\mathcal{O}_0^{\text{det}}$ are expectation values of excited state multipole moment operators, while $h^{(1,2)}(F_i, F_f)$ are geometrical factors that only depend on the initial and final state quantum numbers. After choosing linear input polarization ($\beta = 0$), which is the case the preliminary experiment, Eq. (263) simplifies to

$$I = \frac{I_0}{3}\left(1 - \frac{1}{2}h^{(2)}(F_i, F_f)\left[\mathcal{A}_0^{\text{det}} - 3\mathcal{A}_{2+}^{\text{det}}\right]\right), \tag{264}$$

where the relevant multipole moments are given as

$$\begin{aligned}\mathcal{A}_0^{\text{det}} &= \mathcal{A}_0 P_2(\cos\theta)\\ \mathcal{A}_{2+}^{\text{det}} &= \mathcal{A}_0\left(\tfrac{1}{2}\sin^2\theta\cos 2\chi\right),\end{aligned} \tag{265}$$

where the constants for linearly polarized light are

$$\begin{aligned}\mathcal{A}_0 &= (-1)\frac{2F_i + 3}{5F_i}\\ h^{(2)}(F_i, F_f) &= -\frac{F_i + 1}{2F_i - 1}.\end{aligned} \tag{266}$$

The transition of interest is $F_i = 3$, but without loss of generality for purposes of fitting data and determining general behavior, Eq. (264) further simplifies to

$$I(\theta, \chi) = a\left(1 - b\left[P_2(\cos\theta) - \frac{3}{2}\sin^2\theta\cos 2(\chi - c)\right]\right), \tag{267}$$

where the a, b, and c values are left as fitting parameters. Within this framework, Eq. (267) can be used to evaluate the angle dependent fluorescence. Although it will not be used in this preliminary analysis, the polarization degree is a typical parameter than can be obtained by analyzing the fluorescence at the orthogonal detection channels, and is given by

$$P = \frac{\left(I_\parallel - I_\perp\right)}{\left(I_\parallel + I_\perp\right)}, \tag{268}$$

where $I_\parallel$ and $I_\perp$ correspond to $\chi = 0$ and $\pi/2$ respectively. The polarization degree can be used to determine the amount of depolarization that occurs. Typical behavior of the collected fluorescence and polarization degree, as a function of the Euler angle θ, is shown in Fig. 70. With this framework in mind, the preliminary angle dependent data will be presented.

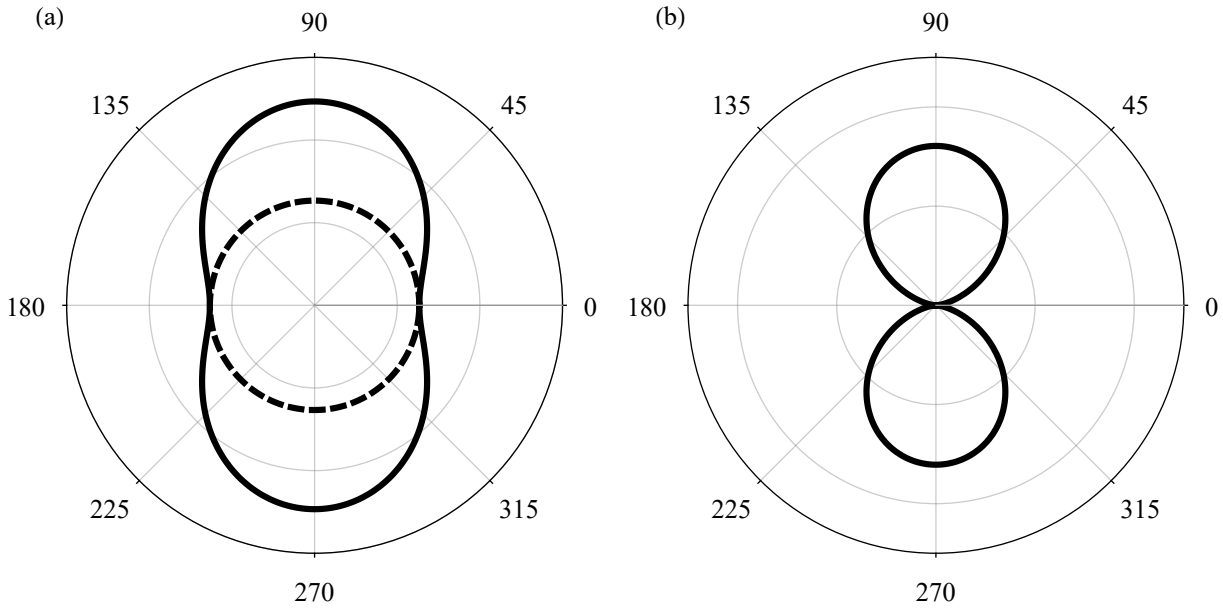

FIG. 70: Angle dependent fluorescence amplitude and polarization degree. The angle θ corresponds the Euler angle between the polarization vector and detection axis. (a) corresponds to the detected fluorescence due to a linearly polarized probe ($\beta = 0$). The solid line corresponds to detection of the same polarization ($\chi = 0$) while the dashed line represents detection of the orthogonal polarization ($\chi = \pi/2$). (b) shows the polarization degree as a function of θ.

Data were taken at two orthogonal probe polarizations and fluorescence was collected with an analyzing polarizer over several angles. The total fluorescence as a function of analyzer angle is shown in Fig. 71. Rotating the input polarization 90° is equivalent to a rotation of χ by 90° and can be seen by the shift. The Euler angle θ for our detection scheme was determined to be 109.6°. Data were also collected for several detuning values which all exhibited the same behavior. The same procedure was also performed on the MOT where similar behavior occurred. Since no abnormal behavior was apparent in the preliminary data, later data runs which utilize the analyzing polarizer were only be performed at orthogonal extremes of 0° and 90°.

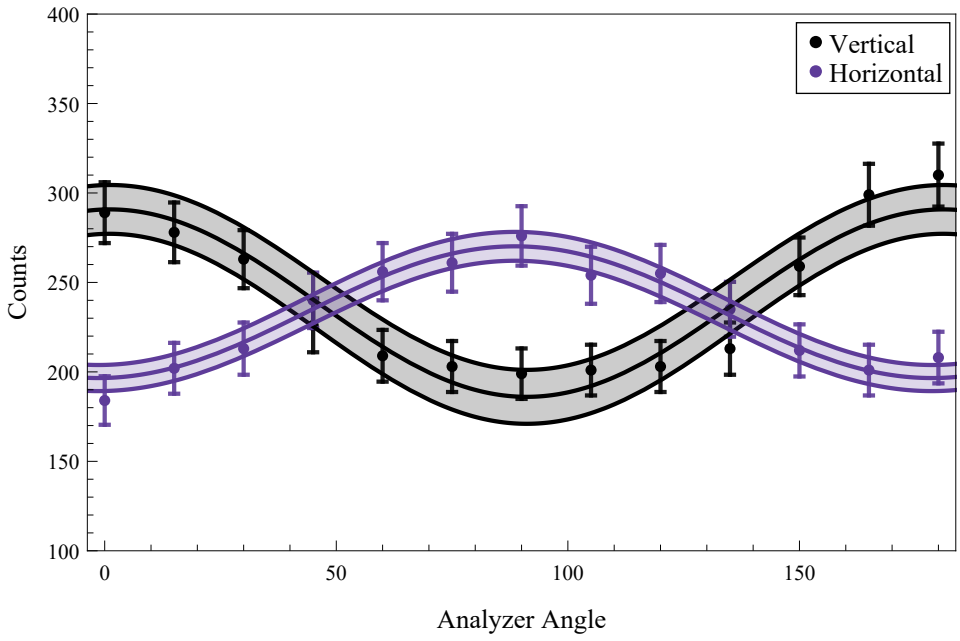

FIG. 71: Total FORT fluorescence as a function of analyzer angle. Rotating the input polarization from vertical (black) to horizontal (blue) is equivalent to rotating the analyzer by 90°. The data corresponds to the fluorescence due to a probe detuning of 90 MHz. The shaded region corresponds to a 95% confidence band from the fit to Eq. (267).

During this preliminary period, a singular data run at a particular detuning and polarization required around an entire day of stable conditions to accumulate fluorescence from 13000 pulses. Over several weeks, data were acquired over four input polarization channels at ten detunings each. The detuning dependent lifetime results for all four input channels are shown in Fig. 72 for regions 1 and 2. The dip in lifetime around 200-250 MHz was an initially unexpected result and suggests the ensemble decays faster than the natural lifetime of 26.24 ns in region 1. The region 2 results suggest that the sample decays slower than the natural lifetimes. A possible explanation for this will be discussed later during the analysis. Since there was no substantial deviation between the four input channels a choice was made to focus on collecting data with linear input polarization to remain consistent with previous works.

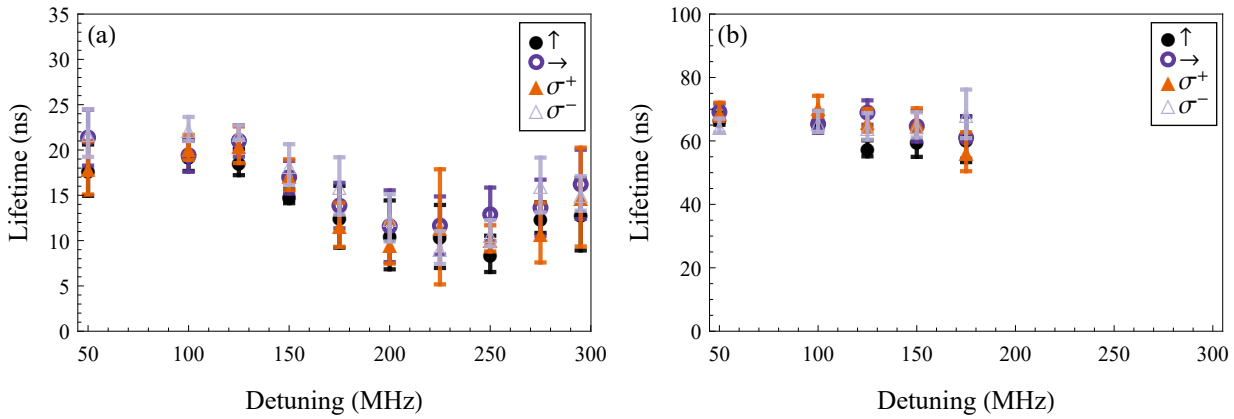

FIG. 72: Lifetime as a function of detuning from preliminary data over four input polarizations. (a) is the fast decay associated with region 1. (b) is associated with region 2. The missing data points are due to the lack of signal at long times. Error bars correspond to the standard error given by the fit.

5.1.2 TEMPORAL DATA

After several improvements to the experimental apparatus, two important features, alluded to in the preliminary stage, were focused on during final data acquisition. The first was to reproduce the detuning dependent lifetime results and the second was to observe the long lived behavior at larger detunings by accumulating more data. Before the lifetimes are addressed, the following discussion will first present all of the collected temporal datasets for both the FORT as well as the MOT. Including a dataset from the MOT allows for comparison to previous results in other research groups as well as to the FORT under the same, or similar, experimental conditions. All data were acquired with linear probe polarization.

The unpolarized temporal data, from the FORT, after 52000 probe pulses and over a detuning range of 150-295 MHz is presented in Fig. 73. The dashed line represents the natural lifetime and will be shown with every figure. In an effort to further increase signal at detunings between 150-295 MHz, a follow-up dataset was taken consisting of the accumulation of 208000 pulses under the same experimental conditions as previously stated and is shown in Fig. 74. The error bars simply correspond to the square root of the number of counts.

Polarization dependent data were also accumulated with an analyzing polarizer in the

detection channel at 0° and 90° for both the FORT and the MOT for 52000 probe pulses. Although the lifetimes will be presented for both polarization channels in the following section, Figs. 75 and 76 represent the sum of both polarization channels for the FORT and MOT respectively. The reason for presenting the sum of the detection channels is because the difference between the two is visually indiscernible at later times. For purposes of clarity, a singular example of temporal data obtained from the FORT at both analyzer positions is shown in Fig. 77, where the signal amplitude at later times is visually indiscernible. Even though the horizontal channel amplitude was smaller, as alluded to by Fig. 71, the temporal behavior showed no appreciable difference between polarization channels, which was in line with findings by Ref. [26]. The ratio of *total* fluorescence between the orthogonal detection channels also remained relatively the same (1.60 ± 0.12).

Finally, the polarization degree of the FORT and MOT fluorescence, in two temporal zones, was also extracted from the polarization dependent data. The initial 30 ns of data were used to determine the first zone, since single scattering events will happen the fastest, and the polarization degree was found to be 0.3 ± 0.03 for both the FORT and the MOT. This result is in line with the theoretical value of 0.296, which was calculated with the application of Eq. (268) with $\theta = 109.6°$. Defining a later zone as $t > 250$ ns, the polarization degree was found to decrease to a value of 0.10 ± 0.04 and 0.13 ± 0.03 for the FORT and MOT respectively. Although this result shows evidence of depolarization at later times, which can be attributed to multiple scattering and dephasing effects due to the coupling of many atoms, some polarization dependence still exists. The observation of the polarization dependence of the light at later times presents evidence that strongly suggests that the subradiant effect cannot be completely attributed to multiple scattering.

It will become more clear in the following section, but all of the presented temporal data has shown two similar behaviors. First, a later temporal region where the lifetime is much longer than the natural lifetime of 26.24 ns. Second, a region which decays faster than the natural lifetime seems to exist in the $\approx$ 150-295 MHz region.

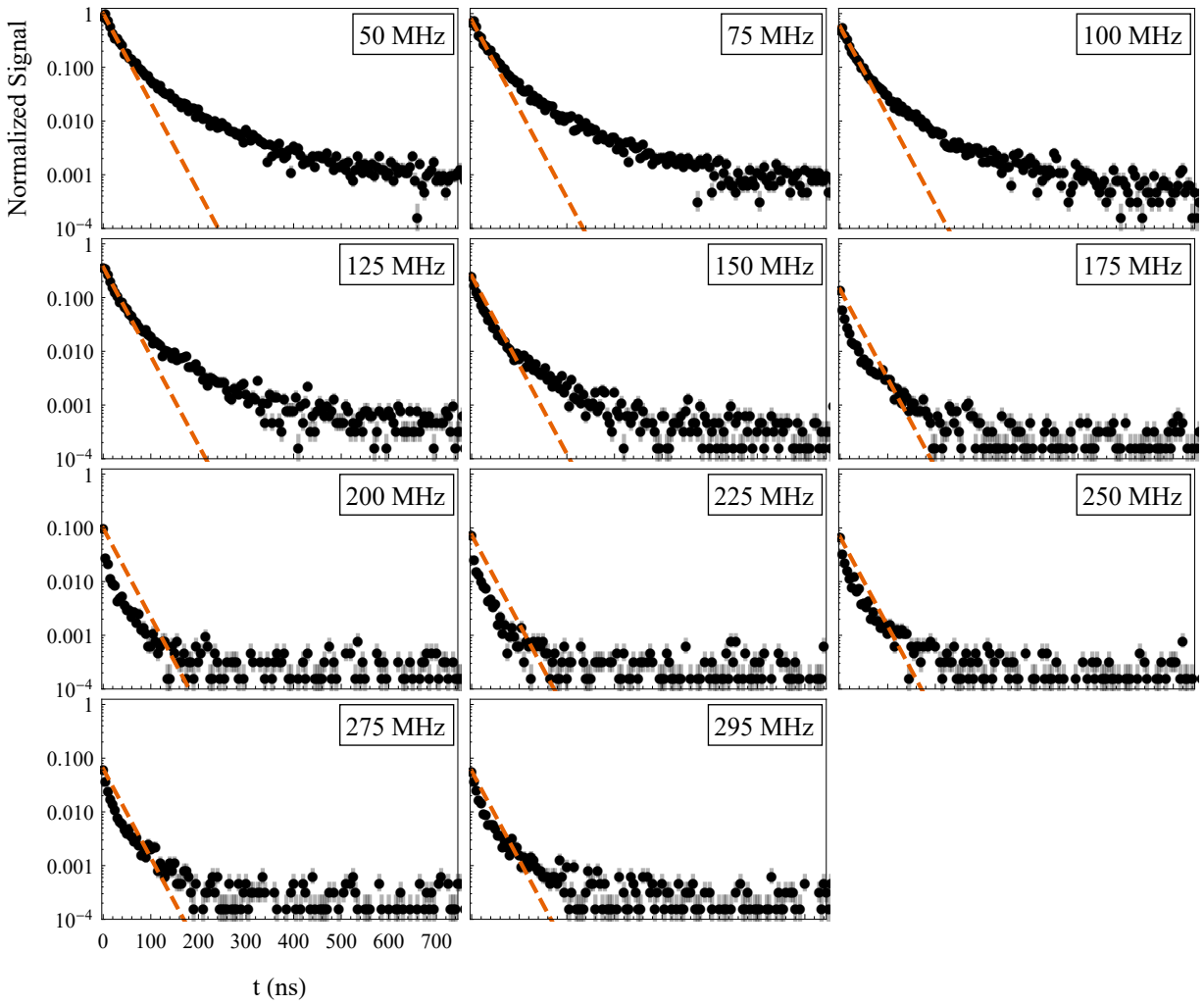

FIG. 73: Temporal data of FORT fluorescence with no analyzing polarizer. The presented data comprised of the accumulation of 52000 probe pulses and normalized to the peak value at 50 MHz which corresponds to 6233 counts. The normalization places the approximate noise floor between 10^{-3}-10^{-4}. The vertical axis is on a log scale. The dashed red line represents the single atom lifetime.

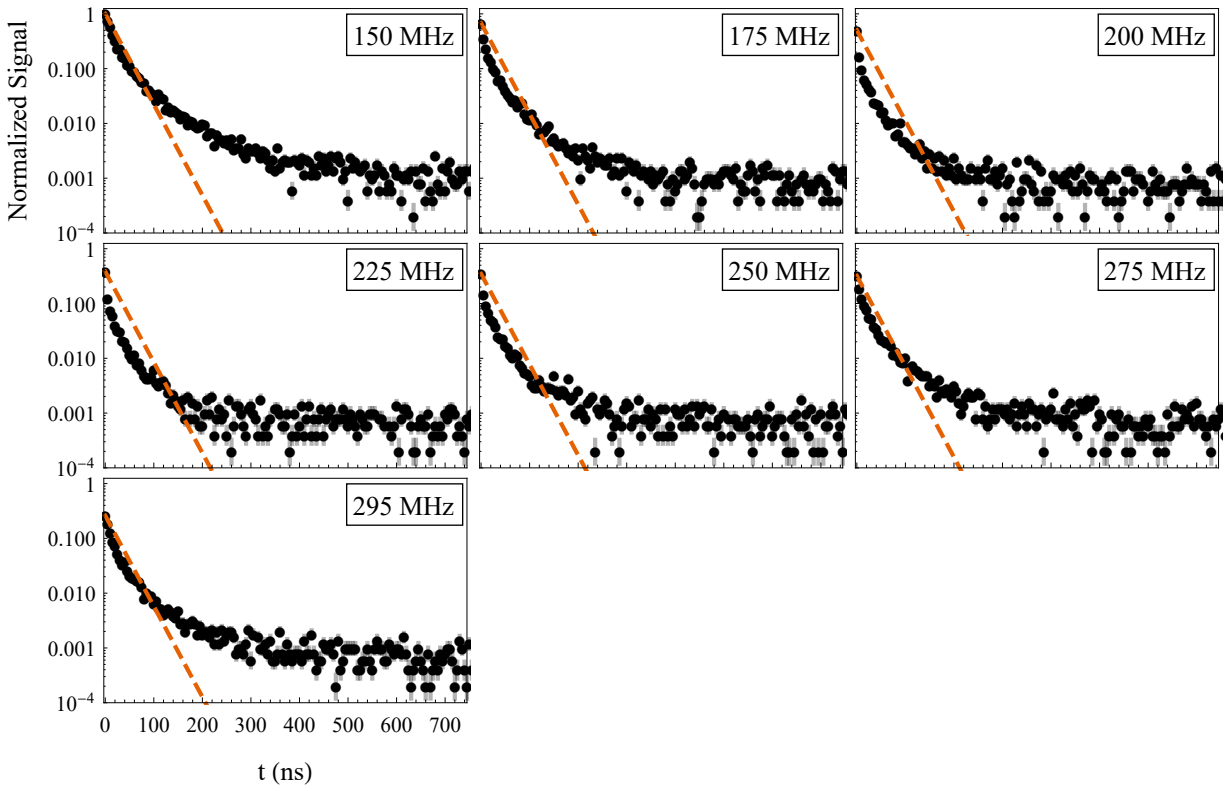

FIG. 74: Temporal data of FORT fluorescence with no analyzing polarizer. Although the presented data corresponds to the same experimental conditions to those in Fig. 73, in an effort to increase signal at larger detunings, a second data acquisition session was performed. The presented data comprised of the accumulation of 208000 probe pulses and normalized to the peak value at 150 MHz which corresponds to 5083 counts. The normalization places the approximate noise floor between 10^{-3}-10^{-4}. The vertical axis is on a log scale. The dashed red line represents the single atom lifetime.

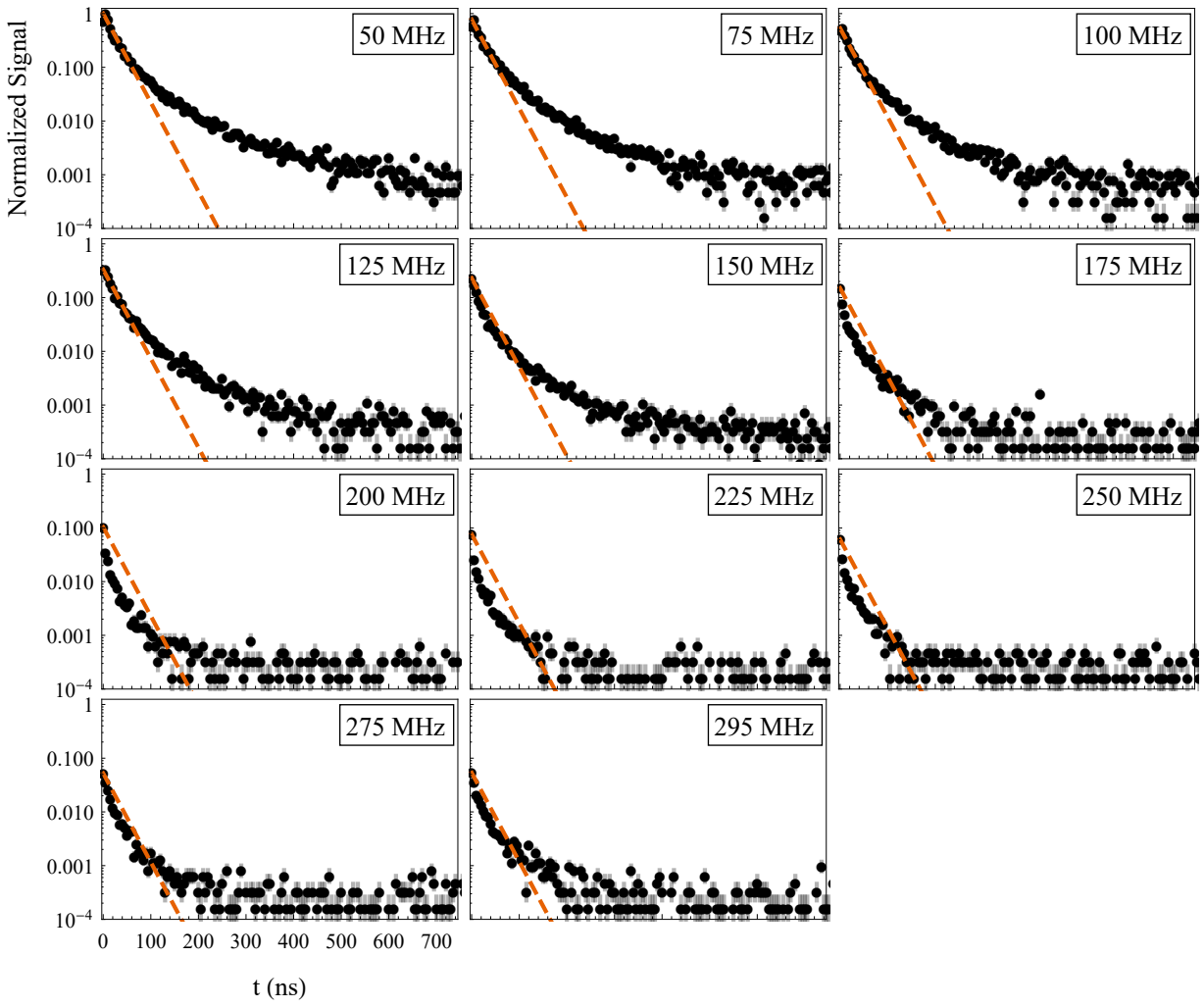

FIG. 75: Temporal data of the combined polarization dependent FORT fluorescence for 50-295 MHz detuning. The presented data comprised of the accumulation of 52000 probe pulses from each analyzer polarization and normalized to the peak value at 50 MHz which corresponds to 6233 counts. For clarity, this data represents the fluorescence collected in the vertical and horizontal detection channels combined. The normalization places the approximate noise floor between 10^{-3}-10^{-4}. The vertical axis is on a log scale. The dashed red line represents the single atom lifetime.

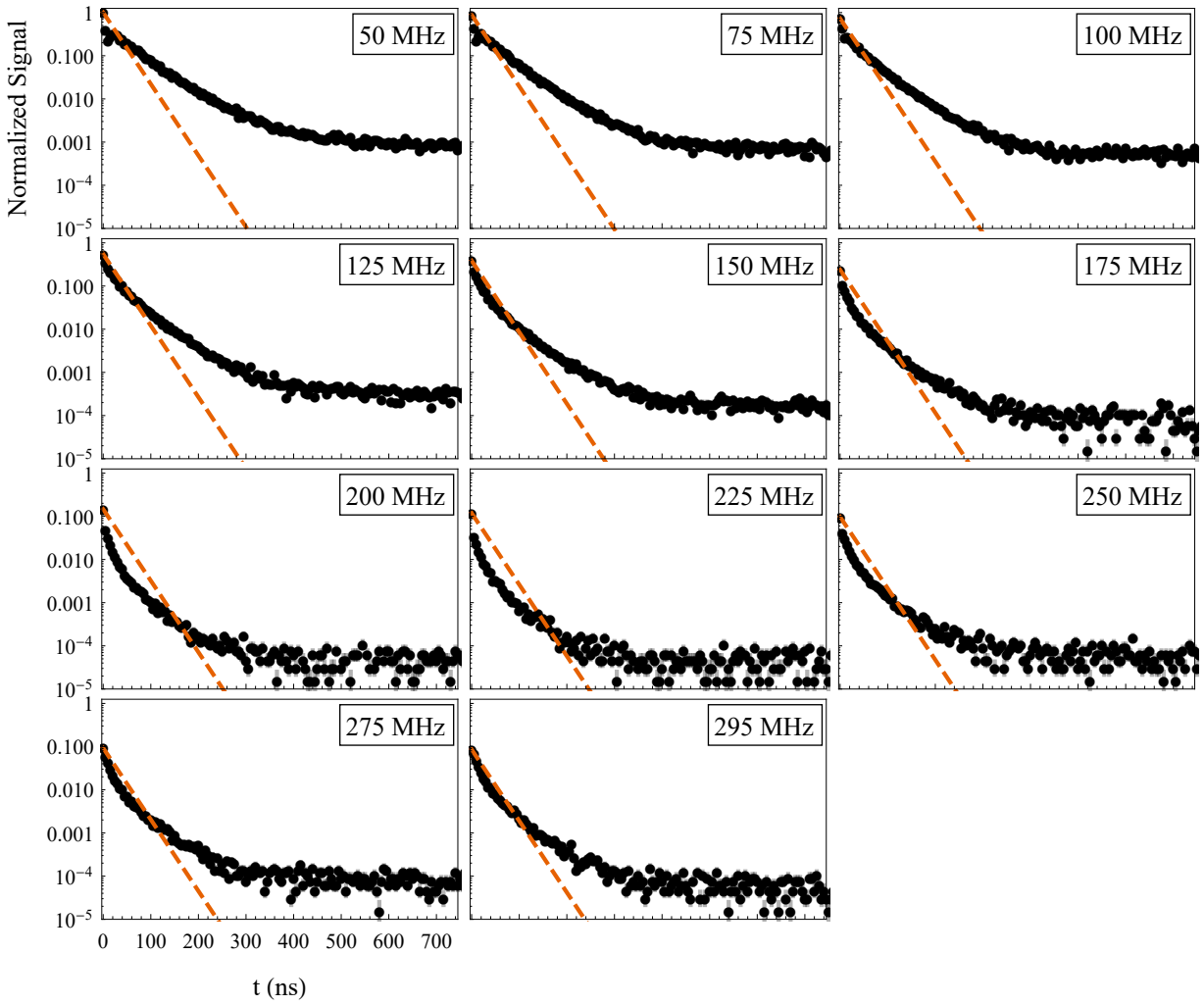

FIG. 76: Temporal data of the combined polarization dependent FORT fluorescence for 50-295 MHz detuning. The presented data comprised of the accumulation of 52000 probe pulses from each analyzer polarization and normalized to the peak value at 50 MHz which corresponds to 65551 counts. For clarity, this data represents the fluorescence collected in the vertical and horizontal detection channels combined. The normalization places the approximate noise floor between 10^{-4}-10^{-5}. The vertical axis is on a log scale. The dashed red line represents the single atom lifetime.

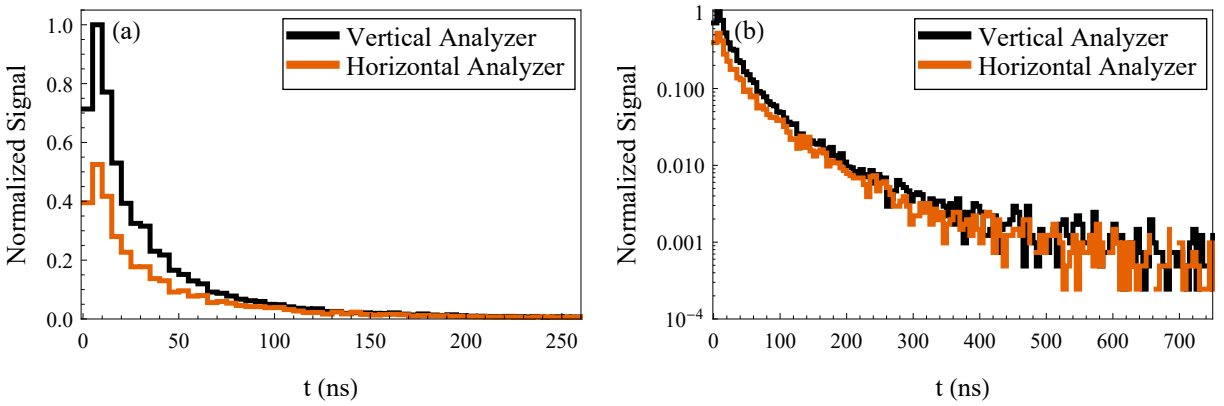

FIG. 77: FORT fluorescence signal at orthogonal analyzer positions. (a) corresponds to the temporal data while (b) corresponds to the natural log of the data. The input polarization was vertical and data were collected with an analyzing polarizer in the detection channel at 0° (Vertical) and 90° (Horizontal). The probe detuning was 50 MHz. Data were accumulated from 52000 probe pulses.

5.1.3 LIFETIME MEASUREMENTS

The following text will present lifetime measurements extracted from the temporal datasets from the three regions described in Fig. 68. The FORT lifetimes will be presented first and then the data associated with the MOT. Extracting fits from region 3 were only able to be performed on a few datasets, therefore all region 3 lifetimes will be combined into a single plot and presented at the end.

The extracted lifetimes associated with the unpolarized temporal FORT data, shown in Figs. 73 and 74, are given in Figs. 78 and 79 respectively. The polarization dependent lifetimes for the FORT are shown in Fig. 80, while the lifetimes associated with the combined temporal data, shown in Fig. 75, are presented in Fig. 81. Results are consistent between the unpolarized and polarized datasets.

The extracted lifetimes associated with the polarization dependent temporal MOT data are shown in Fig. 82, while the lifetimes associated with the combined temporal data, shown in Fig. 76, are presented in Fig. 83. It can be seen that the region 1 and 2 behavior do not significantly differ between detection channels for the FORT or the MOT. There also is evidence of a spectral feature in region 2 for both cases as well. Therefore, at least under the

current experimental conditions, no polarization dependence was found for either the FORT or the MOT with respect to the lifetimes. The important take-aways are the region 1 fast decay behavior and the consistent region 2 slow decay for both the FORT and the MOT.

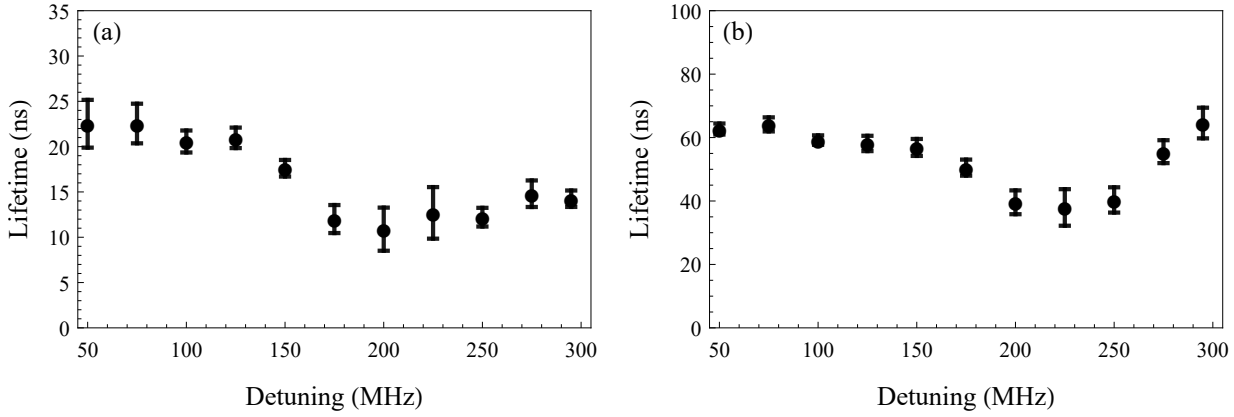

FIG. 78: FORT fluorescence lifetime vs detuning from 52000 probe pulses for (a) region 1 and (b) region 2 associated with the temporal data from Fig. 73. No analyzing polarizer was used. Error bars represent the standard error of the fitting parameter.

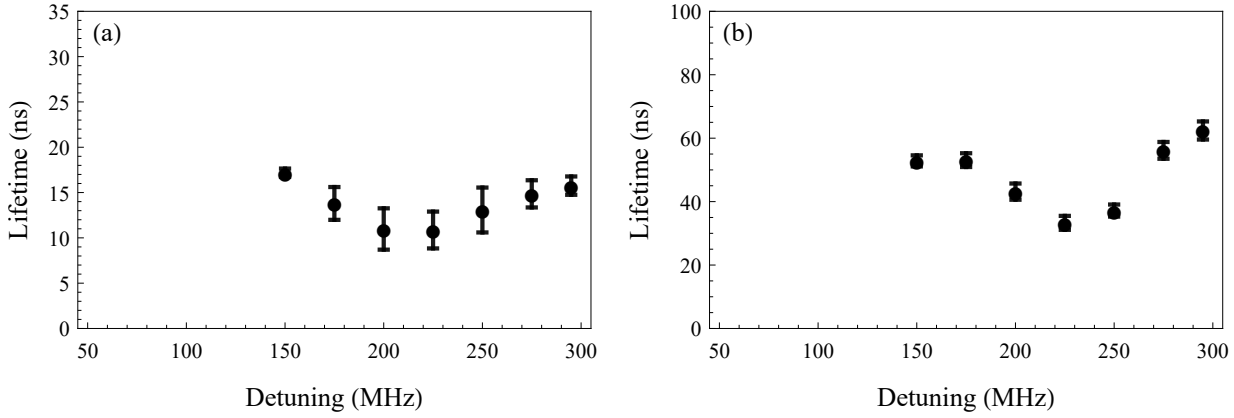

FIG. 79: FORT fluorescence lifetime vs detuning from 208000 probe pulses for (a) region 1 and (b) region 2 associated with the temporal data from Fig. 74. No analyzing polarizer was used. Error bars represent the standard error of the fitting parameter.

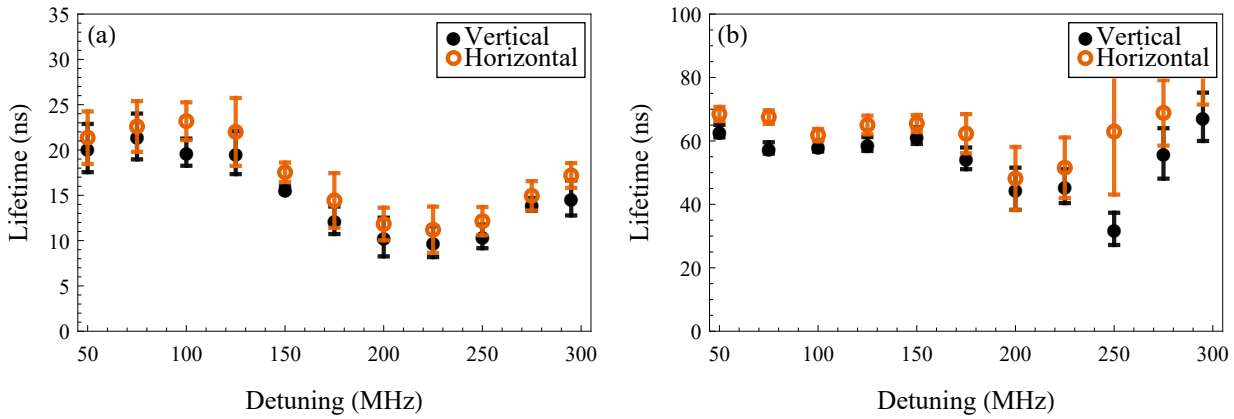

FIG. 80: FORT fluorescence lifetime vs detuning at orthogonal analyzer positions for (a) region 1 and (b) region 2. Data were collected with an analyzing polarizer in the detection channel at 0° (Vertical) and 90° (Horizontal). Error bars represent the standard error of the fitting parameter.

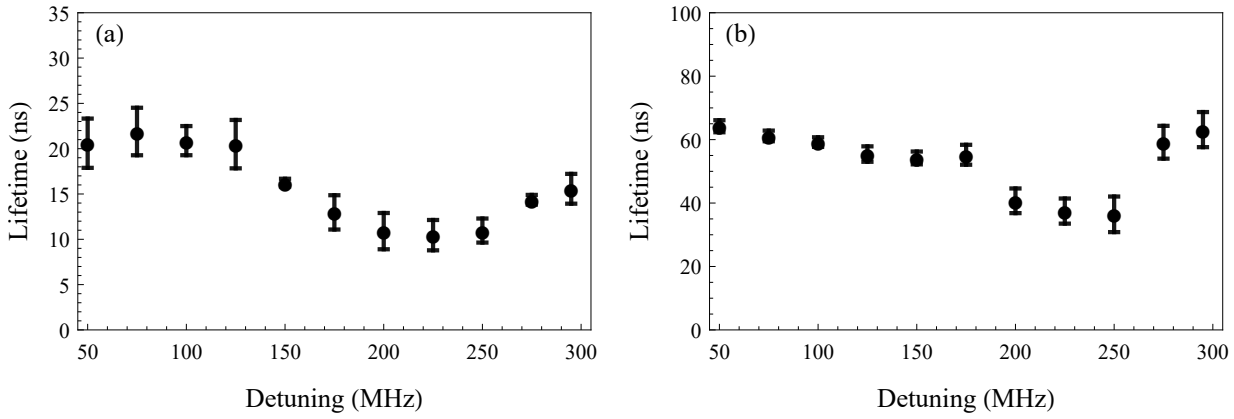

FIG. 81: FORT fluorescence lifetime vs detuning of the combined polarization results for (a) region 1 and (b) region 2. The associated temporal data is shown in Fig. 75. Error bars represent the standard error of the fitting parameter.

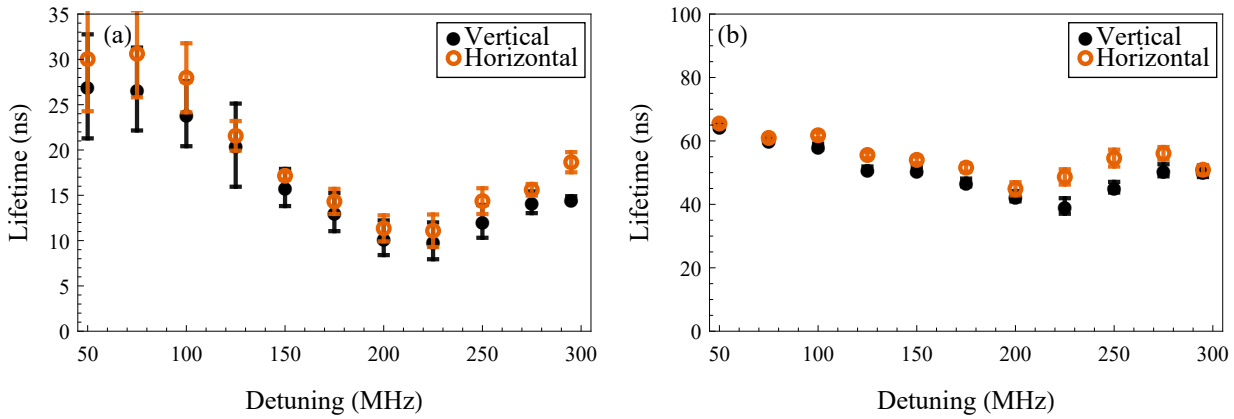

FIG. 82: MOT fluorescence lifetime vs detuning at orthogonal analyzer positions for (a) region 1 and (b) region 2. Data were collected with an analyzing polarizer in the detection channel at 0° (Vertical) and 90° (Horizontal). Error bars represent the standard error of the fitting parameter.

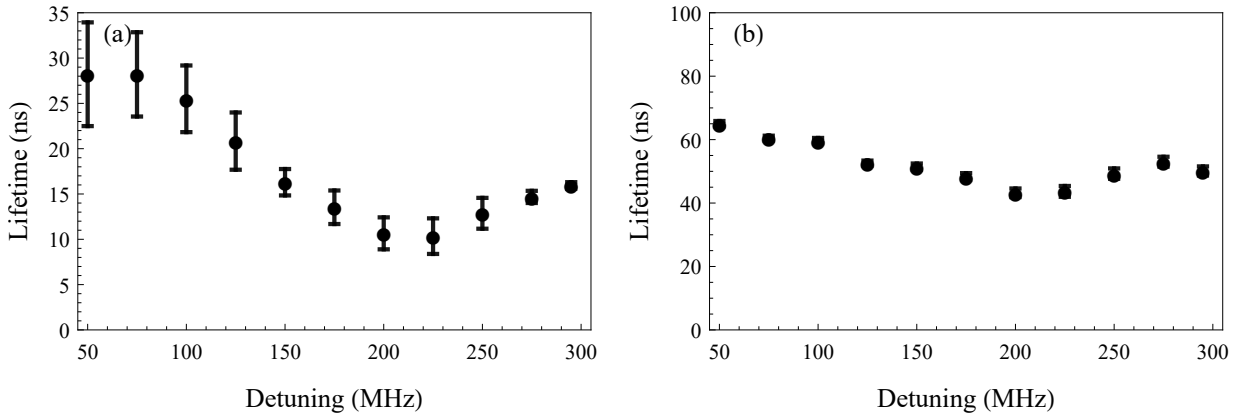

FIG. 83: MOT fluorescence lifetime vs detuning of the combined polarization results for (a) region 1 and (b) region 2. The associated temporal data is shown in Fig. 76. Error bars represent the standard error of the fitting parameter.

Up until this point region 3 has been omitted due to the lack of signal above the noise floor at much larger times for a majority of the datasets. Since only a small handful of

datasets had significant signal above the noise floor in region 3, the lifetimes were combined into one plot and are shown in Fig. 84. Although the region 1 and 2 results were shown to be similar between the FORT and the MOT, region 3 presents a clear separation of decay behavior.

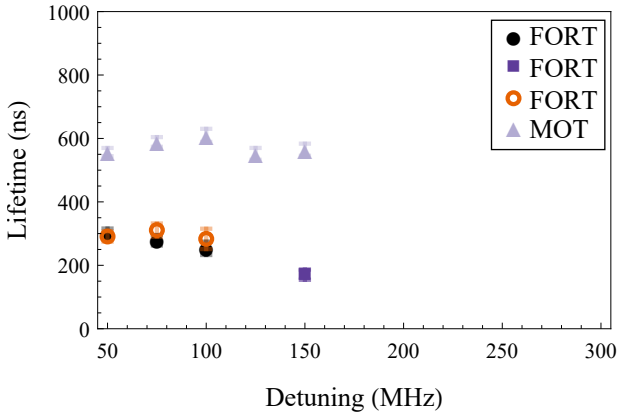

FIG. 84: All region 3 lifetime vs detuning data points. The circle, square, and open circle plot markers are associated with FORT data represented in Figs. 73, 74, and 75 respectively. The triangles are associated with the MOT data from Fig. 76.

5.1.4 TAIL RATIO

The tail ratio is a parameter that was used in previous works to quantify the subradiant behavior of the long-lived tail and is defined as $\int_{4\tau}^{\infty} I(t)dt / \int_{0}^{\infty} I(t)dt$ [26]. This is a ratio of the fluorescence given after $\approx$ 100 ns to the total throughout the process. Although their analysis was only performed near resonance on a FORT after steady state conditions were met, our tail ratio at 50 MHz was found to only differ by $\approx 2\%$ at a similar density. We also present the MOT tail ratio and it can be seen that the ratio follows similar behavior at large detunings with a possible divergence as detuning decreases. The polarization dependent tail ratios are shown in Fig. 86 for both the FORT and the MOT. The behavior is similar to that of the unpolarized tail ratios, the results suggest a possible polarization dependence. Although a full polarization analysis was outside the scope of this dissertation, the presented

tail ratios obtained from the two experimental regimes open a new door of questions for future research.

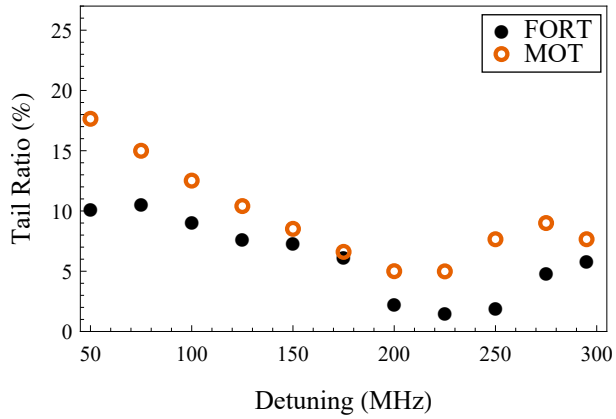

FIG. 85: Tail ratio vs detuning for the FORT (circles) and MOT (open circles). The tail ratio is associated with Figs. 73 and 76 for the FORT and MOT respectively. Error bars are omitted but on the order of 1%.

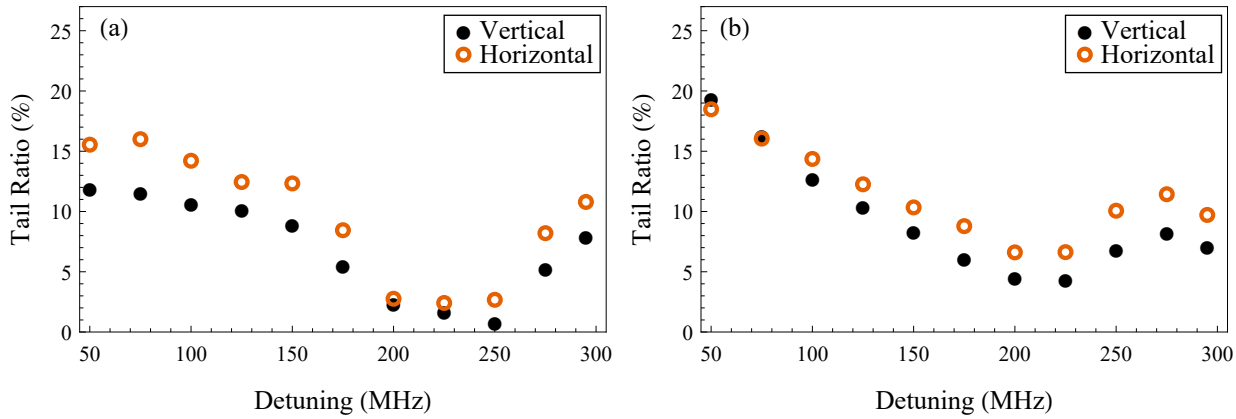

FIG. 86: Polarization dependent tail ratio vs detuning for the (a) FORT and (b) MOT. Circles represent detection of vertically polarized light while open circles represent horizontal. Error bars are omitted but on the order of 1%.

5.2 COUPLED DIPOLE MODEL COMPARISON

The observed temporal signals and spectral dependent decay of the scattered light was shown to exhibit multi-exponential behavior that deviates from the single atom response in the unpolarized and polarized detection channels for both the FORT and the MOT. Decays faster than the natural lifetime, around 225 MHz detuning, of 26.24 ns were found in region 1 for both the FORT and the MOT. Similarly, region 2 decay exhibited longer decay times while still maintaining a feature around 225 MHz detuning.

Decay behavior of many-body systems has been analyzed previously in a MOT [17–21] and FORT [26], where the authors have claimed to observe subradiance from their respective systems, utilized the coupled dipole model. Although there is confidence in the coupled dipole model because it has been shown to be consistent with previous experimental works, it must be noted that the main differences between the aforementioned studies and our experiment is the pulse length and detuning range. The pulse lengths range in previous works from several μs for the MOT and 150 ns for the FORT, which allow the sample to reach steady state conditions before analyzing the decay after the probe was turned off. However, in our experiment, steady state conditions are not achieved with a pulse length of < 5 ns and the radiated field was analyzed during and after probe shut off. The coupled dipole model will now be used to offer an explanation of experimental behavior by analyzing simulated temporal and spectral results.

A simulation was written in Mathematica which numerically solves for the radiated intensity using the framework given in Chapter 2. To ensure consistency with previously published works, results were reproduced under the same conditions and spatial parameters given in [19]. It must be noted that the aforementioned group also includes a so-called exclusion volume where atom pairs separated by a distance $k_0 r \leq 3$ were moved until all atom pairs fulfilled a condition of $k_0 r > 3$. Since rescaling the spatial parameters to achieve the same optical depth with a fewer number of atoms increases the density, the purpose of the exclusion volume was to artificially reduce the amount of strong two-body super and subradiant decay by reducing the density. In an effort to not introduce any bias and to maintain consistency between spatial rescaling in both the MOT and FORT regimes, the exclusion volume procedure will not be used in our analysis. Instead, the rescaling of spatial parameters for both the FORT and the MOT will be performed under regimes of constant optical depth and at constant density to compare with experimental results. It will be shown that, in context to the coupled dipole model, the MOT and FORT behavior follow opposite re-scaling regimes.

Before delving into the temporal decay analysis, a comparison between the coupled dipole model and typical experimental behavior will be examined to provide confidence in the approach. It will be shown that the coupled dipole model predicts four different behaviors that were found to be consistent with experimental data. The first is the peak height of fluorescence comes one MCS bin later at 50 MHz than the data collected at detunings greater than 150 MHz, the second is the total fluorescence as a function of detuning, the third describes the thermal expansion behavior, and finally, and most interesting, the lifetime dip around 200-250 MHz. An example of each of the aforementioned behaviors will be shown. As a reminder this model does not take into account the multi-level structure of the atom, the polarization of the fluorescence, retardation effects, or saturation effects, but offers a guide to the expected overall behavior of the decay. The simulations were performed under the same configuration of probe direction and detection angle as done in the experiment.

5.2.1 SPATIAL RESCALING ANALYSIS

The following discussion will examine several behaviors of the coupled dipole model under constant density and constant optical depth spatial rescaling. The purpose is to determine the significance, if any, between the vastly different geometrical atomic distributions of the FORT and MOT. As a reminder, experimental ensembles cannot be fully simulated due to the computational limitations to the number of atoms. Therefore, a proper rescaling of the spatial parameters must be performed. The rescaled spatial parameters for the FORT that will be used during the following analysis are given in Table 7. Likewise, the rescaled spatial parameters for the MOT are given in Table 8. The first row of values in both tables corresponds to the experimental parameters before rescaling.

TABLE 7: FORT rescaling parameters under constant b_0 and ρ_0.

N	r_0/k_0	z_0/k_0	b_0	ρ_0 (cm^{-3})
4×10^6	20.7043	2021.3	145.016	1.53×10^{14}
10	0.0327	3.196	145.016	9.68×10^{16}
10	0.281	27.4332	1.968	1.53×10^{14}
100	0.1035	10.1065	145.016	3.06×10^{16}
100	0.6054	59.10	4.24	1.53×10^{14}
500	0.23148	22.5988	145.016	1.37×10^{16}
500	1.035	101.065	7.25	1.53×10^{14}
1000	0.32736	31.9595	145.016	9.68×10^{15}
1000	1.30429	127.334	9.135	1.53×10^{14}

TABLE 8: MOT rescaling parameters under constant b_0 and ρ_0.

N	r_0	z_0	b_0	ρ_0 cm^{-3}
7.5×10^7	4026.5	4026.5	6.48	3.8×10^{10}
100	4.65	4.65	6.48	3.3×10^{13}
100	44.32	44.32	0.07	3.8×10^{10}
500	10.4	10.4	6.48	1.48×10^{13}
500	75.78	75.78	0.12	3.8×10^{10}
1000	14.7	14.7	6.48	1.04×10^{13}
1000	95.48	95.48	0.15	3.8×10^{10}

An example of the resulting coupled dipole data in the time domain is shown in Fig. 87 for both constant density and constant optical depth rescaling for the FORT. The temporal data were rebinned to simulate the experimental detection limitations of the MCS. It can be seen that, after the rebinning procedure, the peak is one bin further at 50 MHz than at 200 MHz which mimics the experimental behavior of the FORT. It is also important to note the difference in temporal behavior between the constant density and constant optical depth

signals. Albeit there are similarities with this specific example, it will become clear that the choice of spatial rescaling is vital for predicting experimental behavior.

The total fluorescence as a function of detuning is shown in Fig. 88, where both rescaling regimes follow a very similar trend to that of experimental data from the FORT and MOT. The datasets were normalized to the value at 50 MHz. The important feature shown here is that the total fluorescence reaches a minimum, near 225 MHz, and then begins to increase. Simulations under spatial re-scaling for 500 and 1000 atoms were also performed and produced total fluorescence results consistent to that shown in Fig. 88.

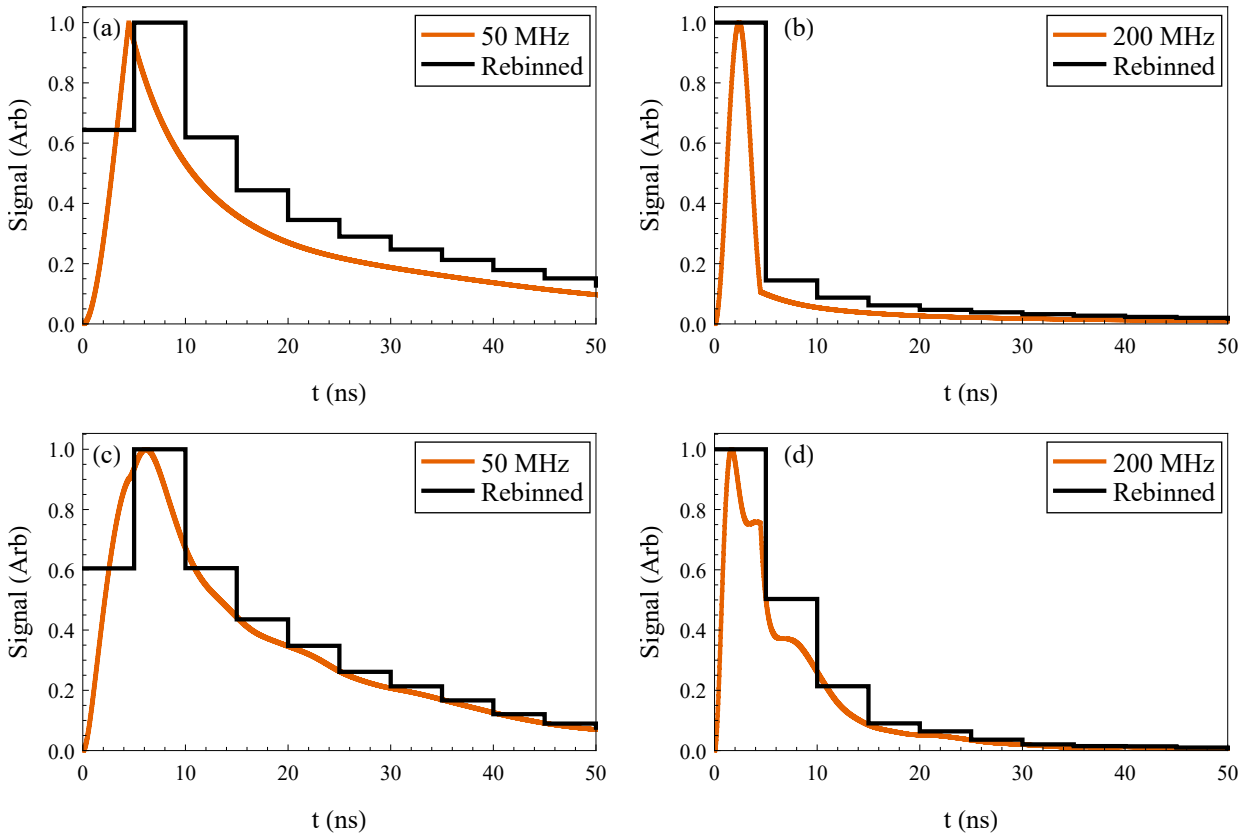

FIG. 87: Time dependent output of the coupled dipole model before and after rebinning. By rebinning the data into 5 ns widths, the peak is shown to be one bin further at 50 MHz than at 200 MHz. (a)-(b) correspond to spatial rescaling of the FORT under constant density where $r_0 = 0.61$ and $z_0 = 59.1$. (c)-(d) correspond to spatial rescaling under constant optical depth where $r_0 = 0.1$ and $z_0 = 10.1$ in units of $1/k_0$. Data averaged over 1000 random ensembles for $N = 100$.

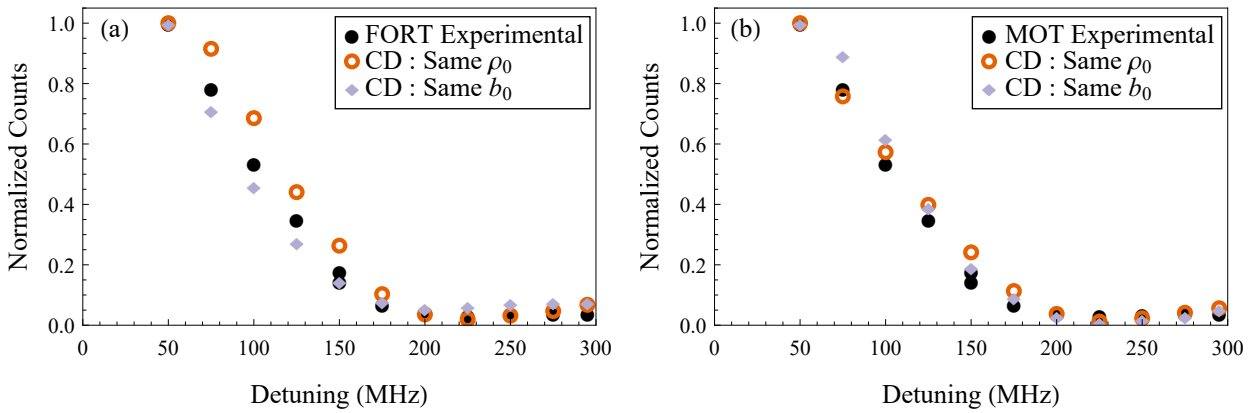

FIG. 88: Total fluorescence as a function of detuning of the coupled dipole model compared to (a) FORT and (b) MOT experimental data. Open circles correspond to spatial rescaling under constant density where $r_0 = 0.61$ and $z_0 = 59.1$ for the FORT and $r_0 = 44.3$ for the MOT. Diamonds correspond rescaling under constant optical depth where $r_0 = 0.1$ and $z_0 = 10.1$ for the FORT and $r_0 = 4.6$ for the MOT in units of $1/k_0$. Data averaged over 1000 random ensembles for $N = 100$. The data were normalized to the value obtained at 50 MHz. The experimental data in (a) corresponds to the FORT data shown in Fig. 73 while (b) corresponds to the MOT data shown in Fig. 76.

Even though the *total* simulated fluorescence from the coupled dipole model was found to be relatively consistent with experimental data, the full temporal behavior was somewhat different between the constant density and optical depth scalings, which an example is shown in Fig. 89 for the FORT and Fig. 90 for the MOT. It can be seen that experimental FORT behavior is modelled well under constant density while the MOT follows constant optical depth scaling. The FORT experiment performed by Ref. [26] analyzed their data using a coupled dipole simulation by keeping the value $\rho_0/k^3 = 0.3$ constant, which is the same as keeping density constant, for $N = 200$. Their result provides confidence, although their experiment involves different detection angles, pulse length, and detuning, that the coupled dipole model under constant density scaling captures the expected behavior of the FORT. On the other hand, the MOT experiments performed by Refs. [17–19] kept the optical depth constant in their simulations, which was also consistent with our MOT results. This apparent dichotomy may be attributed to the vastly different trap geometries and density of atomic pairs, but more work would have to be done to investigate and determine exactly

why the rescaling regime differs between the FORT and the MOT.

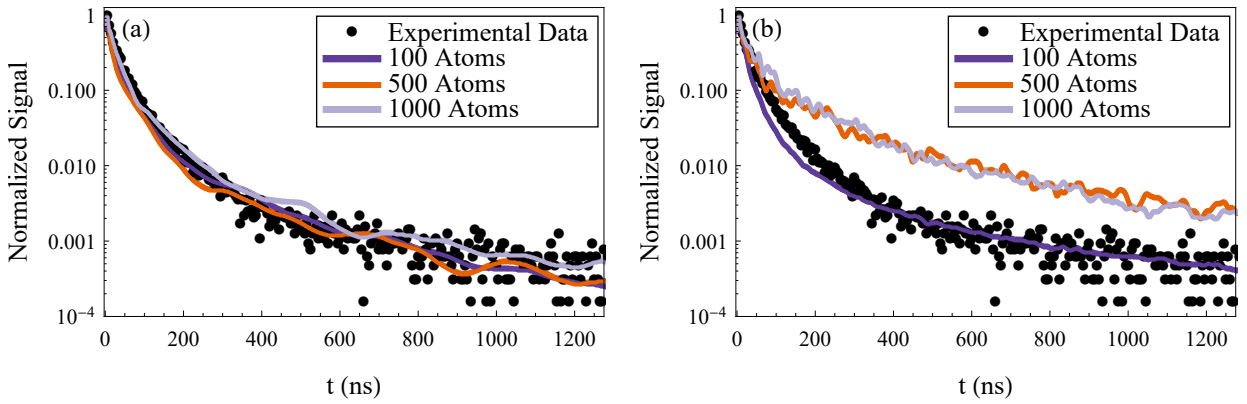

FIG. 89: Coupled dipole model temporal result under FORT rescaling with $N = 100$, 500, and 1000 at 50 MHz detuning. (a) corresponds to rescaling at constant density while (b) corresponds to constant optical depth. Experimental data corresponds Fig. 73 at 50 MHz.

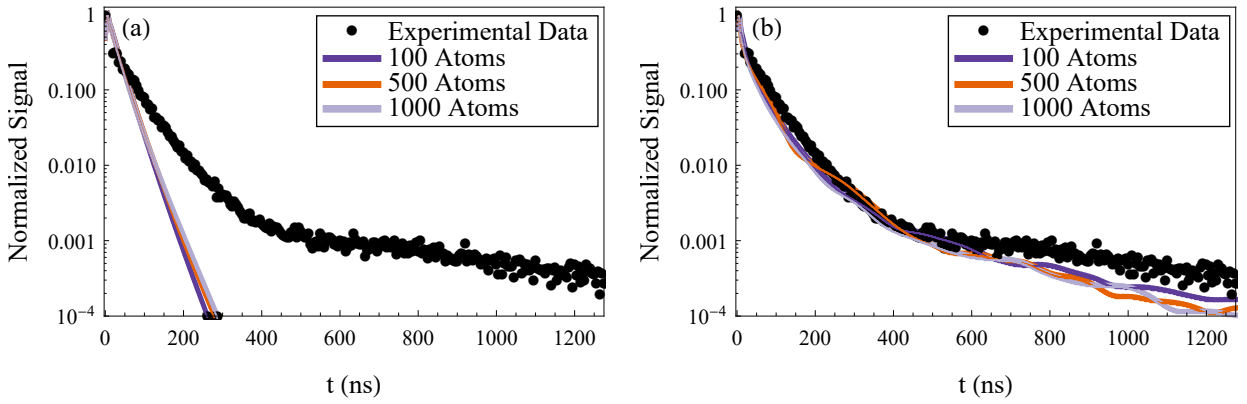

FIG. 90: Coupled dipole model temporal result under MOT rescaling with $N = 100$, 500, and 1000 at 50 MHz detuning. (a) corresponds to rescaling at constant density while (b) corresponds to constant optical depth. Experimental data corresponds Fig. 76 at 50 MHz.

Further evidence of density scaling for the FORT can be seen by simulating the effect of thermal expansion. The spatial parameters were recalculated for the FORT after 1 ms of expansion at 138 μK in both rescaling regimes and is shown in Fig. 91 with comparison to experimental data. The constant density rescaling continues to describe FORT behavior.

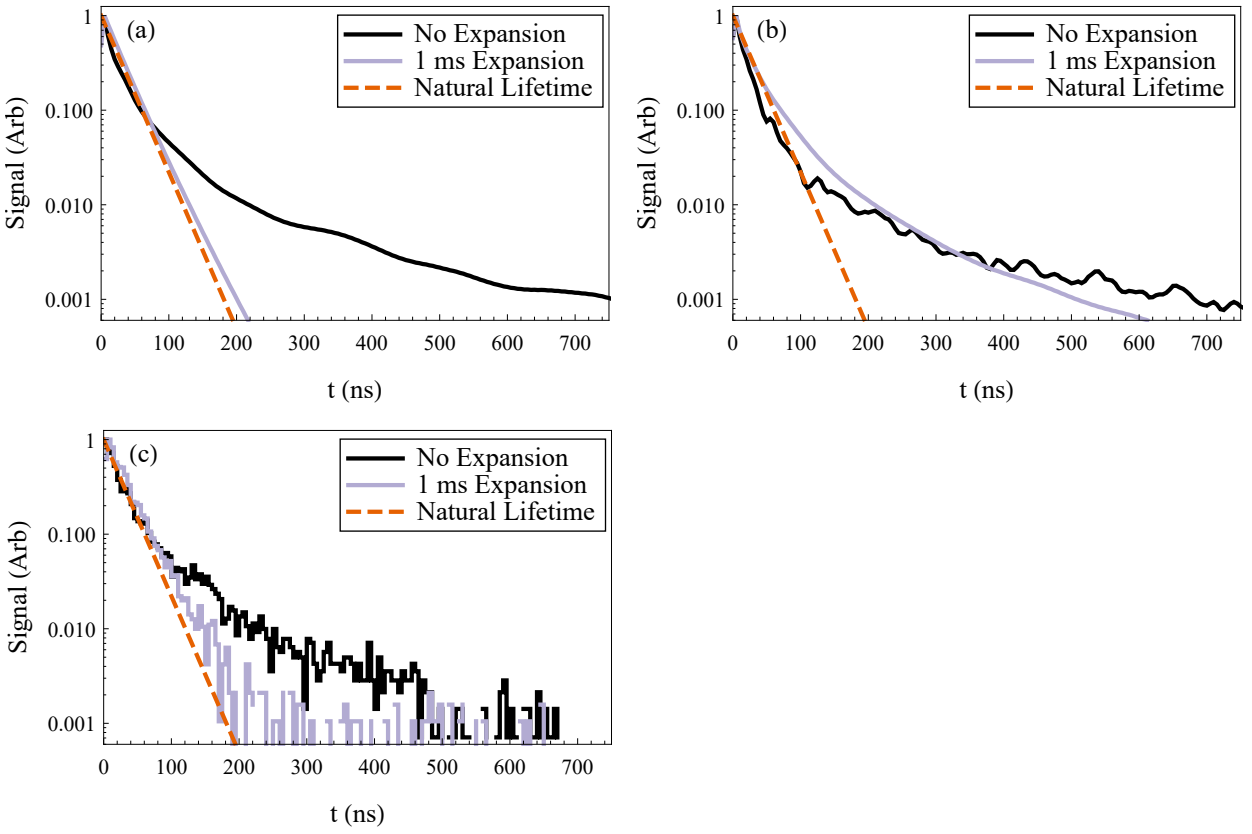

FIG. 91: Comparison of the decay behavior of the FORT before and after 1 ms of expansion time at 138 μK. The detuning is 50 MHz. (a) corresponds the coupled dipole model at constant density while (b) corresponds to constant optical depth. (c) is experimental data taken at the same expansion times and agrees with the constant density scaling results shown in (a). The coupled dipole result was obtained from a simulation with $N = 100$ scaling and averaged over 100 random ensembles. The dashed red line is the single atom lifetime.

As of now, it has been shown that the coupled dipole model results agree with our experimental data and previous works under their respective rescaling regimes. With that in mind, the detuning dependent temporal decay behavior of the coupled dipole model will be presented for both rescaling regimes.

5.2.2 LIFETIME MEASUREMENTS

The extraction of the lifetimes from the coupled dipole temporal data will now be presented. The fitting procedure was the same as for the experimental data. In an effort to maintain consistency during the comparison of simulated data to experimental, the simulated data will be fit using the same bins that were used to fit experimental data and the corresponding datasets will be noted. This also applies to region 3 when applicable, otherwise the fit was performed after the last bin in region 2 until bin 200. Although it was previously determined that the FORT and MOT follow constant density and constant optical depth rescaling respectively, the extracted lifetimes for both regimes will be presented.

Coupled dipole fit results for the FORT associated with the same regions and bins as that were used for Fig. 78 is shown in Fig. 92 for constant density and Fig. 93 for constant optical depth. The legend in Fig. 92 applies for all lifetime measurement figures throughout this section. Similarly, the extracted lifetimes associated with the FORT data in Fig. 79 is given in Fig. 94 for constant density and Fig. 95 for constant optical depth. Finally, the extracted lifetimes associated with the MOT data in Fig. 83 is given in Fig. 96 for constant density and Fig. 97 for constant optical depth.

It is clear to see that the extracted lifetimes of the simulation under FORT conditions and constant density rescaling qualitatively agree with experimental results in all 3 regions. Although the dip in lifetime in region 1 is apparent even for the constant optical depth case, region 2 lifetimes are inconsistent for different atom numbers. Likewise, results are similar for the MOT but under constant optical depth rescaling. Again, the region 1 dip in lifetime occurs in both regimes but the region 2 behavior converges to the natural lifetime under constant density. These results provide further evidence that the coupled dipole model qualitatively describes experimental FORT and MOT behavior under their respective rescaling regimes.

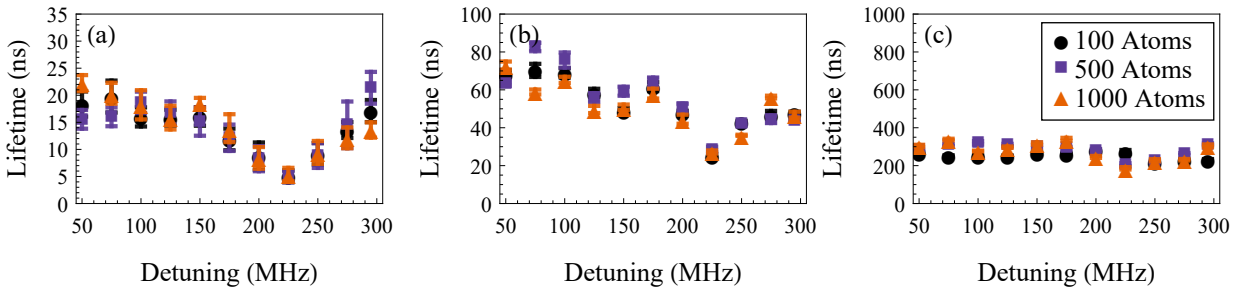

FIG. 92: Constant density rescaled couple dipole model fluorescence lifetime vs detuning under the same fitting conditions to that of FORT given in Fig. 78. (a), (b), (c), represent regions 1, 2, and 3 respectively. Error bars represent the standard error of the fitting parameter.

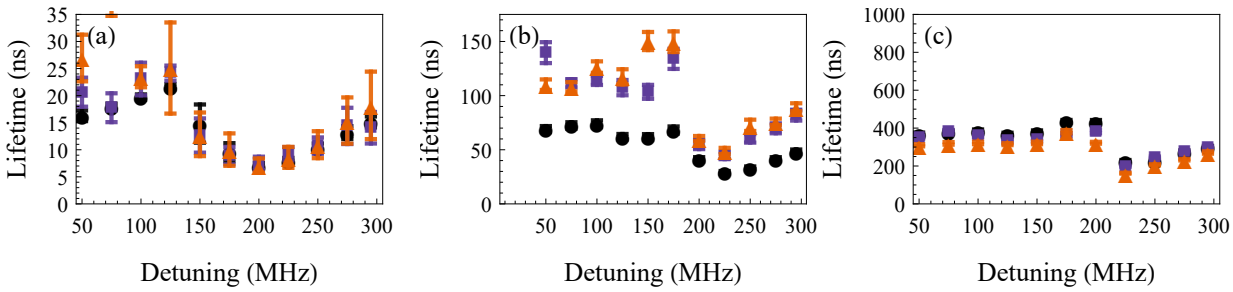

FIG. 93: Constant optical depth rescaled couple dipole model fluorescence lifetime vs detuning under the same fitting conditions to that of FORT given in Fig. 78. (a), (b), (c), represent regions 1, 2, and 3 respectively. Error bars represent the standard error of the fitting parameter.

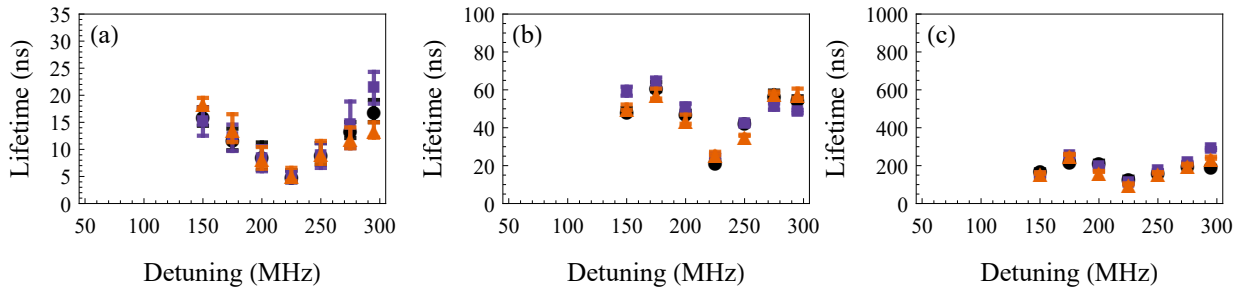

FIG. 94: Constant density rescaled couple dipole model fluorescence lifetime vs detuning under the same fitting conditions to that of FORT given in Fig. 79. (a), (b), (c), represent regions 1, 2, and 3 respectively. Error bars represent the standard error of the fitting parameter.

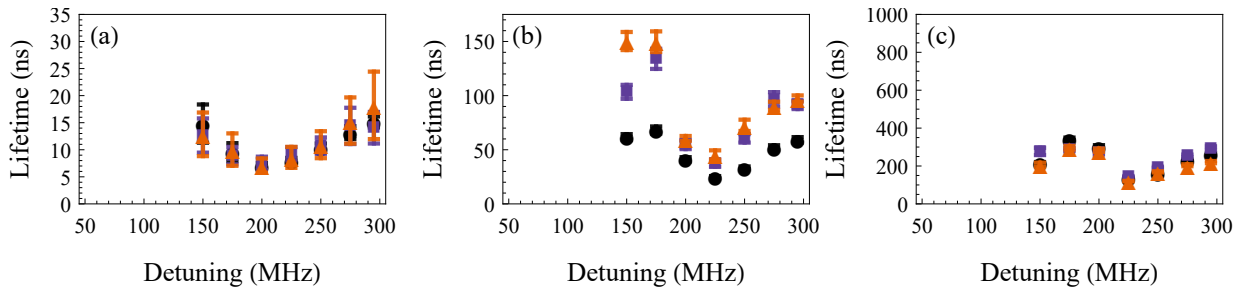

FIG. 95: Constant optical depth rescaled couple dipole model fluorescence lifetime vs detuning under the same fitting conditions to that of FORT given in Fig. 79. (a), (b), (c), represent regions 1, 2, and 3 respectively. Error bars represent the standard error of the fitting parameter.

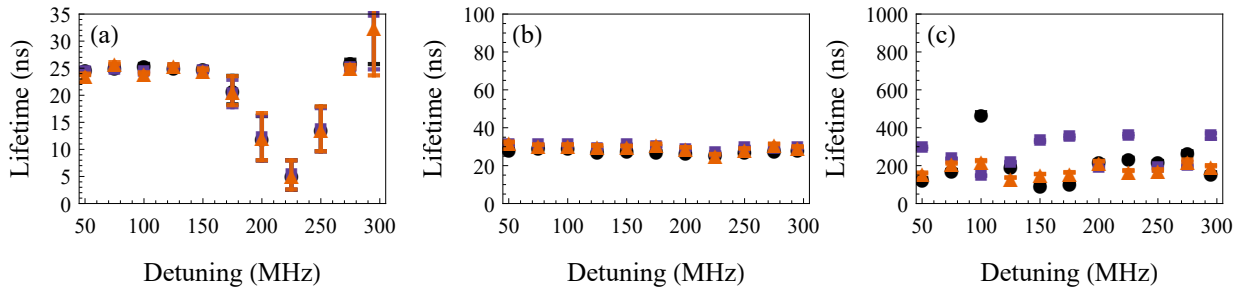

FIG. 96: Constant density rescaled couple dipole model fluorescence lifetime vs detuning under the same fitting conditions to that of MOT given in Fig. 83. (a), (b), (c), represent regions 1, 2, and 3 respectively. Error bars represent the standard error of the fitting parameter.

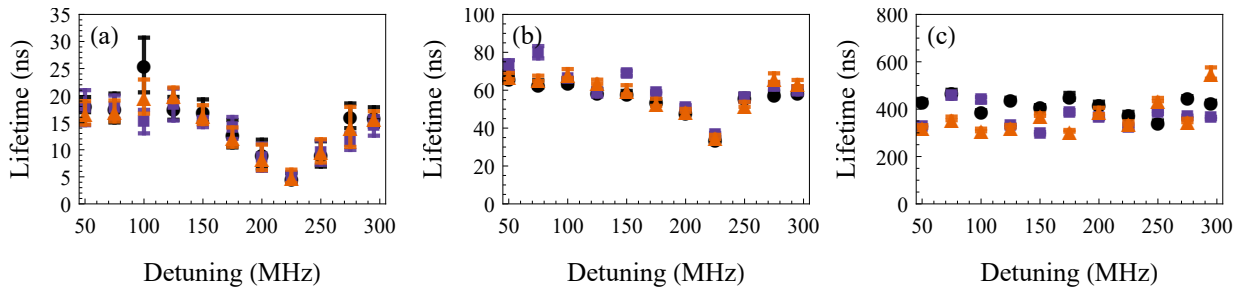

FIG. 97: Constant optical depth couple dipole model fluorescence lifetime vs detuning under the same fitting conditions to that of MOT given in Fig. 83. (a), (b), (c), represent regions 1, 2, and 3 respectively. Error bars represent the standard error of the fitting parameter.

Another interesting result emerges if one ignores the experimental regions and examines the long-lived behavior predicted by the coupled dipole model far beyond the noise floor. Two new fitting regions, defined temporally between 21-57 τ (550-1500 ns) and 57-190 τ (1500-5000 ns) respectively, were fit and the results are shown in Fig. 98. This result defies the claim that there should be no detuning dependence of the long-lived tail, albeit the claim was made under the assumption of a system in steady state. Under our experimental conditions, where the pulse length is associated to a minimum in the intensity oscillation

around 225 MHz, the long-lived lifetimes are predicted to diverge from constant behavior. Although the lifetimes are much longer at 225 MHz the amplitude of the signal is several orders of magnitude smaller, essentially offering a means to suppress long-lived signals with a detuned probe and specific pulse lengths.

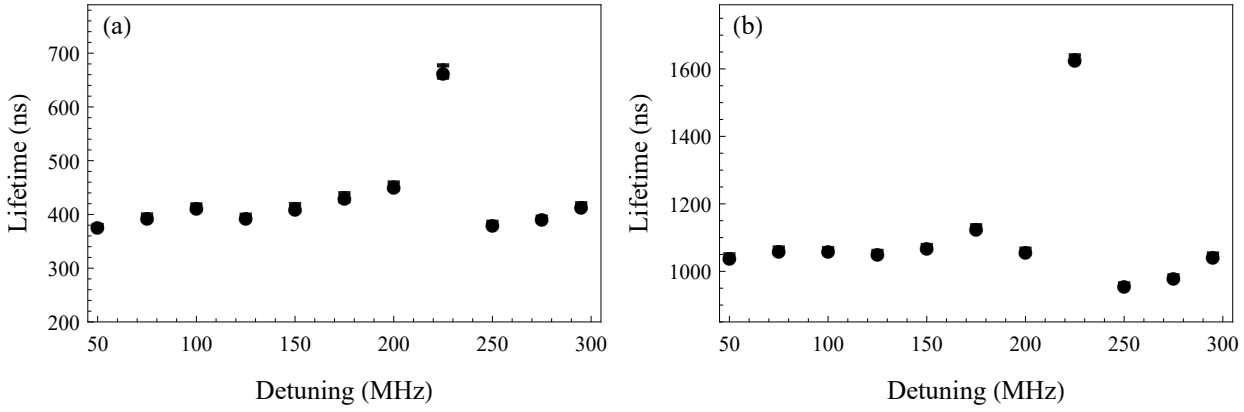

FIG. 98: Coupled dipole model fluorescence lifetime vs detuning for timescales outside of experimental detection capabilities. Rescaling was performed for constant density to that of FORT for $N = 100$. (a) represents the decay between 21-57 τ (550-1500 ns) while (b) corresponds to 57-190 τ (1500-5000 ns).

5.2.3 TAIL RATIO

The tail ratio, as defined in the experimental data section, for the simulated coupled dipole data is presented in Fig. 99. The exact procedure which was used to calculate the experimental tail ratio was used on the associated simulated datasets. The tail ratio for the simulation data shows good consistency with experimental results for the FORT. The simulated MOT data differs from the experimental results by $\approx 5\%$ for the detunings closer to resonance while showing consistency at larger detunings.

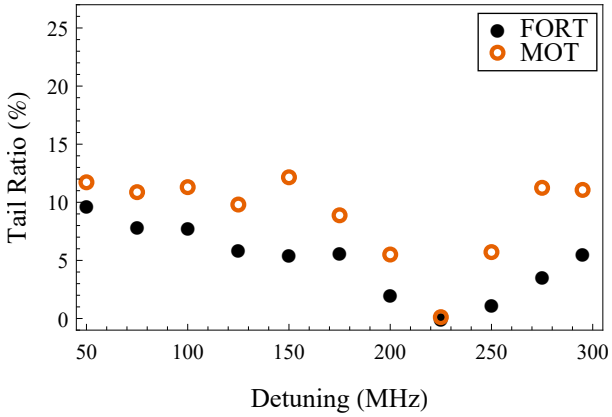

FIG. 99: Coupled dipole model tail ratio vs detuning for the FORT (circles) and MOT (open circles). The FORT simulation was performed under constant density rescaling while the MOT was performed under constant optical depth. Values were obtained using the same number of bins that were used for the experimental data shown in Fig. 85.

5.2.4 SINGLE ATOM COMPARISON

The last comparison that will be made will be against the optical Bloch equations to directly show single atom behavior. As the coupled dipole model is essentially a multi-body optical Bloch equation, one would expect similarities and differences that arise can be attributed to multi-body physics. Comparing the outputs between the coupled dipole model and optical Bloch equations are shown in Fig. 100 for detunings of 50 and 200 MHz. The coupled dipole signal corresponds to constant density rescaling of the FORT with $N = 100$. It is clear to see that the cooperative behavior of the coupled dipole model diverges to that of a single atom. Not only does the coupled dipole model exhibit much longer lived behavior, there is an amplitude enhancement at short times. To go along with this, the optical Bloch data were rebinned in the same way as the coupled dipole data, and then fit to the same three regions associated with experimental FORT data given in Fig. 73. The lifetimes associated with the three regions are shown in Fig. 101. It can be seen that the region 1 decay behaves similarly around a detuning of 225 MHz where the probe shuts off at a minimum of an oscillation. Region 2 and 3 however show the expected single atom natural lifetime result for all detunings. With this in mind, it is clear that the experimental results show behavior far from single atom dynamics.

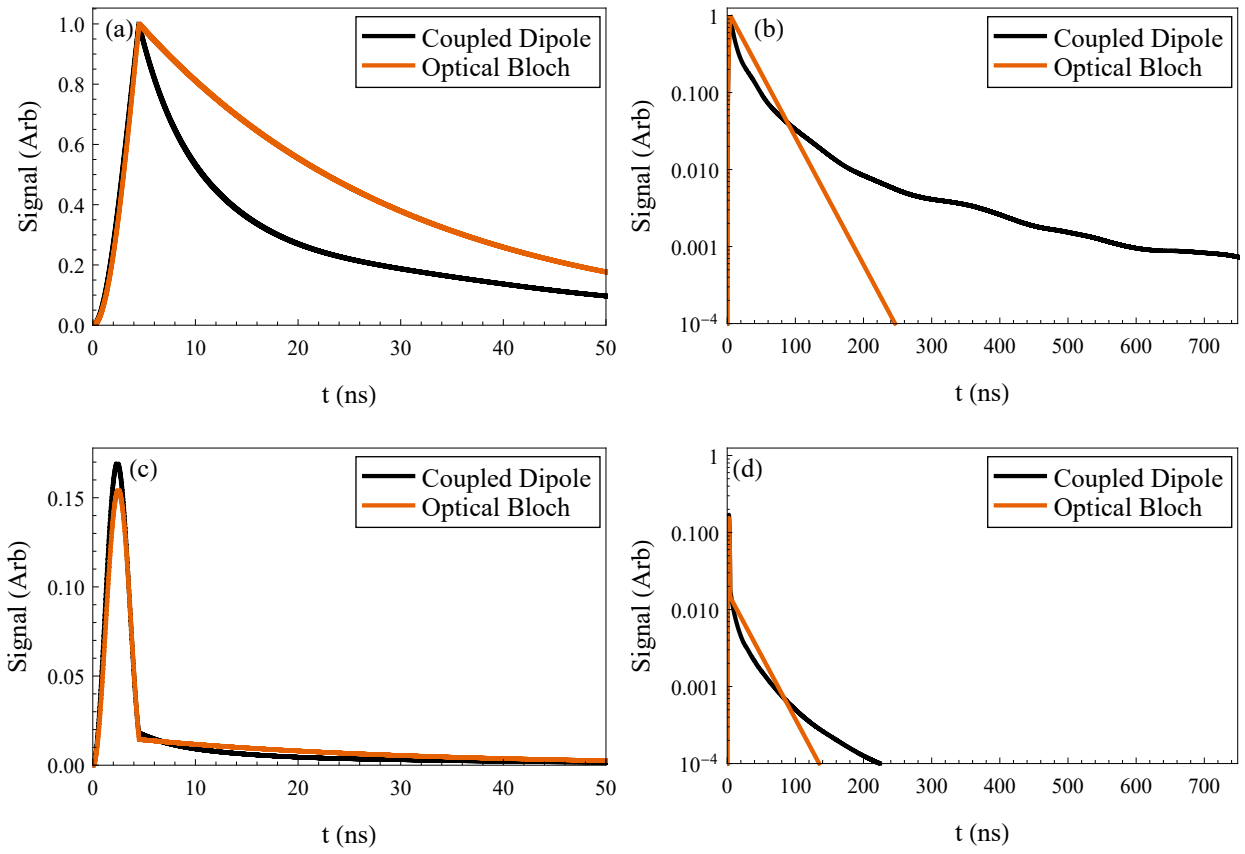

FIG. 100: Signal comparison between the coupled dipole model and the single atom optical Bloch solution. (a)-(b) correspond to 50 MHz detuning where (b) is the log plot of the data with an extended time scale. (c)-(d) correspond to 200 MHz detuning where (d) is the log plot of the data. The coupled dipole data corresponds to constant density rescaling of the FORT at $N = 100$.

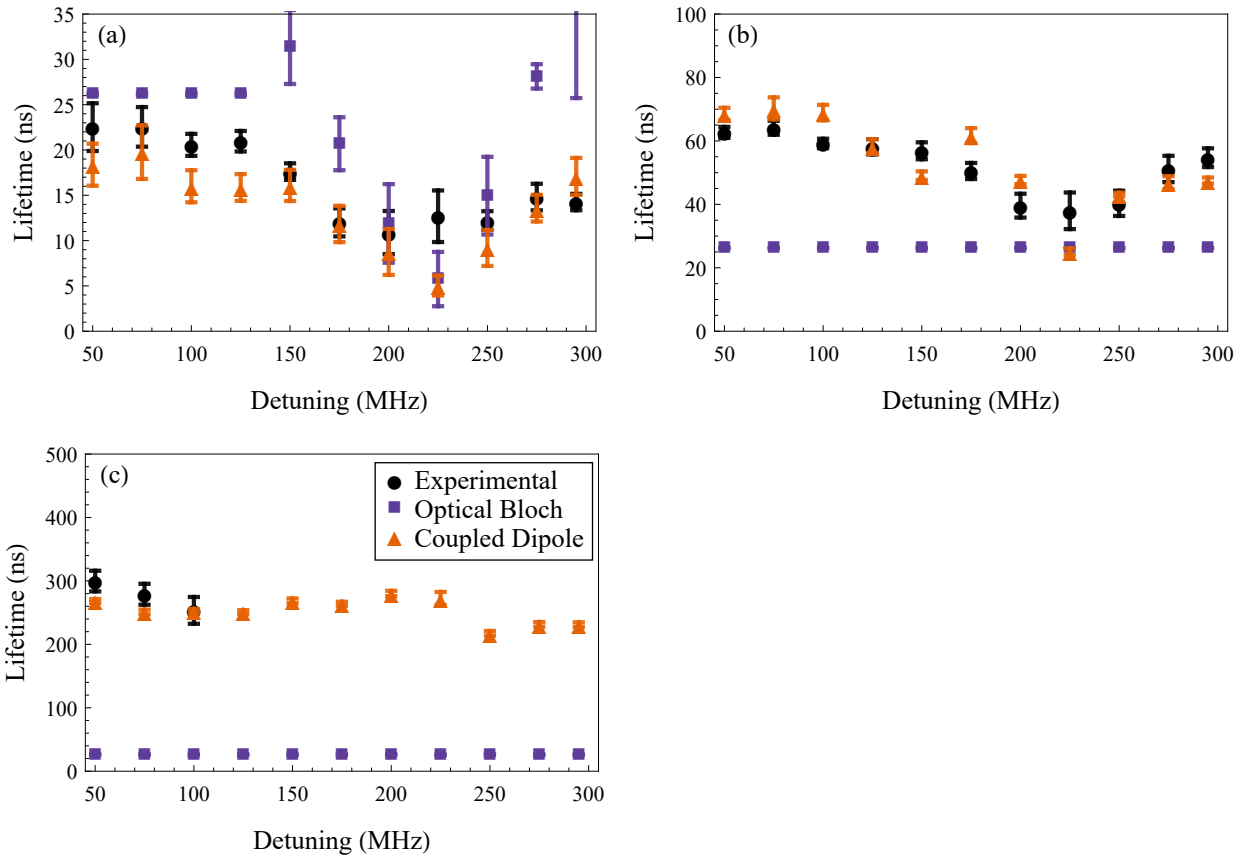

FIG. 101: Fluorescence lifetime vs detuning calculated from the optical Bloch equations compared to the coupled dipole model and experimental data. (a), (b), and (c), represent regions 1, 2, and 3 respectively. The optical Bloch lifetimes in regions 2 and 3 are all exactly the natural lifetime. The coupled dipole data is associated with the lifetimes given in Fig. 92 for $N = 100$. Error bars represent the standard error of the fitting parameter.

5.3 DISCUSSIONS

This section will start with further discussion of the coupled dipole model and offer a qualitative explanation for why a detuning dependent result, within the parameters of the experiment, should be expected. Then the possible significance of the polarization of the scattered light will be discussed.

The coupled dipole model has been shown to qualitatively reproduce experimental temporal and spectral decay dynamics, therefore it will continue to be used to offer a rather

straightforward explanation as to why a detuning dependence in the lifetime results should be expected. A example of the temporal behavior of the radiated fluorescence is shown in Fig. 102 for three different detunings and under constant density rescaling for the FORT. The dashed lines represent the behavior if the probe pulse was left on, while the solid lines represent experimental probe shut off conditions. It can be seen that the probe was shut off where the minimum occurs at 225 MHz. Therefore, almost all of the fluorescence will be radiated within the first oscillation and very little afterwards. Applying the previously mentioned rebinning procedure to the coupled dipole model, that was shown in Fig. 87, clearly demonstrates why a shorter lifetime would be extracted for a probe duration at a detuning associated with a minimum of an oscillation. Although this was consistent with experimental data, the oscillatory behavior was outside the capabilities of our apparatus to observe since the MCS is limited to 5 ns bins.

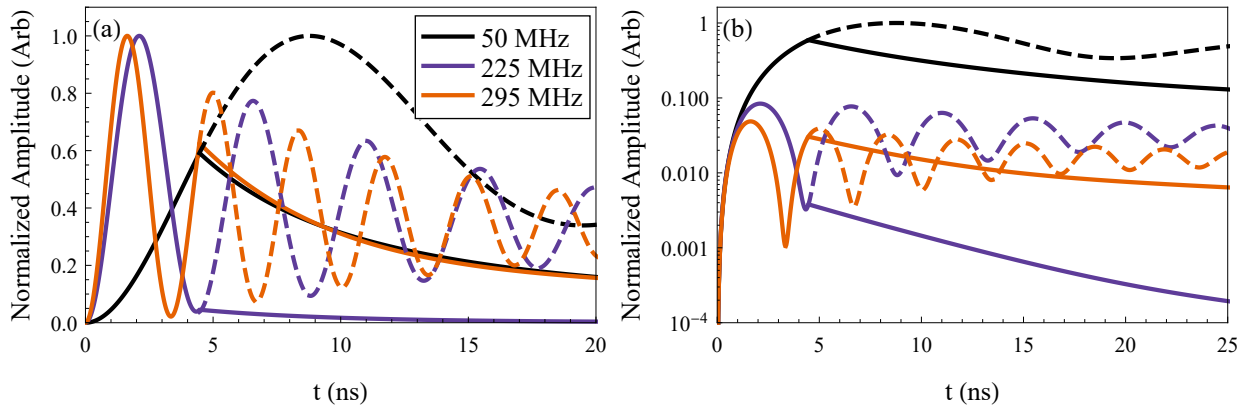

FIG. 102: Time dependent output of the coupled dipole model at various detunings. The solid line represents the fluorescence due to the short pulse while the dashed lines represent the behavior if the driving pulse were left on. (a) is normalized to the maximum of the first peak at each detuning for illustrative purposes. (b) represents the log plot of the same data in (a) where the normalization is to the max value of the 50 MHz peak. The legend corresponds to both plots. Data averaged over 100 random ensembles for $N = 100$. The simulation was performed under rescaled spatial parameters, where $r_0 = 0.605$ and $z_0 = 59.10$, in order to keep ρ_0 the same the experimental conditions.

In summary, experimental region 1 decay lifetimes were found to be shorter than the natural lifetime with a spectral feature associated with the length of the pulse. Region 2 decays were found to be around 2.3 - 2.7 times longer than the natural lifetime, which is in line with the average decay time of $\approx 3\ \tau$ found in a similar FORT system [26]. Region 3 decays, although limited due to signal size, were found to be 7.5-11.5 times longer than the natural lifetime for the FORT and 21-23 τ for the MOT. Therefore, it can be said that region 1 can be associated with superradiant modes, region 2 as a collection of many shorter lived subradiant modes that decay slower than the natural lifetime, and region 3 as the longest lived subradiant modes [70]. With reference to the temporal data shown in Fig. 68(b), it can be seen that the region 2 behavior is not necessarily modeled by a single exponential, which aligns aforementioned interpretation of many shorter subradiant modes decaying at intermediate times. Although the coupled dipole model predicts subradiant behavior for all detunings, the amplitude of the expected signal was below the noise floor of much of the experimental detuning regime.

One of the more important pieces of evidence of cooperative subradiance was found while analyzing the polarization dependence. It was shown that the dynamic behavior of the scattered light carried no distinguishable polarization dependence, for a linearly polarized probe pulse, in all fitting regions. Although the decay behavior did not change between detection channels, the amount of total fluorescence did, which means that the scattered light was not completely depolarized. The change in amplitude between detection channels was expected and shown in Fig. 70(a) of the preliminary experimental section. Furthermore, the polarization degree of the scattered light at later times was shown to strongly suggest that the subradiant effect cannot be completely attributed to multiple scattering. This result is in contrast to the Guerin *et al.* [27] interpretation that subradiance can be completely explained by multiple scattering. The significance of a long-lived cooperative decay that continues to hold onto information, e.g., the polarization of the probe, may provide an avenue for the production of quantum memories. Continued exploration of the polarization dependence may lead to better understanding on how to decouple multiple scattering from cooperative decay.

CHAPTER 6

CONCLUSIONS

The behavior associated with many-body interactions from a cooled atomic ensemble of ^{87}Rb during and after a blue-detuned short laser pulse were investigated in this dissertation. Temporal fluorescence measurements exhibited multi-exponential decay behavior typically involving an initially fast decay followed by a much slower decay, with respect to the natural lifetime. The detuning dependent measurements showed a decrease in the initial lifetime at and around 225 MHz which was found to be associated with the length of the pulse and the effective Rabi frequency. The experimental results were explained and replicated using the coupled dipole model. Although the initial oscillatory behavior was found to be similar to the single atom optical Bloch solutions, the coupled dipole model painted a more detailed picture of the cooperative decay dynamics at later times. The rescaling of spatial parameters was found to be dependent on density for the FORT and optical depth for the MOT, which was found to be consistent with previous experiments in the same regime by other research groups. The polarization degree measurements provided evidence that the long lived behavior cannot be entirely explained by multiple scattering. Although recent advancements in theory have significantly aided in understanding the behavior of many-body cooperative systems, much more work must be done to fully understand the complex intertwining of dynamic effects that occur. Beyond the theoretical improvements that need to occur, computational methods must also improve and evolve to meet the requirements of a more complex model.

Expertise in a plethora of laboratory instrumentation was required in order to perform the experiments described. Precision timing between several control systems was required to create the atomic samples, introduce a fast pulse, detect the scattered light, and acquire data in a consistent systematic manner. Several control programs were written to monitor, acquire data, and provide instruction for the experimental apparatus. Temperature stabilization of the fast pulse generating EOM exponentially increased the ability to run the experiment uninterrupted for several hours. With the introduction of the many apparatus improvements, it was made possible to run the experiment completely hands free.

The experimental ensembles were created using optical forces to cool and trap atoms. A MOT was used to initially cool and confine the atoms before loading into a FORT. The

MOT utilizes radiation pressure and magnetic field gradients to confine and cool a dilute cloud of ^{87}Rb atoms to ≈ 100 μK. The FORT however, takes advantage of the dipole force to substantially increase the confinement of the sample while reducing the scattering rate. The spatial characteristics of the samples were calculated and measured experimentally using techniques such as parametric resonance and ballistic expansion while the number of atoms were determined by optical pumping.

An aside was presented where experimental data for the optical pumping atom number technique was shown over a large range of parameters. Detuning-dependent results were modelled with a simulation that included depumping effects that lead to over-counting due to multiple scattering. A phenomenological explanation was given that scaled with optical depth and agreed with experimental and simulation results within the explored parameter space. Further investigation into multiple scattering during the optical pumping process, both experimentally and theoretically, will be needed to offer a full, clear, and concise picture of the complex dynamics.

An interesting future endeavour of continued study would be to characterize the subradiant behavior in a geometry where the optical depth and density rescaling regimes are equivalent within the coupled dipole model. If such a regime is fragile, the behavior of the subradiant decay could be used as a type of precision sensor. Single photon production may also be an avenue of continued exploration. A single photon source has been created by [103] utilizing an intense, on resonant, short pulse which causes intensity dependent Rabi oscillations. We have shown that in the weak field regime, at a detuning frequency corresponding to the length of the pulse, similar effective Rabi oscillations occur. Not only does all of the excitation happen within the first oscillation, the resulting long lived portion was shown to be suppressed. Therefore, our work provides the groundwork to explore single photon production simply by detuning the laser rather than increasing the intensity. Another intriguing prospect for future research would be to analyze superradiance, not in the forward direction, but in the reflected lobe that was depicted in Fig. 6(c). Collecting superradiance off axis would eliminate the many pitfalls that plague forward scattering experiments.

BIBLIOGRAPHY

[1] R. H. Dicke, Phys. Rev. **93**, 99 (1954).

[2] D. C. Burnham and R. Y. Chiao, Phys. Rev. **188**, 667 (1969).

[3] R. Friedberg, S. R. Hartmann, and J. T. Manassah, Physics Reports **7**, 101 (1973).

[4] M. Gross and S. Haroche, Physics Reports **93**, 301 (1982).

[5] S. Prasad and R. J. Glauber, Phys. Rev. A **61**, 063814 (2000).

[6] S. Roof, Ph.D. thesis, Old Dominion University, 2016.

[7] S. J. Roof, K. J. Kemp, M. D. Havey, and I. M. Sokolov, Phys. Rev. Lett. **117**, 073003 (2016).

[8] P. Solano, P. Barberis-Blostein, F. K. Fatemi, L. A. Orozco, and S. L. Rolston, Nature Communications **8**, 1857 (2017).

[9] Z. Yan, J. Ho, Y. H. Lu, S. J. Masson, A. Asenjo-Garcia, and D. M. Stamper-Kurn, Phys. Rev. Lett. **131**, 253603 (2023).

[10] O. Rubies-Bigorda, S. Ostermann, and S. F. Yelin, Phys. Rev. Research **5**, 013091 (2023).

[11] D. Pavolini, A. Crubellier, P. Pillet, L. Cabaret, and S. Liberman, Phys. Rev. Lett. **54**, 1917 (1985).

[12] T. Bienaimé, N. Piovella, and R. Kaiser, Phys. Rev. Lett. **108**, 123602 (2012).

[13] Y. Takasu, Y. Saito, Y. Takahashi, M. Borkowski, R. Ciuryło, and P. S. Julienne, Phys. Rev. Lett. **108**, 173002 (2012).

[14] M. O. Scully, Phys. Rev. Lett. **115**, 243602 (2015).

[15] B. H. McGuyer, M. McDonald, G. Z. Iwata, M. G. Tarallo, W. Skomorowski, R. Moszynski, and T. Zelevinsky, Nature Physics **11**, 32 (2015).

[16] G. Facchinetti, S. D. Jenkins, and J. Ruostekoski, Phys. Rev. Lett. **117**, 243601 (2016).

[17] W. Guerin, M. O. Araújo, and R. Kaiser, Phys. Rev. Lett. **116**, 083601 (2016).

[18] W. Guerin, M. T. Rouabah, and R. Kaiser, J. Mod. Opt. **64**, 895 (2017).

[19] M. O. Araújo, W. Guerin, and R. Kaiser, J. Mod. Opt. **65**, 1345 (2018).

[20] P. Weiss, M. O. Araújo, R. Kaiser, and W. Guerin, New J. Phys. **20**, 063024 (2018).

[21] P. Weiss, A. Cipris, M. O. Araújo, R. Kaiser, and W. Guerin, Phys. Rev. A **100**, 033833 (2019).

[22] D. Das, B. Lemberger, and D. D. Yavuz, Phys. Rev. A **102**, 043708 (2020).

[23] J. Rui, D. Wei, A. Rubio-Abadal, S. Hollerith, J. Zeiher, D. M. Stamper-Kurn, C. Gross, and I. Bloch, Nature **583**, 369 (2020).

[24] Y. A. Fofanov, I. M. Sokolov, R. Kaiser, and W. Guerin, Phys. Rev. A **104**, 023705 (2021).

[25] A. Cipris, N. A. Moreira, T. S. do Espirito Santo, P. Weiss, C. J. Villas-Boas, R. Kaiser, W. Guerin, and R. Bachelard, Phys. Rev. Lett. **126**, 103604 (2021).

[26] G. Ferioli, A. Glicenstein, L. Henriet, I. Ferrier-Barbut, and A. Browaeys, Phys. Rev. X **11**, 21031 (2021).

[27] W. Guerin, Adv. At. Mol. Phys. **72**, 253 (2023).

[28] E. Akkermans, P. E. Wolf, and R. Maynard, Phys. Rev. Lett. **56**, 1471 (1986).

[29] E. Akkermans and G. Montambaux, *Mesoscopic Physics of Electrons and Photons* (Cambridge University Press, 2007).

[30] C. Miniatura, G. Labeyrie, C. Muller, J.-C. Bernard, and R. Kaiser, in *Conference Digest. 2000 International Quantum Electronics Conference (Cat. No.00TH8504), Nice, France,* (2000) pp. 672–685.

[31] G. Labeyrie, D. Delande, C. A. Müller, C. Miniatura, and R. Kaiser, Europhys. Lett. **61**, 327 (2003).

[32] D. Wilkowski, Y. Bidel, T. Chanelière, D. Delande, T. Jonckheere, B. Klappauf, G. Labeyrie, C. Miniatura, C. A. Müller, O. Sigwarth, and R. Kaiser, J. Opt. Soc. Am. B **21**, 183 (2004).

[33] T. Chanelière, D. Wilkowski, Y. Bidel, R. Kaiser, and C. Miniatura, Phys. Rev. E **70**, 036602 (2004).

[34] D. V. Kupriyanov, I. M. Sokolov, C. I. Sukenik, and M. D. Havey, Laser Phys. Lett **3**, 223 (2006).

[35] I. M. Sokolov, D. V. Kupriyanov, and M. D. Havey, J. Mod. Opt. **58**, 1928 (2011).

[36] F. Jendrzejewski, K. Müller, J. Richard, A. Date, T. Plisson, P. Bouyer, A. Aspect, and V. Josse, Phys. Rev. Lett. **109**, 195302 (2012).

[37] N. M. Estakhri, N. Mohammadi Estakhri, and T. B. Norris, Scientific Reports **12**, 22256 (2022).

[38] M. Safadi, O. Lib, H.-C. Lin, C. W. Hsu, A. Goetschy, and Y. Bromberg, Nature Physics **19**, 562 (2023).

[39] R. R. Moseley, S. Shepherd, D. J. Fulton, B. D. Sinclair, and M. H. Dunn, Opt. Commun. **119**, 61 (1995).

[40] J. Wang, L. B. Kong, X. H. Tu, K. J. Jiang, K. Li, H. W. Xiong, Y. Zhu, and M. S. Zhan, Phys. Lett. A **328**, 437 (2004).

[41] M. Fleischhauer, A. Imamoglu, and P. J. Marangos, Rev. Mod. Phys. **77**, 633 (2005).

[42] A. J. Olson and S. K. Mayer, Am. J. Phys. **77**, 116 (2009).

[43] A. Lazoudis, T. Kirova, E. H. Ahmed, L. Li, J. Qi, and A. M. Lyyra, Phys. Rev. A **82**, 023812 (2010).

[44] S. K. Nath, V. Naik, A. Chakrabarti, and A. Ray, J. Opt. Soc. Am. B **36**, 2610 (2019).

[45] M. H. Oliveira, C. E. Máximo, and C. J. Villas-Boas, Phys. Rev. A **104**, 63704 (2021).

[46] R. Finkelstein, S. Bali, O. Firstenberg, and I. Novikova, New J. Phys. **25**, 035001 (2023).

[47] G. Labeyrie, D. Delande, C. Müller, C. Miniatura, and R. Kaiser, Opt. Commun. **243**, 157 (2004).

[48] S. Pustelny, W. Lewoczko, and W. Gawlik, J. Opt. Soc. Am. B **22**, 37 (2005).

[49] J. Chabé, M. T. Rouabah, L. Bellando, T. Bienaimé, N. Piovella, R. Bachelard, and R. Kaiser, Phys. Rev. A **89**, 043833 (2014).

[50] R. Bachelard, N. Piovella, W. Guerin, and R. Kaiser, Phys. Rev. A **94**, 033836 (2016).

[51] I. M. Sokolov and W. Guerin, J. Opt. Soc. Am. B **36**, 2030 (2019).

[52] K. J. Kemp, S. J. Roof, M. D. Havey, I. M. Sokolov, D. V. Kupriyanov, and W. Guerin, Phys. Rev. A **101**, 033832 (2020).

[53] D. Budker, D. Kimball, and D. DeMille, *Atomic Physics : An Exploration through Problems and Solutions*, 2nd ed. (Oxford University Press, 2008).

[54] A. Edmonds, *Angular Momentum in Quantum Mechanics*, 2nd ed. (Princeton University Press, 1957).

[55] R. N. Zare, *Angular Momentum : Understanding Spactial Aspects in Chemistry and Physics* (Wiley, 1988).

[56] D. Brink and G. Satchler, *Angular Momentum*, 2nd ed. (Oxford University Press, 1968).

[57] I. I. Sobelman, *Atomic Spectra and Radiative Transitions*, 2nd ed. (Springer, 1992).

[58] M. Weissbluth, *Atoms and Molecules* (Academic Press, Inc, 1978).

[59] R. Loudon, *The Quantum Theory Of Light*, 2nd ed. (Oxford University Press, 1983).

[60] J. Weiner, *Light-Matter Interaction : Fundamentals and Applications* (John Wiley & Sons, 2002) pp. 41–60.

[61] J. Carter, Ph.D. thesis, Old Dominion University, 2024 (to be published).

[62] D. A. Steck (2001), *Rubidium 87 D Line Data* (ver. 2.2.2), [Online]. Available: http://steck.us/alkalidata [2016, August 1].

[63] A. McNair and H. W. Wilson, Philos. Mag. **6**, 563 (1961).

[64] A. Kramida, Yu. Ralchenko, J. Reader, and NIST ASD Team (2022), *NIST Atomic Spectra Database* (ver. 5.10), [Online]. Available: https://physics.nist.gov/asd [2022, October 19].

[65] R. W. Schmieder, Am. J. Phys. **40**, 297 (1972).

[66] J. D. Jackson, *Classical Electrodynamics*, 3rd ed. (Wiley, 1999).

[67] T. Walker and D. Pritchard, Laser Physics **4**, 1085 (1994).

[68] F. Spiegelmann, D. Pavolini, and J. P. Daudey, J. Phys. B **22**, 2465 (1989).

[69] T. Bienaimé, M. Petruzzo, D. Bigerni, N. Piovella, and R. Kaiser, J. Mod. Opt. **58**, 1942 (2011).

[70] T. Bienaimé, R. Bachelard, N. Piovella, and R. Kaiser, Fortschr. Phys. **61**, 377 (2013).

[71] M. Samoylova, N. Piovella, M. Holynski, P. W. Courteille, and R. Bachelard, in *Annual Review of Cold Atoms and Molecules* (2014) pp. 193–249.

[72] M. Samoylova, N. Piovella, R. Bachelard, and P. W. Courteille, Opt. Commun. **312**, 94 (2014).

[73] V. Weisskopf and E. Wigner, Physik **63**, 54 (1930).

[74] R. T. Sutherland and F. Robicheaux, Phys. Rev. A **93**, 023407 (2016).

[75] E. L. Raab, M. Prentiss, A. Cable, S. Chu, and D. E. Pritchard, Phys. Rev. Lett. **59**, 2631 (1987).

[76] D. Sesko, T. Walker, T. Monroe, A. Gallagher, and C. Wieman, Phys. Rev. Lett. **63**, 961 (1989).

[77] C. Monroe, W. Swann, H. Robinson, and C. Wieman, Phys. Rev. Lett. **65**, 1571 (1990).

[78] C. D. Wallace, T. P. Dinneen, K. N. Tan, T. T. Grove, and P. L. Gould, Phys. Rev. Lett. **69**, 897 (1992).

[79] R. S. Schappe, T. Walker, L. W. Anderson, and C. C. Lin, Phys. Rev. Lett. **76**, 4328 (1996).

[80] S. D. Gensemer, V. Sanchez-Villicana, K. Y. N. Tan, T. T. Grove, and P. L. Gould, Phys. Rev. A **56**, 4055 (1997).

[81] V. Vuletic, C. Chin, A. J. Kerman, and S. Chu, Phys. Rev. Lett. **81**, 5768 (1998).

[82] H. C. Busch, M. K. Shaffer, E. M. Ahmed, and C. I. Sukenik, Physical Review A **73**, 023406 (2006).

[83] K. J. Matherson, R. D. Glover, D. E. Laban, and R. T. Sang, Phys. Rev. A **78**, 042712 (2008).

[84] K. Ladouceur, B. G. Klappauf, J. Van Dongen, N. Rauhut, B. Schuster, A. K. Mills, D. J. Jones, and K. W. Madison, J. Opt. Soc. Am. B **26**, 210 (2009).

[85] N. B. Vilas, C. Hallas, L. Anderegg, P. Robichaud, A. Winnicki, D. Mitra, and J. M. Doyle, Nature **606**, 70 (2022).

[86] H. J. Metcalf and P. van der Straten, *Laser Cooling and Trapping* (Springer, 2001).

[87] S. Chu, L. Hollberg, J. E. Bjorkholm, A. Cable, and A. Ashkin, Phys. Rev. Lett. **55**, 48 (1985).

[88] P. D. Lett, W. D. Phillips, S. L. Rolston, C. E. Tanner, R. N. Watts, and C. I. Westbrook, J. Opt. Soc. Am. B **6**, 2084 (1989).

[89] S. Balik, Ph.D. thesis, Old Dominion University, 2009.

[90] D. W. Preston, Am. J. Phys. **64**, 1432 (1996).

[91] Y. C. Chen, Y. A. Liao, L. Hsu, and I. Yu, Phys. Rev. A **64**, 031401 (2001).

[92] R. Grimm, M. Weidemüller, and Y. B. Ovchinnikov, Adv. At. Mol. Phys. **42**, 95 (2000).

[93] D. J. Griffiths, *Introduction to Electrodynamics*, 4th ed. (PHI, 2014).

[94] B. Arora, M. S. Safronova, and C. W. Clark, Phys. Rev. A **76**, 052509 (2007).

[95] M. S. Safronova and U. I. Safronova, Phys. Rev. A **83**, 052508 (2011).

[96] B. Arora and B. K. Sahoo, Phys. Rev. A **86**, 033416 (2012).

[97] M. S. Safronova, W. R. Johnson, and A. Derevianko, Phys. Rev. A **60**, 4476 (1999).

[98] M. S. Safronova, C. J. Williams, and C. W. Clark, Phys. Rev. A **69**, 022509 (2004).

[99] E. J. Robertson, N. Šibalić, R. M. Potvliege, and M. P. Jones, Comput. Phys. Commun. **261**, 107814 (2021).

[100] I. Kovacic, R. Rand, and S. M. Sah, Appl. Mech. Rev. **70**, 020802 (2018).

[101] E. Doering (2018), *Event-driven producer-consumer state machine*, [Online]. Available: https://learn-cf.ni.com/teach/riodevguide/code/pc_producer-consumer-state-machine.html [2019, January 2].

[102] C. H. Greene and R. N. Zare, Ann. Rev. Phys. Chem **33**, 119 (1982).

[103] B. Darquié, M. P. Jones, J. Dingjan, J. Beugnon, S. Bergamini, Y. Sortais, G. Messin, A. Browaeys, and P. Grangier, Science **309**, 454 (2005).

[104] E. Tiesinga, P. J. Mohr, D. B. Newell, and B. N. Taylor (2018), *The 2018 CODATA Recommended Values of the Fundamental Physical Constants* (ver 8.1), [Online]. Available: http://physics.nist.gov/constants [2022, October 19].

[105] F. Nez, F. Biraben, R. Felder, and Y. Millerioux, Opt. Commun. **102**, 432 (1993).

[106] W. F. Holmgren, M. C. Revelle, V. P. Lonij, and A. D. Cronin, Phys. Rev. A **81**, 053607 (2010).

[107] Y. J. Chen, L. F. Gonçalves, and G. Raithel, Phys. Rev. A **92**, 060501 (2015).

[108] A. Franzen and the Gravitational Wave Group (2006), *ComponentLibrary*, [Online]. Available: https://www.gwoptics.org/ComponentLibrary [2018, August 7].

APPENDIX A

USEFUL CONSTANTS AND VALUES

The constants given in Tables 9 and 10 were used throughout this dissertation in many calculations. The hyperfine constants given in Tables 11 and 12 were used to calculate the energy level diagram shown in Fig. 1 as well as for the static and dynamic Stark shifts. The polarizabilities given in Table 13 were needed to calculate the static and dynamic Stark shifts. The dynamic polarizabilities are with respect to 1064 nm light. Finally, a small compendium of ^{87}Rb dynamic polarizabilities (1064 nm) are given in Table 14. These values were calculated using the ARC-Alkali python package. It must be noted that the dynamic polarizabilities listed in Table 14 for the $5S_{1/2}$ and $5P_{3/2}$ differ from the values presented in Tables 2 and 3 because ARC uses slightly different RDMEs.

TABLE 9: Useful Constants.[a]

Permittivity of Vacuum	ϵ_0	$8.854\ 187\ 8128(13)\times10^{-12}$ F/m
Electron Mass	m_e	$9.109\ 383\ 7015(28)\times10^{-31}$ kg
Speed of Light	c	$2.997\ 924\ 58\times10^{8}$ m/s
Bohr Radius	a_0	$5.291\ 772\ 109\ 03(80)\times10^{-11}$ m
Boltzmann's Constant	k_B	$1.380\ 649\times10^{-23}$ J/K $2.083\ 661\ 912...\ \times10^{10}$ Hz/K $8.617\ 333\ 262...\ \times10^{-5}$ eV/K
Planck Constant	h	$6.626\ 070\ 15\times10^{-34}$ Js
Hartree Energy	E_h	$4.349\ 744\ 722\ 2071(85)\times10^{-18}$ J
	ω_h	$4.134\ 118\ 709\ 5917\times10^{16}$ Hz

[a]Reference [104].

TABLE 10: ^{87}Rb Physical Properties and Useful Values.[a]

^{87}Rb Atomic Mass	m	1.443 160 648(72)$\times 10^{-25}$ kg
Nuclear Spin	I	3/2
^{87}Rb D_2 ($5^2S_{1/2} \rightarrow 5^2P_{3/2}$) Properties		
Resonant Frequency	ω_0	$2\pi \cdot$ 384.230 484 468 5(62) THz
Wavelength (Vacuum)	λ	780.241 209 686(13) nm
Wavelength (Air)	λ_{air}	780.032 700 9(78) nm
Isotope Shift	$\omega_0(^{87}\text{Rb}) - \omega_0(^{85}\text{Rb})$	$2\pi \cdot$ 78.095(12) MHz
Lifetime	τ	26.2348(77) ns
Decay Rate	Γ	38.117(11)$\times 10^{-6}$ s^{-1}
Natural Line Width (FWHM)		$2\pi \cdot$ 6.06656(178) MHz

[a]Reference [62].

TABLE 11: ^{87}Rb Hyperfine Structure Constants. A represents the magnetic dipole constant while B represents the electric quadrupole constant.

Structure Constant	Value
$A_{5^2S_{1/2}}$	$h \cdot$ 3.417 341 305 452 145(45)[a] GHz
$A_{5^2P_{1/2}}$	$h \cdot$ 407.25(63)[a] MHz
$A_{5^2P_{3/2}}$	$h \cdot$ 84.7185(20)[a] MHz
$B_{5^2P_{3/2}}$	$h \cdot$ 12.4965(37)[a] MHz
$A_{5^2D_{3/2}}$	$h \cdot$ 14.5080(6)[b] MHz
$B_{5^2D_{3/2}}$	$h \cdot$ 0.9320(17)[b] MHz
$A_{5^2D_{5/2}}$	$h \cdot$ -7.4923(3)[b] MHz
$B_{5^2D_{5/2}}$	$h \cdot$ 1.2713(20)[b] MHz

[a]Reference [62].
[b]Reference [105].

TABLE 12: ^{85}Rb Hyperfine Structure Constants. A represents the magnetic dipole constant while B represents the electric quadrupole constant.

Structure Constant	Value
$A_{5^2S_{1/2}}$	$h \cdot 1.011\ 901\ 813\ 0(20)$[a] GHz
$A_{5^2P_{1/2}}$	$h \cdot 120.527(56)$[a] MHz
$A_{5^2P_{3/2}}$	$h \cdot 25.0020(99)$[a] MHz
$B_{5^2P_{3/2}}$	$h \cdot 25.790(93)$[a] MHz
$A_{5^2D_{3/2}}$	$h \cdot$ -4.2221(2)[b] MHz
$B_{5^2D_{3/2}}$	$h \cdot 1.9105(8)$[b] MHz
$A_{5^2D_{5/2}}$	$h \cdot$ -2.1911(12)[b] MHz
$B_{5^2D_{5/2}}$	$h \cdot 2.6804(200)$[b] MHz

[a]Reference [62].
[b]Reference [105].

TABLE 13: ^{87}Rb Static and Dynamic Polarizabilities. Obtained values presented from sources converted, if necessary, to both Hz/(V/cm)^2 and atomic units (a.u.).

^{87}Rb Static Polarizabilities		
Ground State Polarizability	$\alpha_0(5^2S_{1/2})$	$h \cdot 0.0794(16)$[a] Hz/(V/cm)^2 319.091(6.430) a.u.
		$h \cdot 0.079432(35)$ Hz/(V/cm)^2 318.791(1.417) a.u. 47.24(21)[b] 10^{-24} cm^3
D_2 Scalar Polarizability	$\alpha_0(5^2P_{3/2})$	$h \cdot 0.2134(18)$[a] Hz/(V/cm)^2 857.607(7.189) a.u.
D_2 Tensor Polarizability	$\alpha_2(5^2P_{3/2})$	$-h \cdot 0.0406(8)$[a] Hz/(V/cm)^2 $-163.162(3.215)$ a.u.
^{87}Rb Dynamic Polarizabilities (1064 nm)		
Ground State Polarizability	$\alpha_0(5^2S_{1/2})$	$h \cdot 0.17102(13)$ Hz/(V/cm)^2 687.3(5)[c] a.u.
D_2 Scalar Polarizability	$\alpha_0(5^2P_{3/2})$	$-h \cdot 0.2859(55)$ Hz/(V/cm)^2 $-1149(22)$[d] a.u.
D_2 Tensor Polarizability	$\alpha_2(5^2P_{3/2})$	$h \cdot 0.1401(55)$ Hz/(V/cm)^2 563(22)[d] a.u.

[a]Reference [62].
[b]Reference [106].
[c]Reference [96].
[d]Reference [107].

TABLE 14: ^{87}RB Dynamic Polarizabilities at 1064 nm from ARC. Sum over first n=30 states. Values given in a.u. To convert to standard units, multiply by $4\pi\epsilon_0 a_0^3$.

State	α_0	α_2	State	α_0	α_2	State	α_0	α_2
$5S_{1/2}$	687.9931	0	$5P_{1/2}$	-1185.1487	0	$4D_{3/2}$	404.0961	-287.3365
$6S_{1/2}$	-113.4664	0	$5P_{3/2}$	-1077.7955	598.1909	$4D_{5/2}$	373.2297	-362.9142
$7S_{1/2}$	-590.6137	0	$6P_{1/2}$	-634.3448	0	$5D_{3/2}$	-521.6150	15.3594
$8S_{1/2}$	-527.0148	0	$6P_{3/2}$	-540.3885	-200.3582	$5D_{5/2}$	-529.5412	34.1981
$9S_{1/2}$	-519.5515	0	$7P_{1/2}$	-427.3119	0	$6D_{3/2}$	-389.1748	-37.4995
$10S_{1/2}$	-517.4495	0	$7P_{3/2}$	-419.2217	-39.5477	$6D_{5/2}$	-392.2215	-49.9661
			$8P_{1/2}$	-530.5798	0	$7D_{3/2}$	-423.3979	-26.4847
			$8P_{3/2}$	-530.7321	12.8572	$7D_{5/2}$	-423.5073	-37.4494
			$9P_{1/2}$	-471.3418	0	$8D_{3/2}$	-434.7171	-29.1001
			$9P_{3/2}$	-469.8773	-17.5189	$8D_{5/2}$	-434.3610	-41.7723
			$10P_{1/2}$	-480.5100	0	$9D_{3/2}$	-445.8772	-29.6086
			$10P_{3/2}$	-478.6897	-17.3607	$9D_{5/2}$	-445.4646	-42.5783
						$10D_{3/2}$	-454.5882	-29.7161
						$10D_{5/2}$	-454.2300	-42.6069

APPENDIX B

CODES

B.1 MATHEMATICA

Full Mathematica notebooks are available upon request.

B.1.1 ENERGY LEVEL DIAGRAM

This is the basic Mathematica version 10.4 code to calculate the hyperfine shifts and was simply put into a loop to make the energy level diagrams. Output is in units of MHz.

Mathematica functions for hyperfine energy levels.

```
KVal[J_, I_, F_] := F (F + 1) − I (I + 1) − J (J + 1);
WfES[A_, B_, K_, I_, J_] := (1/2) A∗K + B (3/2)(K(K + 1) − 2I(I + 1)J(J + 1)) / (2I(2I − 1)2J(2J − 1));
WfGS[A_, B_, K_, I_, J_] := (1/2) A∗K;

In[1]:= WfES[84.7185, 12.4965, KVal[3/2, 3/2, 2], 3/2, 3/2]
Out[2]= −72.9113
```

B.1.2 POLARIZABILITY

These are the polarizability functions which are defined by Eq. (238) and Eq. (239). EDiff is the difference obtained from the NIST values which must be converted to atomic units using the Hartree energy as described in Section 3.2.1.3.

Basic Mathematica functions for polarizability calculations.

```
Alpha0[J_, ω_, EDiff_, RDME_] :=
        (2/(3(2J + 1)))∗( (RDME^2∗(EDiff))/((EDiff)^2 − ω^2) );

Alpha2[J_, ω_, EDiff_, RDME_, Jk_] :=
        (−4)∗Sqrt[( (5J(2J − 1))/(6(J + 1)(2J + 1)(2J + 3)) )]∗
        (−1)^(J + Jk + 1)∗( (RDME^2∗(EDiff))/((EDiff)^2 − ω^2) )∗
        SixJSymbol[{J, 1, Jk}, {1, J, 2}];
```

B.1.3 COUPLED DIPOLE MODEL - RUNGE KUTTA

Mathematica version 10.4 code to calculate the coupled dipole model time dependent scattered intensity at a particular detection angle. The basic loop performs the 4th order Runge-Kutta method to obtain the excited state amplitudes β_j.

Coupled dipole model simulation using 4th order Runge-Kutta.

```
(*Define Runge-Kutta functions*)
yiPlusOne[yi_,k1_,k2_,k3_,k4_]:=yi+(k1+2*k2+2*k3+k4)/6;
k1[h_,A_,b_, yi_, ti_, pulselength_]:=h(A.yi+If[ti>pulselength,0,b]);
k2[h_,A_,b_, yi_,k1_, ti_, pulselength_]:=h((A.(yi+k1/2))+If[(ti+h/2)>pulselength,0,b]);
k3[h_,A_,b_, yi_,k2_, ti_, pulselength_]:=h((A.(yi+k2/2))+If[(ti+h/2)>pulselength,0,b]);
k4[h_,A_,b_, yi_,k3_, ti_, pulselength_]:=h((A.(yi+k3))+If[(ti+h)>pulselength,0,b]);
(*Initialize Simulation Parameters*)
{numOfEnsembles,tEnd,ss}={100,200,0.001};
{numOfAtoms,pulselength,numOftimesteps}={100,0.17,tEnd/ss};
{thetaValk,phiValk}={(180+(45+22.33)),0}*\[Pi]/180;(*Laser angle*)
{thetaVal,phiVal}={90,0}*\[Pi]/180;(*Detection angle*)
{detuningVal,rabiVal}={0,0.01};(*Units of Natural Decay Rate*)
scatteredIntens=0;

Do[(*Loop for many random ensembles*)

(*Create Random Atom Distribution*)
While[Length[atomPositions] < numOfAtoms,
  {xVal, yVal, zVal} =
   Flatten[{RandomVariate[NormalDistribution[0, r0prob], 2],
     RandomVariate[NormalDistribution[0, z0prob], 1]}];
  atomPositions = Append[atomPositions, {xVal, yVal, zVal}];
];

(*M Matrix function*)
Mjm[\[CapitalDelta]_, j_, m_,atomPositions_]:= If[j==m,(I*\[CapitalDelta]-(1/2)), (I/2)*Exp[I*
    EuclideanDistance[atomPositions[[j]], atomPositions[[m]]]]/EuclideanDistance[atomPositions[[j]],
    atomPositions[[m]]]    ];

(*Create the M matrix, calling it A here*)
A=Table[Table[Mjm[detuningVal,j,m,atomPositions],{j,1,numOfAtoms}],{m,1,numOfAtoms}];
(*Create the b(t)*)
(*The k1-k4 take care of the time dependence based on pulselength*)
```

```
bt=Table[(−I/2)∗rabiVal∗Exp[I∗( {Sin[thetaValk]∗Cos[phiValk],Sin[thetaValk]∗Sin[phiValk], Cos[thetaValk
    ]}.atomPositions[[ i ]])  ],{ i ,1, numOfAtoms}];

(*Loop over the number of time steps∗)
(*initial condition, all betaj's are zero.∗)
X0=Table[0,{i,1,numOfAtoms}];
temptimedep=Append[{},X0];(*yiPlusOne added at end of each timestep∗)
tempti=0;
Do[
  k1i=k1[ss,A,bt,Last[temptimedep],tempti, pulselength ];
  k2i=k2[ss,A,bt,Last[temptimedep],k1i,tempti, pulselength ];
  k3i=k3[ss,A,bt,Last[temptimedep],k2i,tempti, pulselength ];
  k4i=k4[ss,A,bt,Last[temptimedep],k3i,tempti, pulselength ];
(*adds yi+1 to the list, Each component of this "list" will be the value of all betaj's at a particular time step∗)
  temptimedep=Append[temptimedep, yiPlusOne[Last[temptimedep],k1i,k2i,k3i,k4i]];
  tempti=tempti+ss;
  Clear[k1i, k2i, k3i, k4i];
,{ i ,1, numOftimesteps}];

(*Time dependent scattered intensity at the detection angle∗)
scatteredIntens = scatteredIntens+Abs[Sum[temptimedep[[All,i]]∗Exp[−I∗(1)∗{Sin[thetaVal]∗Cos[phiVal],Sin
    [thetaVal]∗Sin[phiVal], Cos[thetaVal]}.atomPositions[[ i ]]  ],{ i ,1, numOfAtoms}]]^2;

,{ j ,1, numOfEnsembles}];
(*Average over the numOfEnsembles∗)
scatteredIntens =scatteredIntens/numOfEnsembles;
(*Add time component, in units of natural lifetime∗)
scatteredIntens =Transpose[{Table[i,{i,0,tEnd,ss }], scatteredIntens }];

Export["NameYourFile.dat",scatteredIntens,"Package"];

(*One may loop the above over many random ensembles∗)
```

B.2 PYTHON

B.2.1 DYNAMIC POLARIZABILITY

All Python code was performed in the JupyterLab 3.4.4. environment due to its similarity to Mathematica. The ARC 3.0 package was used to obtain the dynamic polarizabilities.

n, l, j ranges can be changed to any values. The code automatically ignores errors given by transitions which are forbidden. The output file will provide n, l, j, α_0, α_2, α_{core} on each line.

^{87}Rb dynamic polarizabilities using ARC 3.0.

```
# Brent Jones 10-31-22 Old Dominion University
##Config setup taken from the Arc website##
# Configure the matplotlib graphics library and configure it to show
# figures inline in the notebook
%matplotlib inline
import matplotlib.pyplot as plt # Import library for direct plotting functions
import numpy as np              # Import Numerical Python
from IPython.display import display, HTML #Import HTML for formatting output
import arc
from arc import *               #Import ARC (Alkali Rydberg Calculator)

atom = Rubidium87()
# initialize an array of 6 numbers, [n, l, j, alpha0, alpha2, alphaCore].
DynPolList = np.asarray([ [0,0,0,0,0,0] ])
for n in range(4,6): #loop through n values
    for l in range(0,3):# loops through l (s,p,d,f)
        for j in range(0,l+1): # loops through J starting at 1/2.
            try: # block raising an exception. Basically if there is an error here,
                all values are set to 0.
                calc = DynamicPolarizability(atom, n, l, j+1/2)
                calc.defineBasis(atom.groundStateN, 30)
                alpha0, alpha1, alpha2, alphaC, alphaP, closestState = calc.
                    getPolarizability(1064e-9, units="a.u.",
                    accountForStateLifetime=False)
            except:
                alpha0, alpha1, alpha2, alphaC, alphaP, closestState =
                    0,0,0,0,0,[0,0,0,0]
                pass # doing nothing on exception
            if alpha0 == 0: #if the alpha0 is zero, do not add it to the list
                pass #do nothing
```

```
            else:
                DynPolList = np.append(DynPolList,[ [n, l,j+1/2, alpha0,
                    alpha2, alphaC] ],axis=0)
DynPolList=np.delete(DynPolList,0,axis=0) #deletes the initial [0,0,0,0,0,0,0].

#Export to .csv
np.savetxt("DynamicPolRb87.csv", DynPolList, delimiter=",")
```

APPENDIX C

OPTICAL ELEMENTS

The optical elements used in various optical diagrams throughout this dissertation. While some have been modified, the drawings were created by Alexander Franzen [108].

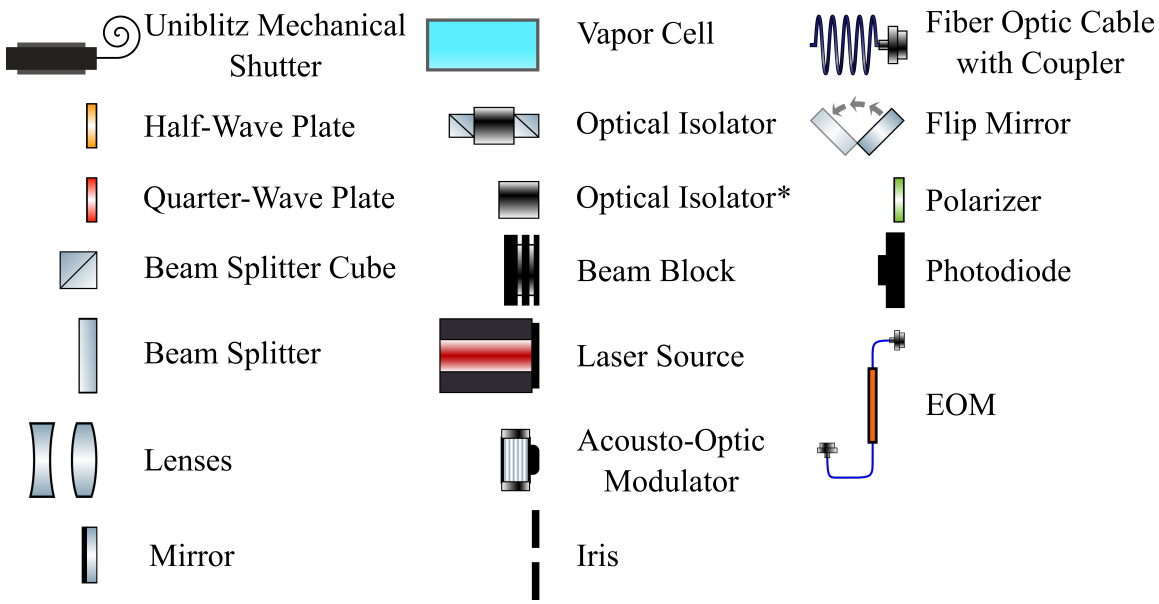

FIG. 103: Legend of optical diagram elements. The optical isolator denoted with a $*$ represent the factory aligned and fixed type.

VITA

Brent Michael Jones
Department of Physics
Old Dominion University
Norfolk, VA 23529

EDUCATION

Ph. D. Physics, *Investigation of cooperative subradiance in dense ultracold rubidium ensembles*, Old Dominion University, Norfolk, VA, August 2024. **Advisor:** Dr. Charles Sukenik
M.S. Physics, Old Dominion University, Norfolk, VA, May 2018.
B.S. Physics, Old Dominion University, Norfolk, VA, August 2016.

PUBLICATIONS

Investigation of Cooperative Subradiance in Dense Ultracold Rubidium Ensembles, B. M. Jones, J. D. Carter, C. I. Sukenik, M. D. Havey, In preparation.
Coherent Backscattering Under Conditions of Electromagnetically Induced Transparency, J. D. Carter, B. M. Jones, C. I. Sukenik, M. D. Havey, In preparation.
Raman Scattering and Atom Counting in Cold Rubidium Gas, B. M. Jones, J. D. Carter, M. D. Havey, C. I. Sukenik, In preparation.
Atom Counting by Hyperfine Raman Optical Pumping in Cold ^{87}Rb, B. M. Jones, J. D. Carter, S. J. Roof, K. J. Kemp, M. D. Havey, DAMOP 2019, Milwaukee, WI.

AFFILIATIONS

College of Sciences Graduate Student Advisory Committee
Physics Graduate Student Association

Typeset using LaTeX.